UNIVERSITY OF OKLAHOMA

GRADUATE COLLEGE

3DVAR AND CLOUD ANALYSIS WITH WSR-88D Level-II DATA FOR THE PREDICTION OF TORNADIC THUNDERSTORMS

A Dissertation

SUBMITTED TO THE GRADUATE FACULTY

in partial fulfillment of the requirements for the

degree of

Doctor of Philosophy

By

Ming Hu

Norman, Oklahoma

2005

Downloaded from SHAREOK. Persistent Handle URL: https://hdl.handle.net/11244/955

UMI Number: 3203315

UMI®

UMI Microform 3203315

Copyright 2006 by ProQuest Information and Learning Company.
All rights reserved. This microform edition is protected against
unauthorized copying under Title 17, United States Code.

ProQuest Information and Learning Company
300 North Zeeb Road
P.O. Box 1346
Ann Arbor, MI 48106-1346

3DVAR AND CLOUD ANALYSIS WITH WSR-88D Level-II DATA FOR THE PREDICTION OF TORNADIC THUNDERSTORMS

A Dissertation APPROVED FOR THE
SCHOOL OF METEOROLOGY

BY

Ming Xue, Chair

Frederick Carr

Lance Leslie

Qin Xu

Luther White

Jidong Gao

© Copyright by Ming Hu 2005
All Rights Reserved.

ACKNOWLEDGEMENTS

I thank my advisor, Dr. Ming Xue, for his support, guidance, and above all his gentle spirit. The weekly meeting times with Dr. Xue over the years have been the most productive and pleasant hours of each week. I thank the members of my doctoral committee, Drs Frederick Carr, Lance Leslie, Qin Xu, Luther White, and Jidong Gao, for their assistance, encouragement, and helpful suggestions.

Thanks are also due to the ARPS developers, most of whom I even did not have a chance to meet. Their hard work in developing this wonderful forecast system laid the foundation for my research. Particularly, Drs. Keith Brewster, Bill Martin, and Alan Shapiro are thanked for very helpful discussions. Yunheng Wang is thanked for his professional help in code development and Scott Hill for his computer system support.

Furthermore, special thanks also go to the School of Meteorology staff Celia and Marcia, and CAPS staff Eileen and Debra. Their kind help made my study here a lot easier.

Last, but not least, I could not have fulfilled my dream here without the support and sacrifice of my family. My parents always understand and support my choices; my parents-in-law helped me out by taking care of my daughter for 3 years; and my wife, Ruifang, and daughter, Xiaoyu, who accompanied me through all challenges, made and continue to make my life such a joy.

This research was supported by NSF Grants ATM-9909007, ATM-0129892, and a DOT-FAA grant via DOC-NOAA NA17RJ1227. Most of the experiments were performed on the supercomputers of OSCER, University of Oklahoma, and supercomputers at Pittsburgh Supercomputing Center.

Table of Contents

ACKNOWLEDGEMENTS ..... **iv**

Table of Contents ..... **v**

List of Tables ..... **viii**

List of Figures ..... **ix**

Abstract ..... **xviii**

Chapter 1 General Introduction **1**

Chapter 2 Motivation, Methodology, and Tools **6**

2.1 Motivation and methodology 6

2.2 ARPS system and ARPS model 8

2.3 ARPS 3DVAR system 10

2.3.1 Basic scheme 10

2.3.2 Radar radial velocity 12

2.3.3 Recursive filter in ARPS 3DVAR 12

2.3.3.1 Standard recursive filter algorithm 12

2.3.3.2 Lateral boundary conditions of recursive filter 13

2.3.3.3 The overshooting problem 15

2.3.3.4 Overshooting problem in radar radial velocity analysis 20

2.3.4 Mass divergence constraint 25

2.4 ARPS cloud analysis 33

2.4.1 The analysis of precipitation species 34

2.4.1.1 The reflectivity equations 34

2.4.1.2 The initial determination of hydrometeors from reflectivity 35

2.4.1.3 The final analysis of hydrometeors 36

2.4.2 The analysis of cloud water and cloud ice 38

2.4.3 In-cloud thermal adjustment 41

Chapter 3 28 March 2000 Fort Worth, Texas, Tornadic Thunderstorm Case **43**

3.1 The case 43

3.2 Design of experiments 44

3.3 Impact of cloud analysis with reflectivity 49

3.3.1 Radar observations 49

3.3.2 Results of experiments CNTLZ and X03 52

3.3.2.1 Subjective evaluation 52

3.3.2.2 Evaluation with ETS 57

3.3.3 Experiments without radar data 60

3.3.4 Sensitivity to details of cloud analysis 61

3.3.4.1 Assimilation results 62

3.3.4.2 Forecast results 66
3.4 Impact of radial velocity analysis via 3DVAR 71
3.4.1 Forecasting results of experiment CNTLVR 71
3.4.2 Forecasting results of experiment using reflectivity only 80
3.4.3 Forecasting results of experiment using radial velocity only 84
3.4.4 Comparison of assimilation results 87
3.4.5 Experiments on mass divergence constraint 89
3.4.5.1 Importance of divergence constraint 89
3.4.5.2 Sensitivity to weighting coefficient of divergence constraint 95
3.4.5.3 Effects of divergence constraint formulations 95
3.4.5.4 Results of assimilation from divergence constraint experiments 97
3.5 Summary and discussion 99
Chapter 4 8 May 2003 Oklahoma City, Oklahoma, Tornadic Thunderstorm Case 104
4.1 The case 104
4.2 Impact of configurations of rapid intermittent assimilation of radar data 107
4.2.1 Design of assimilation and forecast experiments 107
4.2.2 Results of assimilation and forecast experiments 110
4.2.2.1 Experiment with the best forecast 111
4.2.2.2 Impact of the frequency of analysis cycles 114
4.2.2.3 Impact of in-cloud temperature adjustment schemes 119
4.2.2.4 Impact of the length and temporal coverage of assimilation window 124
4.2.2.5 Results of experiment 5B60E30LH 128
4.2.3 Further discussions 130
4.2.4 Summary 135
4.3 High resolution experiments 136
4.3.1 Experiments with 1-km horizontal grid spacing 137
4.3.1.1 Experimental design 137
4.3.1.2 Experiment results 139
4.3.1.2.1 Results of data assimilation 139
4.3.1.2.2 Forecasting results 142
4.3.1.2.2.1 Maximum surface vertical vorticity 142
4.3.1.2.2.2 Forecast in the first period 144
4.3.1.2.2.3 Forecast in the second stage 147
4.3.1.2.3 Remaining problems with 1-km forecasts 157
4.3.1.3 Summary 159
4.3.2 Preliminary experiment with 100-m horizontal grid spacing 161
4.3.2.1 Experimental design 161
4.3.2.2 Experiment results 161
4.3.2.3 Summary and discussion 167
Chapter 5 29 May 2004 Central Oklahoma Tornadic Thunderstorm Case 169

5.1 The case 169
5.2 Design of experiments 176
5.3 Results of phase correction experiments 178
5.3.1 Forecast from experiment PCLD 178
5.3.2 Results of phase-corrected assimilation and forecast 185
5.4 Results of experiments on dual-Doppler analysis of radial velocity data 189
5.4.1 Results of 3DVAR radial velocity analysis 189
5.4.2 Results of the first-hour forecasts 192
5.4.3 Long-term forecasting 201
5.5 Summary and discussion 201
Chapter 6 General Summary and Future Work 205
References 210
Appendix. Boundary Conditions of Multipass Recursive Filters 214

List of Tables

Table 2.1 The boundary conditions of the first 4 filter passes..... 14

Table 3.1. List of 3-km experiments and their main characteristics for the cloud analysis. 48

Table 3.2. List of 3-km experiments and their main characteristics for the radial velocity analysis and mass divergence constraint..... 48

Table 4.1. Assimilation configurations of the 3-km experiments..... 110

Table 5.1* The features of the 29 May 2004 central Oklahoma tornadoes..... 171

Table 5.2 List of the 3-km experiments testing the dual-Doppler analysis 178

List of Figures

Fig. 2.1 Results of ideal experiment on the effectiveness of the boundary conditions..... 16

Fig. 2.2 Results of recursive filter applying to two unit observations with 10 grid points apart. Horizontal decorrelation scale, R, is 5, 10, and 20 grid points. 17

Fig. 2.3 3DVAR analysis is applied to two U observations. The observation values are 10 m s^{-1} and located 10 grid spacings apart. Background field is set to 0. The recursive filter is used to model background error correlation. a) Analysis without the recursive filter. b) Analysis using the recursive filter in which the horizontal decorrelation scale is 10 grid spacings. c) Same as b) but the horizontal decorrelation scale is 40 grid spacings..... 19

Fig. 2.4 3DVAR analysis is applied to 100 U observations concentrated on an area like radar radial wind. The observation values are 10 m s^{-1} and background field is set to 0. The recursive filter is used to model background error correlation. a) Analysis of a square-shaped observation area with the horizontal decorrelation scale set to 1 grid spacing. b) Similar to a) but with the horizontal decorrelation scale set to 3 grid spacings. c) Analysis of four square-shaped observation areas that have 2 grid spacing missing observations or holes among them. The horizontal decorrelation scale set to 1 grid space. d) Similar to c) but with the horizontal decorrelation scale set to 3 grid spacings. e) Analysis of four square-shaped observation clusters that observed U directions in each cluster are opposite to its nearby cluster. The horizontal decorrelation scale set to 1 grid spacing. f) Similar to e) but with the horizontal decorrelation scale set to 3 grid spacings. .. 21

Fig. 2.5 3DVAR analysis is applied to 400 U observations concentrated on an area like radar radial wind. Each grid box has 4 observations in it. The observation values are 10 m s^{-1} and background field is set to 0. The recursive filter is used to model background error correlation. a) Analysis without the recursive filter. b) Analysis using the recursive filter with the horizontal decorrelation scale set to 1 grid spacing. c) Similar to b) but with the horizontal decorrelation scale set to 3 grid spacing. 24

Fig. 2.6. Results of the 3DVAR analyzing a single radial wind measurement (pointing in positive *x* direction) with different mass divergence constraints. The background wind is zero. a) Wind analysis without applying mass divergence constraint, b) the x-y cross-section of u-v wind analyzed with a 2D (horizontal) mass divergence constraint, c) x-z cross-section of u-w wind after applying a 3D mass divergence constraint, and d) as b) but with a 3D mass divergence constraint. The wind units are m s^{-1}. 27

Fig. 2.7. Results of the 3DVAR analyzing two radial wind measurements (the lower one points in positive z direction and the upper one in negative z direction) with different mass continuity constraints. The background wind is zero. a) wind

analysis without applying mass continuity constraint, b) the x-z cross-section of u-w wind analyzed with a 3D mass continuity constraint that weight coefficient λ = 500, c) as b) but with λ = 1000, and d) as b) but with λ = 2000..... 32

Fig. 2.8. Cross sections of snow, hail, and rain fields determined from reflectivity observations by the (left) KRY and (right) SMO schemes using the background analysis, for 2250 UTC 28 March 2000..... 37

Fig. 2.9. Cross section of the final analysis of snow, hail, and rain fields by the cloud analysis used by Xue03, for 2250 UTC 28 March 2000 scheme..... 39

Fig. 2.10. Cross section of reflectivity fields calculated from precipitation mixing ratios of (a) background, (b) the cloud analysis of Xue03, (c) the updated cloud analysis, for 2250 UTC 28 March 2000. 40

Fig. 2.11. Cross section of cloud water and cloud ice fields from the cloud analysis with the entrainment curve used in (left) Xue03 and (right) the new curve with reduced entrainment, for 2250 UTC 28 March 2000. 41

Fig. 2.12. (a) The profile of horizontally averaged temperature increments from adjustments using the moist adiabatic profile (of the updated version) and latent heat (used in Xue03) methods, and (b) the difference in the temperature increment between these two methods at 4.5 km MSL, for 2250 UTC 28 March 2000. 42

Fig. 3.1. Observed reflectivity fields at the 1.45° elevation of the Fort Worth radar (marked as KFWS) based on Level-II data, at 15-minute intervals from 0000 to 0100 UTC 29 March 2000. Major storm cells are marked by capital letters. Fort Worth and Arlington are marked as dots in (a). Tarrant County is highlighted and about 50 km × 50 km in size. The domain shown is about 200 km on each side, representing the portion of the 3-km grid between 100 and 300 km in the east-west direction and from 60 to 260 km in the north-south direction. The reflectivity contours are at 15, 30, 45 and 55 dBZ, and the shaded contour interval is 5 dBZ. Counties around Fort Worth are labeled in (a). 50

Fig. 3.2. Similar to Fig. 3.1, except that they are predicted reflectivity from experiments (left) X03 and (right) CNTLZ..... 53

Fig. 3.3. Predicted surface wind and temperature fields from experiments X03 and CNTLZ at 0015 and 0045 UTC 29 March 2000. The domains shown are the same as in Fig. 3.1..... 58

Fig. 3.4. Equitable threat scores of predicted reflectivity for the (a) 5-, (b) 15-, (c) 30-, and (d) 45-dBZ threshold values from experiments CNTLZ and X03..... 59

Fig. 3.5 Similar to Fig. 3.1, except that it is predicted reflectivity field from experiment NoVRZ at 0030 UTC 29 March 2000. 61

Fig. 3.6. Reflectivity fields at the 1.45° elevation of the KFWS radar from assimilation results of experiments (b) CNTLZ, (c) X03, (d) CTLH, (e) CKRY, and (f) CMAX and (a) the corresponding radar observation. Major storm cells are marked by capital letters in (a). Tarrant County is highlighted and about 50 km × 50 km in size. The domain shown is about 200 km on each side, representing the portion of the 3-km grid between 70 and 270 km in the east-west direction and from 60 to 260 km in the north-south direction. The reflectivity contours are at 15, 30, 45 and 55 dBZ, and the shaded contour interval is 5 dBZ. 63

Fig. 3.7. Surface wind and temperature fields from assimilation results of experiments (b) CNTLZ, (c) X03, (d) CTLH, (e) CKRY, and (f) CMAX, and (a) background. The domains shown are the same as in Fig. 3.6. 65

Fig. 3.8. Cross section (along line in Fig. 3.6a) of vertical velocity fields from the assimilation results of experiments (a) X03, (b) CNTLZ, (c) CKRY, (d) CTLH, and (e) CMAX. 67

Fig. 3.9. Similar to Fig. 3.1, except that they are predicted reflectivity from experiments CMAX, CKRY, and CTLH at 0015 and 0045 UTC 29 March 2000. 68

Fig. 3.10. Similar to Fig. 3.3, except that they are from experiments CMAX, CKRY, and CTLH at 0015 and 0045 UTC 29 March 2000. 69

Fig. 3.11. (left) Observed reflectivity fields at the 1.45° elevation of the Fort Worth radar (marked as KFWS) based on Level-II data, and (right) predicted reflectivity at the same elevation from the control experiment CNTLVR, at 15-minute intervals from 0000 to 0100 UTC 29 March 2000. Major storm cells are marked by capital letters. Fort Worth and Arlington are marked as dot in (b). Tarrant County is highlighted and about 50 km × 50 km in size. The domain shown is about 200 km on each side, representing the portion of the 3-km grid between 100 and 300 km in the east-west direction and from 60 to 260 km in the north-south direction. The reflectivity contours are at 15, 30, 45, and 55 dBZ and the shaded contour interval is 5 dBZ. Counties around Fort Worth are marked in (a). 73

Fig. 3.12. Predicted wind and vertical vorticity fields at (left) the surface and (right) 3 km MSL from control experiment CNTLVR corresponding to the times of Fig. 3.11. The domains shown are the same as in Fig. 3.11. The capital letters in the left column are the positions of the observed storms. 75

Fig. 3.13. Similar to Fig. 3.12, except that they are predicted wind and vorticity fields from experiment CNTLZ at 15-minute intervals from 0015 through 0045 UTC 29 March 2000. 81

Fig. 3.14. Equitable threat scores of predicted reflectivity for the (a) 5-, (b) 15-, (c) 30-, and (d) 45-dBZ threshold values from experiments CNTLVR, CNTLZ, and NoDiv. 84

Fig. 3.15. Similar to Fig. 3.11, except that it is predicted reflectivity field from experiment VR at 0030 UTC 29 March 2000..... 85

Fig. 3.16 (Left) the vertical velocity fields at 5 km MSL and (right) cross section of vertical velocity along the line in figure (a) from the assimilation output of experiments CNTLVR, CNTLZ, and VR..... 88

Fig. 3.17. Similar to Fig. 3.11, except that they are predicted reflectivity fields from experiments (a) CNTLVR, (b) NoDiv, (c) Div2Da, (d) Div2Db, (e) Div3Da, and (f) Div3Db, at 0030 UTC 29 March 2000. 90

Fig. 3.18. Similar to Fig. 3.12, except that they are predicted wind and vertical vorticity fields from experiments NoDiv, Div2Da, Div2Db, Div3Da, and Div3Db, at 0030 UTC 29 March 2000. 91

Fig. 3.19. Same as Fig. 3.14 but for experiments CNTLVR, Div2Da, and Div2Db. 93

Fig. 3.20. Same as Fig. 3.14 but for experiments CNTLVR, Div3Da, Div3Db, and NoDiv. 94

Fig. 3.21 The vertical velocity fields at 5 km MSL from the assimilation output of experiments CNTLVR, NoDiv, Div2Da, Div2Db, Div3Da, and Div3Db. 98

Fig. 4.1. Map of counties and cities related to the 8 May 2003 OKC tornadic thunderstorm. The dark line segment starting at 2210 northwest of Moore and ending at 2238 south Choctaw marks roughly the damage path of the OKC tornado. The *x* and *y* distances are in kilometer and are relative to the KTLX radar marked by × in the figure. Oklahoma County is highlighted. 105

Fig. 4.2. Regions of radar echoes exceeding 35 dBZ as observed by the KTLX radar at the 1.45º elevation. The echoes are at 30-minute intervals from 2101 to 2359, of 8 May 2003. The grayscales of the echoes at two consecutive times are different, so are their outlines. The locations of the maximum reflectivity of the main storm are marked by + signs, together with the corresponding times. The *x* and *y* coordinates are in kilometer and have their origin at the KTLX radar site that is marked by ×. The arrow lines are the paths of the OKC storm and storms A, B, and C. Also, the hook echo at 2201 and Moore are pointed by curved arrows. Oklahoma County is highlighted. 106

Fig. 4.3. As in Fig. 4.2, but for (a) the observations from 2130, 8 May to 0000, 9 May 2003, at 30-minute intervals, and (b) the corresponding predicted fields from experiment 10B30E30LH. Regions with reflectivity exceeding 45 dBZ are shown. The locations of the maximum reflectivity of the OKC storm are marked by + signs together with the corresponding times. The domain shown represents the portion of the 3-km grid between 210 and 410 km in the east-west direction and from 260 to 380 km in the north-south direction..... 112

Fig. 4.4. Observed reflectivity fields at the 1.45° elevation of the KTLX radar (left column), and the corresponding predicted reflectivity from experiment 10B30E30LH (right column), at 2200 and 2300, 8 May 2003. The reflectivity contours are at 30, 40, 50, and 60 dBZ. The domain shown is the same as Fig. 4.3. 113

Fig. 4.5. As Fig. 4.3b, but for experiment 5B30E30MA. 115

Fig. 4.6. Equitable threat scores for the predicted 1.45º elevation reflectivity for 45-dBZ threshold, for experiments 5B30E30MA and 10B30E30LH. 115

Fig. 4.7. The maximum vertical velocities for the first 20 minutes of forecasts starting (a) from the 5B30E30MA analyses at 0 (2030), 30 (2100), and 50 (2120) minutes into the assimilation cycles (solid lines with different thickness for consecutive times) and (b) from the 10B30E30LH analyses at the same times, and in (a) for a set of forecasts starting from the analyses one analysis cycle later (dashed lines) for 5B30E30MA. 118

Fig. 4.8. Same as Fig. 4.3b, but for experiments 10B30E30MA (a) and 5B30E30LH (b). 120

Fig. 4.9. ETSs of predicted reflectivity at the 1.45º elevation for the 45-dBZ threshold for experiments 5B30E30MA, 5B30E30LH, and 10B30E30MA. 120

Fig. 4.10. The vertical velocity fields at 7 km MSL at the end of assimilation in experiments 10B30E30LH (a), 5B30E30MA (b), 10B30E30MA (c), and 5B30E30LH (d). The domain shown represents the portion of the 3-km grid between 205 and 285 km in the east-west direction and from 235 to 315 km in the north-south direction. The contour interval is 4 m s^{-1}. 122

Fig. 4.11. As Fig. 4.3b, but for experiments 10B30E10LH (a), 5B30E10MA (b), 10B30E20LH (c), and 5B30E20MA (d). 125

Fig. 4.12. As Fig. 4.3b, but for experiments 10B40E30LH (a), 5B40E30MA (b), 10B50E30LH (c), 5B50E30MA (d), 10B60E30LH (e), and 5B60E30MA (f). . 126

Fig. 4.13. As Fig. 4.3b, but for experiment 5B60E30LH. 129

Fig. 4.14 The observed radial velocity and reflectivity fields at 2136 UTC from the KTLX radar at the 1.45º elevation (upper panels) and the corresponding fields from the 2135 UTC CNTL1km analysis mapped to the same elevation (lower panels). The x and y distances are in kilometer and are relative to the KTLX radar marked by '×'. Positive radial velocity values are contoured as solid lines from 8 to 24 m s^{-1} with 4 m s^{-1} intervals and negative as dashed lines from -24 to -8 m s^{-1} with the same intervals. The reflectivity values are plotted as shaded contours at 30, 40, 50, and 60 dBZ. The domain shown is 80 km on each side, representing to

the portion of the1-km grid between 70 and 150 km in the east-west direction and from 50 to 130 km in the north-south direction. The short arrows in radial velocity panels show the direction of radial velocities near their peak value..... 140

Fig. 4.15 Similar to radial velocity part of Fig. 4.14, except that they are analyzed radial velocity at 2135 UTC from experiments CNTLZ1km, Div2D1km, and NoDiv1km. 141

Fig. 4.16 Maximum surface vertical vorticity in the predicted OKC tornadic thunderstorm during the first hour of forecast for experiments CNTL1km, CNTLZ1km, Div2D1km, and NoDiv1km. 143

Fig. 4.17 Similar to Fig. 4.14, except that they are observations at 2151 UTC and 10-minute forecast from experiments CNTL1km, CNTLZ1km, Div2D1km, and NoDiv1km..... 145

Fig. 4.18 The observed reflectivity fields at the 1.45º elevation of the KTLX radar (left column), and the predicted reflectivity fields at the same elevation from experiment CNTL1km (right column), at 5-minute intervals from 2210 to 2230 UTC 8 May 2003. The x and y distances are in kilometer and are relative to the KTLX radar marked by X. The reflectivity contours are at 30, 40, 50, and 60 dBZ. The domain shown is 60 km by 50 km, representing the portion of the 1-km grid between 102 and 162 km in the east-west direction and from 80 to 130 km in the north-south direction. 148

Fig. 4.19 The observed radial velocity fields at the 1.45º elevation of the KTLX radar (left column), and the predicted radial velocity fields at the same elevation from experiment CNTL1km, at 5-minute intervals from 2210 to 2230 UTC 8 May 2003. The domain and x and y coordinates are same as Fig. 4.18. The positive radial velocity is contoured as solid lines from 8 m s^{-1} to 24 m s^{-1} with 4 m s^{-1} intervals and negative as dashed lines from -8 m s^{-1} -24 m s^{-1} with the same intervals. The short arrows show the direction of radial velocity in their maximum value area. 150

Fig. 4.20 Predicted vertical vorticity and wind fields at the surface, 1 km, 2 km, and 3 km MSL from the 35-minute forecast (valid at 2215 UTC) of experiment CNTL1km. The domain is the same as Fig. 4.18. 154

Fig. 4.21 Left column is similar to Fig. 4.19 and right column is similar to Fig. 4.18, except that they are for the forecasts of experiment Div2D1km at 2210 and 2220 UTC 8 May 2003. 155

Fig. 4.22 Left column is similar to Fig. 4.19 and right column is similar to Fig. 4.18, but for experiment NoDiv1km at 2210 UTC and 2220 UTC 8 May 2003. 156

Fig. 4.23 Left column is similar to Fig. 4.19 and right column is similar to Fig. 4.18, but

for experiment CNTL1km at 2210 UTC and 2220 UTC 8 May 2003. 157

Fig. 4.24 Composite reflectivity at 2240 UTC from experiment CNTL1km. 159

Fig. 4.25 The time series of maximum surface vertical vorticity, maximum surface wind speed, and minimum surface pressure in the 100-m forecast. 163

Fig. 4.26 Predicted reflectivity and wind fields at the surface (left column) and 2 km MSL (right column) from the 5 to 9 minutes of forecast at 2-minute intervals. Domain is 30 km by 30 km large. The squares in (c) and (d) indicate the area that is zoomed in by the next figure. Wind vectors are plotted every 10 grid points 164

Fig. 4.27 Predicted reflectivity, wind, and vertical vorticity fields at the surface (left column) and 2 km MSL (right column) from the 7 minutes of forecast valid at 2137 UTC. The domain is 5 km by 5 km and covers area indicated by the squares in Fig. 4.26c and d. The numbers at the upper-right corner of panel (c) and (d) are the maximum vertical vorticity value in s^{-1}. 166

Fig. 4.28 Y-Z cross-section of predicted reflectivity (left) and vertical vorticity (right) fields along the line indicated in Fig. 4.27a from the 7 minutes of forecast valid at 2137 UTC. The number at the upper-right corner of (b) is the maximum vertical vorticity value in s^{-1}. 167

Fig. 5.1 Map of Oklahoma Counties and Cities (dot) related to the 29 May 2004 central Oklahoma tornadic thunderstorm case. Sixteen tornadoes were spawned from the same tornadic thunderstorm that swept through central Oklahoma area from Custer County to Mayes County. 170

Fig. 5.2 Observed reflectivity (left) and radial velocity fields (right) at low level scan from the KTLX radar observations. (a) and (b) were observations at 0058 UTC 30 May 2004, while (c) and (d) were observations at 0417 UTC. The short arrows in radial velocity fields indicate the direction of radial velocities near their peak value. 173

Fig. 5.3 Observed reflectivity fields at the 1.67° elevation from the KDFR radar at 1-hour intervals from 2001 to 2200 UTC and at half hour intervals from 2200 to 2329 UTC 29 May. Arrows point to the central Oklahoma tornadic thunderstorm. 175

Fig. 5.4 The observed low-level reflectivity fields from the KTLX radar from 0132 to 0400 UTC May 30 with about half hour intervals. The analysis domain shown is about 250 km on each side, representing the portion of the 3-km grid between 195 and 445 km in the east-west direction and from 170 to 420 km in the north-south direction. 180

Fig. 5.5 Predicted reflectivity at the same elevation as those shown in Fig. 5.4, but from

experiment PCLD. Shown are times at half hour intervals from 0130 to 0400 UTC 30 May 2004. 181

Fig. 5.6 The predicted wind and vertical vorticity fields at the surface (left column) and 3 km MSL (right column) from PCLD at 0200, 0300, and 0400 UTC 30 May. ... 183

Fig. 5.7 Reflectivity fields of radar observations, the analysis background at 0100 UTC (for the last analysis of the assimilation cycles), the initial condition, and the 10-minute forecast from experiment PCLD. Reflectivity fields have been mapped to the 1.14° elevation of the KTLX radar 184

Fig. 5.8 Similar to Fig. 5.5, except that they are from experiment PCLDPC. 187

Fig. 5.9 Similar to Fig. 5.6, except that they come from PCLDPC 188

Fig. 5.10 (a), observed low-elevation level reflectivity from the KTLX radar at 0058 UTC and the locations of the KTLX radar and KVNX radar (marked as ×). The square shows the domain of panels (b)-(d). (b), horizontal wind analysis increments at the 11th level of the analysis grid from 0100 UTC radial velocity analysis using both the KTLX and KVNX radar observations. (c), the same as (b) except that only the KTLX radar observations are used. (d) the same as (b) except that only the KVNX radar observations are used. 190

Fig. 5.11 Vertical velocity (contour) and wind fields (vector) at 4 km MSL from the assimilation results of experiments SnglVrZ, DualVrZ, SnglVr, and DualVr. The domain shown is 60 km × 60 km in size, covering the portion of the 3-km grid between 195 to 355 km in the east-west direction and 170 to 330 km in the south-north direction. 191

Fig. 5.12 Observed low-elevation level reflectivity fields from the KTLX radar at 0058, 0119, 0142, and 0202 UTC 30 May 2004. The domain is the same as Fig. 5.11. The x and y distances are in kilometer and are relative to the KTLX radar marked by ×. Kingfisher County is highlighted..... 193

Fig. 5.13 Predicted reflectivity fields mapped at the 1.23° elevation of the KTLX radar from the first-hour forecast of experiment SnglVrZ at 20 minute intervals. The domain and coordinates are the same as Fig. 5.12. The reflectivity contours are 30, 40, 50, and 60 dBZ. Kingfisher County is highlighted..... 194

Fig. 5.14 Similar to Fig. 5.13, except that they are from experiment DualVrZ..... 196

Fig. 5.15 Similar to Fig. 5.13, except that they are from experiment SnglVr. 197

Fig. 5.16 Similar to Fig. 5.13, except that they are from experiment DualVr. 198

Fig. 5.17 Predicted wind (vectors) and vertical vorticity (contours) fields at 1 km MSL

for 20 and 40 minute forecast of experiments DualVrZ, SnglVrZ, DualVr, and SnglVr. The domain is the same as Fig. 5.11. Kingfisher County is highlighted199

Fig. 5.18 (a)-(d): Predicted reflectivity fields mapped at the 1.14° elevation of the KTLX radar from the 2-hour forecasts of experiments DualVrZ, SnglVrZ, DualVr, and SnglVr. (e): Observed low-elevation level reflectivity field from the KTLX radar at 0301 UTC. The domain shown is 220 km by 160 km, representing the portion of the 3-km grid between 215 to 435 km in the east-west direction and 170 to 330 km in the north-south direction. The reflectivity contours are 30, 40, 50, and 60 dBZ. The x and y distances are in kilometer and are relative to the KTLX radar marked by ×. 202

Abstract

Doppler weather radar observations play a key role in initializing convective storms within storm-scale numerical weather prediction (NWP) models. The radial velocity and reflectivity are the two main parameters measured by Doppler weather radars. Due to their indirect nature and incomplete spatial coverage, the optimal assimilation of these data remains a challenging task.

In this dissertation, the Advanced Region Prediction System (ARPS), a multiscale NWP model, together with its three-dimensional variational (3DVAR) data analysis system and a complex cloud analysis procedure is used to perform high-frequency intermittent data assimilation that includes the radial velocity and reflectivity data. The radial velocity is analyzed using the 3DVAR system that includes a mass divergence constraint for coupling wind components together, while the reflectivity is assimilated through the cloud analysis that also adjusts in-cloud temperature and moisture fields. In the 3DVAR analysis, the background error covariance is modeled using recursive filters, and a multipass strategy is employed to deal with observations representing very different scales.

The assimilation and forecast system is applied to three tornadic thunderstorm cases, specifically, the 28 March 2000 Fort Worth, Texas, tornadic thunderstorm case, the 8 May 2003 Oklahoma City, Oklahoma, tornadic thunderstorm case, and the 29 May 2004 central Oklahoma tornadic thunderstorm case. In general, two one-way nested grids are used, one at a 9-km and one at a 3-km horizontal resolution, and our focus is placed on the 3-km grid which directly assimilates the radar data.

For each of these three cases, the impact of full-volume WSR-88D radar reflectivity and radial velocity data, individually or in combination, on the assimilated initial condition and the subsequent forecast of the individual storm cells is analyzed in detail, usually through a comprehensive set of numerical experiments.

For the Fort Worth case, the current cloud analysis procedure in the ARPS is compared with an earlier version that was used in a previous publication, and the effects of individual modifications that lead to an overall improvement are investigated. The best configuration in this case is able to predict the morphology of individual storm cells on the 3-km grid for up to two hours and the rotating supercell characteristics of the storm

that spawned two tornadoes are well captured. The timing errors in the forecast are less than 15 minutes and location errors are less than 10 km at the time of the tornadoes.

For the second, Oklahoma City case, 3-km experiments with different combinations of the assimilation frequency, in-cloud temperature adjustment schemes, and the length and coverage of the assimilation window are conducted to determine the best configuration and to understand the dynamics of data assimilation. Encouraged by the rather successful forecast at the 3-km resolution for the supercell that spawned several tornadoes, several 1-km experiments are conducted. The best 1-km forecast is able to capture a well-defined mesocyclone and the associated hook-shaped echo for 50 minutes. Furthermore, starting from the 1-km analysis, an attempt was made to produce a forecast at 100-m horizontal resolution. In a forecast of 9 minutes long, a tornado of F1 to F2 intensity is obtained, which represents the first time that a realistic tornado is obtained within a full-physics model starting from an analyzed initial condition.

The third case is that of a long-lasting tornadic thunderstorm that swept through central Oklahoma and produced 16 tornadoes. For the case, two 3-km experiments are conducted to test a simple procedure for correcting position errors of the analyzed storm that occur when assimilating reflectivity data alone from single Oklahoma City radar. A rotating thunderstorm is predicted well for 2.5 to 3 hours, with the phase correction procedure improving the subsequent position forecast. For the same case, four additional 3-km experiments are conducted to test the impact of assimilating radial velocity data from both Oklahoma City and Vance Air Force Base radars. For a good portion of the assimilation window, the main storm was located within the dual-Doppler lobe of these two radars, even though the storm was relatively far from either one. It is found that the dual-Doppler wind analysis helps suppress spurious storms more effectively than the cloud analysis procedure based-on the reflectivity data.

With the data assimilation procedure used in this study, reflectivity data generally have a much greater impact than radial velocity data on the assimilation and forecast of storms. A properly configured mass divergence constraint improves the analysis and forecast, especially that of the wind fields.

Chapter 1

General Introduction

The development of high-resolution nonhydrostatic models and the rapid increase of computer power are making the explicit prediction of thunderstorms a reality (Droegemeier 1990; Lilly 1990; Droegemeier 1997; Xue *et al.* 2003, hereafter Xue03). Data assimilation plays an important role in providing an accurate initial condition for the model forecast. The operational Weather Surveillance Radar-1988 (WSR-88D) Doppler radar network of the United States (Crum and Alberty 1993) is a key source of data for initializing storm-scale numerical weather prediction (NWP) models as it is the only operational platform capable of providing observations of spatial and temporal resolutions sufficient for resolving convective storms.

The analysis of radar data to arrive at a complete set of initial conditions for an NWP model is challenging, because radars only observe a very limited set of parameters, the most important being the radial velocity and reflectivity. Their spatial coverage is often incomplete. To determine atmospheric state variables that are not directly observed, certain retrieval or assimilation techniques have to be used.

Four-dimensional variational (4DVAR) data assimilation, which obtains a full set of model initial conditions that provides the best fit between the model solution and radar observations within a time (assimilation) window, is considered ideal for this purpose. Some encouraging 4DVAR results with both simulated and real radar data have been obtained by Sun et al. (1991) and Sun and Crook (1997; 1998). On the other hand, the complexity of developing and maintaining the adjoint code needed by a 4DVAR system

and the high computational cost of 4DVAR technique for high-resolution applications are limiting its use in research and operation. Another relatively new technique is the ensemble Kalman filter (EnKF) method, which has been shown recently to produce single-Doppler radar analyses of thunderstorms that are of similar quality as the 4DVAR analysis (Snyder and Zhang 2003; Zhang *et al.* 2004; Tong and Xue 2005b). While also expensive because of the need for running an analysis and forecast ensemble of significant sizes, the EnKF method is easier to implement and is much more flexible.

Other simpler, yet faster, methods exist that attempt to retrieve unobserved variables from the radar data. The retrieved state variables can then be analyzed into the model initial conditions. The wind retrieval methods include the so-called simple adjoint method (Qiu and Xu 1992; Qiu and Xu 1994; Xu *et al.* 1994; Gao *et al.* 2001) and two-scalar method of Shapiro et al. (1995), among others. The latter has been used by Weygandt et al. (2002a) to initialize a numerical model. Additionally, the retrieved three-dimensional wind fields at more than one time level can be used to retrieve thermodynamic fields (Gal-Chen 1978). The retrieved fields can then be combined via an analysis procedure, as is done in Weygandt et al. (2002b). Such multistep procedures have an advantage in being able to make use of multiple radar volume scans in an inexpensive way, but the involvement of multiple steps and the use of retrieved instead of direct observations make the optimality of analysis difficult to achieve.

Another alternative is to analyze the radial velocity data directly via a three-dimensional variational (3DVAR) analysis procedure. Certain dynamic or equation constraints can be built into the 3DVAR cost function with relative ease. Such a system has been developed within the ARPS model (Xue *et al.* 1995; 2000; 2001b) framework

and documented in Xue et al. (2003) and Gao et al. (2002; 2004). It is used in this study to analyze radial velocity and other conventional observations. The 3DVAR method is theoretically less optimal than the 4DVAR because it lacks a time dimension, but is much faster. In our study, we bring in the time dimension and therefore utilize data over a period of time by performing high-frequency intermittent assimilation cycles.

The use of reflectivity data for the purpose of thermodynamic and microphysical retrievals and analysis is not straightforward. Semiempirical rules can be used to aid the analysis of these fields. In the current ARPS system, this is done with a complex cloud analysis procedure. This cloud analysis procedure has evolved from that used in the Local Analysis and Prediction System (LAPS, Albers *et al.* 1996) with previous modifications documented by Zhang et al (1998) and Zhang (1999). It is a component of both the ARPS 3DVAR analysis system and ARPS Data Analysis System (ADAS, Brewster 1996)

In Xue03, the Bratseth (1986) scheme-based ADAS with the then-current version of the cloud analysis is applied to the 28 March 2000 Fort Worth, Texas, tornado case. In that work, Level-III (NIDS, NEXRAD Information Dissemination Service) reflectivity data are assimilated at 15-minute intervals. While their results are encouraging, significant discrepancies in the predicted storms are noted in the paper. In this work, as an attempt to improve the assimilation and forecast, we replace the ADAS with the ARPS 3DVAR and in addition assimilate the radial velocity data directly, with a mass divergence constraint to couple the wind components together. We employ an updated version of the cloud analysis that includes a different scheme for temperature adjustment in the cloud regions and modifications to other parts of the procedure. In addition, we use the full-volume Level-II data instead of the Level-III data that are of reduced precision

and only include the four lowest tilts of data.

In addition to the Fort Worth tornadic thunderstorm case, the 8 May 2003 Oklahoma City, Oklahoma, area and the 29 May 2004 Central Oklahoma tornadic thunderstorm cases are also studied with the same assimilation and forecast systems but focus on the different aspects of the radar data assimilation. With the 8 May 2003 Oklahoma City tornadic thunderstorm case, the effects of various assimilation configurations are studied to find the best combination of these configurations to improve the positive impact of assimilating radar data. With the same case, high resolution experiments with 1-km and 100-m grid spacings are tested to capture tornadic circulation and hook echo and even the tornado itself. The study of the 29 May 2004 central Oklahoma case attacks two issues on the convective-scale data assimilation with radar observations: one is the efficacy of applying a simple phase-correction scheme in removing the large position errors of the storm in the analysis background therefore also the initial condition, and the other is the implement of dual-Doppler analysis of radar radial velocity data on the storm forecast.

The organization of this dissertation is as follows. In Chapter 2, we briefly introduce the motivation, methodology, and tools of this research. In Chapter 3, the 28 March 2000 Fort Worth tornadic thunderstorm case is used to examine the impacts of radial velocity data and reflectivity data on storm forecast as well as the modifications to the cloud analysis and the mass divergence constraint. In Chapter 4, the 8 May 2003 Oklahoma City tornadic thunderstorm case is employed to study the impacts of the configurations of radar data assimilation on the storm assimilation and forecast and the high horizontal-resolution assimilation and forecast. In Chapter 5, results from the 29

May 2004 central Oklahoma tornadic thunderstorm case are reported to test the effect of a simple phase-correction procedure and the ARPS 3DVAR dual-Doppler analysis of radial velocity data. In Chapter 6, the general summaries are given on the results of the three cases and the future works are also proposed.

Chapter 2

Motivation, Methodology, and Tools

2.1 Motivation and methodology

For the prediction of storm-scale weather systems, such as tornadic thunderstorms, the numerical model can start from two types of initial conditions distinguished according to the time of storm initiation. The first type of initial conditions is at the time when storms are already initiated and detected by radars. The job of a numerical model is then to predict the evolution of these preexisting storms. A successful prediction requires a high resolution nonhydrostatic model that includes the necessary physical and dynamic processes to be capable of capturing the correct mechanisms of the development of storms and their interactions with the environment. The second type of initial conditions is at the time before storm initiation. A successful storm forecast from this type of initial conditions requires not only that the initial condition includes the weather conditions that lead to the initiation of thunderstorms, but also that prediction model has the ability to accurately predict the evolution of the environmental conditions that lead to the triggering of convection. Both situations pose challenges although the types of challenges are somewhat different. In this study, we focus on the former challenge, that is, on initializing and predicting preexisting storms. For this problem, the assimilation of data from storm-capturing Doppler radars is the key.

As mentioned in the general introduction, the WSR-88D Doppler radar network is the only operational platform in the US capable of providing observations of spatial and temporal resolutions sufficient for resolving convective storms. The analysis of radar data

to arrive at a complete initial condition for storm-scale numerical model is challenging because radar observations only include reflectivity and radial velocity and the spatial coverage of radar observations is often incomplete.

Several assimilation methods have been developed in the past to assimilate radar data into storm-scale forecast models. Among them, the three-dimensional variational (3DVAR) method offers relative simplicity and computational efficiency. In a 3DVAR framework, radar radial velocity data can be easily analyzed, subjecting to dynamic or equation constraints that serve to couple three wind components and other analysis fields together. However, unless very sophisticated balance constraints can be found and used, it is still difficult to obtain very good analyses of the wind fields from single Doppler radar data because of the general problem of underdeterminedness. Multiple time levels of data are usually needed to improve the analysis or assimilated fields.

In this study, Level-II data from the WSR-88D radars for several severe weather outbreak cases are used with the ARPS assimilation and forecast system. The impacts of radar observations on storm forecast are investigated and the assimilation schemes that can improve these impacts are tested. Specifically, the ARPS 3DVAR system is used to analyze the Level-II radial velocity data, while the ARPS cloud analysis procedure is employed to adjust in-cloud temperature and moisture fields and to retrieve precipitation species from the reflectivity data. Conventional data are also analyzed by the 3DVAR when available to better define the storm environment. Rapid update assimilation cycles, which employ the 3DVAR and cloud analysis schemes for analysis updates and the ARPS model for forecast, are used to arrive at the final initial condition for storm forecast. The assimilation windows usually cover the early stages of storm development, when

radar data are available. Starting from the initial condition that already contains the preexisting storms, the ARPS model is run for several hours to predict the further evolution of the storms. The assimilation and forecast results are analyzed and compared with radar observations to investigate the effect of radar observations and the ability of the assimilation and prediction systems for storm forecast.

In the following sections, the ARPS prediction model, the ARPS 3DVAR, and the ARPS cloud analysis procedure and their configurations as used in this study are discussed.

2.2 ARPS system and ARPS model

The ARPS is a fully functioning storm-scale numerical weather prediction (NWP) system that has been developed by the Center for Analysis and Prediction of Storms (CAPS) at University of Oklahoma since the establishment of CAPS in 1989. The primary mission of CAPS was to demonstrate the practicability of storm-scale numerical weather prediction and to develop, test, and validate a regional forecast system appropriate for operational, commercial, and research applications (Droegemeier 1990; Lilly 1990). It is therefore the most suitable tool of this study.

Currently, the ARPS includes data ingest, quality control and objective analysis packages (ADAS and 3DVAR), data assimilation procedures, the prediction model, as well as post-processing packages and validation tools (Xue *et al.* 1995; 2000; 2001a). Its numerical prediction component is a three-dimensional, nonhydrostatic, compressible model formulated in generalized terrain-following coordinates. The model control equations are solved using finite differences on an Arakawa C-grid. The model-splitting technique is employed to integrate the dynamic equations. The leapfrog scheme is used

for the large time step integration except when an alternative scheme such as the flux-corrected transport scheme is used for scalar advection. In the small step, the horizontal winds are integrated using the forward-in-time scheme, and the vertical wind and pressure equations are integrated implicitly in the vertical direction using the Crank-Nicolson scheme. The ARPS model also contains a comprehensive physics package. In the real case study of this research, similar model numerical and physical settings are used to forecast the behaviors of tornadic thunderstorms. These settings are listed in this section and will not be mentioned in individual real case design unless different options are chosen specially for the case.

The common numerical settings used in this research for the ARPS model are:

- Momentum advection scheme has fourth order in both the horizontal and vertical. Scalar advection scheme is a simple positive definite advection (MPDCD) scheme based on flux correction/limiting on leapfrog-centered advective flux.
- Externally-forced lateral boundary conditions that come from coarse grids model forecast and the radiative upper-boundary condition are used. At the low boundary, real surface characteristics and terrain are derived from high resolution terrain, land-use and land-cover data bases.
- Fourth order computational mixing is implied.
- Anisotropic acoustic wave divergence damping is turned on.
- Robert-Asselin time filter is implied for leapfrog time integration.

The physical settings of the ARPS model in this research are:

- The Non-local TKE-based PBL parameterization and 1.5-order TKE-

based subgrid-scale turbulence scheme are used.

- Moist processes are activated with three-phase ice microphysics (Lin *et al.* 1983).
- The time-dependent state of the land surface is predicted by the surface energy and moisture budget equations (soil model) and then surface fluxes are calculated from the stability-dependent surface drag coefficients, and predicted surface temperature and surface volumetric water content.
- Simplified surface radiation physics is used in order to compute the surface energy balance for soil model.

The ARPS model has been designed from the beginning to run on computing platforms ranging from single-processor scalar workstations to massively parallel scalar or vector processors. The ability of run on parallel computation environment is particularly important for storms forecast because high resolution grids covering a large domain are usually need for real case study.

In the following subsections, the ARPS 3DVAR and cloud analysis procedure are detailed, which are the main methods for us to analyze radar observations. Also, several issues related to the application of the 3DVAR and the cloud analysis are discussed.

2.3 ARPS 3DVAR system

2.3.1 Basic scheme

Following Gao et al. (2004), the standard cost function of the 3DVAR system can be written as

$$J(\mathbf{x}) = \frac{1}{2}\left(\mathbf{x}-\mathbf{x}^b\right)^T \mathbf{B}^{-1}\left(\mathbf{x}-\mathbf{x}^b\right) + \frac{1}{2}\left[H(\mathbf{x})-\mathbf{y}^o\right]^T \mathbf{R}^{-1}\left[H(\mathbf{x})-\mathbf{y}^o\right] + J_c(\mathbf{x}), \quad (2.1)$$

where the first term on the right hand side measures the departure of the analysis vector, $\mathbf{x}$, from the background, $\mathbf{x}^b$, weighted by the inverse of the background error covariance matrix $\mathbf{B}$. In the current ARPS 3DVAR system, the analysis vector $\mathbf{x}$ contains the three wind components (u, v, and w), potential temperature (θ), pressure (p), and water vapor mixing ratio (q_v). The second, observation term, measures the departure of the analysis from the observation vector, $\mathbf{y}^o$. The analysis is projected to the observation space by the forward observation operator, H, and the observation term is weighted by the inverse of the observation error covariance matrix $\mathbf{R}$ that includes both the instrument and representativeness errors. The forward operator errors, especially those for conventional data, should be small and are usually neglected. Term $J_c(\mathbf{x})$ in Eq. (2.1) represents dynamic or equation constraints.

Transforming control variables from $\mathbf{x}$ to $\mathbf{v}$, according to $\mathbf{B}^{1/2}\mathbf{v} = \left(\mathbf{x} - \mathbf{x}^b\right)$, the standard cost function is changed into incremental form for new control variable $\mathbf{v}$:

$$J_{inc}(\mathbf{v}) = \frac{1}{2}\mathbf{v}^T\mathbf{v} + \frac{1}{2}\left(\mathbf{H}\mathbf{B}^{1/2}\mathbf{v} - \mathbf{d}\right)^T \mathbf{R}^{-1}\left(\mathbf{H}\mathbf{B}^{1/2}\mathbf{v} - \mathbf{d}\right) + J_c(\mathbf{v}), \tag{2.2}$$

where $\mathbf{H}$ is the linearized version of H and $\mathbf{d} \equiv \mathbf{y}^o - H\left(\mathbf{x}^b\right)$. In the current system, the cross-correlations between variables are not included in the background error covariances. The spatial covariances for background error are modeled by a recursive filter. Following common practice, observation errors are assumed to be uncorrelated; hence the corresponding covariance matrix, $\mathbf{R}$, is diagonal, and its diagonal elements are specified according to the estimated observation errors. Correlated observation errors are usually removed through bias correction procedures before or within the analysis procedure (e.g., Harris and Kelly 2001).

Considering that we are dealing with flows at vastly different scales and different data types also represent very different spatial scales, the ARPS 3DVAR allows for the use of multiple analysis passes, each one including different data types and using different filter scales. In our cases, the selection of the filter scales is guided by the density of observational data to which filter is applied. We call this a multiscale analysis procedure.

2.3.2 Radar radial velocity

For the radial velocity observations, the forward operator, or H in Eq.(2.1), that projects the velocity into the radial direction is

$$V_r = \frac{(x-x_0)u + (y-y_0)v + (z-z_0)w}{r}, \tag{2.3}$$

where u, v, and w are the wind components in Cartesian coordinates (x, y, z); and (x_0, y_0, z_0) are the coordinates of radar; and r is the distance from the radar location to the observation points of radial velocity. In the ARPS 3DVAR, the observed radial velocity data are first interpolated to analysis grid points through preprocessing, and therefore no further spatial interpolation is needed in this forward operator. The actual preprocessing program also includes quality control (velocity dealiasing, clutter removal, etc.) and takes into account the spherical geometry of the earth and the curved path of the radar beam.

2.3.3 Recursive filter in ARPS 3DVAR

2.3.3.1 Standard recursive filter algorithm

In one dimension, a standard recursive filter (Lorenc 1992; Hayden and Purser

1995) is usually constructed by one right-moving filter

$$B_i = \alpha B_{i-1} + (1-\alpha) A_i \tag{2.4}$$

and following one left-moving filter

$$C_i = \alpha C_{i+1} + (1-\alpha) B_i , \tag{2.5}$$

where *i* is the integer index of grid points along the line. A is the initial input value; B is the output value after the right-moving filter; and C is the output value after one pass of the filter in each direction. α is the filter coefficient and is defined by

$$\alpha = 1 + E - \sqrt{E(E+2)} , \tag{2.6}$$

where $E = N\delta x^2 / R^2$ and *N* is pass number, which is the number of Eq. (2.4) and (2.5) applied iteratively; δx is grid spacing and *R* is horizontal decorrelation scale for the recursive filter. As *N* tends to be infinity, the effect of iteration of the recursive filter is equivalent to a single Gaussian filter with decorrelation scale R directly.

In the ARPS 3DVAR, the spatial recursive filter is employed to model homogeneous, isotropic, and Gaussian-shaped spatial correlations in the background error covariance matrix of a single analysis variable. In addition to the above assumptions on spatial correlation, the assumption of an unlimited domain is implicitly imposed and can be partly fulfilled by selecting suitable starting conditions for both boundary points, which is examined in the next section.

2.3.3.2 Lateral boundary conditions of recursive filter

To mitigate lateral boundary effects in a recursive filter, Hayden and Purser (1995) gave out a set of equations to decide the lateral boundary conditions that can simulate the effect of an infinite continuation of the line. In the ARPS 3DVAR, the lateral boundary

conditions of the first several passes of the recursive filter are derived according to this set of equations. In this section, those lateral boundary conditions are listed and examined through idealized experiments. The detailed derivation of those boundary conditions is given in the Appendix.

Assuming 0 is the index of the left boundary condition for a right-moving filter and n+1 is the index of the right boundary conditions for a left-moving filter, and then we can get the following boundary conditions listed in the table:

Table 2.1 The boundary conditions of the first 4 filter passes

Pass number	Right-moving filter	Left-moving filter
1st	$B_0 = (1-\alpha)A_0$	$C_{N+1} = \frac{1-\alpha}{1-\alpha^2} B_{N+1}$
2nd	$B_0 = \frac{1-\alpha}{1-\alpha^2} A_0$	$C_{N+1} = \frac{1-\alpha}{(1-\alpha^2)^2}(B_{N+1} - \alpha^3 B_N)$
3rd	$B_0 = \frac{1-\alpha}{(1-\alpha^2)^2}(A_0 - \alpha^3 A_1)$	$C_{N+1} = \frac{1-\alpha}{1-3\alpha^2+3\alpha^4-\alpha^6}(B_{N+1} -3\alpha^3 B_N + \alpha^4 B_{N-1} + \alpha^5 B_N)$
4th	$B_0 = \frac{1-\alpha}{1-3\alpha^2+3\alpha^4-\alpha^6}(A_0 -3\alpha^3 A_1 + \alpha^4 A_2 + \alpha^5 A_1)$	

To study the effectiveness of the above boundary conditions, recursive filters with different pass numbers are applied to the following one dimensional grid with grid index i from 0 to N+1,

$$A_i = \begin{cases} 1, & i = 0,\ N+1 \\ 0, & i = other \end{cases}$$

In this situation, observations are located at the lateral boundary of analysis domain.

Two boundary condition schemes are used in the experiment for comparison. Scheme 1 uses the first left and right boundary condition for all passes, while scheme 2 uses the equations in Table 2.1 as the boundary conditions for several corresponding initial passes then the 4th right-moving boundary condition as the left boundary condition when the pass number is larger than 4 and the 3rd left-moving boundary condition as the right boundary condition when the pass number is larger than 3.

The results of the experiments that employ the recursive filters with the pass numbers from 2 through 5 are illustrated in Fig. 2.1. Clearly, the recursive filter with the scheme 1 boundary conditions induces errors on the boundary area for all passes and the magnitude of errors increases with the pass number. When scheme 2 is used, no errors in the right boundary area for the first 3 passes and in the left boundary area for the first 4 passes are found because we derived and applied the boundary conditions suitable for those passes to avoid the lateral boundary effects. For the applications of the recursive filter with higher passes, lateral boundary effects begin to emerge, such as the errors on the right boundary of 4 passes and on both boundaries of 5 passes, but they are not as serious as those when scheme 1 is used.

In the applications of the 3DVAR analysis to real cases, observations can be distributed arbitrarily, including locations near the lateral boundary of the analysis domain. The use of a recursive filter with the boundary conditions of scheme 2 can effectively mitigate analysis errors at the lateral boundary.

2.3.3.3 The overshooting problem

Another issue associated with the application of the recursive filter in the 3DVAR is an overshooting problem that occurs in the case that several observations are too near

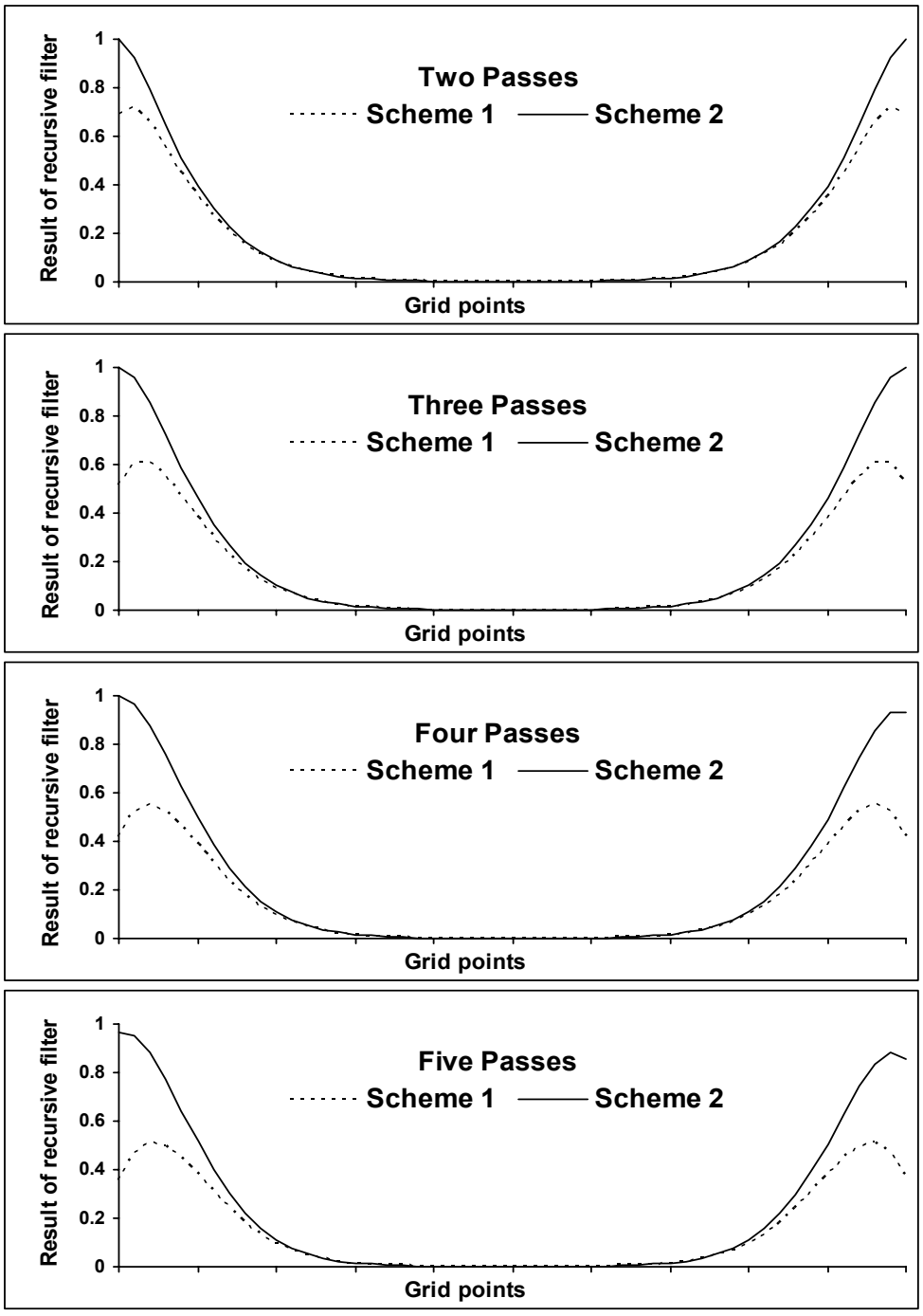

Fig. 2.1 Results of ideal experiment on the effectiveness of the boundary conditions

each other. In this section, two ideal experiments are conducted to illustrate this problem and methods of avoiding this problem in real application are also discussed.

In the first experiment, recursive filers with different decorrelation scales are applied to a one dimensional space that has two unit observations located 10 grid points apart. Fig. 2.2 shows the results of recursive filters with a horizontal decorrelation scale of 5, 10, and 20 grid points. The filter results in values larger than observation at the center of two observations, appears from the horizontal decorrelation scale equaling to 5, and becomes worse as the scale is increased.

Further experiments show that the above overshooting problem of the recursive filter can induce the same problem in the 3DVAR analysis when some observations are

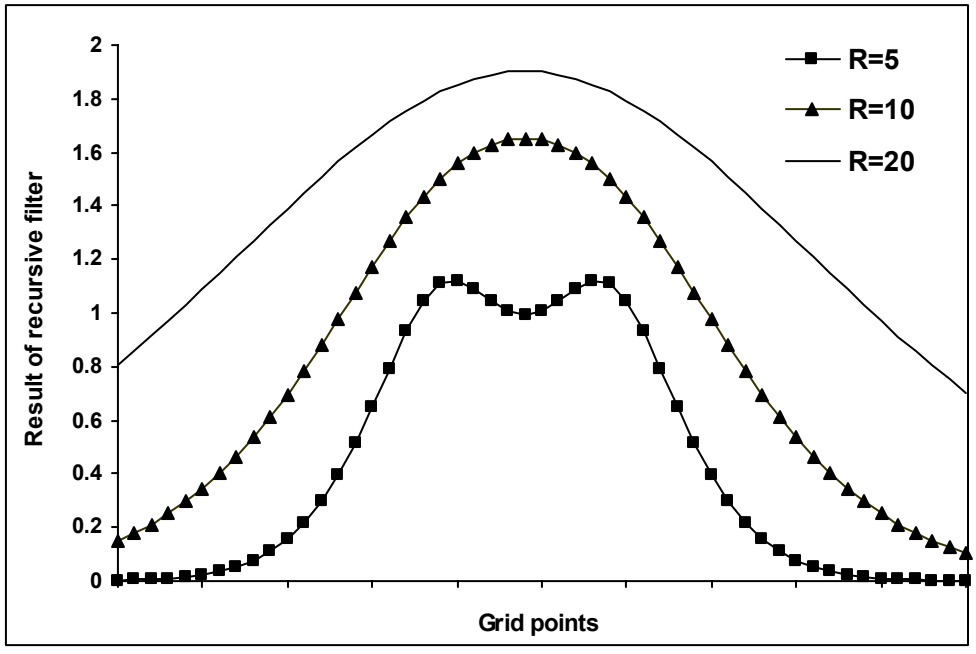

Fig. 2.2 Results of recursive filter applying to two unit observations with 10 grid points apart. Horizontal decorrelation scale, R, is 5, 10, and 20 grid points.

located near each other. Fig. 2.3 shows the results of two U observations, which have values of 10 m s^{-1} and locate 10 grid spacing apart, analyzed via the ARPS 3DVAR with 0 background field. Fig. 2.3a shows that the analysis is two U vectors with speed 6.92 m s^{-1} and both are in the same positions as the observation when the recursive filter is not used in the analysis. That is the situation that no correlations between two analysis points are considered in the 3DVAR analysis. In Fig. 2.3b, the analysis gives a large area of U vectors that spread from the two U observations under the aid of background error correlation that is modeled by the recursive filter with a horizontal decorrelation scale of 10 grid spacings. In the center of the area of analyzed U vectors, the analysis values are larger than these shown in Fig. 2.3a and have a maximum value of 8.48 m s^{-1}. This over analyzed area is usually not a reflection of reality but from the overshooting problem shown in the previous experiment. When the horizontal decorrelation scale of recursive filter is increased to 40 grid points (Fig. 2.3c), the analysis gives even distributed U vectors ranging from 6.64 m s^{-1} to 8.23 m s^{-1}. This result indicates that the problem does not become worse with the increase of the horizontal decorrelation scale as the previous experiment does (Fig. 2.2). Comparing the two experiments, we also can find that the problem in the analysis is not as bad as that shown in the output of the filter itself.

The reason for the overshooting problem is that observations are too close to each other, which happens in real applications when different observation types, such as radiosonde and mesonet data, are analyzed with the same horizontal decorrelation scale or when two observation stations of the same type are located near each other. The first situation can be avoided by grouping observation types representing different spatial

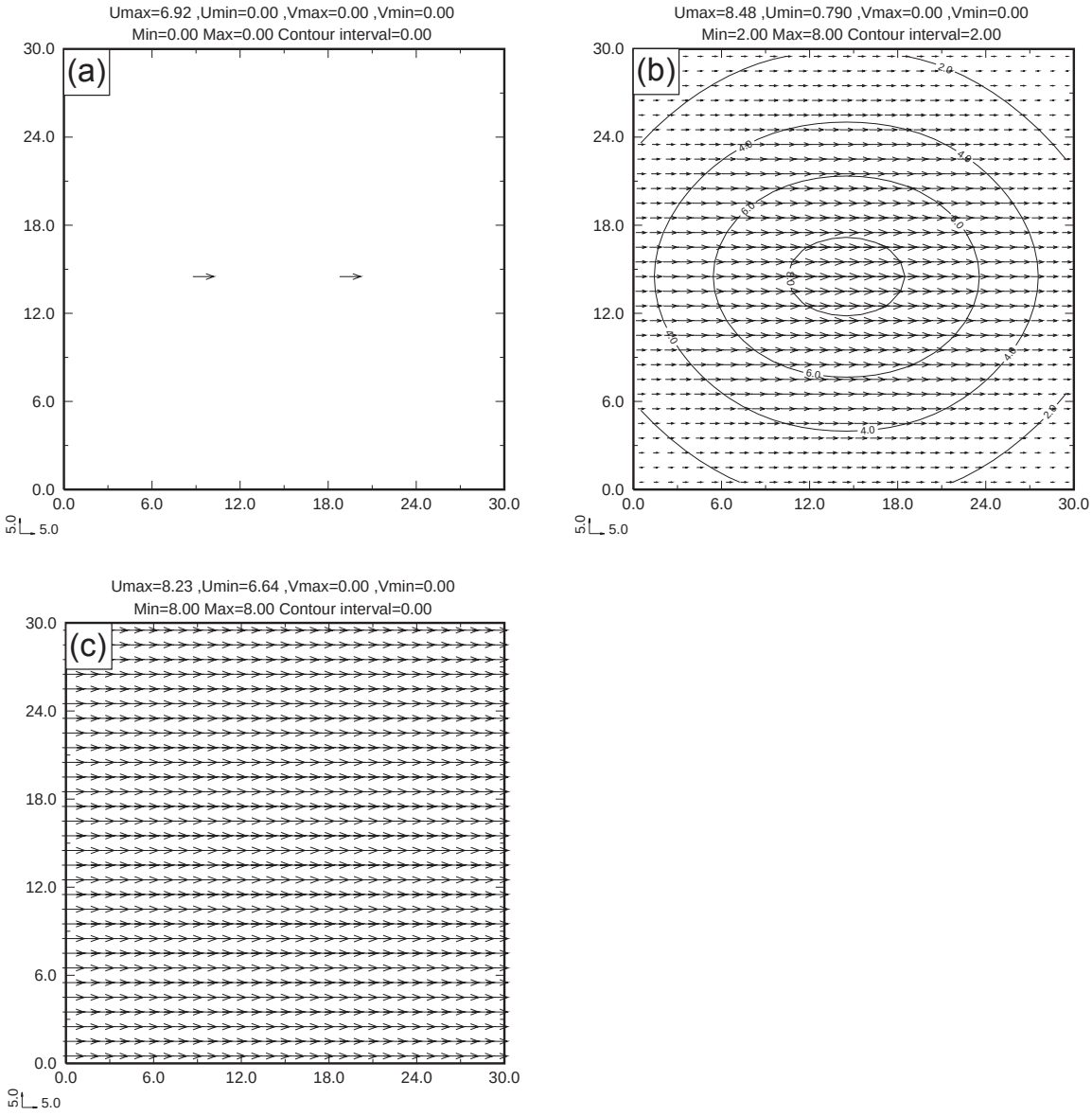

Fig. 2.3 3DVAR analysis is applied to two U observations. The observation values are 10 m s^{-1} and located 10 grid spacings apart. Background field is set to 0. The recursive filter is used to model background error correlation. a) Analysis without the recursive filter. b) Analysis using the recursive filter in which the horizontal decorrelation scale is 10 grid spacings. c) Same as b) but the horizontal decorrelation scale is 40 grid spacings.

scales into different analysis passes. In the ARPS 3DVAR, a fixed horizontal decorrelation scale for the recursive filter is used in each analysis pass, in which observations with similar influence radius or distribution density are collected in the same pass. The second overshooting situation, in which observations of the same type are located near each other, can be mitigated by combining several observations into one superobservation in the data preprocessing procedure, which is contained in one of the quality control steps for the ARPS 3DVAR.

2.3.3.4 Overshooting problem in radar radial velocity analysis

One important observation studied in this research is radar radial velocity observation that can be distributed in high density and cause overshooting problems. In this section, the ARPS 3DVAR analysis is used to analyze simulated radar radial velocity observations and results are used to estimate the extent of the overshooting problem in the analysis.

The first situation simulated assumes many radial velocity observations concentrated on a certain area. For that purpose, 100 U observations with same value of 10 m s^{-1} and distributed one grid point by one grid point in a square-shaped area are created and analyzed via the ARPS 3DVAR with 0 background field. The result from the analysis without the recursive filter gives analysis value of 6.92 m s^{-1} in each grid point that has an observation in it (not shown). The analysis using the recursive filter with the horizontal decorrelation scale, R, set to 1 and 3 grid spacing is shown in Fig. 2.4a and b, respectively. We can see that the analyzed U values in the observation area have been increased by 1.99 m s^{-1} for R = 1 and 3.05 m s^{-1} for R = 3 comparing to the analysis values without the recursive filter.

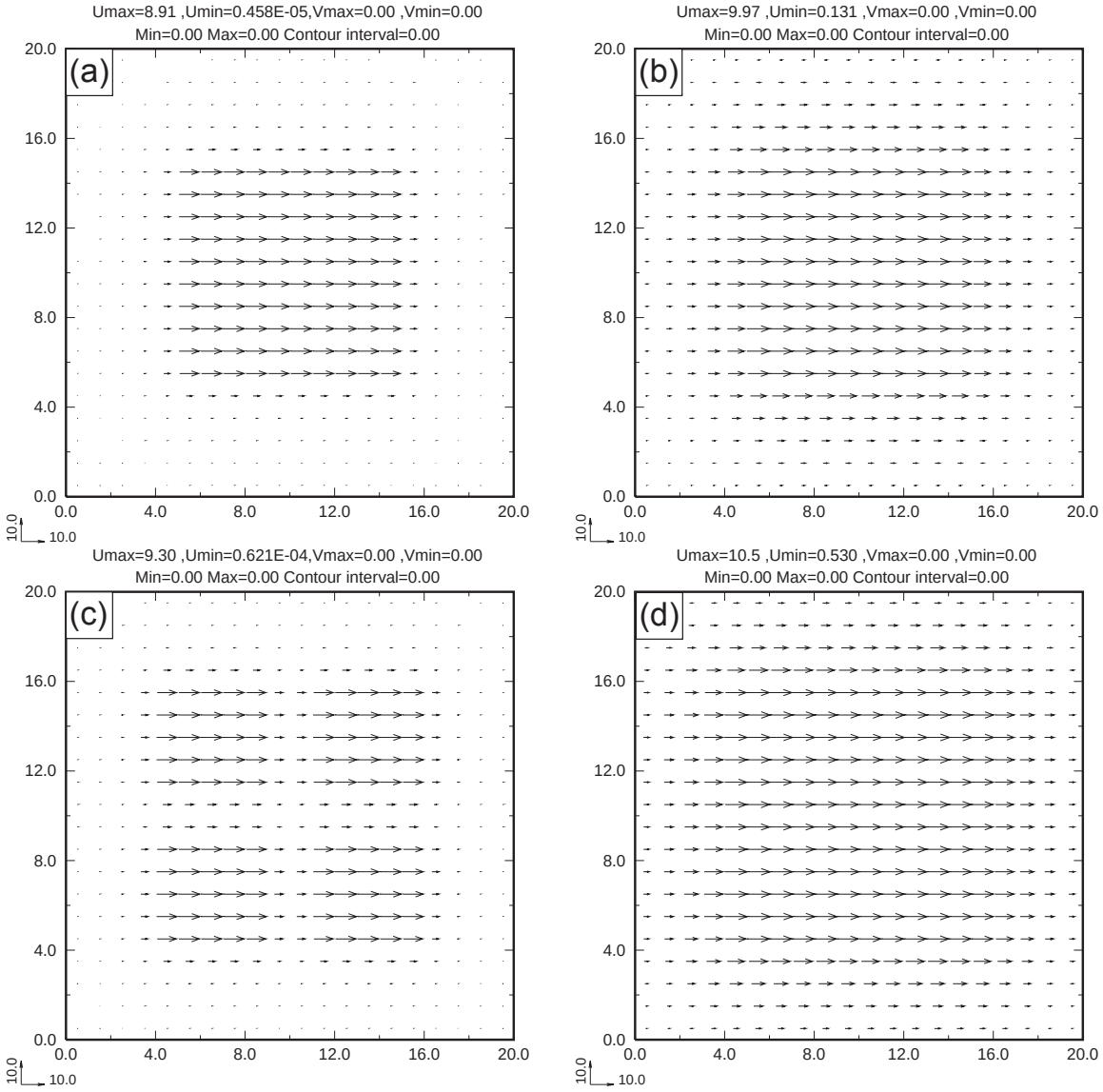

Fig. 2.4 3DVAR analysis is applied to 100 U observations concentrated on an area like radar radial wind. The observation values are 10 m s^{-1} and background field is set to 0. The recursive filter is used to model background error correlation. a) Analysis of a square-shaped observation area with the horizontal decorrelation scale set to 1 grid spacing. b) Similar to a) but with the horizontal decorrelation scale set to 3 grid spacings. c) Analysis of four square-shaped observation areas that have 2 grid spacing missing observations or holes among them. The horizontal decorrelation scale set to 1 grid space. d) Similar to c) but with the horizontal decorrelation scale set to 3 grid spacings. e) Analysis of four square-shaped observation clusters that observed U directions in each cluster are opposite to its nearby cluster. The horizontal decorrelation scale set to 1 grid spacing. f) Similar to e) but with the horizontal decorrelation scale set to 3 grid spacings.

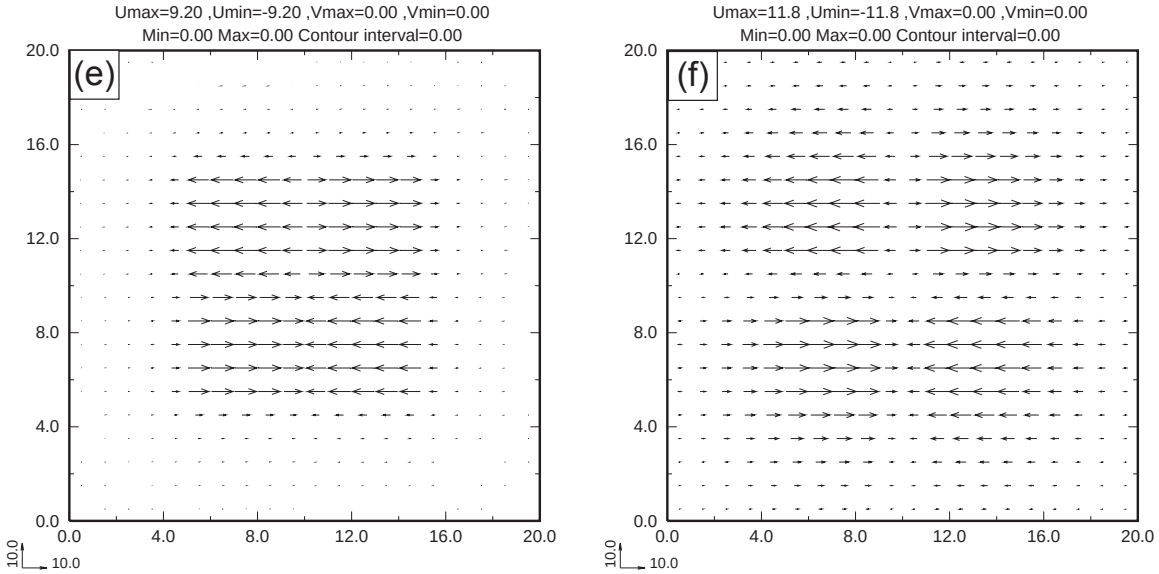

Fig. 2.4 Continued

The second situation assumes that some holes exist in a radial velocity observation area. This time we construct four observation clusters to form a big square-shaped area like the first situation and with 25 U observations in each cluster. Between these four clusters are 2 grid spacing wide missing observations or holes. The same 3DVAR analysis is applied in this observation situation and results are shown in Fig. 2.4c and d. The same as the first situation, analyzed U values in the observation area are increased by 2.38 m s^{-1} for R = 1 and 3.58 m s^{-1} for R = 3, a little larger than those in the first situation. Fig. 2.4d also shows that the holes between four observation areas have been filled by the recursive filter with a large horizontal decorrelation scale.

The third situation assumes radial velocity observations with shear and divergence among them. Using same four U observation clusters and put them together form a large square-shaped area but observed U directions in each cluster are opposite to its nearby clusters. Therefore, between these four clusters, there is a shear line in x-direction and a

divergence line and a convergence line in y-direction. Fig. 2.4e and f show the 3DVAR analysis with the horizontal decorrelation scale set to 1 and 3 grid spacing, respectively. It is found that the 3DVAR analysis correctly gives the existence of shear, divergence, and convergence lines but the overshooting problem can be severe along those lines when a large horizontal decorrelation scale is used (Fig. 2.4f). The results of this experiment indicate that the overshooting problem has been limited under a low level in most situation of the radial velocity analyses in the ARPS 3DVAR.

In further experiments, several observations are set in one grid box, which is how radial velocity observations are used in most current storm-scale simulations. Although, in the ARPS 3DVAR, both reflectivity and radial velocity data have been interpolated to the grid point via a preprocessing procedure that makes observation operator of the 3DVAR analysis much simpler, it is worthwhile to take a look at the situation where the resolution of radial velocity observations is higher that that of analysis space. In this experiment, 4 observations are put into the same grid box and totally 400 observations are distributed in 100 grid boxes that form a square-shaped observation area. The background is set to 0. The observations are set to 10 m s^{-1}. The 3DVAR analysis without the recursive filter is shown in Fig. 2.5a. The most of analysis values are larger than the observation values even without space correlation in the background error covariance. When the 3DVAR analysis with the recursive filter of the horizontal decorrelation scale set to 1 and 3 grid spacing is applied, the recursive filter does not cause overshooting problem in this situation and, interestingly, it can mitigate the overshooting problem induced by high resolution observations as demonstrated in Fig. 2.5b and c.

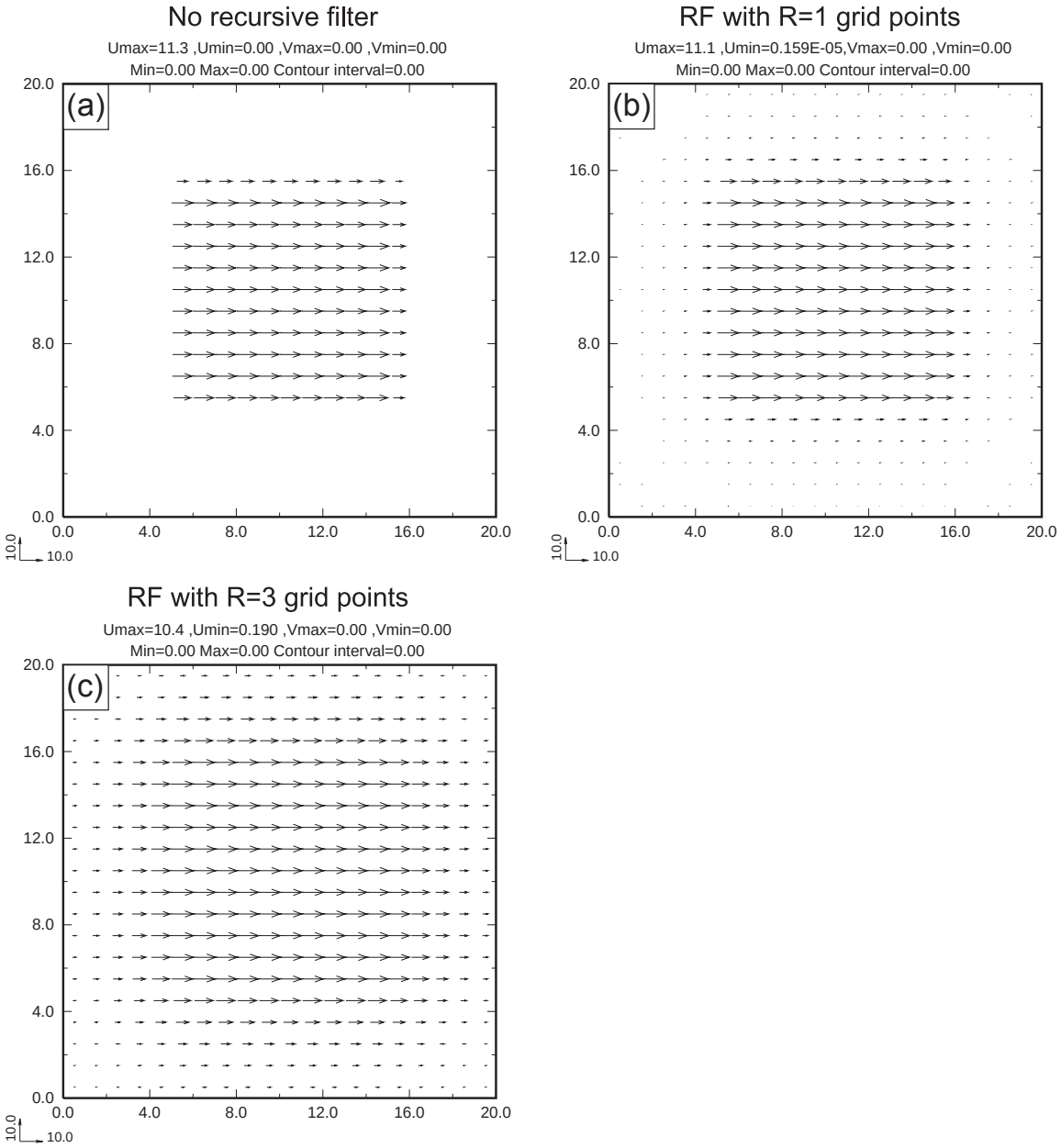

Fig. 2.5 3DVAR analysis is applied to 400 U observations concentrated on an area like radar radial wind. Each grid box has 4 observations in it. The observation values are 10 m s^{-1} and background field is set to 0. The recursive filter is used to model background error correlation. a) Analysis without the recursive filter. b) Analysis using the recursive filter with the horizontal decorrelation scale set to 1 grid spacing. c) Similar to b) but with the horizontal decorrelation scale set to 3 grid spacing.

2.3.4 Mass divergence constraint

In the ARPS 3DVAR analysis, the following weak mass divergence constraint can be imposed on the analyzed wind field:

$$J_c = \frac{1}{2}\lambda_c^2 D^2, \tag{2.7}$$

where λ_c is a weighting coefficient that controls the relative importance of this penalty term in the cost function. Here D has the form of

$$D = \alpha\left(\frac{\partial \bar{\rho}u}{\partial x} + \frac{\partial \bar{\rho}v}{\partial y}\right) + \beta\frac{\partial \bar{\rho}w}{\partial z}, \tag{2.8}$$

where $\bar{\rho}$ is the mean air density at given height levels, and α and β are weighting coefficients for the horizontal and vertical terms, respectively. Different choices of the α and β values will be tested in a set of analysis experiments to be presented later. This constraint acts to couple the wind components together during the analysis. When α = β = 1, the constraint acts to minimize the three-dimensional mass divergence and weakly enforces anelastic mass continuity. Gao et al (1999; 2004) found, for their case of near-unity grid aspect ratio ($\Delta x \sim \Delta z$), that the 3D formulation is effective in producing reasonable analyses of the vertical and horizontal velocity in their dual-Doppler radar wind analyses.

When used in a finite difference form, we find that the vertical mass divergence term in Eq. (2.8) dominates the adjustment of J_c in cases where the vertical grid is stretched to a large Δx to Δz (grid aspect) ratio at the low levels. For example, when $\Delta x = \Delta y = \gamma\Delta z$, Eq. (2.8) is discretized as

$$D = \frac{\Delta(\bar{\rho}u) + \Delta(\bar{\rho}v)}{\gamma\Delta z} + \frac{\Delta(\bar{\rho}w)}{\Delta z}. \tag{2.9}$$

When the grid aspect ratio, γ, is large, say over 100, as in our following cases near the surface, a small adjustment in the vertical velocity can offset a large change in the horizontal wind divergence. The result is that little change due to this constraint is made by the minimization to the horizontal wind components. One possible solution is to use different values of α and β or even set β to zero to alleviate this artifact of discretization.

To illustrate the above points, we conducted three experiments, in which a single radial velocity observation (taken to be along the *x* direction) is analyzed, using (a) no mass divergence constraint ($\alpha = \beta = 0$), (b) using a 2D mass constraint ($\alpha = 1$, $\beta = 0$), and (c) using a fully 3D mass divergence constraint ($\alpha = \beta = 1$). Further, to isolate the effect of the constraint, we do not include spatial filtering in these tests. The results of these experiments are plotted in Fig. 2.6. It can be seen that without the constraint, no *y* (or cross-beam) component of velocity is produced by the analysis; that is, the analysis is purely univariant (Fig. 2.6a). In this case no vertical velocity is created either (not shown). When the 2D mass divergence is used, a single radial velocity observation induces a horizontal flow pattern that is nearly non-divergent (Fig. 2.6b) while no vertical velocity develops (not shown). When a complete 3D divergence appears in J_c, most of the wind adjustment due to the constraint occurs in vertical velocity, as is shown by Fig. 2.6c, while little adjustment occurs to the *y* (horizontal cross-beam) component (Fig. 2.6d), a result very similar to the unconstrained case. In addition, when the spatial filtering (using a recursive filter) is applied, the analysis appears smoother and the analysis increment spreads over a larger area but the general behavior remains the same (not shown).

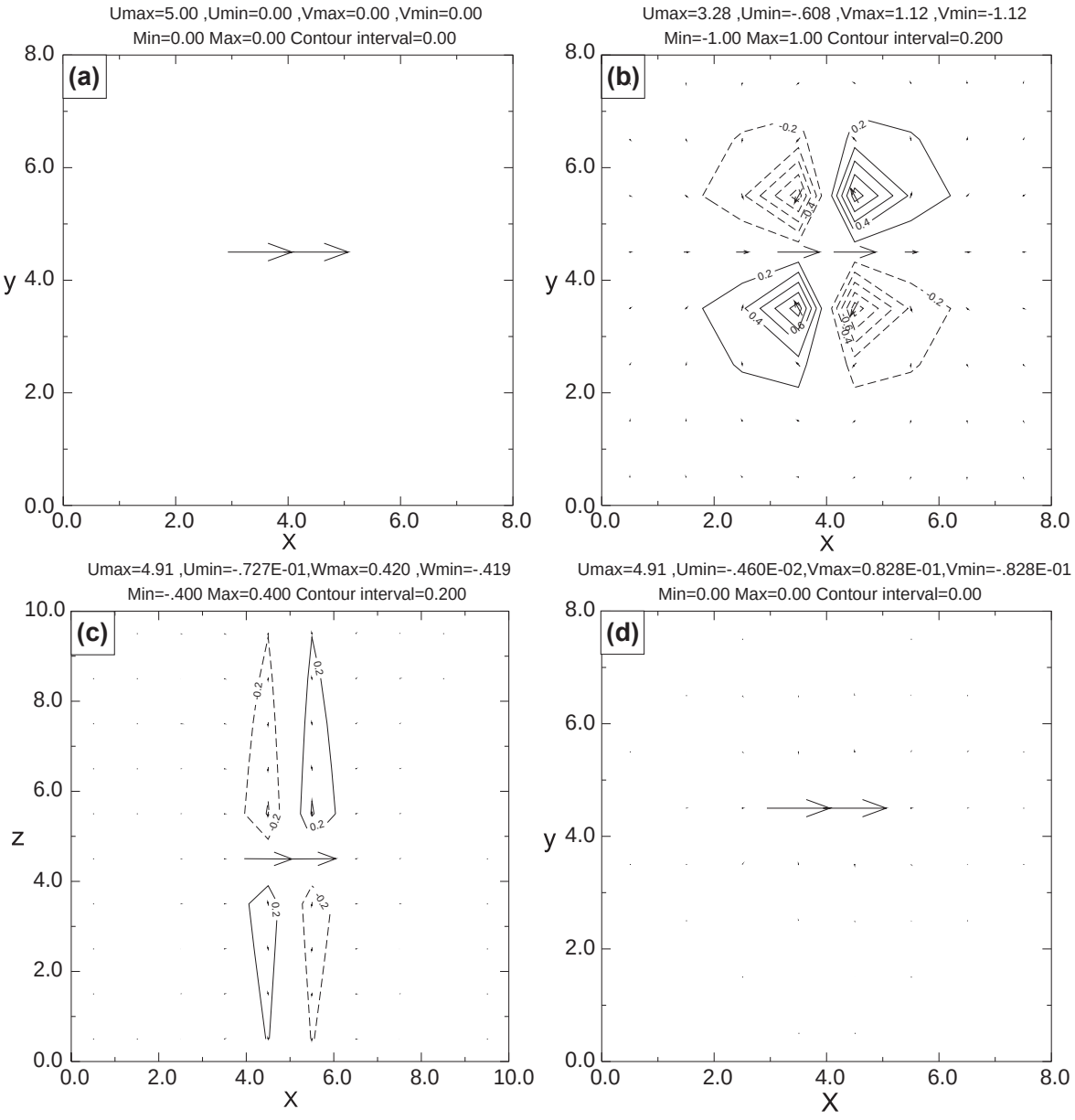

Fig. 2.6. Results of the 3DVAR analyzing a single radial wind measurement (pointing in positive *x* direction) with different mass divergence constraints. The background wind is zero. a) Wind analysis without applying mass divergence constraint, b) the x-y cross-section of u-v wind analyzed with a 2D (horizontal) mass divergence constraint, c) x-z cross-section of u-w wind after applying a 3D mass divergence constraint, and d) as b) but with a 3D mass divergence constraint. The wind units are m s^{-1}.

To further understand the behavior of the true 3D mass divergence constraint in the 3DVAR wind analysis, we need to analyze the gradient of the mass divergence constraint and its discretized form in detail. The gradient of Eq. (2.7) is

$$\nabla J_c = \lambda_c^2 \nabla^T (D) . \tag{2.10}$$

For a 3D mass divergence constraint, $\alpha = \beta = 1$, according to Eq. (2.8), D has the form of

$$D = \frac{\partial \bar{\rho} u}{\partial x} + \frac{\partial \bar{\rho} v}{\partial y} + \frac{\partial \bar{\rho} w}{\partial z} . \tag{2.11}$$

Because $\bar{\rho}$ is the mean air density at given height levels and it nears constant in nearby vertical grid levels, the Eq. (2.11) can be discretized as

$$D = \bar{\rho}(\frac{u^+ - u^-}{\Delta x} + \frac{v^+ - v^-}{\Delta y} + \frac{w^+ - w^-}{\Delta z}) .$$

Using the same grid aspect ratio γ as the previous setting, which is $\Delta x = \Delta y = \gamma \Delta z$, the above discretized mass divergence can be rewritten as

$$D = \frac{\bar{\rho}}{\Delta x}(u^+ - u^- + v^+ - v^- + \gamma w^+ - \gamma w^-) , \tag{2.12}$$

and its matrix form is

$$D = \frac{\bar{\rho}}{\Delta x}[1, -1, 1, -1, \gamma, -\gamma] \begin{bmatrix} u^+ \\ u^- \\ v^+ \\ v^- \\ w^+ \\ w^- \end{bmatrix} . \tag{2.13}$$

So, according to Eq. (2.13), the matrix of the discretized mass divergence operator of wind field is

$$\nabla = \frac{\overline{\rho}}{\Delta x}[1,-1,1,-1,\gamma,-\gamma],$$

and its adjoint matrix is

$$\nabla^T = \frac{\overline{\rho}}{\Delta x}\begin{bmatrix} 1 \\ -1 \\ 1 \\ -1 \\ \gamma \\ -\gamma \end{bmatrix}.$$

Now, the gradient of the discretized divergence constraint in matrix form is:

$$\nabla J_c = \frac{\lambda^2 \overline{\rho}}{\Delta x}\begin{bmatrix} 1 \\ -1 \\ 1 \\ -1 \\ \gamma \\ -\gamma \end{bmatrix} D. \qquad (2.14)$$

The Eq. (2.14) is the equation that controls the adjustment of wind field to approach divergence constraint in the 3DVAR wind analysis. In the 3DVAR framework, the gradient of the cost function decides the direction (opposite to the direction of gradient) and the rate of the adjustment of analysis variables in each grid point. According to Eq. (2.14), a convergence (negative divergence) point like right end of the U vector shown in Fig. 2.6a will induce the following wind adjustment in its surround grid points via the 3D divergence constraint:

u^+ increases for $-(\nabla J_c)_{u^+} = \dfrac{\lambda^2 \overline{\rho}}{\Delta x}|D| > 0$;

u^- decreases for $-(\nabla J_c)_{u^-} = -\dfrac{\lambda^2 \overline{\rho}}{\Delta x}|D| < 0$;

v^+ increases for $-(\nabla J_c)_{v^+} = \dfrac{\lambda^2 \overline{\rho}}{\Delta x}|D| > 0$;

v^- decreases for $-(\nabla J_c)_{v^-} = -\dfrac{\lambda^2 \overline{\rho}}{\Delta x}|D| < 0$;

w^+ increases for $-(\nabla J_c)_{w^+} = \gamma \dfrac{\lambda^2 \overline{\rho}}{\Delta x}|D| > 0$;

w^- decrease for $-(\nabla J_c)_{w^-} = -\gamma \dfrac{\lambda^2 \overline{\rho}}{\Delta x}|D| < 0$.

This shows the adjustment creates divergence wind field in three wind components for this case and we should see reduced U value in original observation grid point (u^- point) and new created positive u^+, v^+, w^+ and negative v^-, w^- in the analysis results. In the case of large grid aspect ratio, γ, the rates of adjustment for above 6 wind components are significant different. The 2 vertical wind values, which decide the vertical part of divergence constraint, can be adjusted much faster (γ times faster) than that of horizontal direction. Before horizontal wind field can be changed obviously, a weak vertical divergence has been built up quickly to offset the horizontal convergence because the vertical divergence only needs to get 1/γ of the horizontal convergence to fulfill the constraint. That explains why the analysis results with a 3D mass divergence constraint shown in Fig. 2.6d so resembles Fig. 2.6a, and the vertical velocity is weak in the Fig. 2.6c.

Another experiment is conducted to investigate the problem of high grid aspect

ratio in different weighting coefficients. Now two radial velocity observations (taken to be along z direction) are analyzed with the 3DVAR, using (a) no mass continuity constraint, (b) using a fully 3D divergence constraint with weight coefficient $\lambda = 500$, (c) same as (b) but with weighting coefficient $\lambda = 1000$, and (d) as (b) but with weighting coefficient $\lambda = 2000$. The results of the experiment are plotted in Fig. 2.7.

Fig. 2.7a shows the analysis increment without the mass divergence constraint. A strong convergence center is found in the analyzed *w* field. The mass divergence constraint is a weak constraint in the ARPS 3DVAR and its relative importance is decided by the weighting coefficient λ. When λ approaches infinity, the mass divergence constraints become a strong constraint in the 3DVAR. In this experiment, three λ values are used and they produce three typical results in analysis. For $\lambda = 500$, Fig. 2.7b shows that the analyzed *w* only decreases a little compared to that in Fig. 2.7a and the newly created horizontal divergence is weak. Apparently, the divergence constraint is only a very weak constraint in the analysis. When λ increases to 1000 (Fig. 2.7c), analyzed vertical winds are reduced a lot when compared to the experiment shown in Fig. 2.7a and b, and horizontal wind increments only increase a little (maximum from 0.84 m s^{-1} in Fig. 2.7b to 1.04 m s^{-1} in Fig. 2.7c). Under values $\lambda = 1000$, the importance of the mass divergence constraint is increased but a large unbalance still exists in the vertical and horizontal divergence parts. When a large λ value is used (2000, Fig. 2.7d), the analysis only gives a weak wind field, both in the vertical and the horizontal. Recall that the grid aspect ratio is large in the experiment and the rate of vertical adjustment is much faster than that of horizontal one.

The above experiment clearly shows that the reducing of the vertical convergence

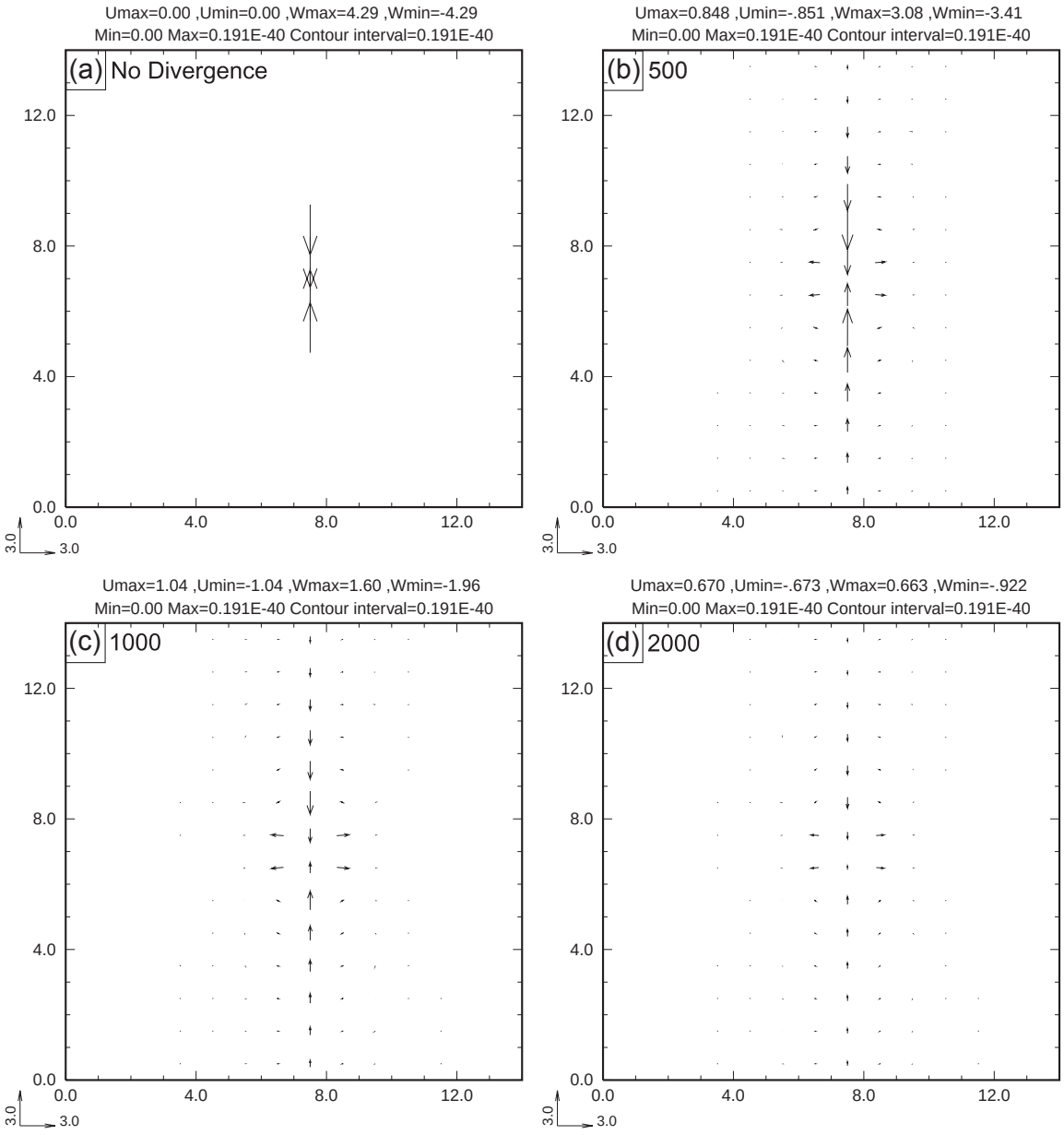

Fig. 2.7. Results of the 3DVAR analyzing two radial wind measurements (the lower one points in positive z direction and the upper one in negative z direction) with different mass continuity constraints. The background wind is zero. a) wind analysis without applying mass continuity constraint, b) the x-z cross-section of u-w wind analyzed with a 3D mass continuity constraint that weight coefficient $\lambda = 500$, c) as b) but with $\lambda = 1000$, and d) as b) but with $\lambda = 2000$.

is much faster than the building up of the horizontal divergence with λ increasing. Combining with the analysis in the first experiment in this section, we can see that the application of a 3D divergence constraint in the 3DVAR can change wind field little when only the horizontal divergence exists and kills all wind components when only the vertical divergence exists in the case of high grid aspect ratio and large weighting coefficient. In the case of small weight coefficient (Fig. 2.7b), the analysis increments are supported by the observation innovations and the 3D divergence constraint can built up a weak horizontal circulation complementing part of the vertical convergence.

The main goal of including mass divergence constraint in the radial velocity analysis is to derive wind information perpendicular to radar beams. From the above analysis, the three-dimensional formulation cannot achieve the desired goal when the grid aspect ratio is large, which is unfortunately true in our case. This was not an issue in the earlier variational dual-Doppler wind analyses (Gao et al. 1999; 2004) and has therefore not been recognized until now. Since the mass divergence constraint is a weak constraint, zero mass divergence is not strictly satisfied; the analysis has some flexibility in determining the amount of adjustment to different wind components, depending on the weighting coefficients.

2.4 ARPS cloud analysis

The cloud analysis procedure incorporates cloud reports from surface observations from Global Observing System (GOS) of the World Meteorological Organization (WMO), METARs (translated roughly from French as aviation routine weather reports), geostationary satellite infrared and visible imagery data, and radar reflectivity data to construct three-dimensional cloud and precipitate fields. The products

of the analysis package include three-dimensional cloud cover, cloud liquid and ice mixing ratios, cloud and precipitate types, icing severity index, and rain, snow, and hail mixing ratios. Cloud base, cloud top, and cloud ceiling fields are also derived. A latent heat adjustment to temperature based on added adiabatic liquid water content is applied in order to make the in-cloud temperature consistent with the cloud fields. More details on the package can be found in the references cited in Chapter 1.

The above version of the cloud analysis was used in Xue03. Since then, several improvements have been made to the cloud analysis procedure in order to make it more suitable for thunderstorm initialization. Some improvements are described in Brewster (2002). In this section, we introduce the original and updated cloud analysis schemes and the corresponding modifications, together with example analyses.

2.4.1 The analysis of precipitation species

2.4.1.1 The reflectivity equations

Reflectivity equations that link the precipitation species or hydrometeors (rain, snow, and hail mixing ratios in our case) with the reflectivity are needed to determine the former from the latter. The process of determination also utilizes information, such as temperature, from the background analysis, which usually is an analysis that has already incorporated other observations.

In our updated cloud analysis, the three equations that define the contributions of rain, snow, and hail to the total reflectivity are based on Smith et al. (1975) and the exact form used can be found in Tong and Xue (2005b). Based on precipitation types identified according to reflectivity and the background state, the rain, snow, and hail mixing ratios are determined using the reflectivity equations. We refer to this precipitation species

determination procedure as the SMO scheme. In the cloud analysis procedure used by Xue03, the rainwater mixing ratio is retrieved using the Kessler reflectivity equation (Kessler 1969), and snow and hail are retrieved using Rogers and Yau (1989) reflectivity formula. This procedure is referred to as the KRY scheme.

The SMO reflectivity equations were derived based on cloud physics and hydrometeor backscattering models, while the KRY equations were based on curve and parameter fitting to observations. The SMO scheme is believed to be more accurate.

2.4.1.2 The initial determination of hydrometeors from reflectivity

To perform the cloud analysis, the reflectivity data are first remapped to the analysis grid using a procedure that employs a local least squares fitting to the polar-coordinate data assuming that the reflectivity varies quadratically in the x and y directions and linearly in the vertical. Quality control, including screening for anomalous propagation, is applied in the remapping step.

In the SMO scheme, within the radar scan volume, the grid points are classified into clear or precipitation-filled categories based on a 10 dBZ reflectivity threshold. This threshold is chosen because most nonhydrometeor targets, such as ground clusters, have reflectivity values less than 10 dBZ but often above 0 dBZ. Where observations are flagged as missing, the corresponding grid points are categorized as missing too. The precipitation species at the precipitation-filled points are retrieved from the observed reflectivity while those at the clear points are set to zero. For the points below the lowest radar elevation, the SMO scheme uses the background values but limits the total mixing ratio of the hydrometeors to be no larger than the maximum of total mixing ratios in the column above.

In the KRY scheme, the threshold is set at 0 dBZ instead. The points with reflectivity greater than 0 dBZ are considered to be precipitation-filled, and all other points are flagged as missing. For the points below the lowest radar elevation, the KRY scheme sets the precipitation species to zero. In both cases, for the missing points and in the areas beyond the radar range, the background values are used in the final analysis.

Figure 2.8 shows, as an example, the initial determinations of precipitation species (referred to as observation-based retrievals hereafter) by the KRY (left column) and SMO (right column) schemes. The background field in this case is a 10-minute ARPS model forecast at 3-km resolution. The radar data are from the Fort Worth WSR-88D radar and are valid at 2250 UTC 28 March 2000. It can be seen that the KRY scheme gives much more hail and rain but less snow than the SMO scheme, reflecting the warm-rain root of the KRY scheme. In the rain field of the SMO scheme, the large values under the lowest radar elevation came from the forecast background.

2.4.1.3 The final analysis of hydrometeors

The next step of hydrometeor analysis consists of a judiciary combination of the background values with those determined from reflectivity observations. In the scheme used in Xue03 (denoted as the Xue03 scheme), the greater one among the background and observation-based retrievals is taken. In our updated scheme, based on the belief that the radar-observed precipitation is much more reliable than the model prediction, the values determined from the observations are used whenever available. This new procedure helps remove spurious precipitation in the forecast background. With the updated scheme, where valid radar observation is present, the reflectivity-based retrieval is chosen over the background value.

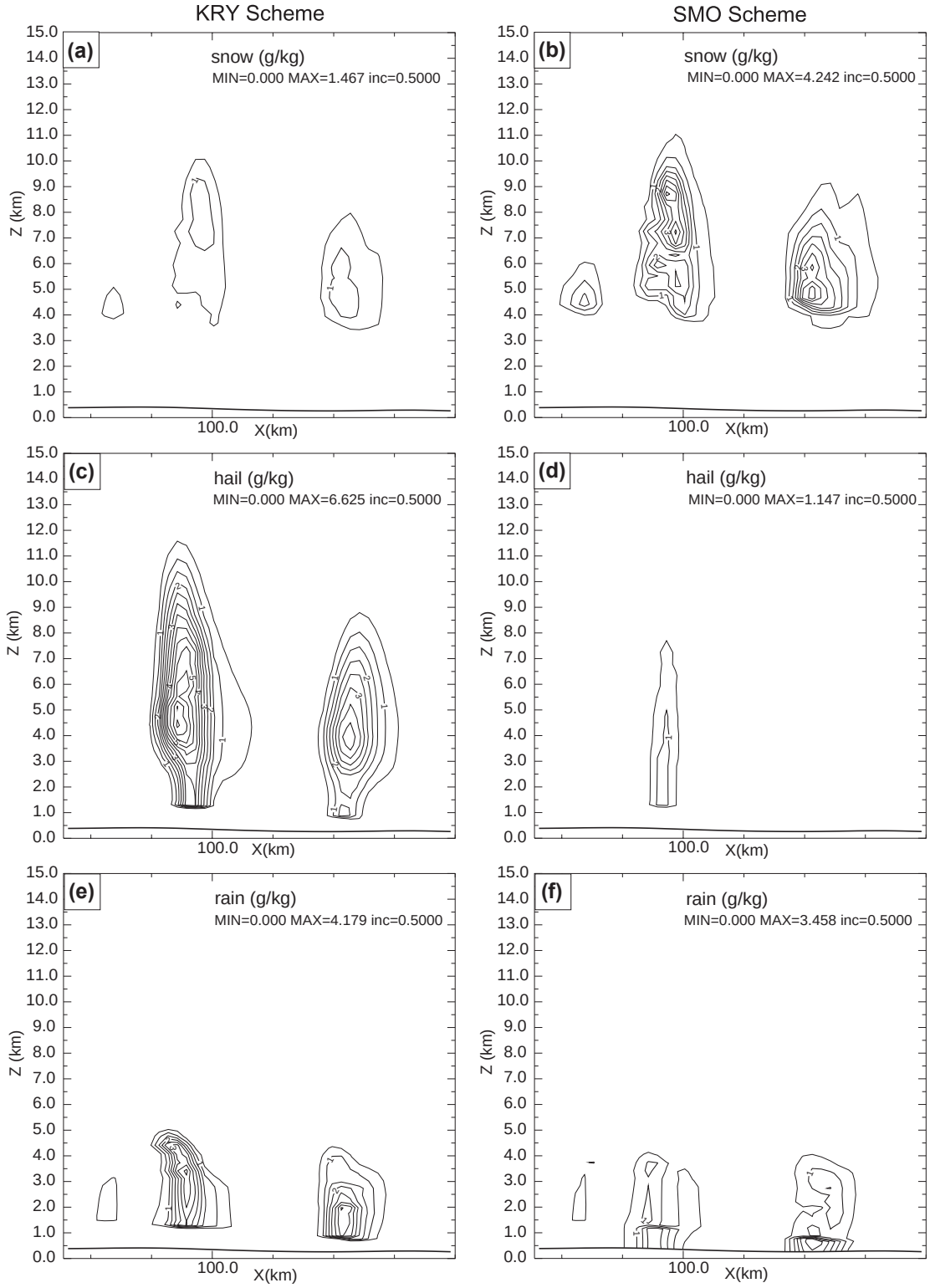

Fig. 2.8. Cross sections of snow, hail, and rain fields determined from reflectivity observations by the (left) KRY and (right) SMO schemes using the background analysis, for 2250 UTC 28 March 2000.

As an example, the final analysis of precipitation species by the Xue03 scheme is shown in Fig. 2.9, which corresponds to the initial determination shown in the left column of Fig. 2.8. In the Xue03 scheme, the background values dominate the final analysis for all three species. The reflectivity fields calculated from the background hydrometeors, the final analysis of the Xue03 scheme, and that of the updated scheme are plotted in Fig. 2.10. The reflectivity from the Xue03 scheme largely mirrors the background, while the reflectivity using the updated scheme shows more detailed observed structures inside the storms.

2.4.2 The analysis of cloud water and cloud ice

To estimate cloud water and cloud ice mixing ratios, the adiabatic liquid water content (ALWC) is estimated by assuming a moist-adiabatic ascent from cloud base to cloud top. A reduction is applied to the ALWC to account for entrainment. In the scheme used by Xue03, the curve of reduction was determined from field data collected largely from isolated towering cumulus clouds (Warner 1970). This curve tends to produce liquid and ice water contents that are too low. In the cases of supercell and widespread thunderstorms, clouds have much larger vertical and horizontal extent and less entrainment in the center of storm cells. Based on this consideration, a new entrainment curve is devised in the updated scheme to limit the reduction of cloud water and ice due to entrainment. Fig. 2.11 shows the analyses of cloud water and cloud ice using the curve of Xue03 (left) and the new curve (right). The increase in cloud mixing ratio with the latter is evident. In our experiments at 3-km horizontal resolution, the cloud water and cloud ice analyzed using the updated scheme can usually sustain the model reflectivity for no less than 10 minutes.

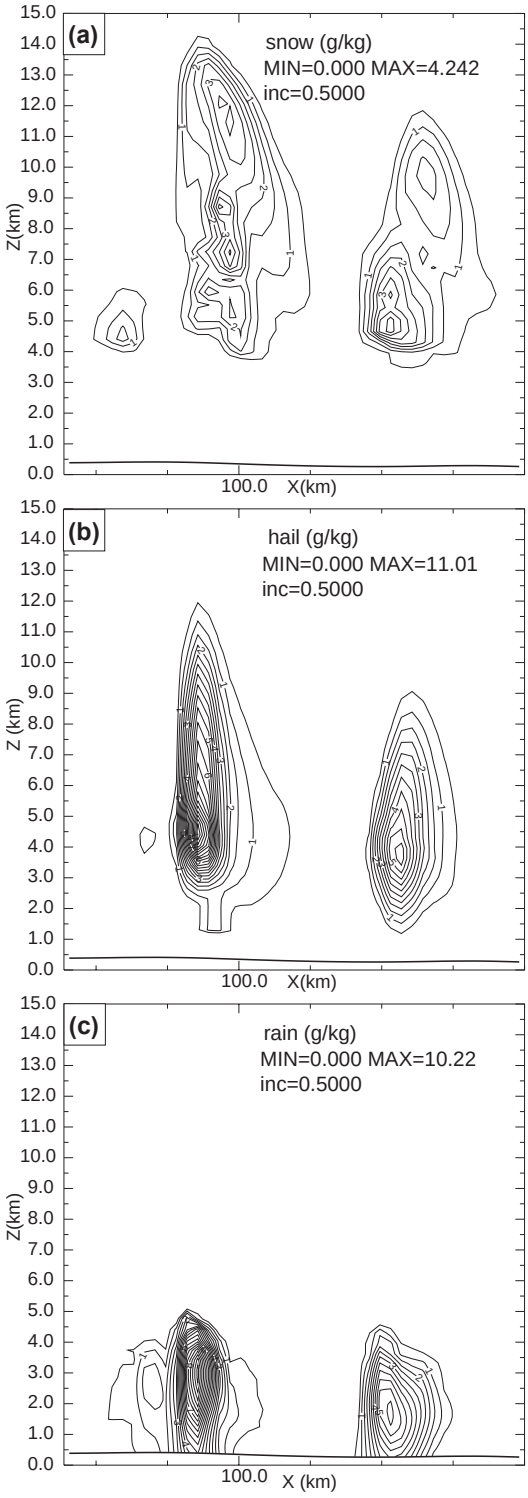

Fig. 2.9. Cross section of the final analysis of snow, hail, and rain fields by the cloud analysis used by Xue03, for 2250 UTC 28 March 2000 scheme.

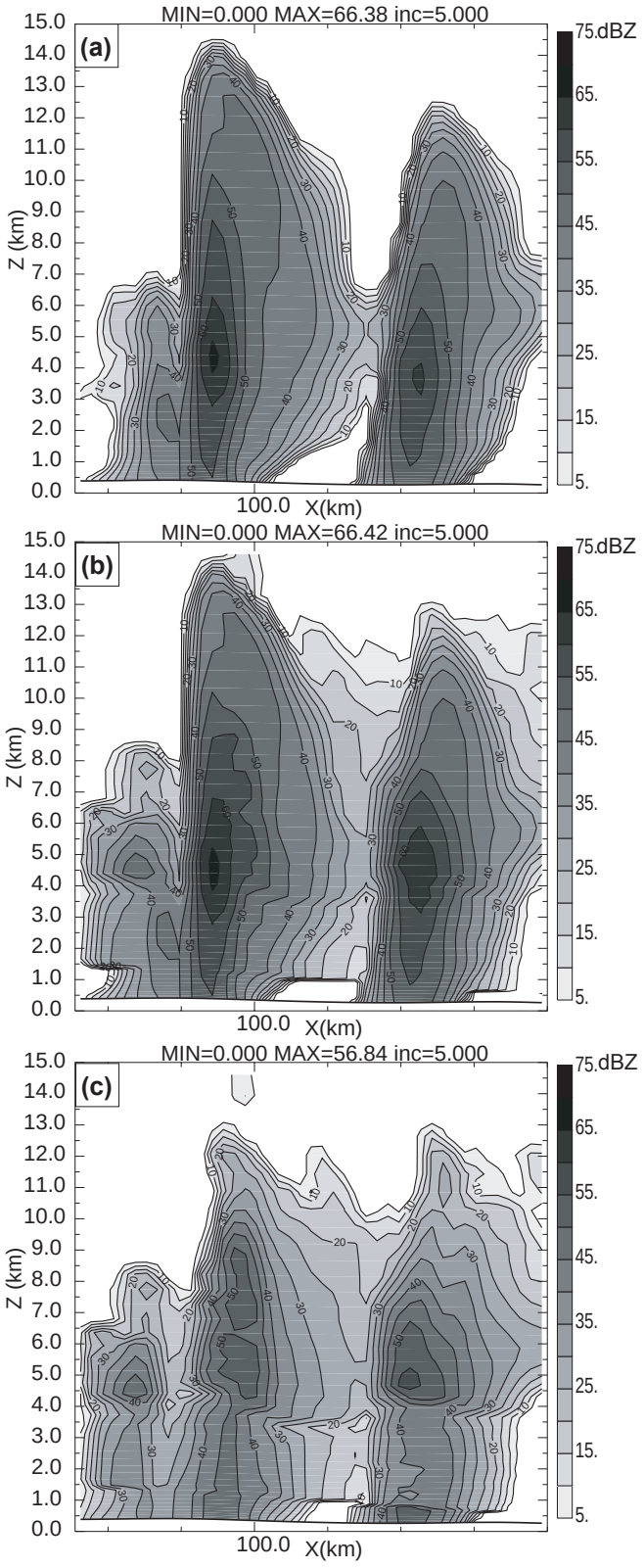

Fig. 2.10. Cross section of reflectivity fields calculated from precipitation mixing ratios of (a) background, (b) the cloud analysis of Xue03, (c) the updated cloud analysis, for 2250 UTC 28 March 2000.

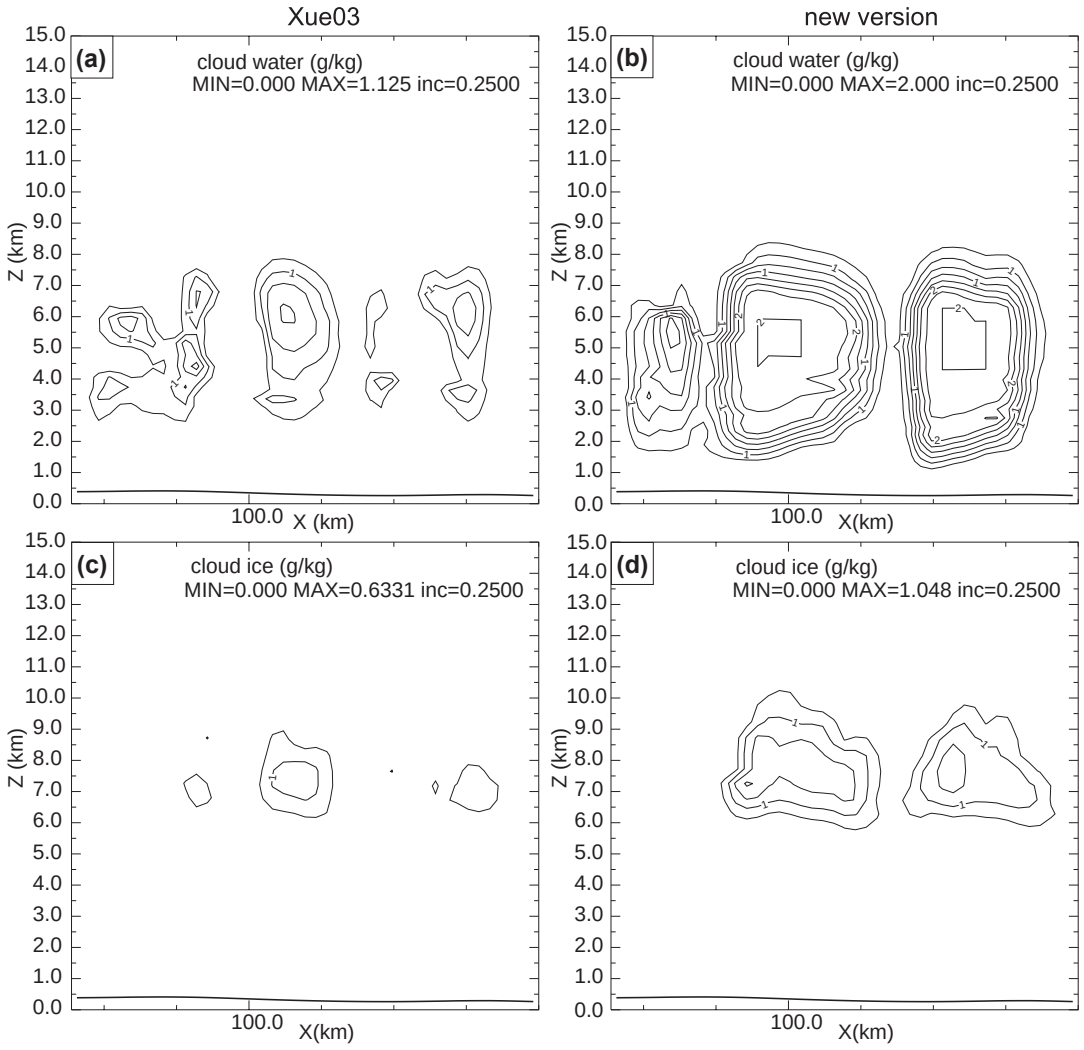

Fig. 2.11. Cross section of cloud water and cloud ice fields from the cloud analysis with the entrainment curve used in (left) Xue03 and (right) the new curve with reduced entrainment, for 2250 UTC 28 March 2000.

2.4.3 In-cloud thermal adjustment

Temperature adjustment associated with precipitating clouds is very important in sustaining existing convection. In the cloud analysis used in Xue03, the temperature adjustment is calculated from the latent heat release corresponding to the added cloud water and ice (referred to as the latent heat scheme). In the updated scheme, a moist-adiabatic temperature profile with the same entrainment factor as applied to the cloud

water is used to adjust the temperature after determination of cloud and precipitation contents. This adjustment scheme is more consistent with the physics of a convective storm because it reflects the temperature change in an ascending moist air parcel. The typical temperature adjustments due to the two schemes are plotted in Fig. 2.12. The profile of horizontally averaged temperature increments show that the moist-adiabat-based scheme heats the atmosphere through a greater depth, while the latent heat scheme warms the atmosphere more at the middle and lower levels where cloud water and ice are concentrated (Fig. 2.12a). The difference in the temperature adjustments of the two schemes at 4.5 km MSL shown in Fig. 2.12b has a similar pattern as the observed reflectivity.

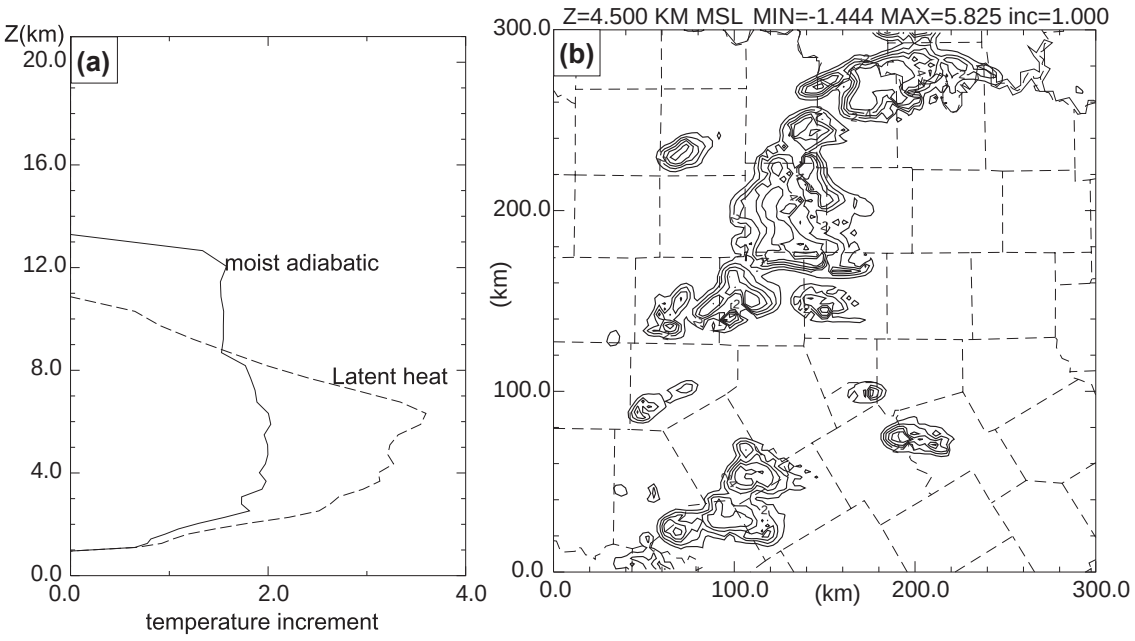

Fig. 2.12. (a) The profile of horizontally averaged temperature increments from adjustments using the moist adiabatic profile (of the updated version) and latent heat (used in Xue03) methods, and (b) the difference in the temperature increment between these two methods at 4.5 km MSL, for 2250 UTC 28 March 2000.

Chapter 3

28 March 2000 Fort Worth, Texas, Tornadic Thunderstorm Case[*]

3.1 The case

In this Chapter, we apply our 3DVAR and the updated cloud analysis procedure to the 28 March 2000 Fort Worth tornadic thunderstorm case studied by Xue03. We evaluate the performance of the analysis mainly by examining the quality of the subsequent forecast.

On 28 March 2000, two tornadoes were observed in the Fort Worth, Texas area. One reached F2 intensity (maximum winds 51 m s^{-1} to 70 m s^{-1}) and struck downtown Fort Worth at around 6:15 P.M. LST 28 March (0015 UTC 29 March) 2000. The tornado funnel developed directly over the city, descended, and stayed on the ground for at least 15 minutes. The tornado caused extensive damage to several structures, including high-rise buildings. It directly caused two fatalities and many injuries. The parent storm also brought torrential rains and softball-size hailstones, causing two deaths from flooding in the eastern portion of Tarrant County (highlighted in Fig. 3.1a), near Arlington, and one additional death due to hail. Another tornado from the same complex of storms touched down in south Arlington, approximately 25 km east of Fort Worth, about 30 minutes after the Fort Worth tornado, at about 7:00 P.M. LST 28 March (0100 UTC 29 March) 2000. These tornadoes have special significance because they struck the center of a major metropolitan area.

---

[*]This chapter is a combined version of a two-part paper accepted by Monthly Weather Review (Hu et al 2006a, b).

The mesoscale and synoptic-scale settings in which the tornadic thunderstorms occurred are described in Xue03.

3.2 Design of experiments

The primary goal of this work is to test the impact of Level-II WSR-88D reflectivity and radial velocity data on the ability of a high-resolution model and its data assimilation system to initialize and forecast preexisting thunderstorms. The capabilities of the ARPS 3DVAR and the improved cloud analysis procedure are also examined through real data experiments. Because all thunderstorms to be studied occurred within the range of Fort Worth (KFWS) radar during the period of assimilation, only data from KFWS are used. The reflectivity data from the same radar are also used to verify the model forecast.

Similar to the experiments reported by Xue03, two one-way nested grids are used here, with the resolutions of 9 and 3 km, respectively. The two grids cover areas of 1000 km × 1000 km and 450 km × 300 km, respectively, and the vertical grid spacing is increased from 20 m at the surface to about 770 m at the model top located at 21.1 km height**.** The same model grids are used for the analysis and forecast, and the increased near-surface vertical resolution allows for better resolution of the boundary layer features. The model settings used are listed in Chapter 2 and they are essentially the same as in Xue03, except that an updated version of ARPS is used. Specifically, we employ Lin et al (1983) ice microphysics without cumulus parameterization. At 3-km resolution, cumulus parameterization is usually not needed while the 9-km resolution falls into a "gray" area where neither explicit nor parameterization precipitation physics works well. A corresponding 9-km experiment with the Kain-Fritsch cumulus parameterization scheme

led to poorer results on the 3-km grid.

The 9-km grid is initialized at 1800 UTC 28 March, from a single 3DVAR analysis that combined rawinsonde, wind profiler, METAR surface observations, and Oklahoma Mesonet data, using the National Center for Environmental Prediction (NCEP) Eta model 1800 UTC analysis as the background. At the lateral boundaries, the 9-km grid is forced by the Eta 1800 UTC forecasts at 3-hour intervals. No data assimilation is performed for the 9-km grid and the forecast is run for 12 hours, ending at 0006 UTC 29 March. With the primary goal of initializing preexisting storms, the 3-km grid is started at a later time (2200 UTC), when some of the thunderstorms had already formed and were captured by the KFWS radar.

Different from the 3-km experiments of Xue03, we use the ARPS 3DVAR instead of the ADAS as the analysis tool. Further, we use and examine an improved version of the cloud analysis. In addition, we use Level-II instead of Level-III data with 10-minute instead of 15-minute intermittent assimilation cycles. As in Xue03, the hour long assimilation period starts at 2200 UTC and ends at 2300 UTC, about 1 hour 15 minutes before the tornado touched down in Fort Worth. The Level-II data contain 9 (in the first half hour) or 14 (in the second half hour) instead of the 4 elevation levels of Level-III data used in Xue03, and that data do not have the Level-III's degradation in the radial velocity data precision (Level-III radial velocity data were used in Xue03 through a simple radial velocity adjustment procedure of the ADAS). The reflectivity data are used in the cloud analysis procedure to retrieve cloud and hydrometers fields and to make adjustments to in-cloud temperature and moisture. The radial velocity data are analyzed by the 3DVAR subject to a mass divergence constraint

Since data representing very different spatial scales are used, we employ the multipass strategy available with our 3DVAR system. Specifically, three analysis passes are performed on the 3-km grid, with each pass using different data types. Filter scales of 120 and 75 km are used in the first and second passes when the wind profiler data and surface data are used, respectively. When radial velocity data are analyzed in the third pass in some experiments, filter scale of 9 km is used.

The 3-km forecasts start at 2300 UTC 28 March from the assimilated initial conditions and end at 0200 UTC 29 March. Because few surface and upper-air data are available within the 3-km domain during the assimilation period, the storm environment is defined primarily by information carried over from 1800 UTC (when there are more observations) by the 9-km ARPS forecast or from even earlier by the Eta model. The 9-km preforecast period is generally helpful in reducing the spinup time on the 3-km grid for both the assimilation and model forecast.

In this Chapter, six experiments are designed to specifically examine the impact of reflectivity data and the improved cloud analysis procedure (see Table 3.1). Only reflectivity data are employed in the assimilation cycles of experiment CNTLZ at the 3-km resolution. The 3DVAR analysis is used to analyze conventional data but no radial velocity data are used.

The control experiment of Xue03 is repeated in this research for comparison (listed as experiment X03 in Table 3.1). It uses exactly the same data as CNTLZ but a slightly different version of the ARPS model and ADAS analysis, which are configured as close to those in Xue03 as possible. Differences between our current experiments and X03 are described earlier.

Based on experiment CNTLZ, three experiments, CTLH, CKRY, and CMAX are performed to examine, respectively, the impact of different schemes of in-cloud temperature adjustment, the initial determination of hydrometers from reflectivity, and the final analysis of hydrometeors in the X03 and updated cloud analysis procedures (Table 3.1). Experiment without radar data, NoVRZ, is also conducted for comparison purpose.

To study the impact of assimilating radial velocity data and the use of divergence constraint, eight experiments, including experiment CNTLZ listed in Table 3.1, are conducted (see Table 3.2). The first three are designed to specifically investigate the impact of assimilating radar radial velocity data. The control experiment, CNTLVR, includes both Level-II reflectivity and radial velocity data in its assimilation cycles. For the reason discussed in section 2.3.4, the weak two-dimensional mass divergence constraint is used in the control and related experiments. Two other experiments, namely CNTLZ and VR, examine the effect of including reflectivity (denoted as Z), or radial velocity (denoted as V_r) data alone. The experiments are otherwise the same as CNTLVR.

The next five experiments are designed to examine the role and effect of various formulations of the mass divergence constraint in the 3DVAR cost function (Table 3.2). They differ from CNTLVR in the use of the constraint only. Experiment NoDiv does not include any divergence constraint while experiments Div3Da and Div3Db use a 3D formulation with different and equal values of α and β in Eq. (5), respectively. Two other experiments, Div2Da and Div2Db, test the sensitivity of storm forecasts to weighting coefficient, λ_c, with a 2D formulation (Table 3.2).

Table 3.1. List of 3-km experiments and their main characteristics for the cloud analysis.

NAME	Temperature adjustment	Final analysis of hydrometeors	Initial determination of hydrometeors	Radar data
CNTLZ	Moist adiabatic profile	Observation-based retrievals	SMO	Level-II
X03	Latent heat	Maximum of observation-based retrievals and background	KRY	Level-III
CTLH	Latent heat	Observation-based retrievals	SMO	Level-II
CKRY	Moist adiabatic profile	Observation-based retrievals	KRY	Level-II
CMAX	Moist adiabatic profile	Maximum of observation-based retrievals and background	SMO	Level-II
NoVRZ	N.A.	N.A.	N.A.	No

Table 3.2. List of 3-km experiments and their main characteristics for the radial velocity analysis and mass divergence constraint.

Experiment	Use of reflectivity	Use of radial velocity	Mass divergence constraint	
			Dimension	Weighting coefficients
CNTLVR	Yes	Yes	2D	$\alpha \lambda_c = 1000$, $\beta=0$
CNTLZ	Yes	No	N.A.	$\lambda_c = 0$
VR	No	Yes	2D	$\alpha \lambda_c = 1000$, $\beta=0$
NoDiv	Yes	Yes	N.A.	$\lambda_c = 0$
Div2Da	Yes	Yes	2D	$\alpha \lambda_c = 500$, $\beta=0$
Div2Db	Yes	Yes	2D	$\alpha \lambda_c = 2000$, $\beta=0$
Div3Da	Yes	Yes	3D	$\alpha \lambda_c = 1000$, $\beta \lambda_c = 100$
Div3Db	Yes	Yes	3D	$\alpha \lambda_c = \beta \lambda_c = 1000$

3.3 Impact of cloud analysis with reflectivity

In this study, we use reflectivity data, at the original radar elevation levels, as the primary observations for forecast verification, because there is no other observation with similar temporal and spatial resolutions as the model forecast. The next possible source of information would be the hourly surface observations; since there are less than 20 surface observations within the model domain and they do not provide information on the 3D storm structure, their use for quantitative verification is limited. Rain gauge data do not have sufficient resolution for precipitation verification either.

In this section, the forecast results from experiments CNTLZ, X03, and NoVRZ are first analyzed to investigate the impact of the updated cloud analysis procedure and the Level-II WSR-88D reflectivity data. It also serves to establish the improvement of the new configuration over the old one (as used in Xue03). The impacts of each modification in the cloud analysis procedure are then examined by comparing assimilation and forecast results of all experiments except for NoVRZ.

3.3.1 Radar observations

Observed reflectivity at the 1.45° elevation from Level-II data of the KFWS radar at 15-minute intervals for 1 hour starting from 0000 UTC 29 March are plotted in Fig. 3.1. This hour covers the forecast period in which two tornadoes struck in Tarrant County (one at 0015 UTC at Forth Worth and one at 0100 UTC near Arlington). Tarrant County is highlighted by the bold rectangle in the figure. Downtown Fort Worth and Arlington are marked by black dots in Fig. 3.1a. Names of most counties to be referenced are also found in Fig. 3.1a.

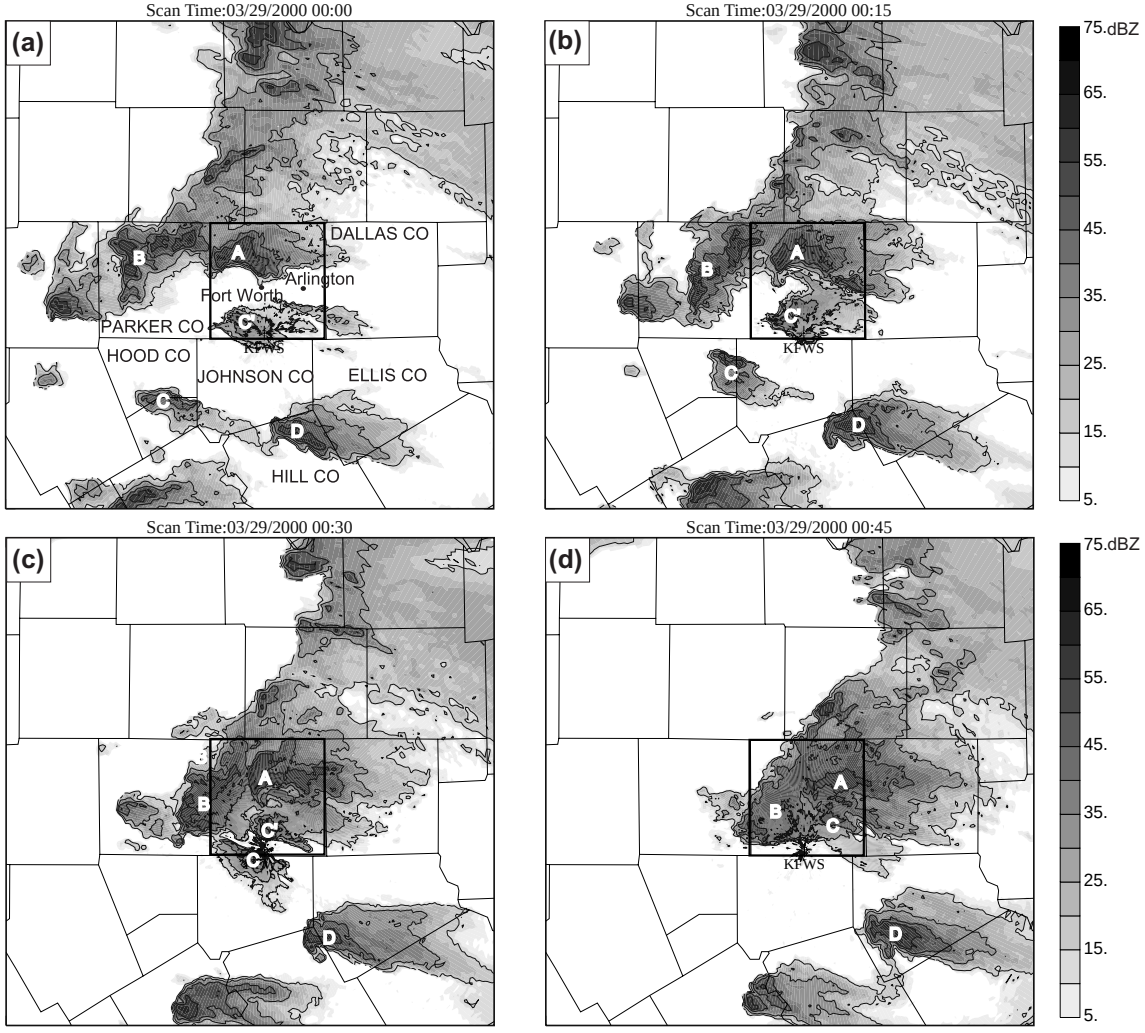

Fig. 3.1. Observed reflectivity fields at the 1.45° elevation of the Fort Worth radar (marked as KFWS) based on Level-II data, at 15-minute intervals from 0000 to 0100 UTC 29 March 2000. Major storm cells are marked by capital letters. Fort Worth and Arlington are marked as dots in (a). Tarrant County is highlighted and about 50 km × 50 km in size. The domain shown is about 200 km on each side, representing the portion of the 3-km grid between 100 and 300 km in the east-west direction and from 60 to 260 km in the north-south direction. The reflectivity contours are at 15, 30, 45 and 55 dBZ, and the shaded contour interval is 5 dBZ. Counties around Fort Worth are labeled in (a).

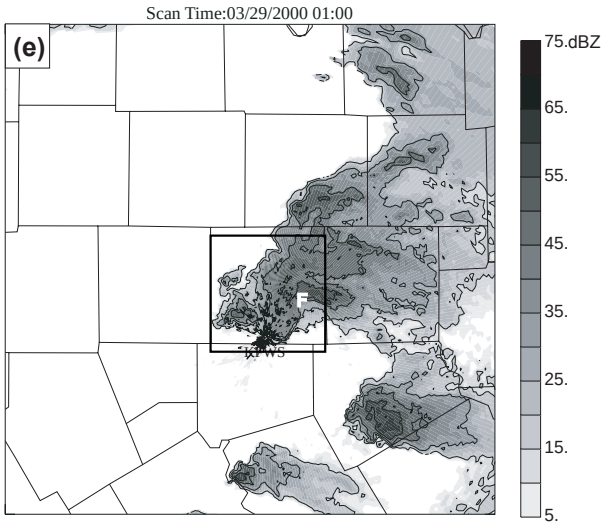

Fig. 3.1 Continued

Five individual thunderstorms can be identified around Forth Worth from the observed radar reflectivity at 0000 UTC 29 March (Fig. 3.1a). They are labeled A, B, C, C' and D in the plots. Storm A is the storm that spawned the downtown Forth Worth tornado at 0015 UTC and the Arlington tornado 45 minutes later. Storm B followed storm A from the west. It approached storm A from 0000 to 0045 UTC (Fig. 3.1a-d) and then merged with storm A to form a combined storm that is indicated as F (Fig. 3.1e). Storms C and C' formed after the end of the assimilation cycles, propagated toward storm A from the south and also merged into storm A (Fig. 3.1) at about 0100 UTC. Storm D was located initially near the northeastern corner of Hill County and later propagated east-northeastward into Ellis County. Storm D formed during the assimilation cycles and remained strong throughout the hour (Fig. 3.1). It is a significant challenge for the data assimilation and model forecasting system to accurately forecast these individual storms and their complex interactions.

3.3.2 Results of experiments CNTLZ and X03

3.3.2.1 Subjective evaluation

For direct comparison with radar observations, we derive reflectivity from model-predicted hydrometeor fields that also take into account the ice phases, and the reflectivity equations follow mostly Smith et al. (1975), with the actual formulations used given in Tong and Xue (2005a). Reflectivity fields at the 1.45° elevation (corresponding to the elevation of the radar observed reflectivity in Fig. 3.1) derived from predicted hydrometeors of CNTLZ and X03 are plotted in Fig. 3.2. The plots show the reflectivity fields from 0000 UTC 29 March, which is 2 hours after the data assimilation cycle is started and 1 hour after the forecast initial time, through 0100 UTC 29 March at 15-minute intervals. The left column of Fig. 3.2 shows results of X03 while the right column shows the counterparts from CNTLZ.

At 0000 UTC 29 March, the one-hour forecast of CNTLZ exhibits reasonable structures of the storms around Fort Worth (Fig. 3.1a, Fig. 3.2b) but with some position errors. Predicted storm A lags the observation by approximately 20 km. Predicted storm B only shows as a weak echo and lags the observation by about 20-25 km. The model produces storm C with a northward displacement of about 5 km and does not produce storm C'. Considering that little information on storms C and C' was provided by the assimilation cycles directly, it is encouraging that the model produces storm C by itself at this time. The model produces an accurate forecast of storm D, but at the same time, it generates a spurious storm, D', which split from storm D in the first hour of the forecast and moves north into the southeast corner of Tarrant County. Another spurious storm appears southwest of storm A and is labeled as A'. Comparing these storms to their

counterparts in X03 (Fig. 3.2a), they are stronger except for spurious storm D'. At this time, X03 gives much better position forecast for both storms A and B than CNTLZ. However, the forecast of X03 misses storms C and C', and produces a spurious storm, A', southwest of storm A.

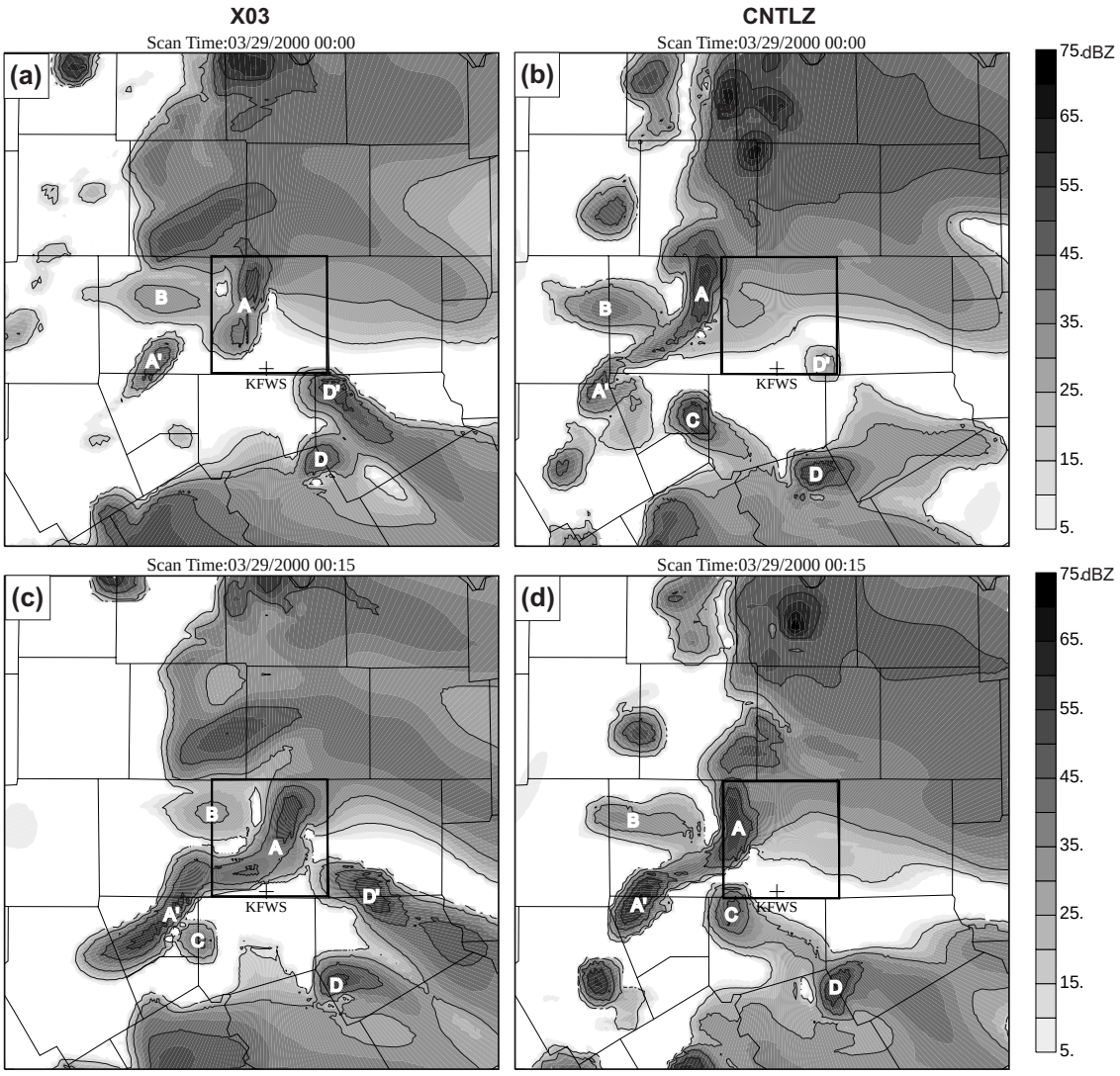

Fig. 3.2. Similar to Fig. 3.1, except that they are predicted reflectivity from experiments (left) X03 and (right) CNTLZ.

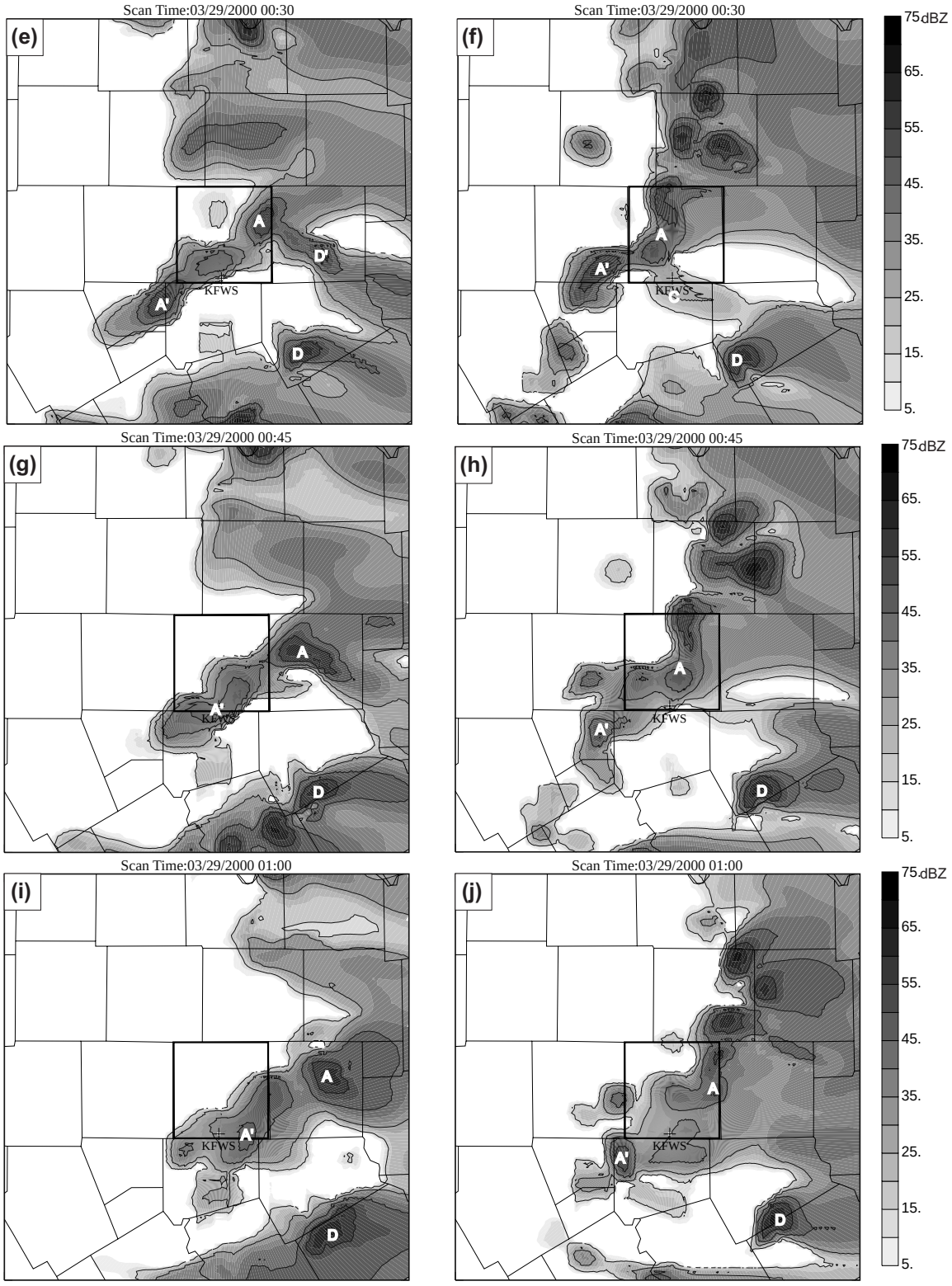

Fig. 3.2. Continued.

Fifteen minutes later, at 0015 UTC, the time of the first tornado touchdown, in downtown Fort Worth, experiment CNTLZ correctly predicts tornadic storm A strengthening and approaching Forth Worth from the west, although the forecast reflectivity maximum of storm A still lags the observations (Fig. 3.1b and Fig. 3.2d). Predicted storm B remains weak and lags the observation by about 25 km. Predicted storm C is located midway between observed storms C and C'. Storm D is well reproduced by CNTLZ and the spurious storm D' that appeared earlier has dissipated by this time. The spurious storm A' has grown and remains southwest of storm A. In comparison, the storms in X03 moved eastward too quickly in the period from 0000 to 0015 UTC and the reflectivity maximum of storm A had already passed downtown Fort Worth (Fig. 3.2c) by 0015 UTC. A weak echo at the center of the western border of Johnson County gives the only hint of observed storm C in X03 forecast. Just to the west of predicted storm C, spurious storm A' has developed into a long band-shaped echo connected with storm A and subsequently sweeps through the weak storm C. Unlike CNTLZ, spurious storm D' in X03 remains as a strong northbound storm.

At 0030 UTC, in the CNTLZ forecast, storm A is nearly colocated with the observed cell except that it extends too broadly in the north-south direction and has two maximum reflectivity centers (Fig. 3.1c and Fig. 3.2f). Its shape does suggest an inflow notch on its southeastern flank. At this time, storm B is not identifiable as a separate storm, though the southwestern quadrant of storm A and the northeastern corner of storm A' overlay the position of storm B. Predicted storm C appears as a weak echo that covers the location of observed storm C and C'. There is reason to believe the CNTLZ forecast is a bit fast with the merger of cells that occurs in Tarrant County. Storm D is well

reproduced except that it moves a little faster than the observation, and spurious storm A' still exists with a strong reflectivity center. In the X03 forecast, intense reflectivity composed by storms A and A' is found extending from storm A in the northeastern corner of Tarrant County through the southwestern corner of the county and reaching the center of Hood County (Fig. 3.2e). This may be due to incorrect positioning of storm A with a 30 km displacement, possibly to be ascribed to a merger with the spurious storm D'.

At 0045 UTC, the main characteristics of storm A are successfully reproduced in the CNTLZ forecast (Fig. 3.1d, Fig. 3.2h). The predicted southern reflectivity maximum of storm A has intensified and is just south of Arlington. Together with the northern reflectivity maximum of storm A and the westward-extending part of storm A, the area of predicted storm A covers the bulk of the combined area of observed storms A, B, and C. At this time, isolated spurious storm A' is weak. Predicted storm D is still few kilometers southeast of the observed cell. In the X03 forecast, the storm D' has merged with storm A and has made the latter move into the center of Dallas County (Fig. 3.2g). The northeast part of storm A' is in the same area as the south center of storm A in CNTLZ and is also near south Arlington.

By 0100 UTC, observed storms A, B, and C had merged into one storm, F, and produced the Arlington tornado (Fig. 3.1e). In CNTLZ run (Fig. 3.2j), the location of storm A corresponds to the correct location of observed storm F, while in the X03 forecast (Fig. 3.2i), storm A leads the observed storm F by approximately 35 km and storm A' covers part of storm F, but its center deviates from the main part of observed F by 15 km. At this time the position forecast for storm D in CNTLZ is also more accurate than that of X03.

The surface wind and temperature fields from CNTLZ and X03 are plotted in Fig. 3.3. At the time of the downtown Fort Worth tornado, approximately 0015 UTC, CNTLZ predicts areas of strong convergence along the gust front produced by tornadic storm A approaching downtown Fort Worth from the northwest (Fig. 3.3b), while in experiment X03, the convergence coincident with the gust front of storm A is much weaker and has passed downtown Fort Worth (Fig. 3.3a). At 0045 UTC, the gust front and low-level convergence related to storm A are still strong and approach south Arlington in the CNTLZ run (Fig. 3.3d). In X03 (Fig. 3.3c), the gust front of storm A is weaker and storm A has moved east of Tarrant County. Almost the entire county is covered by the cold pool of storm A' at this time.

From the above comparison, it is found that using the new cloud analysis procedure with the Level-II reflectivity data through the 10-minute assimilation cycles improves the prediction of the tornadic thunderstorms, over the results of Xue03 (or equivalently experiment X03 here). In the CNTLZ run, the tornadic thunderstorm A, appearing with high reflectivity and strong low-level convergence centers, approaches and passes downtown Fort Worth and Arlington around the times of tornado occurrence, while in X03, the reflectivity center of storm A and the related gust front move too fast and have obvious location errors during the tornado outbreaks.

3.3.2.2 Evaluation with ETS

Quantitative evaluation of numerical forecast of discrete features such as convective cells is difficult and remains an active area of research. Traditional skill scores, such as the equitable threat score (ETS), which are originally designed for large scale precipitation prediction, have limited utility when applied to small-scale convective

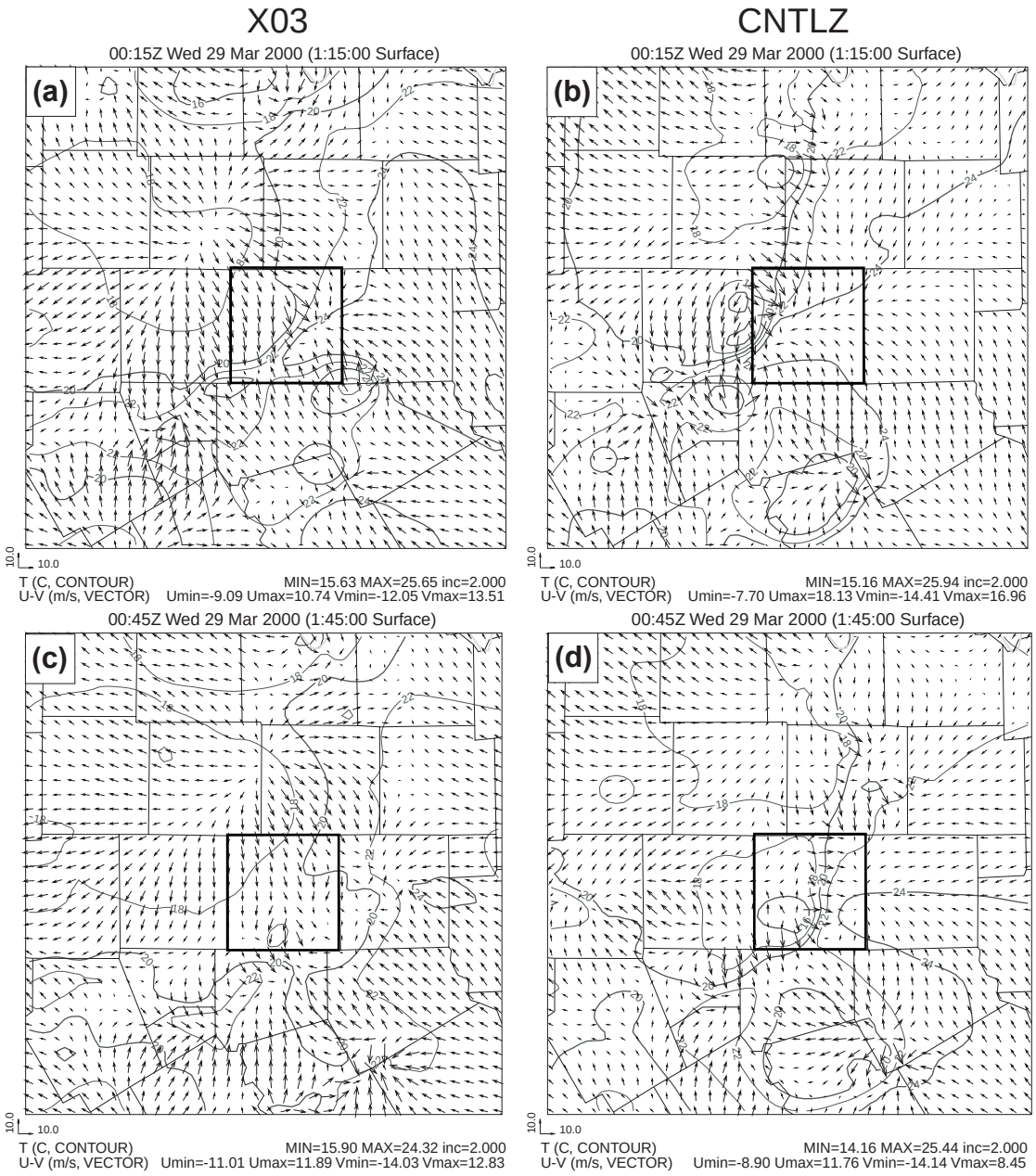

Fig. 3.3. Predicted surface wind and temperature fields from experiments X03 and CNTLZ at 0015 and 0045 UTC 29 March 2000. The domains shown are the same as in Fig. 3.1.

system (Baldwin et al. 2002). Because of the predictability limit of individual convective cells and the discrete nature of such systems, the displacement in space of predicted cells is often as large as cells themselves and can make skill scores very low, even when the strength and morphology are well captured by the forecast. Still, to more quantitatively evaluate the quality of forecast, the ETS (Schaefer 1990) of predicted reflectivity fields are calculated against observations.

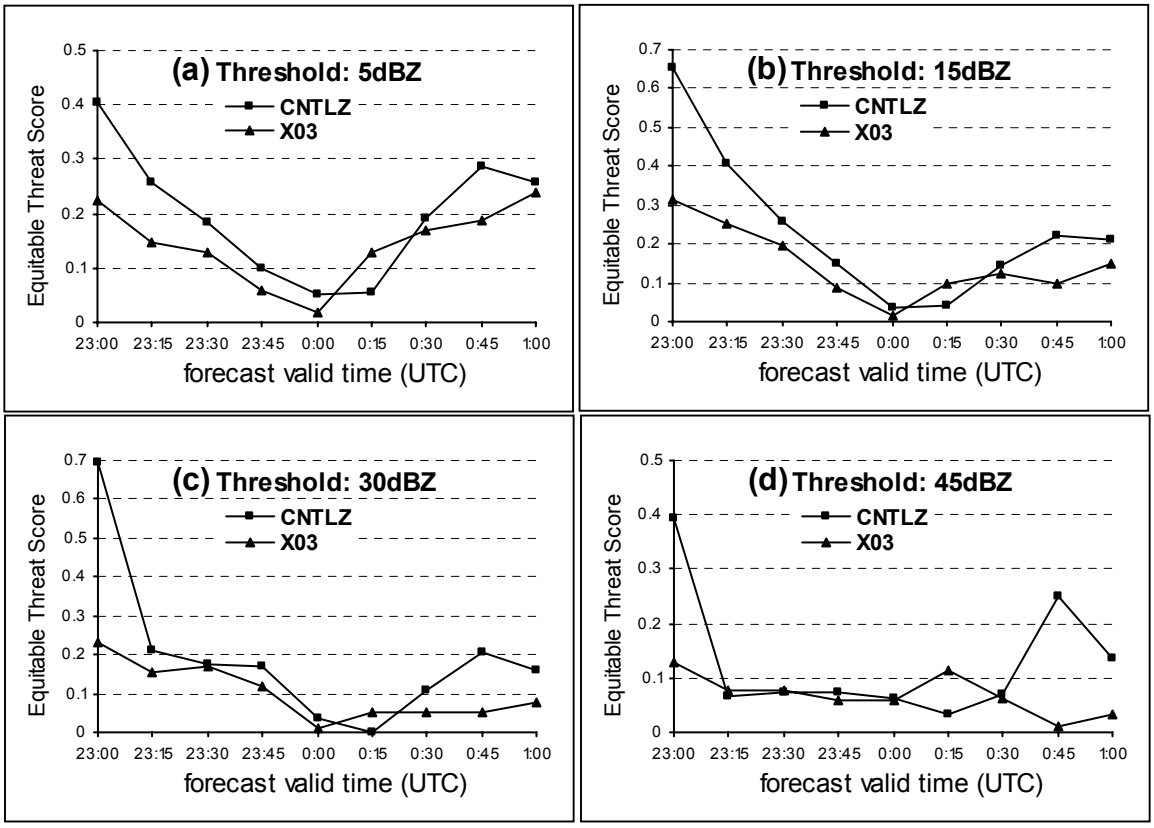

Fig. 3.4. Equitable threat scores of predicted reflectivity for the (a) 5-, (b) 15-, (c) 30-, and (d) 45-dBZ threshold values from experiments CNTLZ and X03.

Figure 3.4 shows the ETS of predicted reflectivity fields at the 1.45º elevation for the 5-, 15-, 30- and 45-dBZ thresholds. We can see that the scores decrease quickly in the first hour of forecast then increase in the second hour for all thresholds. This behavior reflects the adjustments of the initial storms in the first hour of forecast. It can be seen that all scores are better for CNTLZ than for X03 from 0030 to 0100 UTC, in agreement with the previous subjective assessment of the forecast cells. Our subjective analysis does suggest that the forecast of CNTLZ is superior at 0015 UTC for storm A; however, the scores for the entire domain do not reflect this. The reason is that both CNTLZ and X03 have some position errors in the predictions of storms A, B, and C, and both contain some spurious storms at this time. The disagreement between the ETS at 0015 UTC and our subjective analysis suggests that the ETS for the entire domain should be used carefully when the position errors have a significant impact on the scores.

3.3.3 Experiments without radar data

In this subsection, we present results from experiment NoVRZ, which does not use any radar data. The predicted reflectivity field from experiment NoVRZ mapped to the same elevation as the previous figures is plotted in Fig. 3.5 at 0030 UTC 29 March, which is in-between the times of the two tornadoes.

Compared to the observed reflectivity (Fig. 3.1c), experiment NoVRZ completely fails to predict storm cells around Fort Worth (Fig. 3.5), indicating a failure to build and support storm cells in a short-term forecast. There are two storm cells to the southwest of Tarrant County and they originated from the 9-km forecast that was used as the background for the initial 3-km analysis at 2200 UTC.

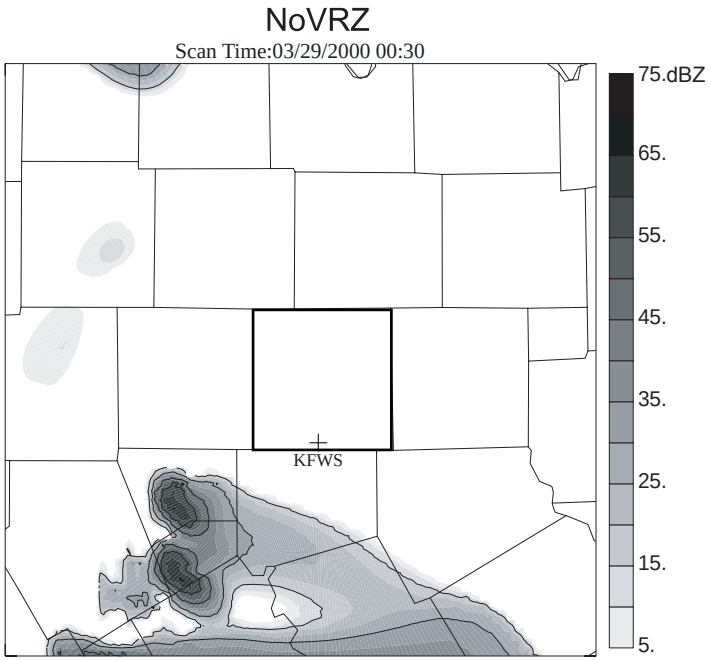

Fig. 3.5 Similar to Fig. 3.1, except that it is predicted reflectivity field from experiment NoVRZ at 0030 UTC 29 March 2000.

Based on the above results, we conclude that the assimilation of reflectivity data from a single-Doppler radar via an efficient intermittent assimilation procedure is effective in building up preexisting storms in a nonhydrostatic model given a 3-km horizontal resolution. The forecast starting from the assimilated initial condition is able to capture most of the supercell characteristics of the observed storms for a two-hour period.

3.3.4 Sensitivity to details of cloud analysis

To identify the impact of each modification in the cloud scheme on the results of assimilation and forecast, three experiments are performed (see Table 3.1): 1) CTLH, in which in-cloud temperature adjustment is based on latent heat conversion instead of moist adiabatic temperature profile; 2) CKRY, which uses the KRY scheme instead of

the SMO scheme to determine the initial values of hydrometeors from reflectivity; and 3) CMAX, in which the quantities of the precipitation species are determined by the maximum of background and observation-based retrievals. All other options in these experiments are the same as CNTLZ.

3.3.4.1 Assimilation results

The reflectivity fields at the end of 1 hour assimilation period, mapped to the 1.45° elevation of the KFWS radar, are plotted in Fig. 3.6 for the five experiments together with the corresponding observed field (Fig. 3.6a). With CNTLZ (Fig. 3.6b), the storm structures look similar to the observations, though the interpolation scheme and cloud processing make the features smoother than those observed (Fig. 3.6a). Given that CNTLZ uses the observation-based retrievals directly in the analysis, it is expected that the reflectivity after the assimilation matches the observed reflectivity. In contrast, the initial reflectivity in X03 does not capture many details of storm cells (Fig. 3.6c). In CTLH, the analyzed reflectivity is similar to that of CNTLZ in the area near the radar (Fig. 3.6d), but has higher reflectivity maxima than their counterparts in CNTLZ in the areas away from the radar because the two experiments have different midlevel temperature fields (c.f., section 4.3 of Chapter 2). CKRY (Fig. 3.6e) uses simple radar reflectivity equations to retrieve precipitation species, which result in reflectivity fields smoother than those of CNTLZ. In Fig. 3.6f, which shows the analyzed reflectivity of CMAX, the influence of the background values of the precipitation species is evident. In this case the maximum value of background and observation-based retrievals is taken as the analysis; at this time the background reflectivity is generally greater than the observations.

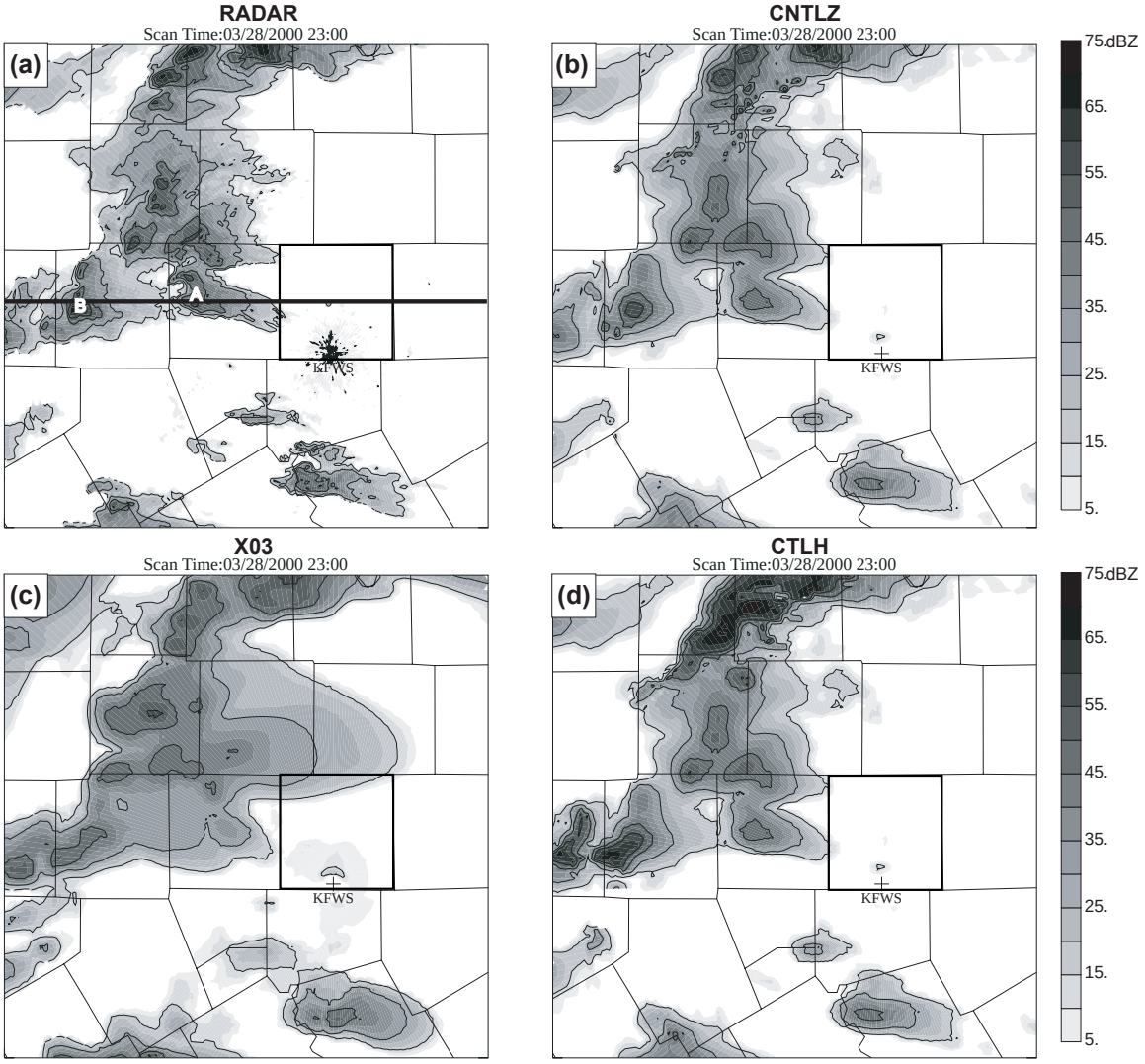

Fig. 3.6. Reflectivity fields at the 1.45° elevation of the KFWS radar from assimilation results of experiments (b) CNTLZ, (c) X03, (d) CTLH, (e) CKRY, and (f) CMAX and (a) the corresponding radar observation. Major storm cells are marked by capital letters in (a). Tarrant County is highlighted and about 50 km × 50 km in size. The domain shown is about 200 km on each side, representing the portion of the 3-km grid between 70 and 270 km in the east-west direction and from 60 to 260 km in the north-south direction. The reflectivity contours are at 15, 30, 45 and 55 dBZ, and the shaded contour interval is 5 dBZ.

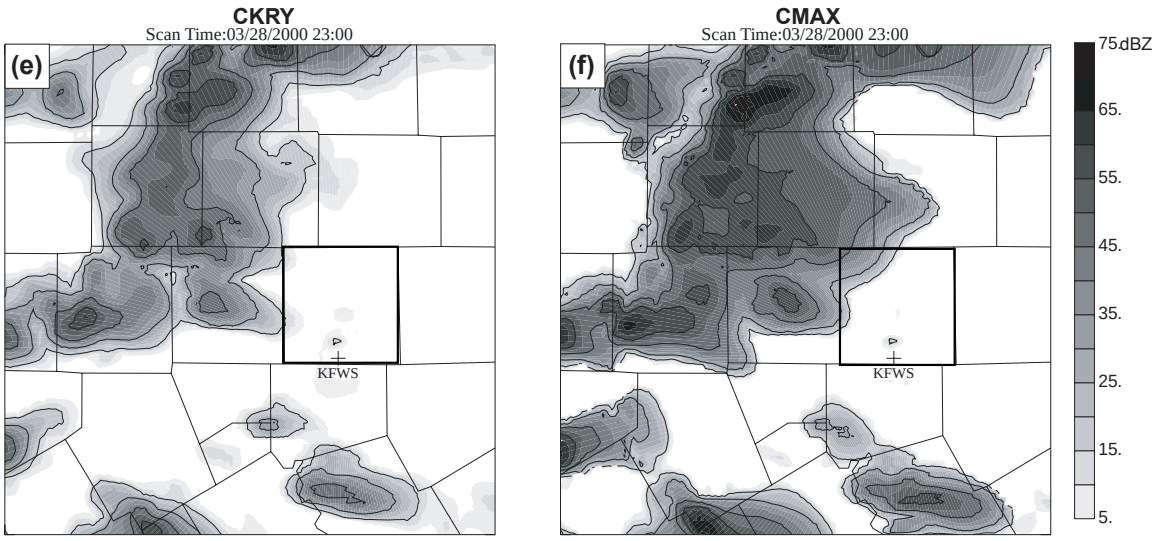

Fig. 3.6 Continued

The surface wind and temperature fields from these five experiments and from the background before the analysis are plotted in Fig. 3.7. In this figure the storm-related gust fronts and cold pools are found in all cases. As also noted with the reflectivity fields, CNTLZ (Fig. 3.7b) presents more storm details than X03 (Fig. 3.7c). In the surface wind and temperature analyses of CTLH, CKRY, and CMAX (Fig. 3.7d, e, f), only CTLH shows large differences from CNTLZ; its appearance is more similar to X03. Both CTLH and X03 underestimate the strength of the cold pool and gust front related to storm A (Fig. 3.7c, d). This indicates that the formation of cold pool and gust front is sensitive to the choice of temperature adjustment scheme, presumably through the direct effect of the latter on storm intensity.

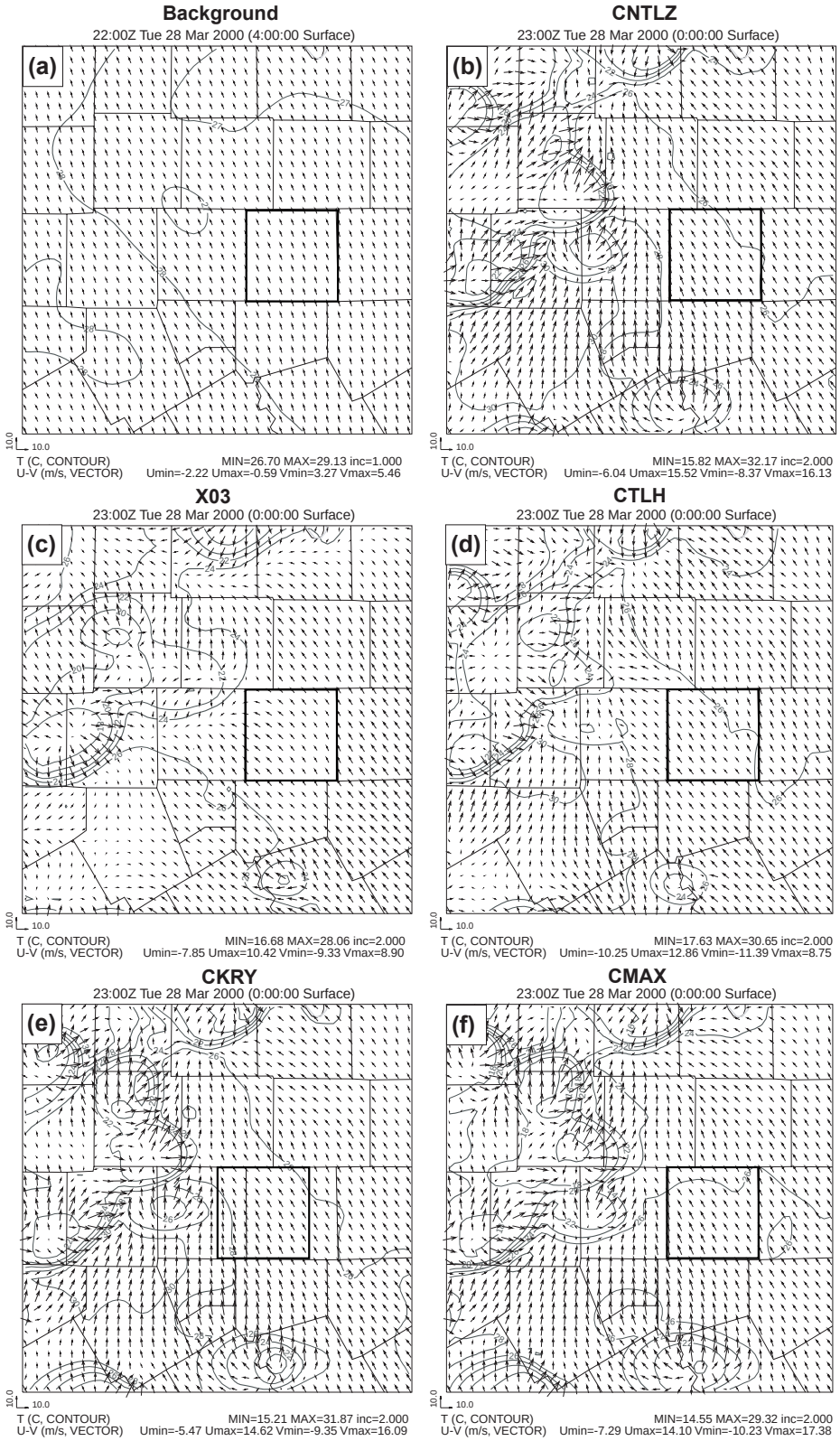

Fig. 3.7. Surface wind and temperature fields from assimilation results of experiments (b) CNTLZ, (c) X03, (d) CTLH, (e) CKRY, and (f) CMAX, and (a) background. The domains shown are the same as in Fig. 3.6.

The strength of the updraft is an important indicator of the vigor of a thunderstorm. Fig. 3.8 shows the cross section of vertical velocity, *w*, along a line through storms A and B (c.f., Fig. 3.6a). In X03, the updraft related to storm B is weak and there is no sign of the existence of storm A (Fig. 3.8a), while in CNTLZ (Fig. 3.8b), two large updraft centers associated with storms A and B are found. It shows that storms have been built up well through assimilating Level-II reflectivity data by the new cloud analysis procedure. The vertical velocity fields from CMAX, CKRY, and CTLH reflect different impacts of each modification (Fig. 3.8c, d, and e). Each of them has one strong updraft center and one weak updraft center. Comparing Fig. 3.8 to the corresponding surface wind and temperature fields in Fig. 3.7, it is found that the vertical motion of storm A is strongly correlated to the strength of the surface cold pool and gust front.

3.3.4.2 Forecast results

In the above subsection, we have seen that assimilation results are obviously affected by the modifications to the cloud analysis procedure. In this subsection, forecasts starting from the results of assimilation are compared in order to make further inferences on the effects of these modifications. Fig. 3.9 shows the predicted reflectivity mapped to the 1.45° elevation of the KFWS radar from CMAX, CKRY, and CTLH near the time of the tornadoes. The surface wind and temperature fields from the same experiments and times are plotted in Fig. 3.10.

The main characteristics of the predicted storm cluster in CMAX, CKRY, and CTLH are similar to that of CNTLZ at the time of the downtown Fort Worth tornado (Fig. 3.9a, c, e, and Fig. 3.2d). Focusing on the details of storm A, it is found that storm A in CKRY and CTLH has the same shape and position as in CNTLZ, while the storm

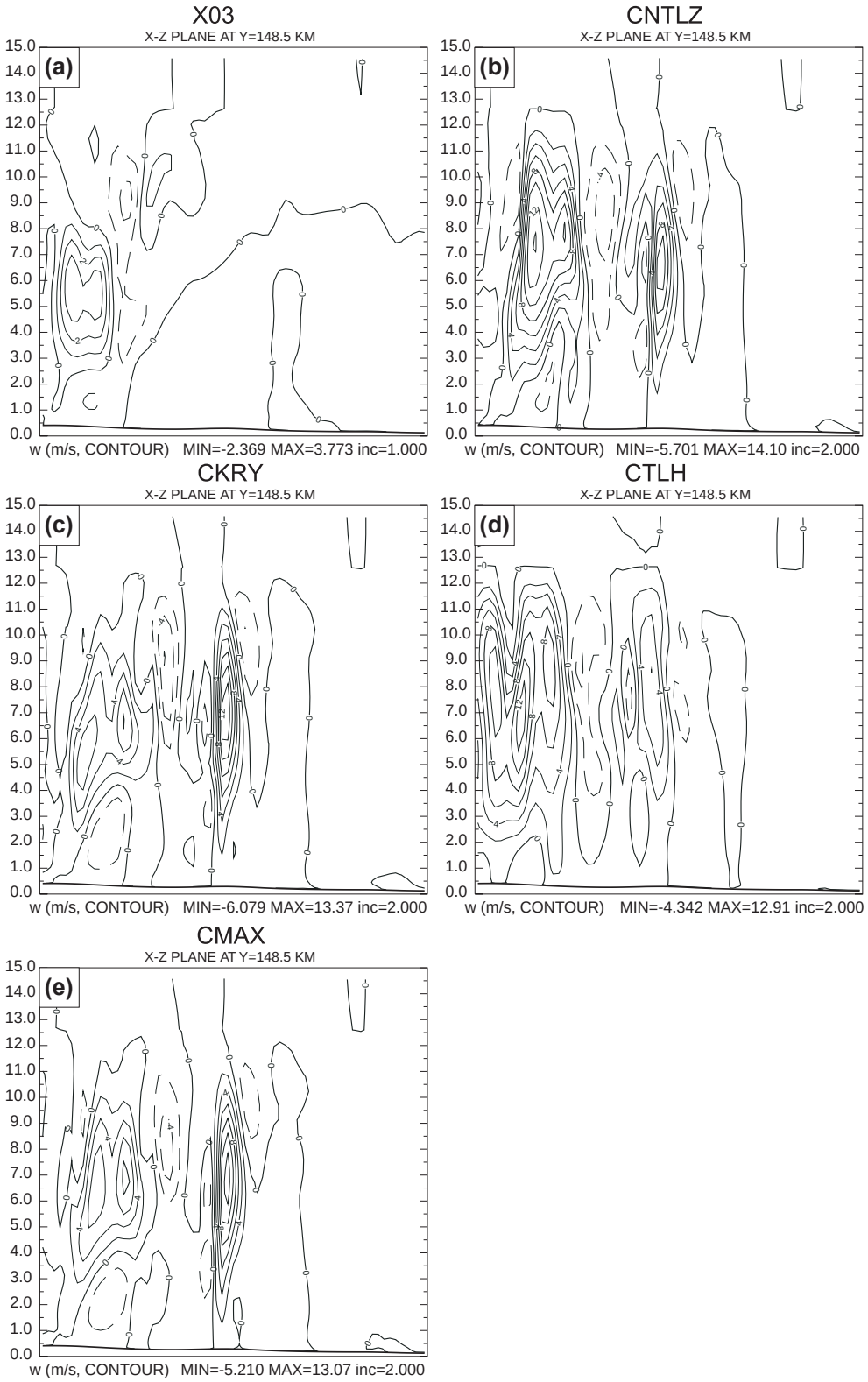

Fig. 3.8. Cross section (along line in Fig. 3.6a) of vertical velocity fields from the assimilation results of experiments (a) X03, (b) CNTLZ, (c) CKRY, (d) CTLH, and (e) CMAX.

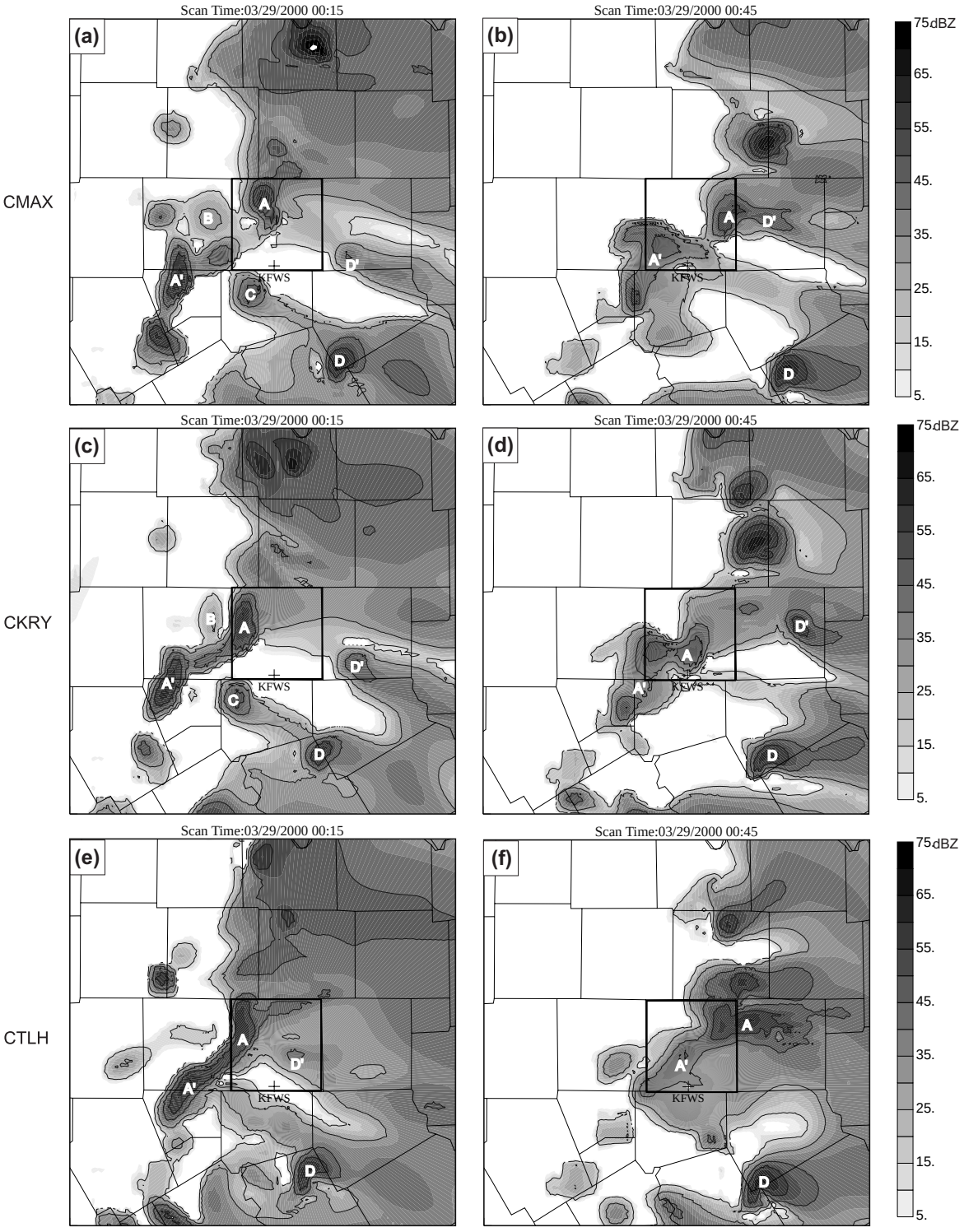

Fig. 3.9. Similar to Fig. 3.1, except that they are predicted reflectivity from experiments CMAX, CKRY, and CTLH at 0015 and 0045 UTC 29 March 2000.

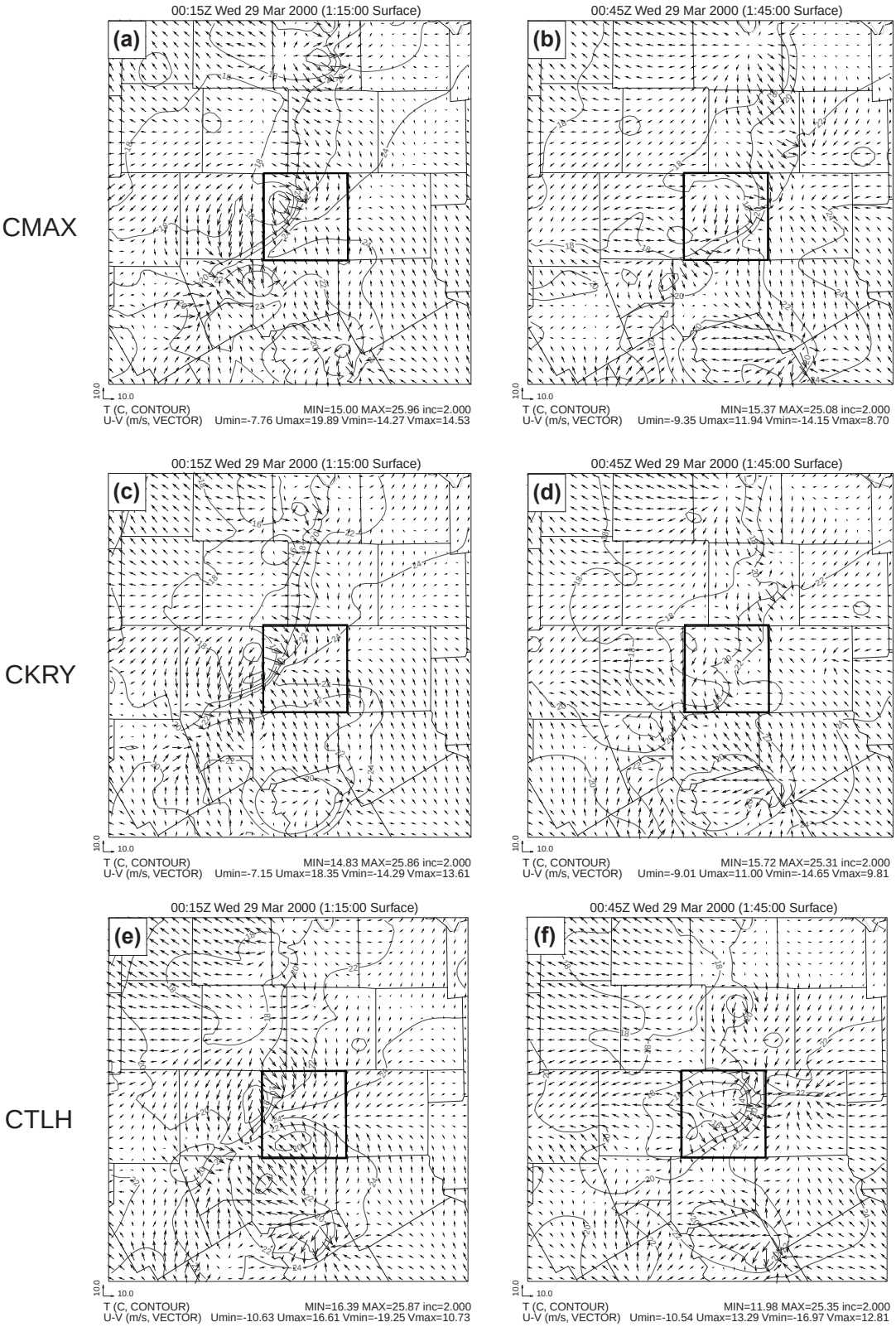

Fig. 3.10. Similar to Fig. 3.3, except that they are from experiments CMAX, CKRY, and CTLH at 0015 and 0045 UTC 29 March 2000.

moves faster in CMAX than in CNTLZ. A similar behavior is shown in the gust fronts related to storm A: the gust fronts of storm A in CKRY, CTLH, and CNTLZ are in similar positions (Fig. 3.3b, Fig. 3.10c, e), while that in CMAX moves faster (Fig. 3.10a). All three experiments have spurious storms A' and D' appearing in the forecast at this time (Fig. 3.9a, c, e).

By 0045 UTC, the differences among CMAX, CKRY, CTLH, and CNTLZ have increased (Fig. 3.9b, d, f, and Fig. 3.2h). Storm A in CMAX has obviously led its counterpart in CNTLZ and connected with spurious storm D'. It then propagates into the center of Dallas County in the next 15 minutes of the forecast, as storm A does in X03 (Fig. 3.2i). The northern part of the gust front associated with storm A in CMAX has reached the eastern boundary of Tarrant County and the southern part is approaching the southeastern corner of the county (Fig. 3.10b). Although storm A in CKRY and CTLH has the same position at 0015 UTC, it propagates in different directions in these two experiments during the following half hour. In CKRY, storm A moves southeast to the center of Tarrant County and lags storm A in CNTLZ. In CTLH, storm A propagates northeast and exits Tarrant County from its northeastern corner. In the surface wind and temperature fields of CKRY and CTLH (Fig. 3.10d, f), the cold pool and gust front of storm A follow the same motion direction and reach the same position as the reflectivity.

Another big difference among these experiments at 0045 UTC is the behavior of spurious storm D'. It remains as a strong isolated echo center in CKRY (Fig. 3.9d), connects with storm A in CMAX (Fig. 3.9b), and merges into storm A in CTLH (Fig. 3.9f), which partly accounts for the fast motion of storm A in that experiment. The spurious storm D' does not exist after 0015 UTC in the forecast of CNTLZ (Fig. 3.2),

while it merges with storm A at 0030 UTC in the forecast of experiment X03 and causes large location errors of storm A at 0045 UTC.

The above comparisons show that adjusting in-cloud temperature based on a moist-adiabatic profile and choosing the values of observation-based retrievals over those of background in the updated cloud analysis procedure act to slow down the motion of predicted tornadic storm A during the period of the tornado occurrence. These two modifications, together with the use of the SMO scheme for the initial determination of precipitation species, contribute to the elimination of spurious storm D' and avoid the erroneous acceleration of storm A found in the X03 forecast. For the current experiments, experiment CNTLZ gives the best forecast for the tornadic thunderstorms during the critical tornado outbreak period.

3.4 Impact of radial velocity analysis via 3DVAR

In this section, we first discuss the forecast of experiment CNTLVR by comparing the forecast radar reflectivity fields to the observed ones. The forecasts of CNTLZ and VR are then analyzed to examine the additional impact of radial velocity data. The results of assimilation from these three experiments are also intercompared. Finally, the results from the experiments with different formulations of the mass divergence constraint are discussed.

3.4.1 Forecasting results of experiment CNTLVR

Since both tornadoes occurred between 0000 and 0100 UTC 29 March in the Fort Worth area, we focus our discussion of the forecast on this period. The predicted reflectivity fields from the CNTLVR, which includes both reflectivity and radial velocity

data, are mapped to the 1.45° radar elevation of the KFWS radar (labeled in the plots) and plotted in the right column of Fig. 3.11 at 15-minute intervals for a 1 hour period starting from 0000 UTC 29 March. The corresponding observed reflectivity fields, which are also shown in Fig. 3.1, are replotted in the left column for the convenience of comparison. Fort Worth and Arlington are labeled in Fig. 3.11b.

The one-hour model forecast at 0000 UTC 29 March also depicts five storm cells in the vicinity of Fort Worth (Fig. 3.11b). Four of them can be directly linked to an observed one (Fig. 3.11a), but the one labeled C" has no real world counterpart. Storms A and B have location errors of about 20-25 km while storms C and D have position errors of less than 5 km. Observed storm C' is missed by the forecast at its location near the southwestern corner of Tarrant County while the model placed a storm cell, C", further to the south, in west-central Johnson County. When we examine the forecast during the first hour (2300-0000 UTC; not shown here), it is found that all storm cells that existed at the beginning of forecast underwent varying degrees of adjustment. Storms A and B weaken initially and grow again from 2345 UTC, while storm C remained relatively weak until about 2350 UTC. Given that little information on storm C was provided by the radar or the assimilation process, the model did a good job in initiating storm C. Apart from some error in propagation speed (a little too fast), storm D was well predicted throughout the period by the model. Both the observed and predicted low-level reflectivity of storm D showed clear hook echo shapes.

Fig. 3.12 shows the predicted wind vector and vertical vorticity fields from the control experiment at the surface (left column) and 3 km MSL (approximately 2.8 km AGL, right column) at the same times as the reflectivity fields shown in Fig. 3.11. From

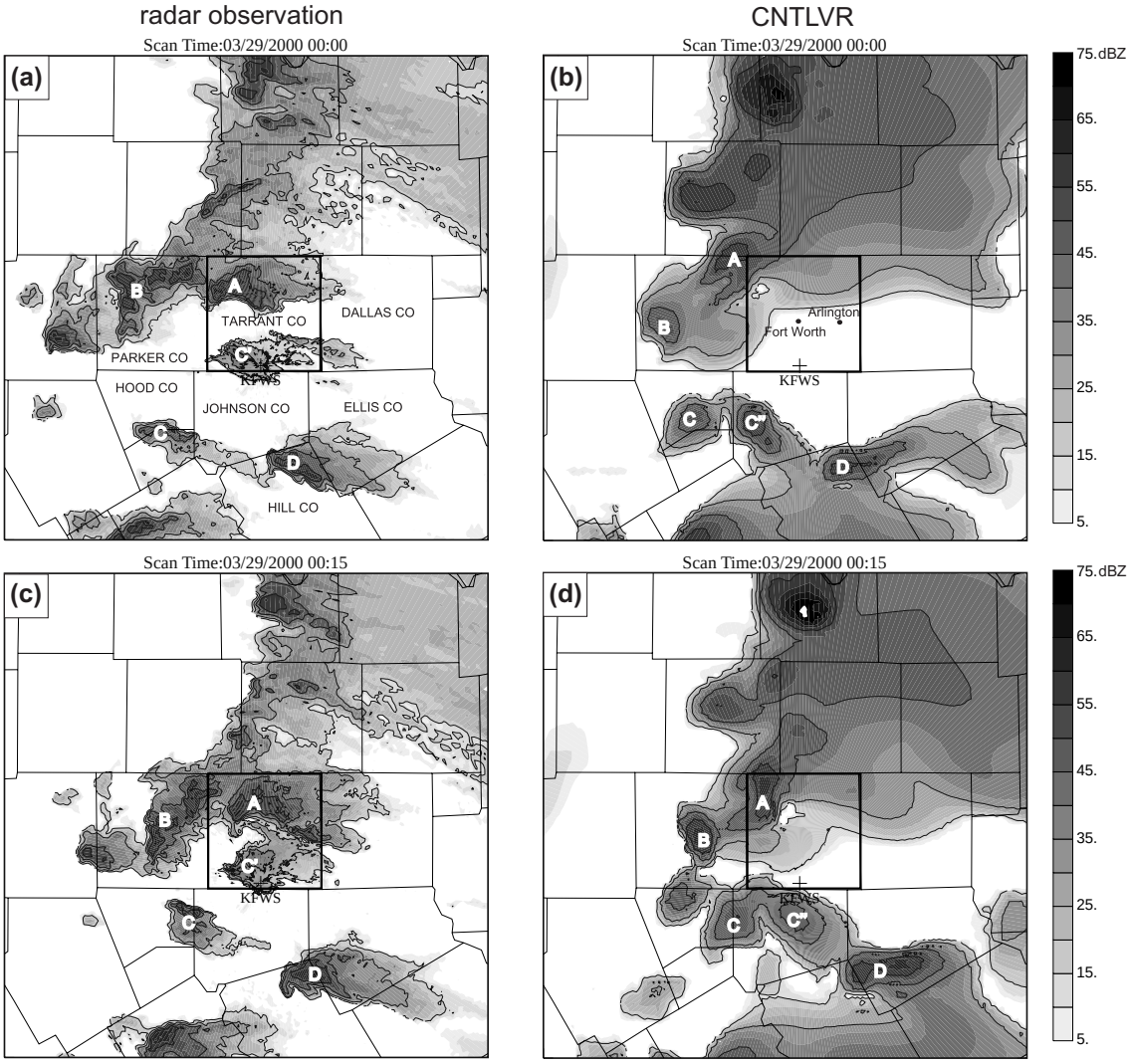

Fig. 3.11. (left) Observed reflectivity fields at the 1.45° elevation of the Fort Worth radar (marked as KFWS) based on Level-II data, and (right) predicted reflectivity at the same elevation from the control experiment CNTLVR, at 15-minute intervals from 0000 to 0100 UTC 29 March 2000. Major storm cells are marked by capital letters. Fort Worth and Arlington are marked as dot in (b). Tarrant County is highlighted and about 50 km × 50 km in size. The domain shown is about 200 km on each side, representing the portion of the 3-km grid between 100 and 300 km in the east-west direction and from 60 to 260 km in the north-south direction. The reflectivity contours are at 15, 30, 45, and 55 dBZ and the shaded contour interval is 5 dBZ. Counties around Fort Worth are marked in (a).

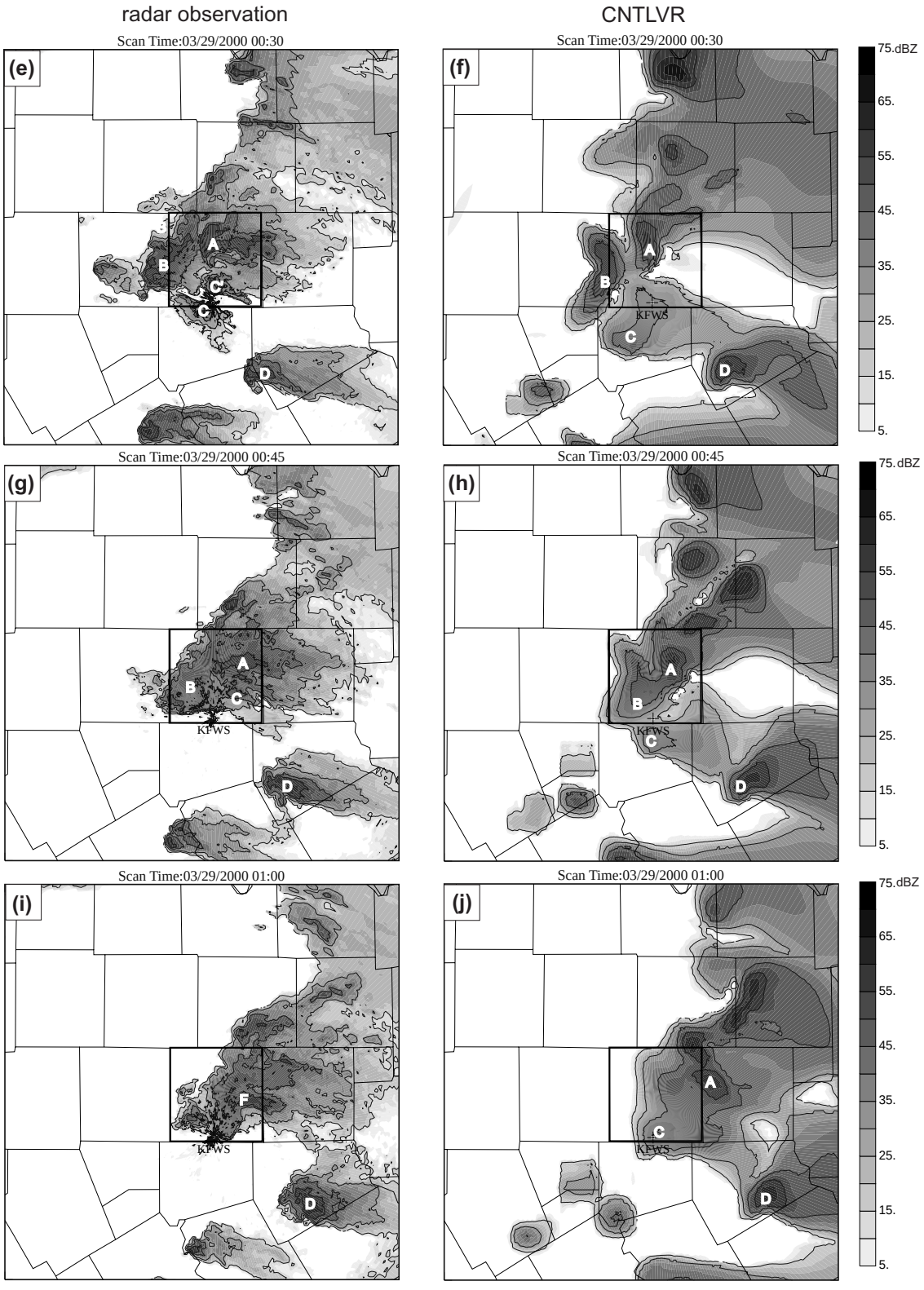

Fig. 3.11. Continued.

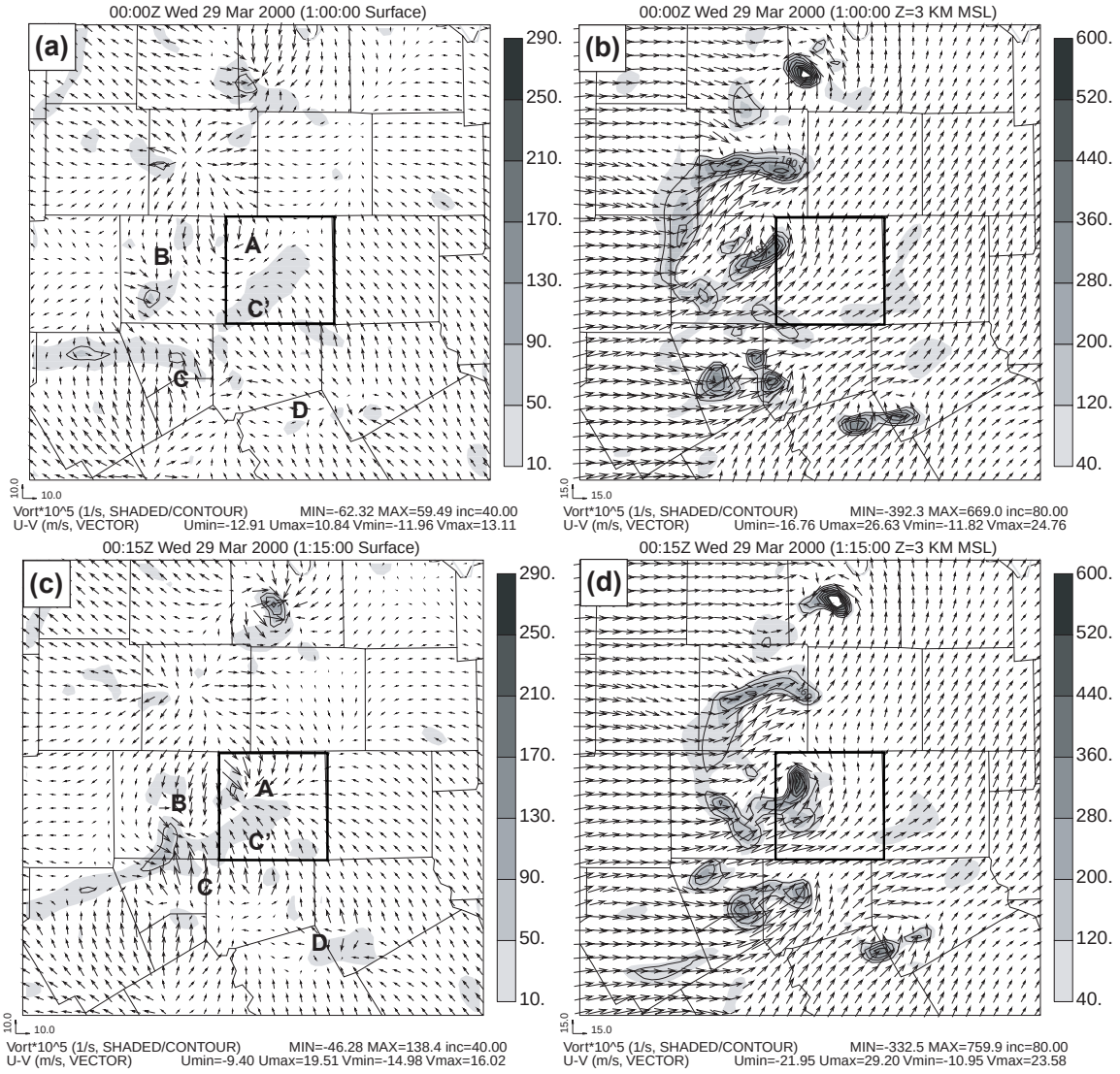

Fig. 3.12. Predicted wind and vertical vorticity fields at (left) the surface and (right) 3 km MSL from control experiment CNTLVR corresponding to the times of Fig. 3.11. The domains shown are the same as in Fig. 3.11. The capital letters in the left column are the positions of the observed storms.

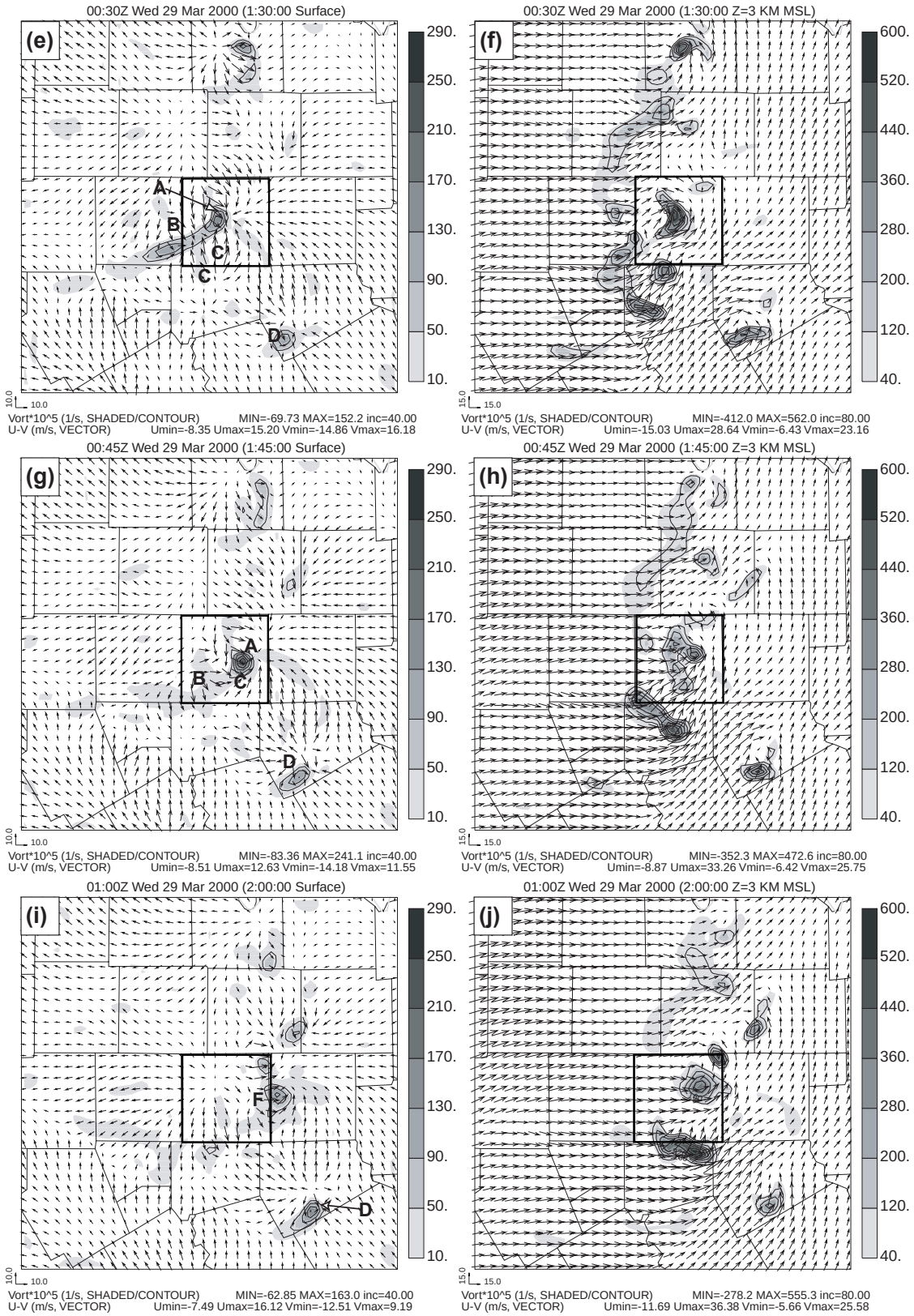

Fig. 3.12. Continued.

the surface wind field at 0000 UTC, strong and fairly isolated convergence centers are indicated for storms A, B, and D (Fig. 3.12a). The gust fronts associated with the downdrafts of storms A and B are still relatively weak at this time while a much stronger downdraft is found to the northwest of A, associated with a storm that is decaying. Vertical vorticity associated with A is still weak at the surface. In the flow field at 3 km MSL, however, a strong vorticity maximum is found within storm A (Fig. 3.12b).

Fifteen minutes later, at 0015 UTC, the time of the formation of the Fort Worth tornado, both predicted storms A and B are enhanced significantly (Fig. 3.11d). The location error of the maximum reflectivity center of storm A is reduced significantly, to within 10 km of the observed one (Fig. 3.11c, d). The predicted locations of B and C are also very accurate at this time. Spurious storm C" remains and appears as a strong reflectivity center. Storm D moves east a little too fast in the 15-minute period, with the reflectivity core entering Ellis County by this time. The wind fields exhibit a strong convergence center and a weak vorticity center at the surface (Fig. 3.12c) but a strong vorticity center at 3 km MSL (Fig. 3.12d) associated with A. The convergence and vorticity centers related to storm B are also enhanced. A new spurious storm south of storm B is generated by collision of gust fronts from storms B and C (Fig. 3.11d and Fig. 3.12c). These results show that the main storm A is predicted with high low-level reflectivity and strong midlevel rotation and approaches Fort Worth city from the northwest. Despite some delay in the intensification of low-level rotation in the forecast, it contains clear indications of the potential of a tornado from this cell.

In reality, an F2 tornado spawned from storm A struck downtown Fort Worth from 0015 to 0030 UTC. At 0030 UTC, the control forecast gives good indications, in

both reflectivity and wind fields, of possible tornadogenesis from storm A. The predicted reflectivity matches very well with observation (Fig. 3.11e, f). The southern flank of the predicted storm is sweeping through Fort Worth city consistent with the observations at this time. The weaker surface vorticity center found in Fig. 3.12c earlier has developed into a strong vorticity center by 0030 UTC, with a maximum value of about 1.5×10^{-3} s^{-1} (note that the grid resolution is 3 km, which is very coarse for the estimation of vorticity associated with tornadoes), and the maximum is located almost right over Fort Worth (Fig. 3.12e). Colocated with the vorticity maximum is also strong surface convergence, indicating the presence of strong near-surface updraft and associated vertical stretching. An isolated maximum vorticity center within storm A is even better defined at 3 km MSL (Fig. 3.12f) but is not as strong as it was at 0015 UTC. The intensification of ground-level vorticity and slight weakening of midlevel rotation suggest shifting of strong rotation to the lower levels, which typically occurs during tornadogenesis and in the later life cycle of tornadoes (see, e.g., Davies-Jones 2001). The development of this strong, well-organized, deep vorticity column during the period that coincides with the Fort Worth tornado indicates good fidelity of the predicted storm, even though the model resolution is much too coarse to produce flow on the scale of a tornado or even the tornado-parent vortex. Simulations starting from the analyzed initial conditions but at much higher resolutions are planned.

At 0030 UTC, storm B is also reproduced well by the forecast as seen from the reflectivity field. The spurious storm cell to its south found at 0015 UTC has merged with storm B by this time. The vorticity center related to storm B is much weaker than that of storm A at both the surface and 3 km MSL. Predicted storm C covers the area of

observed storms C and C', and there is no identifiable surface vorticity center associated with it. Predicted storm D is located northeast of the observed one by about 10 km because of its faster northeastward propagation. At this time, the main characteristics of the storm cells A through D are all very accurately predicted by the model, and the representations are an improvement over that reported in Xue03 as well as that of experiment CNTLZ, which did not include radial velocity data.

At around 0045 UTC, the reflectivity core of storm A has moved to eastern Tarrant County, near Arlington, and a well-organized, deep, and stronger vorticity column is nearly colocated with Arlington (Fig. 3.11g, h and Fig. 3.12g, h), which indicates high potential of tornadogenesis at this area. The surface maximum vorticity is now 2.4×10^{-3} s^{-1}, even higher than earlier. The model successfully predicts storm B's decay and merger with storm A around this time. The predicted storm C lags behind the observed one by nearly 30 km and does not merge with storm A as the real one did. The forecast for storm D matches the observed radar echoes well. At the surface, the northwest side of outflow of storm D is approaching storm A located to its northwest, which probably contributed to the weakening of storm A and its subsequently merged storm.

In reality, storms A, B, and C merged together and formed storm F, which produced the Arlington tornado at 0100 UTC 29 March (Fig. 3.11i). The model has some success at forecasting this process, as the predicted storms A and B do merge and storm C's reflectivity field become combined with A and B's although its core remain separate at 0100 UTC. Further, the predicted reflectivity maximum center has a displacement to the northeast (Fig. 3.11j). Predicted storm D remains strong, as the observed one, and

again is located slightly ahead of the observed storm. At the surface, the maximum vorticity centers associated with storms A and D are still clearly identifiable (Fig. 3.12i), but the one associated with storm A is weaker with the former. At 3 km MSL, the disturbances and vorticity that appear to be associated with the decaying storm C may be too strong (Fig. 3.12j); we do not have good data to verify their fidelity, however.

Based on the results of experiment CNTLVR, it can be concluded that starting from an initial condition that assimilates WRS-88D radar Level-II data together with conventional observations through the 3DVAR and cloud analysis, the model is able to predict the timing, location, and key characteristics of convective storms with good accuracy. The accurate prediction of the development of a strong, well-organized, deep vorticity column associated with the tornadic storm in a period spanning the two observed tornado outbreaks is especially encouraging. Our results also show that when several storms are spaced closely, complex storm interactions can occur, through, for example, gust front collisions. Spurious cells can be triggered when such interactions are incorrectly or inaccurately handled by the model. Such a situation requires an accurate analysis of all aspects of the convective storms.

3.4.2 Forecasting results of experiment using reflectivity only

In this subsection, the forecasting results from experiment CNTLZ, which has been discussed in section 3.3.2, are compared to those of CNTLVR. The two experiments differ only in that CNTLZ does not include radial velocity data.

The predicted reflectivity fields from experiment CNTLZ are plotted in the right column of Fig. 3.2. The predicted wind and vorticity fields are given in Fig. 3.13 for the surface (left column) and 3 km MSL (right column) at 15-minute intervals for a half hour

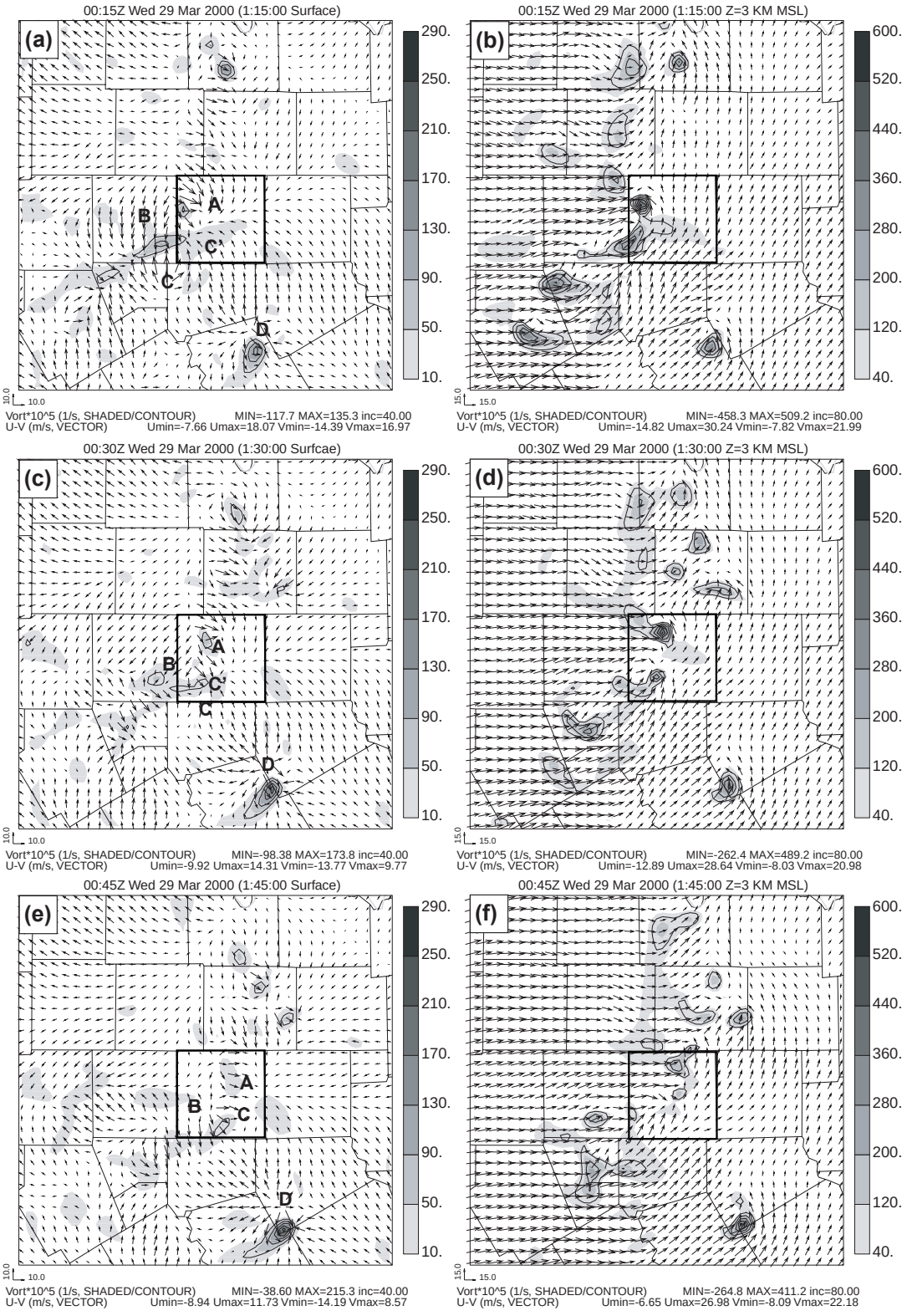

Fig. 3.13. Similar to Fig. 3.12, except that they are predicted wind and vorticity fields from experiment CNTLZ at 15-minute intervals from 0015 through 0045 UTC 29 March 2000.

starting from 0015 UTC 29 March.

During the critical period from 0015 to 0045 UTC, CNTLZ reproduced the main characteristics of storm A quite successfully (c.f. Fig. 3.11c, e, g and Fig. 3.2d, f, h) although the location errors are somewhat larger than that of CNTLVR from 0030 to 0045 UTC (c.f. Fig. 3.11d, f, h and Fig. 3.2d, f, h). Both experiments also give similar forecast for storm D and spurious storm C". Predicted storm B in experiment CNTLZ appears as a large area of weak reflectivity at 0015 UTC and disappears after that time. Instead of merging with storm B, storm A is followed by and merges with a strong spurious storm A', which is triggered by a collision of the gust fronts from storms A, B, and C" at 0015 UTC (Fig. 3.13a). The forecast of CNTLZ also misses observed storm C in this period. Overall, the forecast of CNTLZ is not as good as that of CNTLVR and the differences clearly demonstrate the positive impact of assimilating additional radial velocity data in CNTLVR.

This positive impact can be seen more clearly in the wind and vorticity fields. The well-organized, deep column of strong vorticity that develops near Fort Worth and moves to Arlington from 0015 to 0045 UTC in the forecast of CNTLVR does not exist in the forecast of CNTLZ (Fig. 3.12 and Fig. 3.13). CNTLZ does not develop a strong surface vorticity center within Tarrant County, and the 3 km MSL vorticity maxima found at 0015 and 0030 UTC have larger displacement errors. By 0045 UTC the 3 km MSL vorticity maximum is considerably weaker than the one depicted in the control experiment. The differences in morphology of these features indicate that the forecast of the wind fields has been improved significantly by assimilating radial velocity data via our 3DVAR analysis.

The equitable threat scores of predicted reflectivity at the 1.45º elevation for the 5-, 15-, 30-, and 45-dBZ thresholds are plotted in Fig. 3.14. From the figure, we can see a tendency for the scores to decrease quickly in the first hour of forecast then increase in the second hour for all four thresholds. This U-shape of ETS curves for all cases is due to the imbalance among different variables, especially for wind and temperature, in the initial analysis. During the initial period of forecast, significant adjustments occur in the model among the cloud variables for them to better fit the model dynamics and physics. Also, during the period, the reflectivity is over-predicted and some spurious cells are created. Thus, the ETS decreases during this adjustment period. After the initial adjustment, the main characteristics of observed cells are better captured in the forecast and the ETS score increases. The reason of the lowest score at 0000 UTC is complex. It is related to the limitations of both analysis procedure (the ability of generating balanced initial fields) and model (the ability to establish a suitable balance quickly).

It can be seen that all scores in the 45-dBZ threshold are better for CNTLVR than for CNTLZ from a little after 0000 to 0100 UTC (Fig. 3.14d), in agreement with the earlier subjective assessment of the forecast of cell centers. The improvement of CNTLVR over CNTLZ for other thresholds are not as evident during this hour, although the score is generally better at 0100 UTC, while the score is lower at 0045 UTC for the other three thresholds (The scores for experiment NoDiv will be discussed later). Our subjective analysis does suggest that the forecast of CNTLVR is superior at 0045 UTC, however, and the high threshold (45-dBZ) ETS confirms this. The less than clear cut signal from the ETS suggests that the ETS should be used carefully for evaluating forecasts containing discrete features, for which propagation and mispositioning errors

can have a significant impact on the calculated scores.

3.4.3 Forecasting results of experiment using radial velocity only

In the previous subsection, we found that radial velocity data, when used (via the 3DVAR analysis) together with reflectivity data (via the cloud analysis), can positively impact a storm forecast. In this subsection, we present results from experiment VR in which the cloud analysis with reflectivity data is not performed, while radial velocity is assimilated the same way as in control experiment CNTLVR.

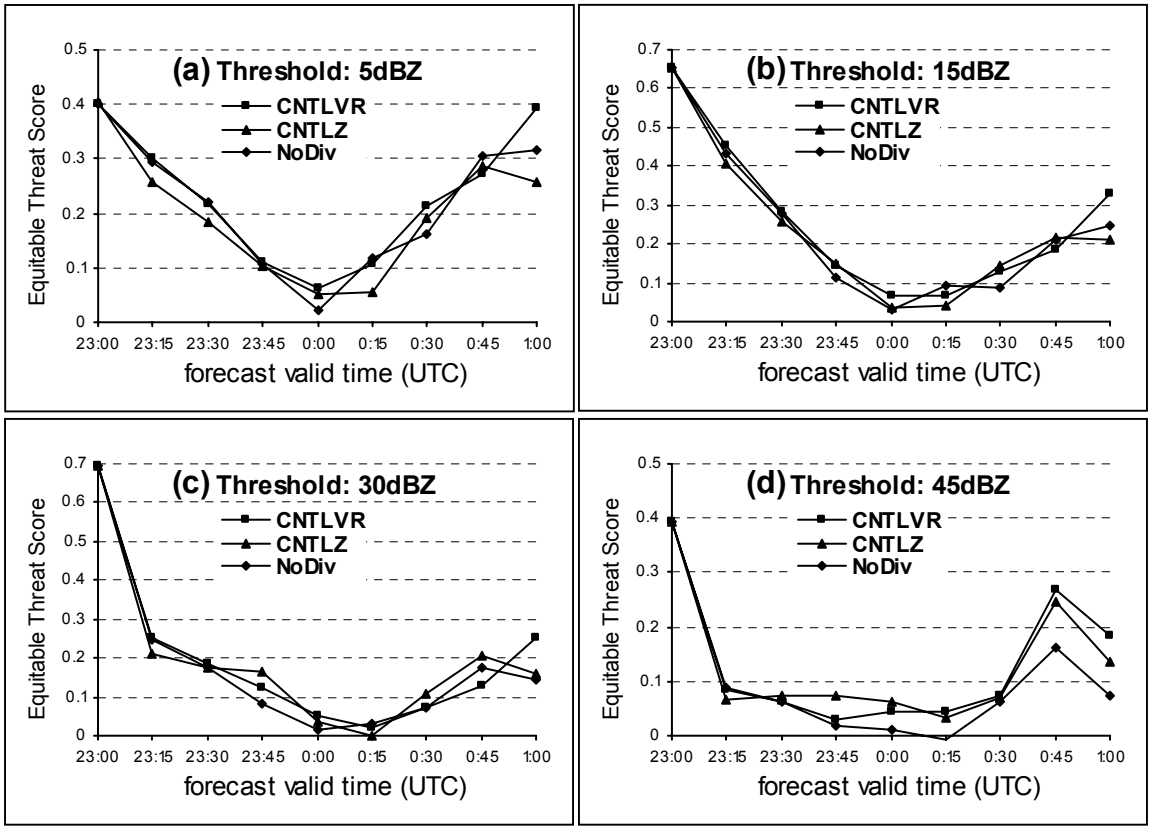

Fig. 3.14. Equitable threat scores of predicted reflectivity for the (a) 5-, (b) 15-, (c) 30-, and (d) 45-dBZ threshold values from experiments CNTLVR, CNTLZ, and NoDiv.

The predicted reflectivity field from experiment VR mapped to the 1.45° elevation is plotted in Fig. 3.15 at 0030 UTC 29 March, which is in-between the times of the two tornadoes. Compared to the observed reflectivity (Fig. 3.11e), it can be seen that experiment VR completely failed to predict storm cells around Fort Worth (Fig. 3.15). There are two storm cells to the southwest of Tarrant County and they originated from the 9-km forecast that was used as the background for the initial 3-km analysis at 2200 UTC. The storms do not match the observed reflectivity, indicating a failure of forecast to build and support storm cells in a short-term forecast. Still, some positive impact of assimilating radial velocity data can be found during and shortly after the assimilation cycles. The fields of VR show weak reflectivity centers to the northwest of Fort Worth at the end of assimilation cycles. They decay, however, soon after the forecast period begins (not shown).

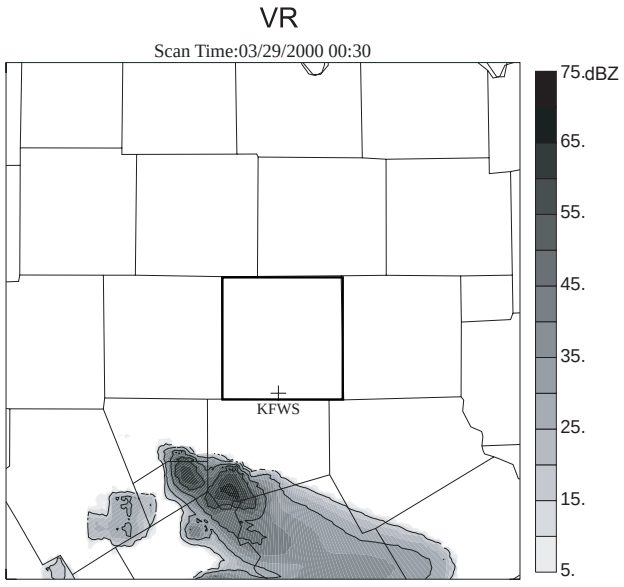

Fig. 3.15. Similar to Fig. 3.11, except that it is predicted reflectivity field from experiment VR at 0030 UTC 29 March 2000.

The above results tell us that assimilating the radial velocity alone via the current 3DVAR procedure is far from enough to create a properly balanced storm in this case. This is not very surprising because of availability of radial velocity data from a single radar, and the lack of strong, reliable link between radial velocity data with other model variables, particularly the buoyancy. More sophisticated equation constraints that better couple model state variables together or flow-dependent background error covariances should help. The former is true with the 4DVAR and the latter with the ensemble Kalman filter method. Tong and Xue (2005a) found with observing system simulation experiments (OSSE) that radial velocity has a greater positive impact than reflectivity when assimilated using the ensemble Kalman filter method for a simulated supercell storm. Radial velocity also plays a key role in the 4DVAR assimilation work as discussed by Sun and Crook (1997).

Based on the above results, we conclude that the assimilation of both radial velocity and reflectivity data from a single Doppler radar via an inexpensive intermittent assimilation procedure that involves the 3DVAR and cloud analyses is effective to build preexisting storms in a nonhydrostatic model at a marginally storm-resolving 3-km resolution. The forecast starting from the assimilated initial condition is able to capture most of the key characteristics of the observed storms for a two-hour period. Although reflectivity data are found to have a greater positive impact on the storm forecast than radial velocity with the current analysis procedure, the use of radial velocity along with reflectivity does improve the quality of forecast. The impact of the radial velocity assimilation is most evident in the strong low-level vorticity centers associated with the expected tornadogenesis.

The possible reason for the smaller impact of radial velocity data is that the initial thermal, moisture, and cloud field disturbances introduced by the reflectivity can sustain during forecast and induce corresponding changes in wind field, but initial wind disturbances from radial velocity disperse quickly in the form of acoustic waves in the absence of proper balances with other fields and among the three wind components themselves.

3.4.4 Comparison of assimilation results

To understand the above forecast results further, the impact of assimilating radar observation on the assimilated initial conditions are examined here. The vertical velocity, *w*, fields at 5 km MSL from the assimilation output of experiments CNTLVR, CNTLZ, and VR are plotted in the left column of Fig. 3.16, while the corresponding cross section of *w* along a line through storms A and B are plotted in the right column of the same figure.

At the end of the assimilation period, the strong, isolated updraft centers related to storms A and B are well established in both experiments CNTLVR and CNTLZ (Fig. 3.16a-d). When only radial velocity data are analyzed (experiment VR), the updrafts are much weaker (Fig. 3.16e and f). Starting form these initial conditions, the forecasts of CNTLVR and CNTLZ are expected to be better. Still, for experiment VR, the updrafts are colocated with the observed cells, indicating that the 3DVAR analysis of radial velocity does add useful storm information into the initial fields.

Comparing CNTLVR and CNTLZ (Fig. 3.16a-d), the updrafts of CNTLZ are much stronger than those of CNTLVR. This indicates that the 3DVAR analysis of radial velocity data acts to constraint the magnitude of updraft. In CNTLVR, the updraft of

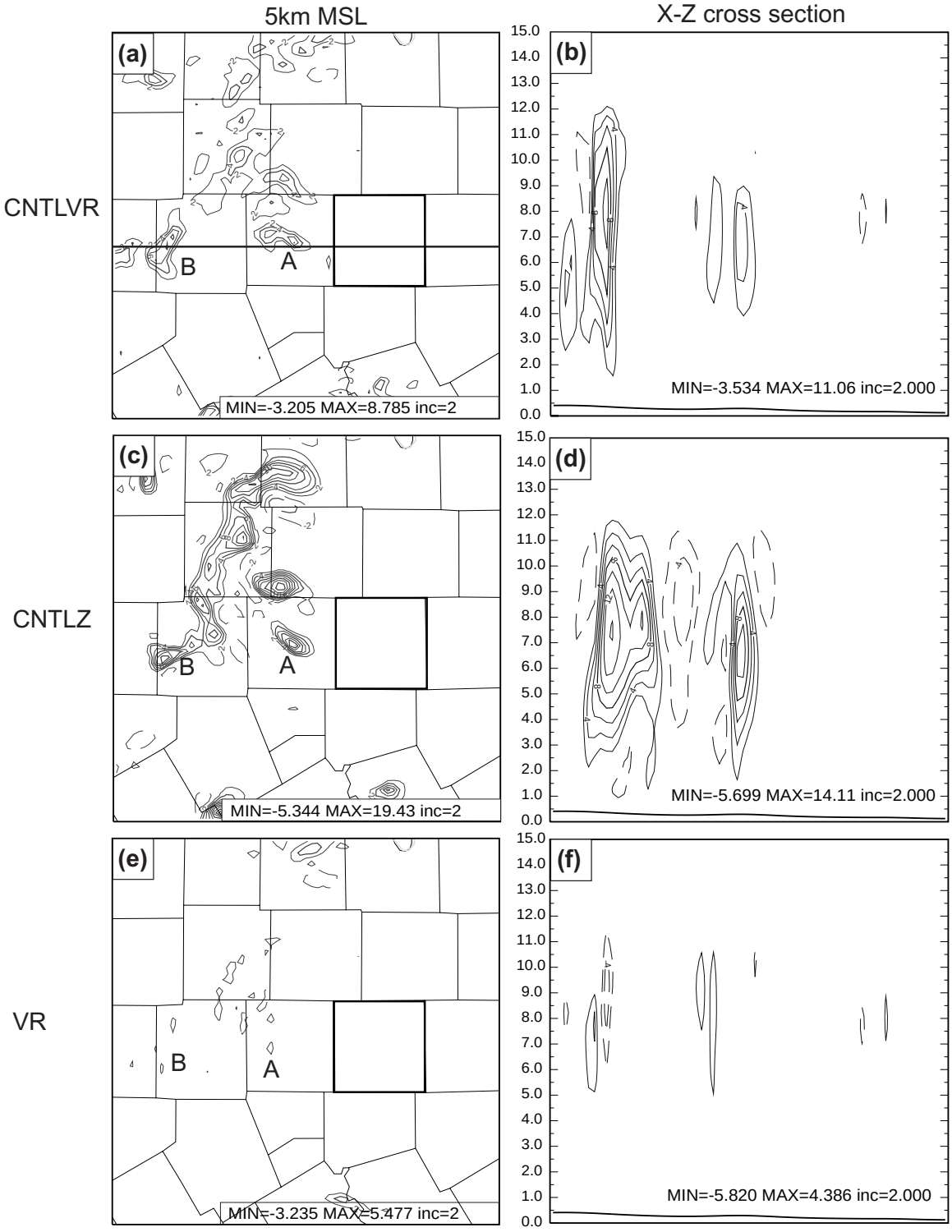

Fig. 3.16 (Left) the vertical velocity fields at 5 km MSL and (right) cross section of vertical velocity along the line in figure (a) from the assimilation output of experiments CNTLVR, CNTLZ, and VR.

storms A and B are dominant and show some hook shape on their southern flank, while in CNTLZ much stronger updrafts exist, with the strongest one being associated with a storm north of storm A. The radar observations indicate that storms A and B are at their early stage of development while the cells north of them are in a decaying stage. This suggests that the analysis of radial velocity data correctly improves the relative strength and structure of the cells in the initial condition and contributes to the improvement of forecast.

Next, we will examine various formulations of the mass divergence constraint.

3.4.5 Experiments on mass divergence constraint

All of the above experiments that assimilate radial velocity data use a two-dimensional mass divergence as a weak constraint. To better understand the impact of the divergence constraint, five additional experiments, namely, NoDiv, Div2Da, Div2Db, Div3Da, and Div3Db, are conducted. For brevity, we mainly present the results of these experiments at 0030 UTC 29 March, corresponding to 1.5-hour forecast time. The predicted reflectivity mapped to the same 1.45° radar elevation of the KFWS radar is plotted in Fig. 3.17 for CNTLVR and the above five experiments. The corresponding surface and 3 km MSL wind and vertical vorticity fields are plotted in Fig. 3.18. The ETS scores for reflectivity for these experiments are plotted in Fig. 3.19 and Fig. 3.20, together with those for CNTLVR. The ETS scores for NoDiv are also plotted in Fig. 3.14 instead for easier comparison with those of CNTLVR and CNTLZ.

3.4.5.1 Importance of divergence constraint

Experiment NoDiv in which the mass divergence constraint is not imposed at all

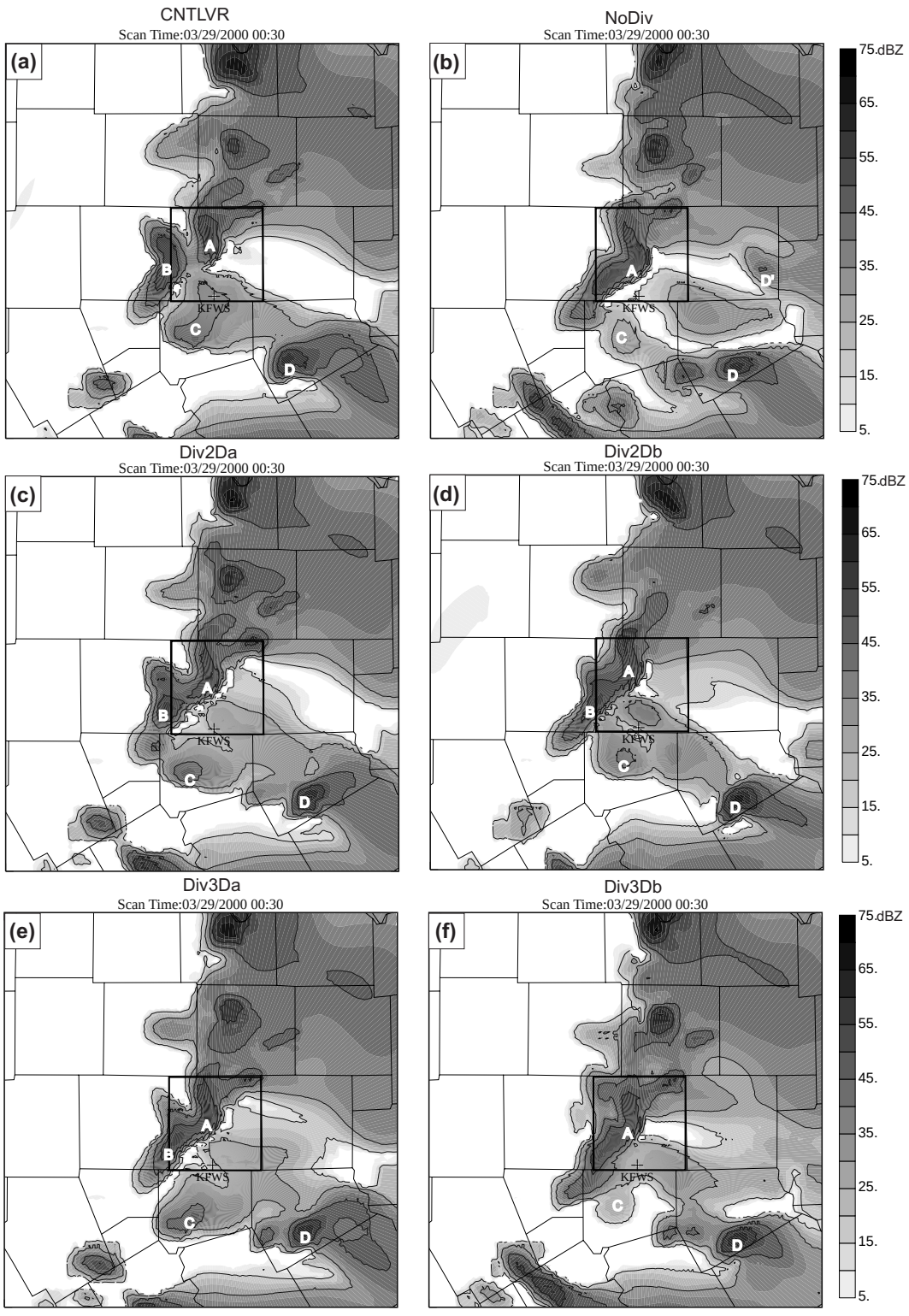

Fig. 3.17. Similar to Fig. 3.11, except that they are predicted reflectivity fields from experiments (a) CNTLVR, (b) NoDiv, (c) Div2Da, (d) Div2Db, (e) Div3Da, and (f) Div3Db, at 0030 UTC 29 March 2000.

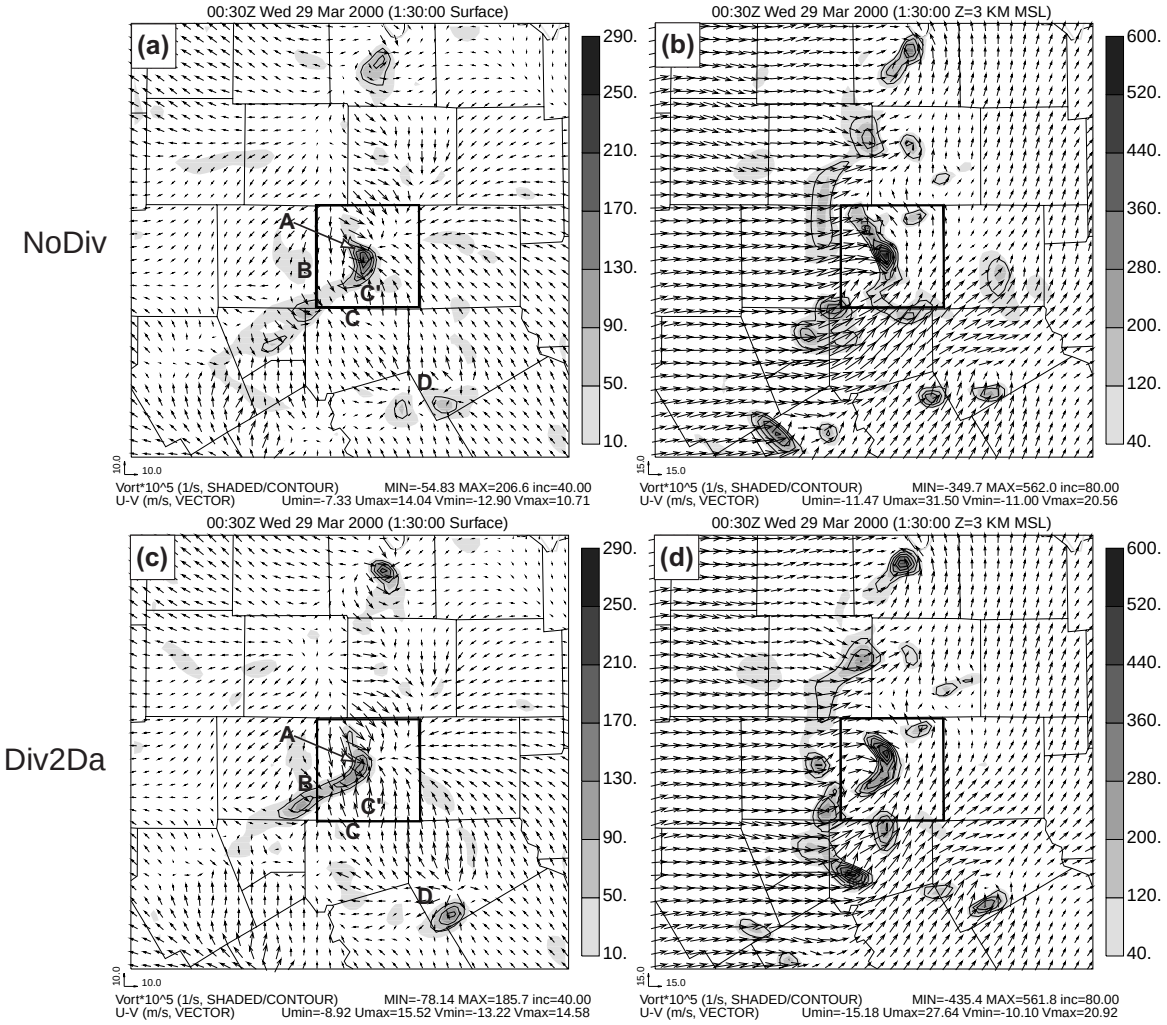

Fig. 3.18. Similar to Fig. 3.12, except that they are predicted wind and vertical vorticity fields from experiments NoDiv, Div2Da, Div2Db, Div3Da, and Div3Db, at 0030 UTC 29 March 2000.

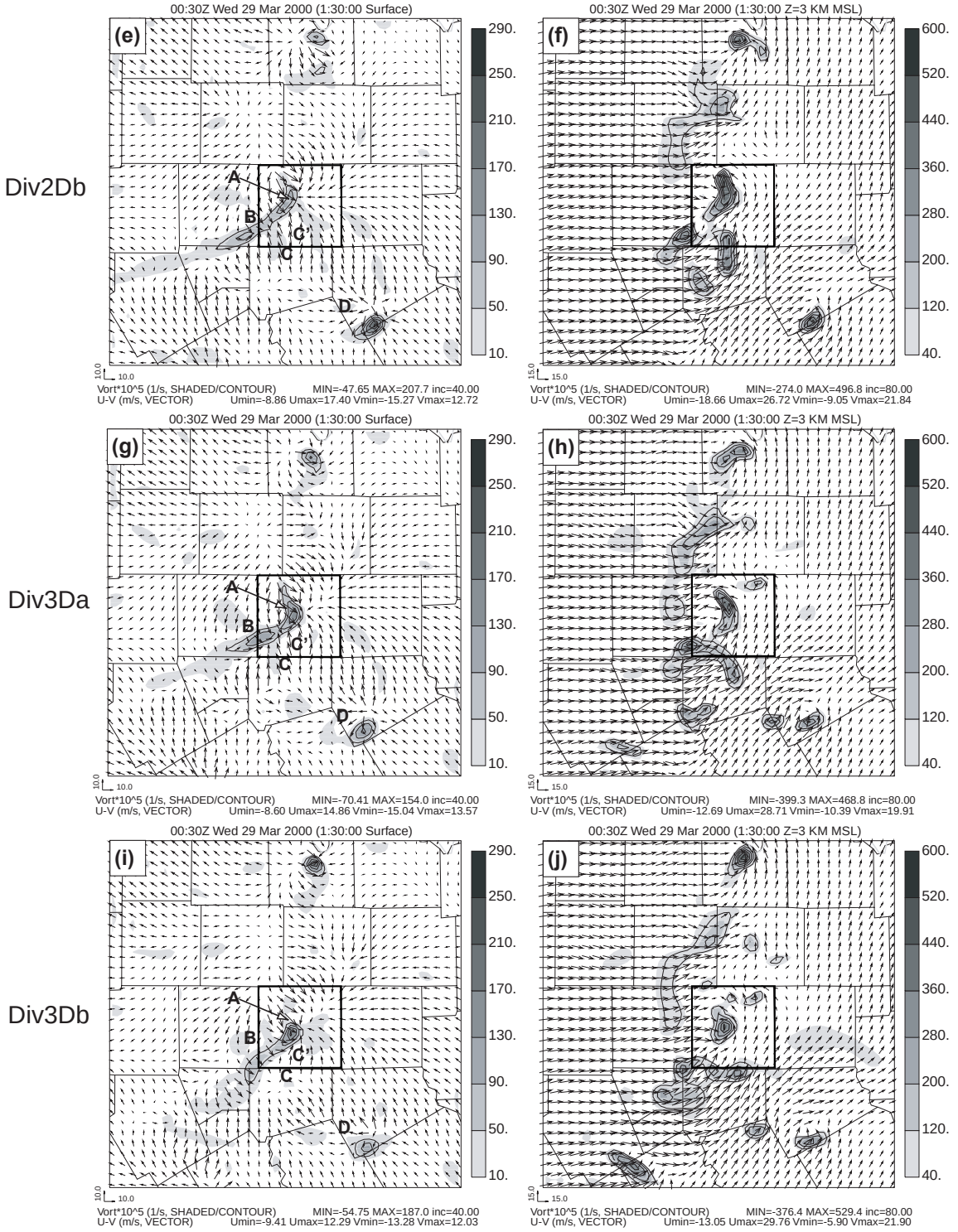

Fig. 3.18. Continued.

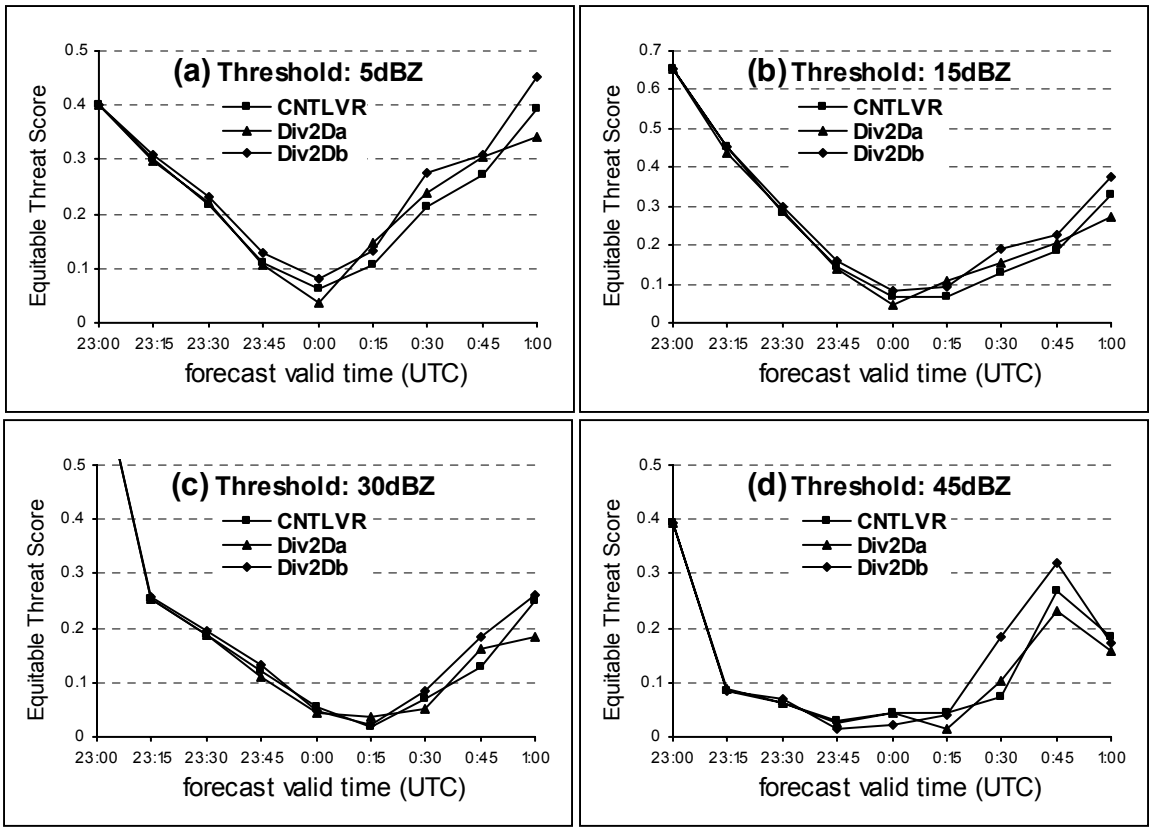

Fig. 3.19. Same as Fig. 3.14 but for experiments CNTLVR, Div2Da, and Div2Db.

is designed to separate the effect of mass divergence from that of radial velocity data. Comparing Fig. 3.17b with the corresponding observation in Fig. 3.11e, it is seen that storm A is overpredicted by NoDiv in size and its location has a southward displacement while storm B is completely missed. Storm D is located too far to the east, by approximately 30 km, and it is trailed by a spurious, though weaker, cell to its west. Another spurious cell, labeled D' in the figure, is found to the north-northeast of cell D. It is labeled D' because it is a cell that split from storm D in the first half hour of forecast (not shown). As shown in Fig. 3.17a for this time and discussed in detail for other times earlier, the forecast of CNTLVR is clearly more accurate than that of NoDiv. The ETS of NoDiv for the 45-dBZ threshold are lower than both CNTLVR and CNTLZ during the

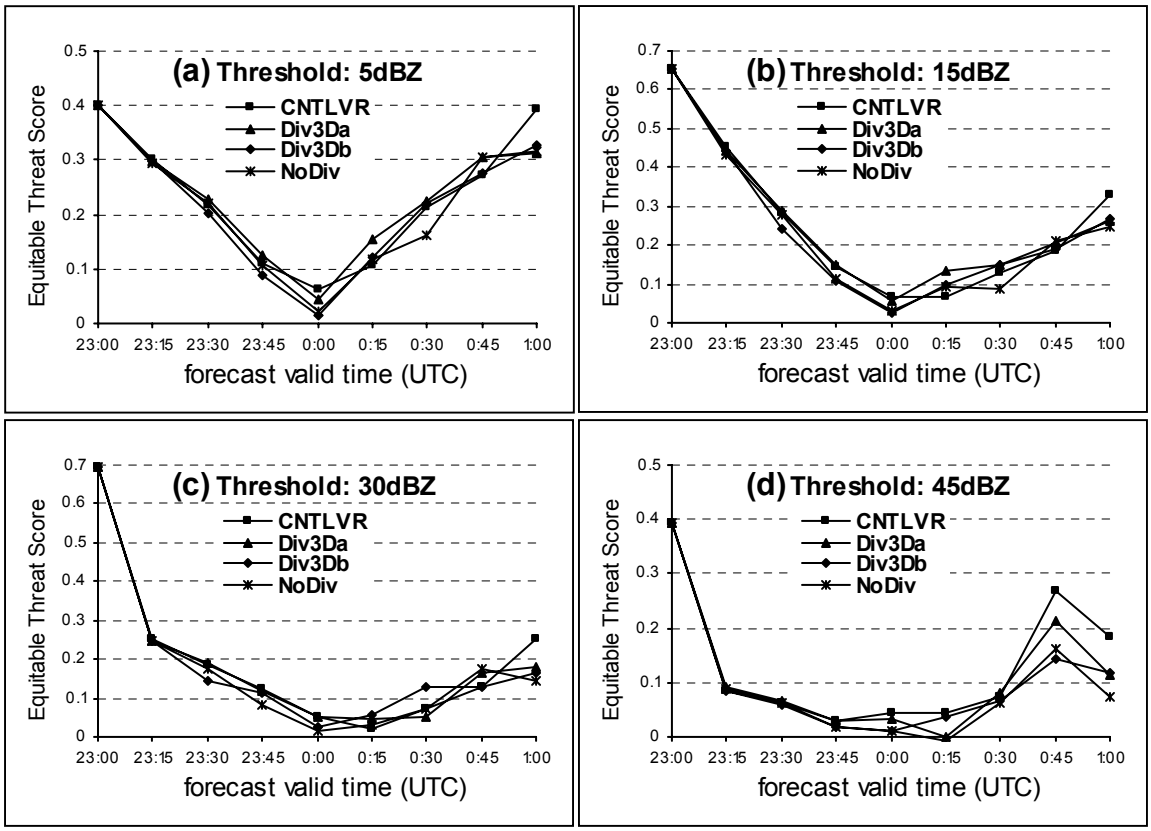

Fig. 3.20. Same as Fig. 3.14 but for experiments CNTLVR, Div3Da, Div3Db, and NoDiv.

important period between 0000 and 0100 UTC (Fig. 3.14d).

The above comparisons demonstrate the importance of including the mass divergence constraint when analyzing radial velocity data. This is because, as discussed earlier, a single-Doppler radar observes wind along the radial direction only. The cross-beam components cannot be determined by the 3DVAR analysis without additional information that links the three components. Without any constraint, the 3DVAR tends to make adjustments of background winds along the radial direction only, leaving the other components essentially unchanged. The inclusion of a mass divergence constraint forces the other wind components to respond to changes along the radial direction. Further, large amplitude acoustic oscillations are found in the time series plots of surface pressure

in NoDiv (not shown). Imposing the mass divergence constraint helps control such noise. Treating the constraint as a weak constraint gives the system necessary flexibility, as discussed for dual-Doppler analysis by Gao et al (1999). In the case of dual-Doppler wind analysis, two of the three wind components can be determined while the mass-continuity equation gives the third, yielding an easier problem than we have here.

3.4.5.2 Sensitivity to weighting coefficient of divergence constraint

The sensitivity of storm forecast on weighting coefficient, λ_c, of the mass divergence constraint in the cost function is studied through experiments Div2Da and Div2Db in which λ_c is half or double the value of CNTLVR (Table 3.2), respectively. In the 1.5-hour forecasts of these three experiments (Fig. 3.17a, c, d), the storms show a similar general pattern with several differences in the fine structures. First, storms A and B in experiment Div2Db are not separate as in the other two experiments and in the real world. Second, the maximum reflectivity center of storm A in Div2Db has greater displacement errors. Third, storm D in Div2Da and Div2Db has a greater eastward displacement error than in CNTLVR. Although the pattern comparison shows that the forecast of experiment CNTLVR is somewhat better than that of Div2Da and Div2Db at this time, the latter achieved generally better ETS (Fig. 3.19). For the 45-dBZ threshold, Div2Db outperforms the other two at 0030 UTC, but overall, the scores of the three are similar. In general, it appears that the analysis and forecast are not very sensitive to the coefficient of the divergence constraint for this case.

3.4.5.3 Effects of divergence constraint formulations

In section 2.3.4, we illustrated the problem with using a 3D mass divergence

constraint on a grid with large aspect ratios. In such a situation, the vertical part of the mass divergence dominates the wind adjustment so that horizontal wind components are little adjusted. This is the main reason why a 2D mass divergence constraint is used in all the earlier experiments. It should be pointed out, however, the 2D mass divergence constraint is not really physical for convective-scale flows, which can exhibit significant horizontal divergence beneath strong updrafts. To study this problem further, two experiments employing 3D mass divergence constraint are performed. Experiment Div3Da uses different weighting coefficients for the horizontal and vertical parts of the 3D mass divergence constraint, while experiment Div3Db uses the same weighting coefficient for both parts, which is effectively a true 3D mass divergence constraint. The exact values of the weighting coefficients are listed in Table 3.2.

As we expected, experiment Div3Db gives very similar forecast for main storm cells at 0030 UTC as experiment NoDiv (Fig. 3.17b, f) because almost all wind adjustment were applied to the vertical velocity, and the adjustment is expected to be one order of magnitude smaller (because of the large aspect ratio) than those of the horizontal winds for the 3D mass divergence constraint to be satisfied. The ETS of Div3Db and NoDiv shown in Fig. 3.20 are also similar for most of the times and threshold values, consistent with our subjective evaluation.

Experiment Div3Da decreases the weighting coefficient for the vertical divergence by a factor of 10 compared to CNTLVR or the horizontal term in Div3Da. Doing so decreases the effect of vertical velocity adjustment, thereby giving greater adjustments to the horizontal winds. The forecast reflectivity field plotted for Div3Da in Fig. 3.17 looks similar to that of Div2Db, and is better than that of Div3Db, indicating the

increased role of adjustments to horizontal wind fields. The ETS of experiment Div3Da for the 45-dBZ threshold are in between those of experiments CNTLVR and NoDiv (Fig. 3.20d).

The surface and 3 km MSL wind and vorticity fields from the above five experiments, (i.e., NoDiv, Div2Da, Div2Db, Div3Da, and Div3Db) are plotted in Fig. 3.18 and they can be compared to the corresponding times of CNTLVR in Fig. 3.12. Interestingly, all five experiments predicted a well-defined column of high vorticity over Fort Worth just as in experiment CNTLVR, but their shape and intensity differ somewhat. However, considering the fact that the forecast with no radial winds (experiment CNTLZ) failed to produce this high vorticity column, we can credit the radial velocity for the formation of this mesocyclone.

3.4.5.4 Results of assimilation from divergence constraint experiments

The vertical velocity, *w*, fields at 5 km MSL from the assimilation output of experiments CNTLVR, NoDiv, Div2Da, Div2Db, Div3Da, and Div3Db are plotted in Fig. 3.21. Although the strengths of updrafts vary significantly among the different experiments, the updrafts of storms A and B are dominant when compared to other updraft centers in the same experiment. Also, the updraft of storm A shows two centers at this time in most of the experiments, which reflects the splitting process of storm A in this stage just as observed. These features indicate that the analysis of radial velocity data can add useful information to the intrastorm wind fields and explain why the six experiments including radial velocity data produce a stronger low-level vorticity center near the location and time of the Fort Worth tornado.

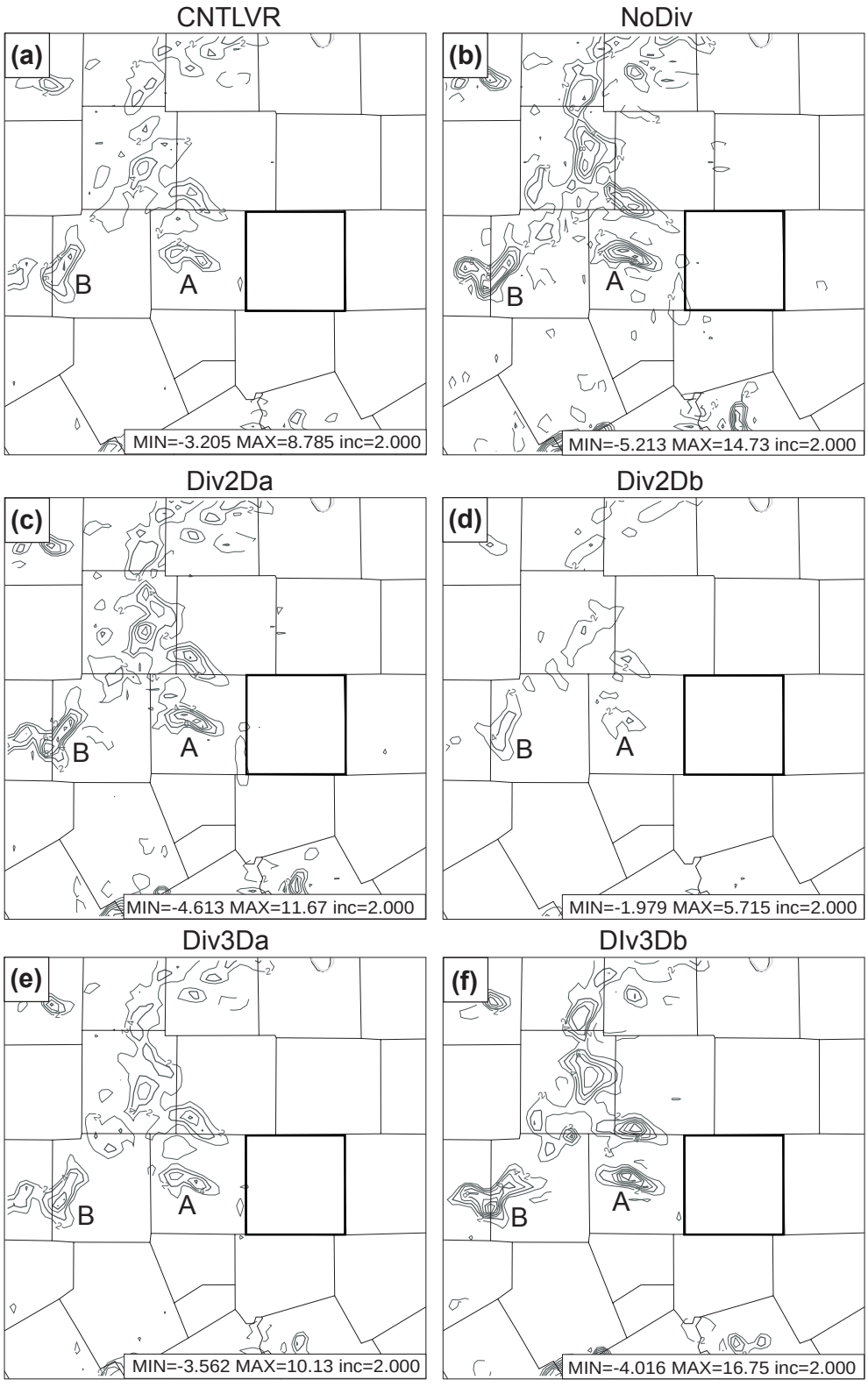

Fig. 3.21 The vertical velocity fields at 5 km MSL from the assimilation output of experiments CNTLVR, NoDiv, Div2Da, Div2Db, Div3Da, and Div3Db.

From Fig. 3.21, the effects of the mass divergence constraint in reducing the horizontal divergence and updraft intensity can also be clearly seen. Different from the forecast, the strength of the initial updraft is significantly affected by the weighting coefficients in the mass divergence constraint (Fig. 3.21a-d). Again, the similarity between the updrafts of NoDiv and Div3D indicates the problem of applying a 3D constraint on a grid with large grid aspect ratios (Fig. 3.21b and f).

In summary, we found in this section that the proper implementation of a mass divergence constraint in the 3DVAR analysis increases the positive impact of radial velocity data on the thunderstorm analysis and forecast. But in terms of the predicted wind fields, the differences due to different divergence formulations are much less than the impact of adding radial velocity. In our case of large grid aspect ratios, especially at the low levels, a 2D mass divergence constraint or a 3D formulation with a small coefficient for the vertical component is found to work most effectively.

3.5 Summary and discussion

In this chapter, the impact of Level-II WSR-88D reflectivity and radial velocity data on the prediction of a cluster of tornadic thunderstorms is studied. The 28 March 2000 Fort Worth tornado outbreak observed by the Fort Worth (KFWS) radar, which was also studied by Xue et al. (2003), is used as a test case. Radial velocity data are used in a 3DVAR analysis that contains a mass divergence constraint in the cost function and reflectivity data are assimilated through the updated cloud analysis procedure. A 3-km grid nested inside a 9-km one is used for both assimilation and prediction experiments. For all 3-km experiments except for X03, a one-hour long assimilation with analysis cycles at 10-minute intervals is performed, which is followed by a three-hour forecast

starting from the assimilated initial condition. Among the experiments, X03 is a repeat of the 3-km experiment reported in Xue et al. (2003) and used 15-minute instead of 10-minute analysis cycles.

Results from six 3-km experiments in Table 3.1 are discussed to examine the impact of reflectivity data and the updated cloud analysis procedure. Eight more 3-km experiments in Table 3.2 are conducted to investigate the impact of assimilating radial velocity data and the use of the mass divergence constraint.

The results demonstrate that the ARPS 3DVAR is capable of successfully analyzing observations from different sources, including those from radiosonde (available at 1800 UTC), wind profilers, surface stations, and Doppler radars. Combined with intermittent assimilation cycles, positive impact of radial velocity data is obtained for the forecast of a cluster of thunderstorms.

The best prediction is obtained when both reflectivity and radial velocity data are assimilated. The ARPS model is able to predict individual storm cells on the 3-km grid up to two hours into the prediction, and the supercell characteristics of the storm that spawned two individual tornadoes are well predicted, with timing errors of less than 15 minutes and location errors of less than 10 km at the time of the tornadoes.

Starting from an initial condition that assimilates Level-II reflectivity data through the updated cloud analysis procedure, the experiment CNTLZ successfully reproduces the evolution of the most significant thunderstorms in the Fort Worth tornado case. The forecast captures a storm with strong reflectivity gradients in the hook echo region and a low-level center of strong convergence and rotation that approaches and passes through downtown Fort Worth and Arlington around the time of the tornado occurrences.

Compared to a reconstructed experiment following Xue03 that uses an earlier version of the cloud analysis with Level-III reflectivity data, the experiment with all recent modifications to the cloud analysis, CNTLZ, shows reductions in both timing and location errors for the tornadic thunderstorm in the complex.

The comparisons of data denial experiments show that reflectivity data have a greater positive impact on the storm forecast than radial velocity data using the current 3DVAR and cloud analysis procedure, while the use of radial velocity along with the reflectivity via the cloud analysis does incrementally improve the storm forecast, especially in terms of the strong low-level vorticity centers associated with the tornadogenesis. When radial velocity (in addition to conventional data) is used without reflectivity, the model fails to forecast nearly all storms around Fort Worth. The small impact of using radial velocity alone is related to the limitation of the current 3DVAR analysis procedure, which does not make use of radar scans at multiple times and uses only a simple mass divergence constraint that does not solve the under-determinedness problem for single-Doppler wind analysis. Specifically, the lack of buoyancy perturbations associated with the ongoing convection limits the positive impact on the forecast. This is overcome by the cloud analysis scheme, which is effective in sustaining the model storms.

The analysis shows that the initial state and the evolution of the storm in the forecast can be impacted by each individual modification in the cloud analysis scheme. Adjusting in-cloud temperature based on a moist adiabatic profile and choosing observation-based retrievals of the precipitation species over background values in the cloud analysis can slow the movement of storms and improve the forecast of the tornadic

storm. These two modifications, together with the SMO scheme for the initial determination of hydrometeors, prevent a spurious storm from appearing in the forecast.

Adding hydrometeors and adjusting the in-cloud temperature and moisture fields in the analysis work to reduce the spinup problem of forecast. In our experiments, the forecasts still undergo a period of adjustment, indicating the existence of inconsistencies among the model fields. More investigation on the nature of this adjustment is needed to further improve the cloud analysis procedure.

It is also found that the use of a mass divergence constraint in the 3DVAR analysis increases the positive impact of radial velocity data on the storm forecast. This constraint acts to couple three wind components together during the analysis. Without the constraint, the radial velocity data tends to create too many horizontal discontinuities or small regions of horizontal divergence; the mass divergence constraint, though closer to 2D in formulation, helps smoothing out the small scale features while keeping larger-scale divergence little affected. The divergence at larger scales was beneficial to the support of existing convection.

The rather good forecast of the tornadic thunderstorm in the control experiment shows that a high-resolution model like ARPS together with an adequate system that assimilates WSR-88D Level-II data is able to initialize preexisting thunderstorms and predict them with reasonable accuracy on the cell-by-cell basis for 2 to 3 hours. The 3-km resolution used here is reachable operationally in the near future, over large enough domains. The need to assimilate radar data every or every other radar volume scans (as done in this study) may place a significant burden on operational systems. For our studies in Chapter 4, we investigate the impact of assimilation frequency on the analysis and

forecast. We also point out that the 3DVAR-based procedure used in this study is no more expensive than the ADAS-based procedure used in Xue03.

Our conclusions presented in this chapter are mainly based on a single case. Two more cases will be examined in the next two chapters, using a similar methodology.

Chapter 4

8 May 2003 Oklahoma City, Oklahoma,

Tornadic Thunderstorm Case

4.1 The case

At about 2210 UTC (1610 Local Standard Time or LST) on 8 May 2003, Moore, a suburb city about 15 km south of Oklahoma City (OKC thereafter), Oklahoma, was struck by a major tornado for the 4th time in 5 years. The tornado tracked east-northeast for about 30 km on the ground, from Moore to Choctaw, and dissipated at 2238 UTC (Fig. 4.1, all times will be in UTC in this Chapter unless otherwise noted). It caused large areas of F3 (on Fujita scale of tornado intensity) and small areas of F4 damages south and east of OKC, and many F2 damages in the Moore area. This tornado caused $370 million worth of damages and more than 100 injuries, but fortunately no death. It is named the OKC tornado by National Weather Service as it struck the general OKC area. The parental storm is referred as the OKC tornadic thunderstorm.

Two additional short-lived tornadoes from the same storm were reported near Moore. The first brief tornado occurred at 2200. The second F0 tornado began at 2204 and stayed on the ground and moved nearly 3 km in 6 minutes but dissipated just before the OKC tornado outbreak.

On 8 May 2003, the synoptic-scale environment over Oklahoma was favorable for tornadic thunderstorms. A surface low formed in the early morning in southeastern Colorado and propagated northeastward across Kansas during the daytime. Oklahoma and Texas had been exposed to southerly flows for all day and a north-south oriented

dryline formed over western Texas and the Texas-Oklahoma panhandle area by 1200 (0006 LST). The dryline then moved eastward into western Oklahoma and by 1800 (1200 LST) it was located about 200 km west of OKC. During the daytime, the upper level flows over Oklahoma were mainly southwesterlies with the wind speed slightly increasing before the thunderstorms.

The 1200, 8 May Norman, Oklahoma, (OUN) sounding shows a moderate to large instability with a 2277 J kg^{-1} CAPE and a 137 J kg^{-1} CIN. The vertical shear of horizontal winds over the lowest 6 km is about 56 m s^{-1} and 3 km storm relative environmental helicity is 238 m^2 s^{-2}. These parameters suggest a high potential for supercell and tornado.

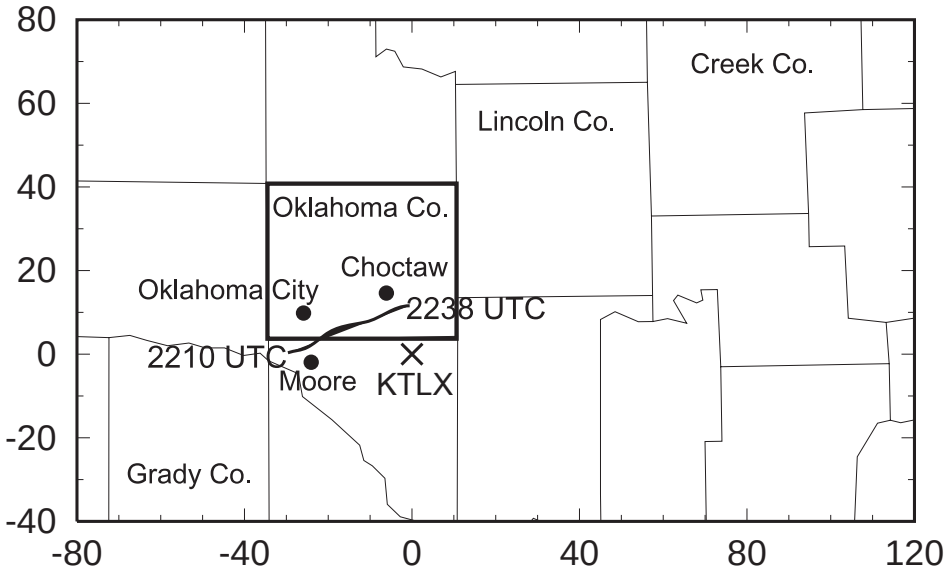

Fig. 4.1. Map of counties and cities related to the 8 May 2003 OKC tornadic thunderstorm. The dark line segment starting at 2210 northwest of Moore and ending at 2238 south Choctaw marks roughly the damage path of the OKC tornado. The *x* and *y* distances are in kilometer and are relative to the KTLX radar marked by × in the figure. Oklahoma County is highlighted.

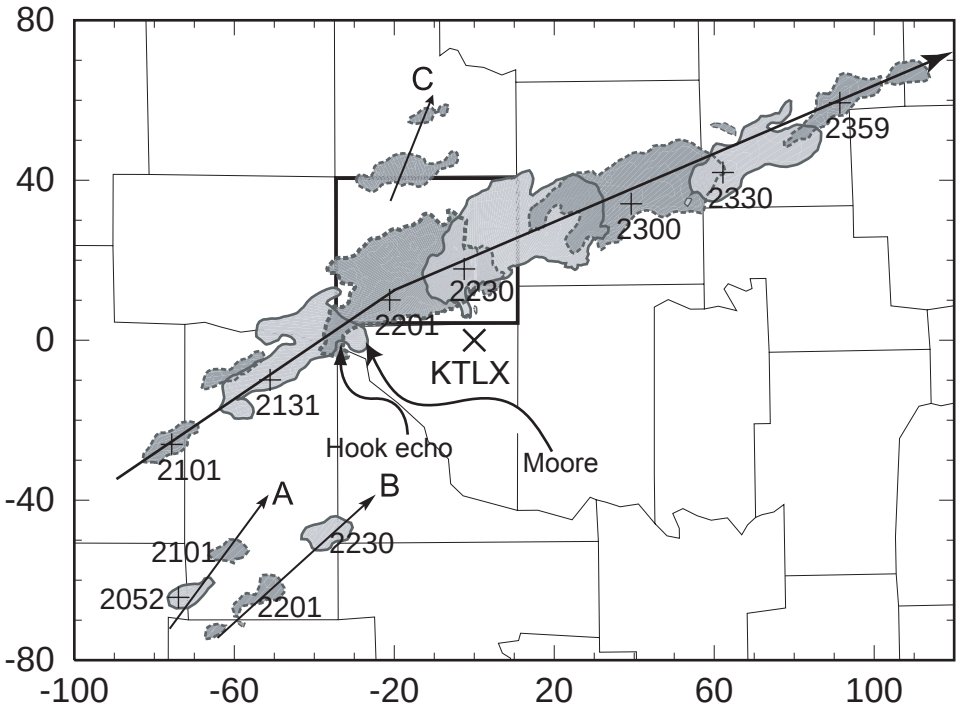

Fig. 4.2. Regions of radar echoes exceeding 35 dBZ as observed by the KTLX radar at the 1.45º elevation. The echoes are at 30-minute intervals from 2101 to 2359, of 8 May 2003. The grayscales of the echoes at two consecutive times are different, so are their outlines. The locations of the maximum reflectivity of the main storm are marked by + signs, together with the corresponding times. The *x* and *y* coordinates are in kilometer and have their origin at the KTLX radar site that is marked by ×. The arrow lines are the paths of the OKC storm and storms A, B, and C. Also, the hook echo at 2201 and Moore are pointed by curved arrows. Oklahoma County is highlighted.

At 2040, the OKC tornadic thunderstorm was initiated east of the dryline, as a weak echo observed by Oklahoma City (KTLX) radar. The evolution of the storm is displayed by a series of low-level reflectivity regions whose values are greater than 35 dBZ (Fig. 4.2). The storm developed into a strong cell by 2101 and was located at (-75 km, -50 km) relative to the KTLX radar. It then propagated northeastward and grew significantly in size in the next hour. At 2201, a pronounced hook appendage structure is

found at the southwestern end of the storm, northwest of Moore, indicating the presence of a tornado or mesocyclone. The supercell storm propagated east-northeastward, and then became weaker from 2300, 8 May and dissipated by 0020, 9 May. In addition to the OKC storm, three other storms are also shown in Fig. 4.2 and are referred to storms A, B, and C. Storm A was initiated a little earlier than the OKC storm east of the dryline but dissipated by 2130. Storm B was initiated later than the OKC storm and lasted for only about one hour. Storm C was split from the OKC storm and dissipated quickly during its leftward propagation.

4.2 Impact of configurations of rapid intermittent assimilation of radar data*

The organization of this section is as follows. In section 4.2.1, we introduce the design of a set of experiments for studying the impact of the assimilation configurations. A detailed comparison among experiments is presented in section 4.2.2 and the results are further discussed in section 4.2.3. Section 4.2.4 provides a brief summary of the key findings.

4.2.1 Design of assimilation and forecast experiments

In this section, data from the KTLX radar are assimilated to study the impact of different assimilation configurations on the initialization and prediction of the OKC storm. The low-level reflectivity observations from the same radar are used to evaluate the quality of the forecasts, which are the only available observations having enough temporal and spatial resolutions for resolving the storm.

* This section is based on a paper conditionally accepted by Monthly Weather Review (Hu and Xue 2006).

For all experiments, two one-way nested grids, with 9- and 3-km horizontal resolutions, respectively, are used. The 9-km grid covers an area of 2300 km × 2300 km with Oklahoma located roughly at the center. The 3-km grid is 580 km × 580 km in size and covers the entire state of Oklahoma and parts of Texas and Kansas. Both 9-km and 3-km simulations use the same vertical grid that stretches from about 20 m at the surface to 770 m at the model top that is located at 21.1 km height. The ARPS model with full physics is used during the assimilation and in the forecast. The ARPS 3DVAR is used to analyze conventional data (wind profiler, Oklahoma mesonet) and radial velocity data, while the cloud analysis procedure is used to adjust in-cloud temperature, moisture, and hydrometers fields according to reflectivity data.

Only one 9-km simulation is conducted and its forecast results provide the background for the first 3-km analysis, and the boundary conditions for 3-km assimilation and forecast. The 9-km simulation includes 1-hour assimilation cycles over a 6 hour period from 1800, 8 May to 0000, 9 May. The 9-km analysis uses the NCEP Eta model 1800 analysis as the background. Only rawinsonde and wind profiler data are used in the analyses. The lateral boundaries are forced by the Eta 1800 forecasts at 3-hour intervals.

The 3-km control experiment starts at 2030, slightly earlier than the initiation time of the OKC storm. A one-hour long assimilation window with 10-minute analysis cycles covers the entire initial development stage of the storm. Both reflectivity and radial velocity data are assimilated along with the upper air data when available. The two-pass strategy with different horizontal decorrelation scale for each pass is used in the 3DVAR. The upper-air data are analyzed in the first pass using a horizontal de-correlation scale

length of 120 km and the radial velocity data are analyzed in the second pass using a scale length of 6 km. For the 3-km control experiment, a 2.5-hour forecast is conducted from the end result of assimilation at 2130, 40 minutes before the storm produced the OKC tornado northwest of Moore.

Based on the control experiment, a series of other 3-km experiments are conducted, using different assimilation configurations to study their impacts on the assimilation and subsequent forecast. The configuration parameters varied include assimilation frequencies (or intervals), in-cloud temperature adjustment schemes, and the lengths and coverage of assimilation window (AW).

A total of fifteen 3-km experiments (Table 4.1) are conducted, including the control. These experiments can be classified into two groups according to assimilation frequency, that is., the experiments with 5 or 10-minute analysis cycles. In each group, the length of the AW varies from 30 to 60 minutes and the AW covers different stages of the OKC storm development. The latter include the entire initial development stage (from 2030 to 2130), the early stage of initiation (from 2030 to 2110 or 2120), and the late stage of initiation (from 2040, 2050, or 2100 to 2130). For in-cloud temperature adjustment, two schemes are available in the ARPS cloud analysis package and both are introduced in detail in section 2.4.3. Here, we refer the scheme that is based on the latent heat release to LH scheme and the scheme that is based on a moist adiabatic temperature profile as MA scheme. All experiments with 5-minute intervals use the MA scheme except for experiments 5B30E30LH and 5B60E30LH, which use the LH scheme. All experiments with 10-minute analysis intervals use the LH scheme except for experiment 10B30E30MA, which uses the MA scheme. The ideal combination of one of the two

temperature adjustment schemes with other configuration parameters are discussed in the next section.

Table 4.1. Assimilation configurations of the 3-km experiments

Name*	Interval (minutes)	Length (minutes)	Coverage (UTC)	In-cloud temperature adjustment
10B30E30LH (CNTL)	10	60	2030–2130	LH
10B30E30MA	10	60	2030–2130	MA
10B30E20LH	10	50	2030–2120	LH
10B30E10LH	10	50	2030–2110	LH
10B40E30LH	10	50	2040–2130	LH
10B50E30LH	10	40	2050–2130	LH
10B60E30LH	10	30	2100–2130	LH
5B30E30MA	5	60	2030–2130	MA
5B30E30LH	5	60	2030–2130	LH
5B30E20MA	5	50	2030–2120	MA
5B30E10MA	5	40	2030–2110	MA
5B40E30MA	5	50	2040–2130	MA
5B50E30MA	5	40	2050–2130	MA
5B60E30MA	5	30	2100–2130	MA
5B60E30LH	5	30	2100–2130	LH

* Characters B and E followed by a number denote, respectively, the beginning and ending time of the assimilation window in minutes.

4.2.2 Results of assimilation and forecast experiments

In this section, we first discuss the results of control experiment 10B30E30LH (also called CNTL), which produces the best OKC storm forecast among the 15 experiments in terms of the intensity and propagation. The experiments with different assimilation frequencies, in-cloud temperature adjustment schemes, and assimilation lengths and coverage are then discussed and compared. Finally, the results of experiment

5B60E30LH, in which the assimilation configurations are adjusted to suit a shorter AW, are discussed.

4.2.2.1 Experiment with the best forecast

The experiment that produces the best forecast, that is, control experiment 10B30E30LH, employs a 1-hour-long AW from 2030 to 2130 with 10-minute analysis cycles (about every other radar volume scan). The LH scheme is used for in-cloud temperature adjustment (Table 4.1). As mentioned before, the first echo of the OKC storm appeared at 2040 and the first tornado from the storm occurred at 2200. The AW of this experiment, therefore, covers the entire initial development stage of the storm and the final analysis has a half-hour lead time from the tornadogenesis stage of the storm.

The regions with reflectivity exceeding 45 dBZ, as observed by the KTLX radar at the 1.45° elevation, are shown in Fig. 4.3, together with the corresponding predicted reflectivity fields from 10B30E30LH. The time period shown in Fig. 4.3 is from 2130, 8 May to 0000, 9 May. The observed storm first formed at the northeastern corner of Grady County (c.f., Fig. 4.1), propagated east-northeastward through Oklahoma and Lincoln Counties, and arrived at east-central Creek County 2.5 hours later (Fig. 4.3a). Experiment 10B30E30LH predicts the observed storm motion accurately (Fig. 4.3b); the predicted storm moves in essentially the same direction and at about the same speed as the observed storm. The location errors of the maximum reflectivity of the predicted OKC storm are within 8 km in the entire 2.5 hours of forecast. The observed storm grew quickly from 2131 to 2201, and then remained as a supercell with a large area of strong reflectivity (> 45 dBZ, shown as shaded regions in Fig. 4.3) until 2300. Pronounced hook echo existed at the southwestern end of the high-reflectivity region between 2201 and

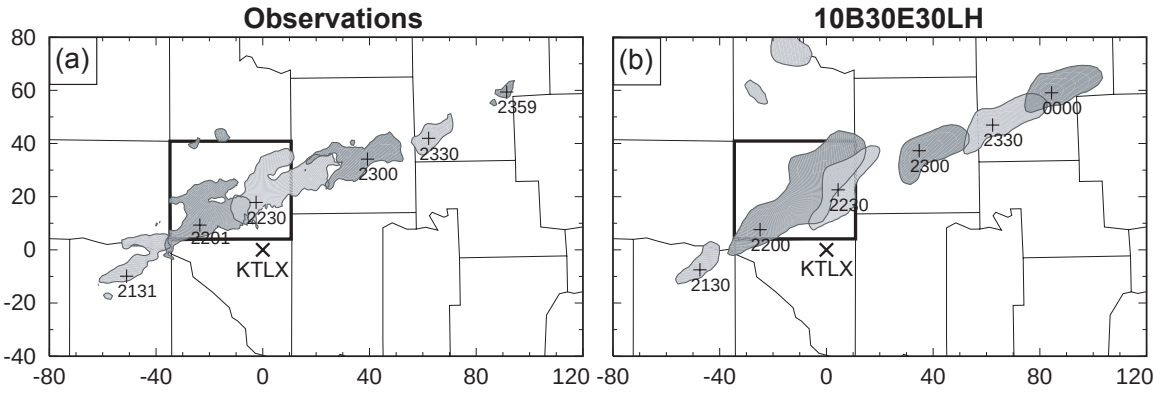

Fig. 4.3. As in Fig. 4.2, but for (a) the observations from 2130, 8 May to 0000, 9 May 2003, at 30-minute intervals, and (b) the corresponding predicted fields from experiment 10B30E30LH. Regions with reflectivity exceeding 45 dBZ are shown. The locations of the maximum reflectivity of the OKC storm are marked by + signs together with the corresponding times. The domain shown represents the portion of the 3-km grid between 210 and 410 km in the east-west direction and from 260 to 380 km in the north-south direction.

2300. After 2300, the storm weakened, and by 2359 only a small area of high reflectivity (> 45 dBZ) remained. The main characteristics of the development of the observed storm are also captured by the forecast; the predicted storm reaches its maximum intensity at about 2200, but remains a strong supercell until the end of forecast at 0000. Overall, 10B30E30LH successfully predicts the development and propagation of the OKC thunderstorm even though it is somewhat too strong in the last hour of the forecast.

The predicted reflectivity fields at the 1.45° elevation at 2200 and 2300 from 10B30E30LH are shown in more detail in Fig. 4.4 (right column), together with the corresponding observations (left column). At 2200, the time when the OKC storm produced the first tornado, a clear hook echo was seen at the southwestern end of the observed storm (Fig. 4.4a) and two small left-moving cells were seen north of the storm. The half-hour forecast of 10B30E30LH at this time produces the right position and

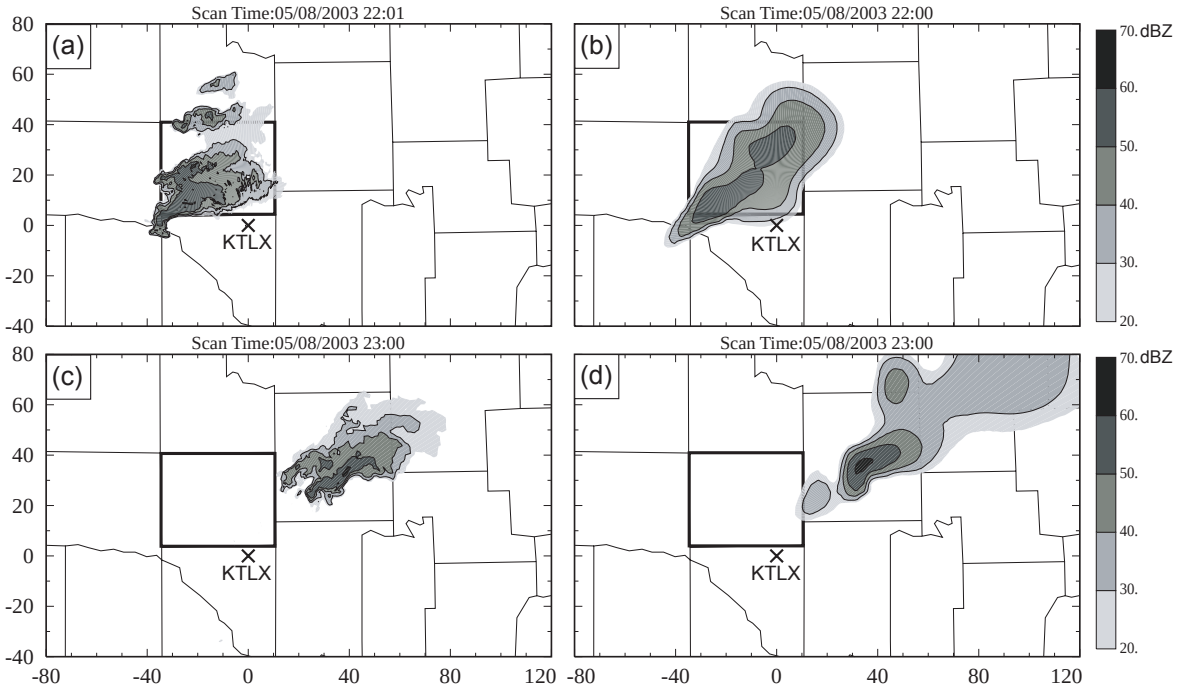

Fig. 4.4. Observed reflectivity fields at the 1.45° elevation of the KTLX radar (left column), and the corresponding predicted reflectivity from experiment 10B30E30LH (right column), at 2200 and 2300, 8 May 2003. The reflectivity contours are at 30, 40, 50, and 60 dBZ. The domain shown is the same as Fig. 4.3.

intensity of the storm, but does not exhibit a clear hook shape at the SW end (Fig. 4.4b). The predicted storm system also exhibits a sign of splitting at this time, but the left-moving cell is located to the NE instead of north of the main cell and is stronger than the observed ones. One hour later, the observed storm remained strong and moved to central Lincoln County (Fig. 4.4c). Although the OKC tornado ended about 20 minutes earlier, the storm still possessed strong reflectivity gradient and hook-shaped echo at its southern flank, indicating its supercell characteristics. Again, the 1.5 hour forecast of 10B30E30LH at 2300 gives accurate position and intensity of the storm (Fig. 4.4d); as observed, the predicted storm also exhibits supercell characteristics, a hook-shaped echo with strong reflectivity gradient at its southern flank. The predicted low-level and

midlevel flows also show strong rotation related to the OKC storm during this period (not shown). Therefore, many details of the observed storm are captured well by the prediction in control experiment 10B30E30LH.

4.2.2.2 Impact of the frequency of analysis cycles

In the control experiment, the KTLX radar data are used every 10 minutes, while the volume scan interval of operational WSR-88D Doppler radars (such as KTLX) operating in precipitation mode is about 5 minutes. To study the impact of the frequency of analysis cycles on the prediction of storms, experiment 5B30E30MA is conducted. This experiment is the same as the control except for its 5-minute analysis cycles and the use of the MA scheme for in-cloud temperature adjustment (Table 4.1). The reason for using a different in-cloud temperature adjustment scheme is discussed in the next subsection.

The regions with predicted reflectivity exceeding 45 dBZ at the 1.45º elevation are shown in Fig. 4.5 for experiment 5B30E30MA every 30 minutes. Compared with the observations (Fig. 4.3a), 5B30E30MA predicts the motion of the OKC storm very well, but gives a wrong trend of storm evolution. Contrary to the observations, the predicted storm becomes weaker from 2200 to 2300 and then stronger from 2300 on. The positions of the predicted maximum reflectivity in 10B30E30LH are also better than those of 5B30E30MA most of the times (Fig. 4.3b, Fig. 4.5) and the evolution of storm strength is better captured by 10B30E30LH too, even though 10B30E30LH over-predicts the intensity of the storm at the dissipation stage.

To quantitatively compare the quality of the forecasts from 10B30E30LH and 5B30E30MA, equitable threat scores (ETS, Schaefer 1990) of the predicted reflectivity at

the 1.45º elevation for the 45-dBZ threshold are calculated against the observations and plotted in Fig. 4.6. The ETS is originally designed for large scale precipitation prediction and should be applied with caution for small-scale convection systems. ETS here is used in a similar way as we do in Chapter 3. Fig. 4.6 shows that the first-hour forecasts (from 2130 to 2230, 8 May) of the two experiments are similar except for 0.75 hour when

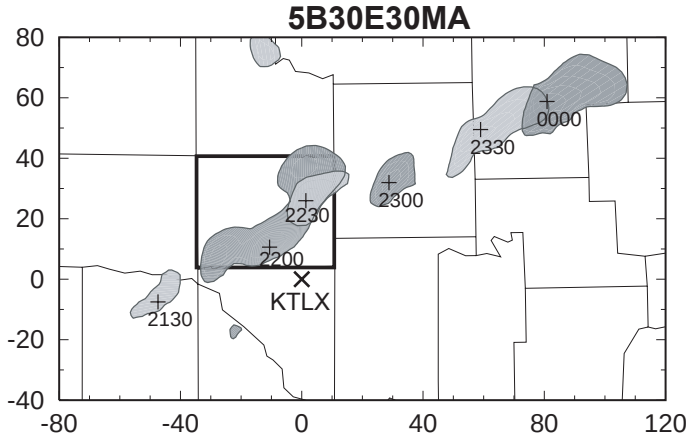

Fig. 4.5. As Fig. 4.3b, but for experiment 5B30E30MA.

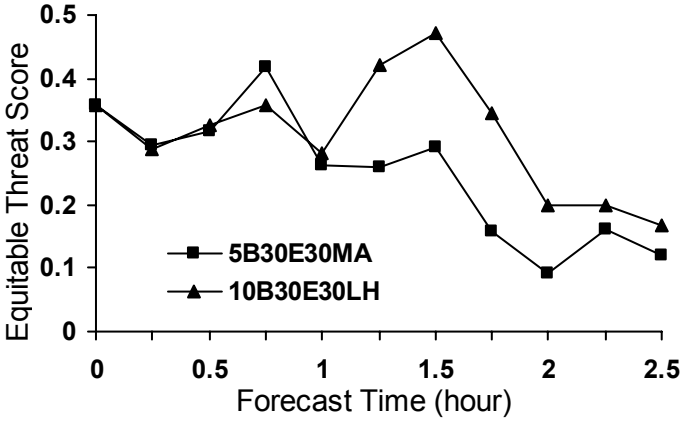

Fig. 4.6. Equitable threat scores for the predicted 1.45º elevation reflectivity for 45-dBZ threshold, for experiments 5B30E30MA and 10B30E30LH.

5B30E30MA is better. For the next 1.5 hours, 10B30E30LH has much higher scores than 5B30E30MA. The largest difference occurs at 1.5 hours (2300), when the scores for 10B30E30LH and 5B30E30MA are 0.48 and 0.29, respectively. This is the time when the storm in 5B30E30MA is too weak (Fig. 4.5). The comparisons of ETSs of these two experiments agree with the earlier subjective evaluation.

Usually, the data assimilation tries to use all available observations to obtain the best possible initial conditions for forecast, but both subjective evaluation and ETS for the previous two experiments suggest that the experiment with lower assimilation frequency (10-minute intervals) gives a better forecast. The reason is complex and appears to be related to both the ability of the analysis procedure to generate balanced storms in the initial fields and the ability of the model in establishing a suitable balance among different variables through adjustment. In our experiment, the radial velocity data are analyzed by the ARPS 3DVAR under a mass divergence constraint and the reflectivity data are used through the cloud analysis to adjust in-cloud temperature, moist, and hydrometer fields. Apart from the velocity components that are coupled through the mass continuity equation, the other analysis variables are analyzed more or less independently. Therefore, the analysis fields are not balanced in general or consistent with model dynamics and physics. Starting from such initial conditions, the model forecast must undergo some adjustments during the initial period to build up a balanced storm and such adjustments take some time to complete. For this reason, it is desirable that a new analysis is started at the time when a reasonable balance has been reached through model adjustment; too short analysis cycles do not necessarily lead to better final analysis. This is in general not true for more sophisticated data assimilation techniques

such as the ensemble Kalman filter method, in which flow-dependent background error covariances help produce balanced analysis that allows for high frequency analysis cycles without degrading the final analysis. Xue et al. (2005) show, with simulated data, that radar data at 1-minute volume scan intervals produce better analysis than those collected at lower volume scan frequencies.

The maximum vertical velocity (Wmax) can be used as an indicator of the initial adjustment during the model forecast. The maximum vertical velocities of the first 20 minutes of model forecasts starting from the analyses of assimilation experiments 5B30E30MA and 10B30E30LH, at 0 (2030, the initial development stage), 30 (2100, the middle stage), and 50 (2120, the late stage) minutes into the AW, are plotted as solid curves in Fig. 4.7. The dashed curves in Fig. 4.7a are for the forecasts starting from the analyses one analysis cycle or 5 minutes later. The curves of Wmax at all three stages show similar shapes in both experiments (Fig. 4.7). For the forecasts starting from the first analysis, over the period from 0 to 20 minutes, Wmax increases from values below 5 m s^{-1} to maximum values above 33 m s^{-1} in 12 to 14 minutes and then drop sharply in the next 6 to 8 minutes. For the forecasts starting at 30 minutes, Wmax values increase from analyzed values between 20 and 25 m s^{-1} to their maximum values close to 40 m s^{-1} in 5 to 7 minutes and then drop more slowly. For the forecasts starting at 50 minutes, Wmax values increase sharply in the first 1 to 2 minutes, reach the maximum values slowly in 7 to 8 minutes, then decrease slowly. It is clear that even for the forecasts that start from cycled initial conditions, such as those at 30 and 50 minutes, the model still needs more than 5 minutes to establish strong vertical motion and to produce a more balanced state. Further, Wmax values at 35 and 55 minutes in experiment 5B30E30MA (dash lines in

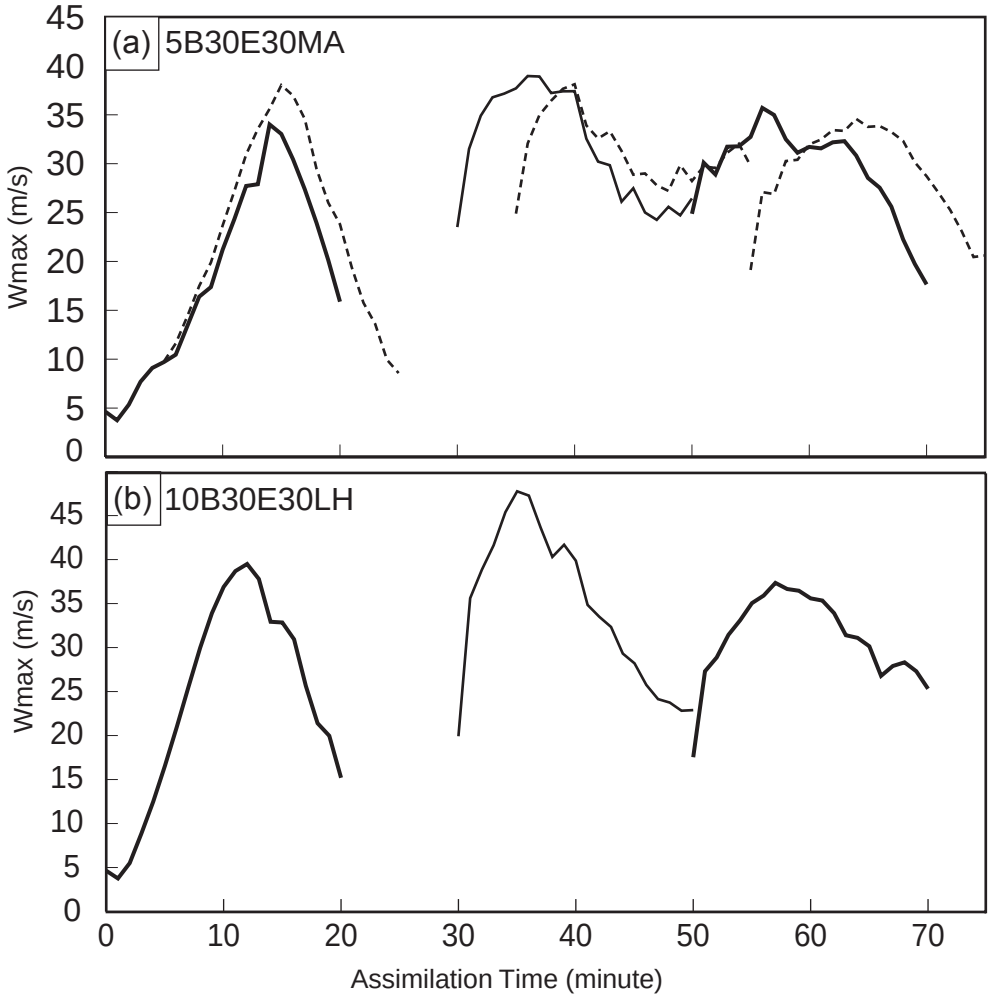

Fig. 4.7. The maximum vertical velocities for the first 20 minutes of forecasts starting (a) from the 5B30E30MA analyses at 0 (2030), 30 (2100), and 50 (2120) minutes into the assimilation cycles (solid lines with different thickness for consecutive times) and (b) from the 10B30E30LH analyses at the same times, and in (a) for a set of forecasts starting from the analyses one analysis cycle later (dashed lines) for 5B30E30MA.

Fig. 4.7a) are clearly lower than the values from the forecasts starting 5 minutes earlier. Therefore, when analysis cycles shorter than 10 minutes are used, the model does not have enough time to spin up the updraft in the model from the new analysis whose updraft strength tends to be reduced by the analysis step. For these reasons, 10-minute analysis cycles work better than 5-minute cycles. On the other hand, when the analysis

intervals are too long, such as 15 minutes, the insufficiently spun-up storms in the model would have weakened significantly by the time of next analysis. This explains why the 10-minute analysis cycles work better than 5 and 15-minute cycles (not shown).

4.2.2.3 Impact of in-cloud temperature adjustment schemes

As mentioned earlier, the ARPS cloud analysis has two in-cloud temperature adjustment schemes: the latent heat scheme (LH) that calculates the temperature adjustment from the latent heat release corresponding to the added cloud water and ice by the analysis, and the moist-adiabat (MA) scheme that adjusts in-cloud temperature based on a moist adiabat corresponding to an air parcel lifted from the low-level. The effect of entrainment is considered for the latter scheme. The MA scheme is more consistent with the physics of a convective storm because it reflects the temperature change in an ascending moist air parcel, while repeated applications of the LH scheme can lead to multiply counting the same latent heating associated with the condensed water or ice.

The temperature adjustment is very important for sustaining existing convection and the use of different schemes can impact the storm forecast significantly (Chapter 3). To further study the impact of the temperature adjustment schemes and their interaction with the other assimilation parameters, experiments 10B30E30MA and 5B30E30LH are conducted. They are same as 10B30E30LH and 5B30E30MA, respectively, except for the temperature adjustment scheme used (Table 4.1). The regions of predicted reflectivity exceeding 45 dBZ, at the 1.45º elevation, are shown in Fig. 4.8 for 10B30E30MA and 5B30E30LH. The ETSs of the same reflectivity fields, for the 45-dBZ threshold, are plotted in Fig. 4.9. The scores from 5B30E30MA are also included for the convenience of comparison.

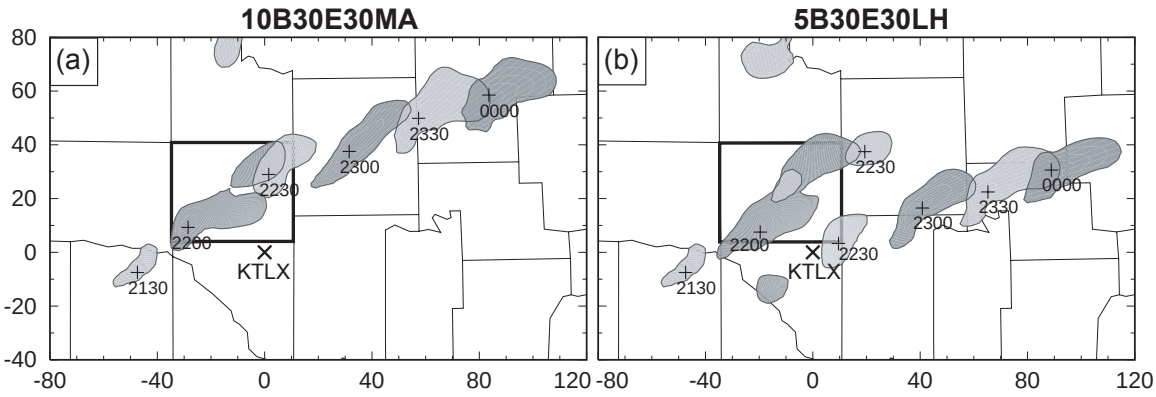

Fig. 4.8. Same as Fig. 4.3b, but for experiments 10B30E30MA (a) and 5B30E30LH (b).

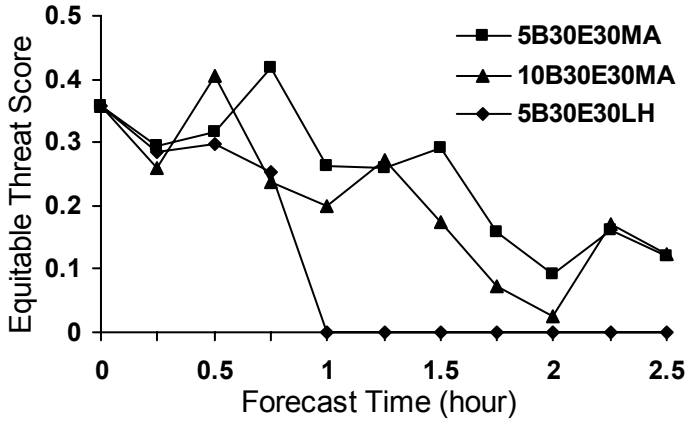

Fig. 4.9. ETSs of predicted reflectivity at the 1.45º elevation for the 45-dBZ threshold for experiments 5B30E30MA, 5B30E30LH, and 10B30E30MA.

Similar to 5B30E30MA, 10B30E30MA predicts the propagation of the OKC storm well but the predicted change in the storm intensity is opposite to that observed (Fig. 4.8a and Fig. 4.5). Compared to 10B30E30LH, the predicted storm in 5B30E30LH dissipates too early. This early dissipation appears to be related to the spurious cell that develops in the model south of the OKC storm and propagates east-northeastward during the last two hours of forecast (Fig. 4.8b and Fig. 4.3b).

The ETSs of these four experiments agree with the subjective evaluation (Fig. 4.9 and Fig. 4.6). 10B30E30LH has the highest scores most of the times, especially for forecasts over 1 hour; 10B30E30MA has lower scores than 5B30E30MA most of the times because the former over-predicts the OKC storm even more at those times; 5B30E30LH has zero scores after 1 hour because the predicted OKC storm dissipates after 1 hour of forecast.

The in-cloud temperature adjustment increases the temperature inside the storm therefore increases potential energy (or buoyancy) in the system that supports the development of the storm. To quantitatively estimate the effect of temperature adjustment by two different schemes, the total potential energy added to the model atmosphere by the temperature adjustment in all analysis cycles is calculated for the above four experiments and the results are 9.54×10^{16} J in 10B30E30LH, 16.79×10^{16} J in 5B30E30LH, 2.35×10^{16} J in 10B30E30MA, and 4.16×10^{16} J in 5B30E30MA. The LH scheme adds much more, or approximately 4 times as much potential energy than the MA scheme for the assimilations with the same number of cycles. Further, the use of more cycles tends to add more energy into the system and it is more so with the LH scheme by design.

As an important indicator of the vigor of a storm, the vertical velocity fields at 7 km MSL are shown in Fig. 4.10 for 10B30E30LH, 5B30E30MA, 10B30E30MA, and 5B30E30LH. Two updraft centers, one related to the OKC storm and the other related to storm A (c.f., Fig. 4.2), are found at the end of the assimilation in all four experiments. However, their strengths are very different, because of the use of the different temperature adjustment schemes and different analysis frequencies (Fig. 4.10). With a

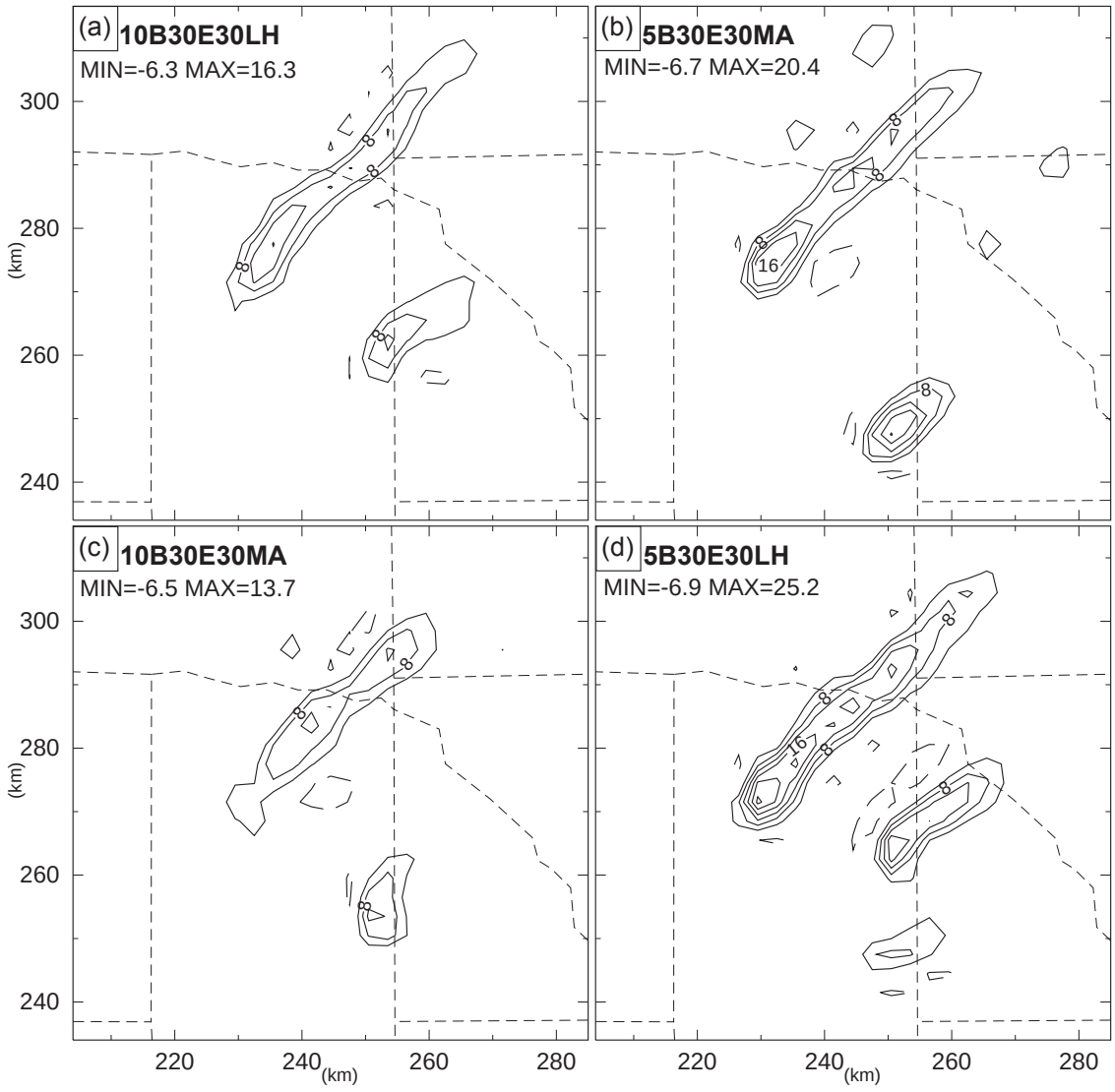

Fig. 4.10. The vertical velocity fields at 7 km MSL at the end of assimilation in experiments 10B30E30LH (a), 5B30E30MA (b), 10B30E30MA (c), and 5B30E30LH (d). The domain shown represents the portion of the 3-km grid between 205 and 285 km in the east-west direction and from 235 to 315 km in the north-south direction. The contour interval is 4 m s^{-1}.

higher analysis frequency (5-minute interval) and the LH scheme, 5B30E30LH produces the strongest main updraft of the OKC storm (Fig. 4.1d) among all four experiments, but the predicted OKC storm dissipates in about one hour (Fig. 4.8b). At the same time,

storm A, shown as a southern updraft, develops into a strong storm in the forecast instead dissipating as observed. The wrong behaviors of both the OKC storm and storm A and the extra strength of the updrafts indicate that too much potential energy (16.79×10^{16} J) had been added into both the storms. The over-loaded energy causes the OKC storm to develop too fast and dissipate too earlier, and the spurious intensification of storm A. The dissipation of the OKC storm might be caused by the low-level outflow from storm A. At the opposite end, using a lower frequency (10-minute interval) and the MA scheme, 10B30E30MA adds only about 1/8 of the potential energy as 5B30E30LH and the resulting updrafts are much weaker and smaller in size (Fig. 4.10c). Although storm A correctly dissipates quickly in the forecast, the predicted OKC storm intensifies very slowly in the entire 2.5 hours of forecast (Fig. 4.8a), indicating that too little potential energy has been added into the OKC storm. This slows the development of the OKC storm and delays the predicted storm entering dissipation stage.

The strength and area coverage of the updrafts of 10B30E30LH and 5B30E30MA are between those of 10B30E30MA and 5B30E30LH. As pointed out earlier, the forecast of 10B30E30LH on the OKC storm is the best among all experiments, while the forecast of 5B30E30MA is reasonably good, although both forecasts miss the dissipation stage of the OKC storm to some degree.

The above analyses clearly show that to obtain a good forecast, right combinations of the in-cloud temperature adjustment scheme and analysis frequency are necessary, given the length of the AW. When the analysis cycles are of 10 minutes long and spans over a one hour AW, the LH scheme outperforms the MA scheme. This is however opposite when 5-minute analysis cycles are used. In this case, the MA scheme

outperforms the LH scheme. Based on the analyses on the amount of potential energy added into the model by the assimilation procedure and the response of the model atmosphere in terms of storm evolution, it is clear that the right amount of energy input is the key in promoting and sustaining observed storms, yet not over-intensifying them, leading to good forecasts over the life cycle of the storm. Since the LH scheme tends to add more energy into the system than the MA scheme, the use of the LH scheme is generally preferred when analysis frequency is low (e.g., 10-minute), while the MA scheme is usually preferred when using 5-minute frequency. For this reason, most of the additional experiments to be examined next use the combinations of 5-minute interval and the MA scheme or 10-minute interval and the LH scheme (see Table 1).

4.2.2.4 Impact of the length and temporal coverage of assimilation window

In the earlier experiments of this section, the assimilations start about 10 minutes before the OKC storm initiation and cover the entire development stage of the storm. Here, ten additional experiments, classified into two groups, are conducted to study the impact of different lengths and coverage of AW (Table 4.1). For the first group of experiments, including 10B30E10LH, 10B30E20LH, 5B30E10MA, and 5B30E20MA, the assimilation starts at 2030, the same as the earlier four experiments, but ends at 2110 or 2120. The second group includes 10B40E30LH, 10B50E30LH, 10B60E30LH, 5B40E30MA, 5B50E30MA, and 5B60E30MA and their AWs all end at 2130 but start at 2040, 2050, or 2100. Both 5 and 10-minute assimilation frequencies are tested in these two groups. For brevity, we only show the summary reflectivity plots. Those for the first group of experiments are shown in Fig. 4.11 and those for the second group in Fig. 4.12.

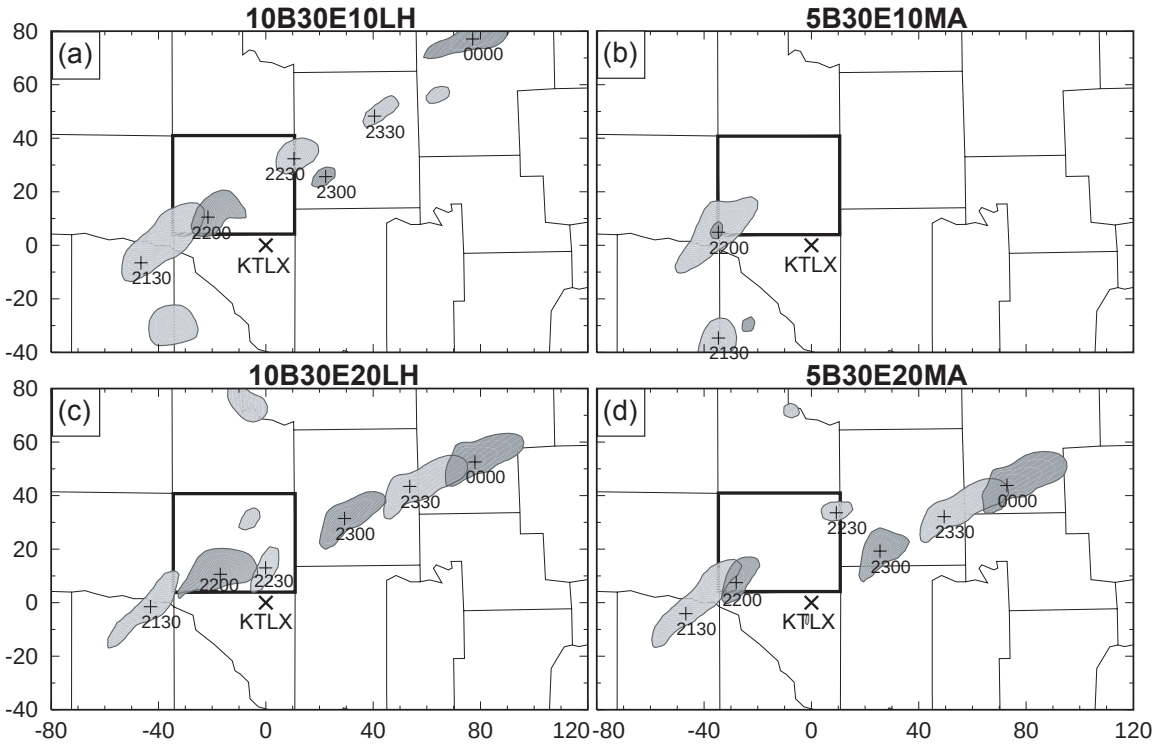

Fig. 4.11. As Fig. 4.3b, but for experiments 10B30E10LH (a), 5B30E10MA (b), 10B30E20LH (c), and 5B30E20MA (d).

As stated in the case introduction, the first echo of the OKC storm appeared at about 2040 and the echo exceeded 35 dBZ by 2101. From then on, the OKC storm grew quickly and developed into a strong supercell by 2131 (c.f., Fig. 4.2). The AWs of the first group of experiments mainly cover the early part of the development stage (from 2040 to 2110) of the OKC storm. In 10B30E10LH and 5B30E10MA, the first 30 minutes of storm life (2040-2110) is covered by the 40-minute AWs (2030-2110). The predicted storm in 5B30E10MA disappears completely after 2200, or 50 minutes into the forecast (Fig. 4.11b), while that in 10B30E10LH lasts until 2230 (80 minutes into the forecast) and has correct maximum echo locations at 2130 and 2200 (Fig. 4.11a). A spurious cell develops in 10B30E10LH, however, southeast of the OKC storm, and is visible from

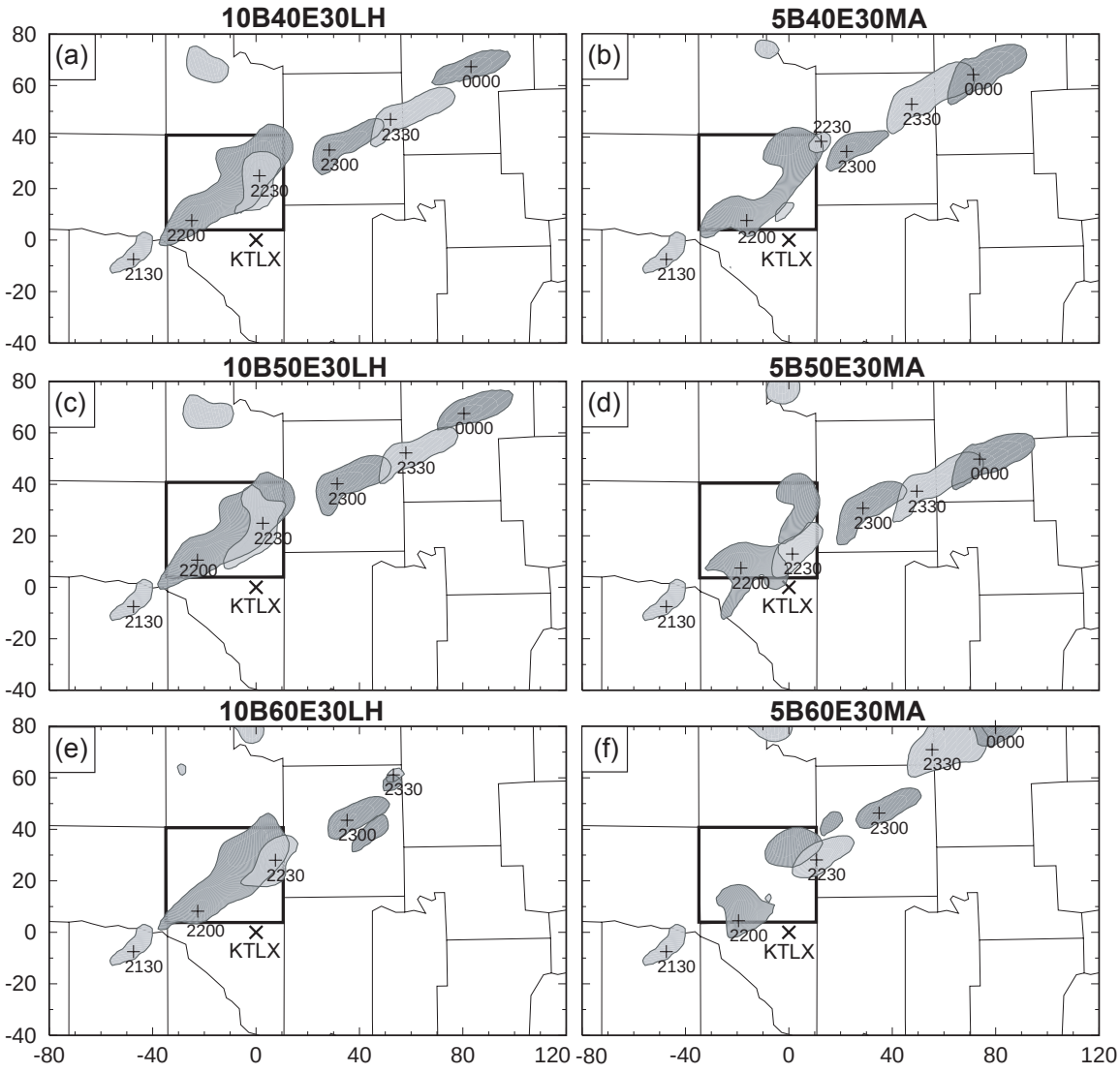

Fig. 4.12. As Fig. 4.3b, but for experiments 10B40E30LH (a), 5B40E30MA (b), 10B50E30LH (c), 5B50E30MA (d), 10B60E30LH (e), and 5B60E30MA (f).

2300 on. Obviously, the OKC storm is not fully built up by the assimilation and the spurious storm developing to its southeast probably has negative impact too.

When the AW is extended by 10 minutes in 10B30E20LH and 5B30E20MA, to 2120, now including more radar observations, the forecast is improved for both. The predicted OKC storm in 5B30E20MA lasts until 2230 and has better positioning at 2130 and 2200 (Fig. 4.11d). Similar to 10B30E10LH, a spurious cell also develops in the model and has become stronger than the OKC storm by 2300. The OKC storm later dissipates while this spurious storm becomes stronger. The forecast of 10B30E20LH is much better than that of 10B30E10LH and appears close to the best forecast, that of 10B30E30LH (Fig. 4.11a, c and Fig. 4.3b). A more detailed look at the forecast reflectivity fields every 5 minutes between 2200 and 2230 indicates that the predicted OKC storm actually dissipates quickly after 2200 while a new storm quickly develops in its place and propagates along the path of the observed OKC storm in the rest of the forecast.

The AWs of the second group of experiments mainly cover the later development stage, from 2100 to 2130, of the OKC storm. Although the AWs from 2040 to 2130 of 10B40E30LH and 5B40E30MA include all radar observations used in 10B30E30LH and 5B30E30MA, the forecasts of the former are worse than those of the latter (Fig. 4.12a, b, Fig. 4.3, and Fig. 4.5), mainly because of larger northwestward displacement errors at the later forecast times. These results indicate that, even though the first 10 minutes of the 3-km assimilation precede the initiation of the OKC storm therefore the availability of radar data, the additional period of AW is still beneficial. The spinning up of the 9-km solution at 2030 on the 3-km grid to arrive at a better forecast background for the 3-km analysis at

2040 must be the reason. When the AW is started even later, at 2050 or 2100, and includes only the later part of the development stage of the OKC storm, the predicted paths of the OKC storm in 10B50E30LH, 10B60E30LH, and 5B60E30MA deviate northward even more (Fig. 4.12c, e, f), while that in 5B50E30MA has correct direction but lags the observation by about 15 km at the end of forecast (Fig. 4.12d). There is also some discontinuous development around 2230 in 5B50E30MA.

The results of the two groups of experiments and those from 10B30E30LH and 5B30E30MA clearly suggest that an AW of about 1-hour long, covering the entire developmental stage of the OKC storm as well as a pre-storm period is necessary in this case to obtain a good analysis and subsequent forecast of the storm. When the AW is relatively short, covering the later part of the developing stage is more effective in building a sustainable storm in the model.

4.2.2.5 Results of experiment 5B60E30LH

It is found that experiment 5B60E30MA, which uses 5-minute analysis cycles over a 30 minute AW and the MA scheme, initializes the OKC storm that dissipates quickly (Fig. 4.12f). Another storm that develops to the southeast of the OKC storm maintains its intensity but propagates too far north. Experiment 5B30E30LH, which uses a 1-hour AW with 5-minute intervals and the LH scheme, produces a storm that develops too fast (Fig. 4.8b), apparently due to too much potential energy added by the LH scheme. Based on these observations, a new experiment, 5B60E30LH, is performed, which is the same as 5B60E30MA except for the LH scheme used. The question to ask is: when the assimilation window is short, can the extra potential energy afforded by the LH scheme help sustain the initialized storm?

The results of 5B60E30LH are shown in Fig. 4.13. Compared to 5B60E30MA, 5B30E30LH, and the observations (Fig. 4.13, Fig. 4.12f, Fig. 4.8b, and Fig. 4.3a), 5B60E30LH captures the general evolution and propagation of the OKC storm rather well and the storm remains a strong supercell up to the end of the 2.5 hours of forecast. The significant improvement in the forecast of 5B60E30LH, when compared to 5B60E30MA, reflects the importance of a proper combination of assimilation parameters, especially when certain parameters, such as the AW length, are constrained by practical limitations, such as those found with real time applications. In the case of 5B60E30LH, the insufficient AW length can be compensated by using a temperature adjustment scheme that adds more energy into the system than can otherwise be justified. In real time applications where the truth is unknown and data and computational constraints exist, careful consideration and setup of the assimilation systems according to the findings of experiments like ours are necessary, at least when using similar methods as used here.

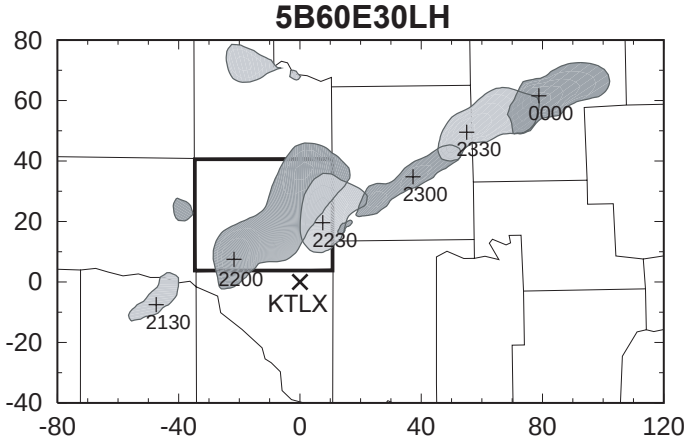

Fig. 4.13. As Fig. 4.3b, but for experiment 5B60E30LH.

4.2.3 Further discussions

In this section, the ARPS 3DVAR and cloud analysis procedures are successfully applied to the analysis and prediction of the 8 May 2003 Oklahoma City tornadic thunderstorm case, using an intermittent procedure that assimilates the scan volumes of the Oklahoma City WSR-88D Doppler radar (KTLX) with proper assimilation configurations.

A 3-km grid nested within a 9-km grid is used for both assimilation and forecast. The model storm in the 3-km grid is established through the intermittent assimilation cycles. For each analysis, the 3DVAR is used to analyze conventional observations and radial velocity data, in a similar way as used in Chapter 3, and the cloud analysis is performed to analyze reflectivity data. Forecasts for up to 2.5 hours are performed starting from the assimilated initial conditions, and their quality is used to evaluate the performance of assimilation.

A total of fifteen 3-km experiments with different assimilation configurations are conducted to study the impact of the analysis frequency, in-cloud temperature adjustment scheme, and the length and coverage of the assimilation window (AW) on the final analysis and forecast.

The best forecast for the OKC storm comes from the experiment that uses a one-hour long AW with 10-minute analysis cycles and an in-cloud temperature adjustment scheme that is based on latent heat release related to the input of cloud condensate, or the LH scheme. The experiment accurately predicts the propagation of the OKC storm with position errors of less than 8 km throughout the 2.5 hours of forecast, in terms of the maximum reflectivity center of the main storm. The supercell characteristics of the storm

during the forecast are also well captured even though the grid spacing of the experiment is 3 km, which is relatively coarse for the purpose of resolving the tornado vortex or even the mesocyclone. The predicted midlevel and low-level fields show a column of strong vorticity associated with the predicted OKC storm during the entire forecast.

It is interesting to note here that a preliminary study by Wicker and Dowell (2004) performed an assimilation and prediction study on this same case. The theoretically more advanced ensemble Kalman filter (EnKF) method is used, using a 1-km horizontal resolution and assimilating six scan volumes of an experimental WSR-88D radar (KOUN) located in Norman, Oklahoma. The assimilation spans over nearly 40 minutes. The radar reflectivity field at the end of assimilation looks very close to the observed one, and the wind fields appear dynamically consistent too, and probably more so than the analyzed fields in our experiments. Unfortunately, the predicted storm in the case does not last beyond 40 minutes of the forecast. Apart from the assimilation methods used, another significant difference between our and their studies lies in the fact that a single sounding is used to define the storm environment in their case - the representativeness of this time-invariant environment may be a cause of the less successful prediction. Further, our experiments employ a full physics package rather than cloud physics only.

When a higher assimilation frequency, that is, once every 5 minutes, is used with a 1-hour AW and the moist-adiabat (MA) scheme (in 5B30E30MA), the quality of the forecast is worse than the control experiment (10B30E30LH) with 10-minute intervals and the LH scheme, even though more radar observations are assimilated in the former. This behavior is partly related to the capabilities of our analysis scheme. The correlation among different analysis variables or the balance among them is not considered in either

the ARPS 3DVAR or cloud analysis, even though the latter employs a cloud physics model to determine the cloud and hydrometeor contents. Starting from such initial conditions that are not in balance with the prediction model, significant adjustment occurs within the initial period of prediction. This is clearly seen from the time series of maximum vertical velocity. It is found that the model almost always requires more than 5 minutes to complete the initial adjustments and a 10-minute analysis interval is needed to give the model enough time to establish balance among the model fields and to build a sustainable storm. When more advanced analysis methods that can produce well-balanced analysis fields, such as the ensemble Kalman filter and the 4DVAR methods, are used, the more data are assimilated, the better the final analysis should be. This is shown to be true in Xue et al. (2005) through OSSEs (Observing System Simulation Experiments) that the assimilation of 1-minute volume scans produces better results than volume scans taken at lower frequencies, for a supercell storm.

The impact of two in-cloud temperature adjustment schemes available in the ARPS cloud analysis procedure is also studied. The experiments show that the assimilation (5B30E30LH) using the latent heating-based (LH) scheme at 5-minute intervals over a 1-hour AW adds too much potential energy into the storm system, which causes a too fast development of the main storm and the triggering and intensification of a spurious cell. On the other hand, the assimilation using the moist-adiabat based (MA) scheme with 10-minute intervals over the same length of AW adds too little potential energy instead, which delays the development of the main storm during the assimilation and forecast. A combination of 10-minute analysis intervals with the LH scheme or 5-minute intervals with the MA scheme is found to work the best for 1-hour long AWs

because both combinations can add an suitable amount of potential energy during the assimilation and produce a reasonable forecast for the OKC storm. But we also found that the former combination is better than the latter because the model needs more than 5 minutes to complete initial adjustment, as explained in detail earlier.

The experiments testing the impact of the lengths and coverage of the AW are also interesting. It is found that taking only 10 minutes out of the 1-hour long AW either at the beginning or the end can significantly reduce the forecast quality of the main storm, and in general the shorter the AW, the worse the forecast. In practice, it is desirable to use an AW that is as short as possible, in order to have an as-long-as-possible forecast lead time, and in this case a long lead time for forecasting the storm behaviors at the tornado outbreak. Our experiments also indicate that an AW of at least 30 minutes is necessary. In Chapter 3, the 28 March 2000 downtown Fort Worth tornadic thunderstorm case, a lead time of over one hour is achieved for the prediction of strong low-level rotation that appears to be closely linked to the observed tornadogenesis.

To see what we can do with a 30 minute AW located in the later stage of the storm development, experiment 5B60E30MA which produces an OKC storm that is too weak and dissipates quickly, is repeated using the LH scheme in 5B60E30LH. As expected, the extra heating added by the LH scheme accelerates the development of the main storm in the assimilation and the subsequent forecast of the OKC storm is as a result rather good. Compared to 10B30E30LH, the shortened AW is compensated by about twice as many analysis cycles. Since the LH scheme has a tendency to add an amount of heating that is somewhat independent of the background state, the total amount of heating added tends to be proportional to the number of analysis cycles, hence the observed

behavior. Such results are also consistent with the analysis on the temperature adjustment by Chapter 3.

The above conclusions are mainly based on the 8 May 2003 Oklahoma City tornadic storm case, although some have also been drawn from our earlier study on the Fort Worth tornadic thunderstorm case. The quantitative aspects may also be tied to the specific analysis schemes used, that is, the ARPS 3DVAR and cloud analysis. A general conclusion is that the assimilation configurations can significantly impact the results of radar data assimilation and subsequent storm forecast. The configurations should be carefully evaluated and tested, in a similar but perhaps even more thorough way than is done here. When continuous assimilation cycles are used, at, say, 5-minute intervals, the optimal AW length and coverage are still an issue for a given scheme. The experiments on AW coverage provide us with some guidance on the design of post-real-time assimilation experiments, and for real time applications provide some guidance on the results we can expect.

Even though theoretically less than optimal, the current intermittent assimilation procedure for incorporating full-volume Doppler radar data into a storm prediction model is computationally inexpensive and operationally feasible. For real time operational applications, the computation efficiency of a configuration may carry more weight. When similar forecast qualities are obtained, an assimilation configuration that requires the least amount of data processing and computation, and provides the longest forecast lead time for the features that we are most interested is obviously preferred, and such a configuration may be one of the choices even if the resultant prediction is slightly worse. Future, similar issues for other types of convective systems, such as the less persistent

multi-cellular storms and the larger scale squall line and MCCs (mesoscale convective complexes) should also be investigated.

4.2.4 Summary

Finally, we briefly summarize the key results of this section as follows.

1) The ARPS 3DVAR and cloud analysis procedure are applied to the 8 May 2003 Oklahoma City tornadic thunderstorm case in a cycled mode on a 3-km grid. Volume scans of data from the OKC WSR-88D radar are assimilated.
2) Successful predictions are obtained by using several different combinations of analysis cycle interval, AW length, and in-cloud temperature adjustment scheme. Experiment with 10-minute interval, 1-hour AW, and the LH temperature adjustment scheme (10B30E30LH), experiment with 5-minute interval, 1-hour AW, and the MA scheme (5B30E30MA), and experiment with 5-minute interval, 30-minute AW, and the LH scheme (5B60E30LH) all produce reasonable forecasts for up to 2.5 hours, with the forecast of 10B30E30LH being the best.
3) The configuration of 5B30E30MA is theoretically the best, because all radar scan volumes within an AW that covers the entire development period of the main storm are used, together with a temperature adjustment scheme that is based on a simple cloud physics model and is less sensitive to the number of cycles applied because it makes only the adjustment necessary to fit a diluted moist adiabat (Brewster 2002; Hu *et al.* 2006b).
4) The configuration used by 5B60E30LH has a shorter AW therefore has a lower computational cost and allows for a longer forecast lead time. The reduced AW length is compensated by the extra potential energy input provided by the LH

scheme, resulting in a reasonably well developed storm by the end of AW.

5) Due to significant adjustment in the forecast following each analysis, shorter assimilation cycles does not necessarily produce better final analysis. 10-minute cycles that assimilate every other scan volumes are found to work better.
6) A short spin-up period (~10 minutes) on the high resolution grid before any radar data are available is found to be beneficial.
7) When the AW length is limited, to e.g., 30 minutes, an AW at the later part of the development stage of storm is more effective than that applied at the early part, although difference in the actual time of the initial condition of forecast may have also played a role.

4.3 High resolution experiments

In the previous sections, we found that for the 8 May 2003 case, the current ARPS model can capture well the propagation and general evolution of the tornadic thunderstorm up to 2 hours into forecast, using a 3-km horizontal resolution when starting from an initial condition into which radar data are properly assimilated. However, with a relatively coarse 3-km grid spacing, the forecasts miss many important details of the tornadic features, such as the hook echo and mesocyclone, which are indicative of the tornadic activities or potential. In this section, experiments with higher resolutions are conducted with the hope of being able to resolve more of the tornadic features or even the tornado itself. Additional rationales for this study are listed as follows:

- The observation resolution of the operational WSR-88D Doppler radar is 1-km for reflectivity and 250-m for radial velocity along the radial beams and 1º in the azimuth direction. In the assimilations using a 3-km horizontal

resolution, many detailed structures of thunderstorms are smoothed out by the data preprocessing and the analysis. When a smaller grid spacing, such as 1-km or smaller, is used, more detailed structures can be resolved and the high-spatial resolutions of the radar data can be better taken advantage of. The impact of radar data and assimilation configurations on the storm forecast may also be different from what we found at the coarser 3-km resolution.

- Sub-kilometer resolution is usually believed to be necessary (e.g., Bryan *et al.* 2003) in order to properly resolve the internal structures in thunderstorms. So far, prediction and simulation experiments of real convective systems at sub-kilometer resolutions have been few. In this section, we examine the sensitivity of the data assimilation and prediction to the model resolution.
- When small-scale features such as mesocyclones or even tornados are resolved and simulated realistically, the model data at high spatial and temporal resolutions can be analyzed to help us better understand the mechanisms of the initiation and development of these important features.

For the above reasons, 1-km and 100-m horizontal-resolution experiments for the 8 May 2003 OKC tornado case are discussed in the following 2 subsections, respectively, with each of which containing subsections on experimental design, results, and summary.

4.3.1 Experiments with 1-km horizontal grid spacing

4.3.1.1 Experimental design

Similar to the 3-km experiments for the 8 May 2003 OKC tornadic thunderstorm case, the data from Oklahoma City WSR-88D radar (KTLX) are first preprocessed onto

the 1-km grid and then used in data assimilation cycles. The low-level observations from the same radar are used to evaluate the results of assimilation and forecast.

All 1-km experiments are one-way nested within the 3-km control experiment described in the previous sections of this chapter. The 1-km grid is 280 km × 280 km in size and covers central and northern Oklahoma. The vertical grid configuration is the same as the 3-km experiments of this case, with the grid stretched from 20 m at the surface to about 770 m at the model top that is located at about 21 km height.

In 1-km control experiment, CNTL1km, radial velocity data are analyzed using the ARPS 3DVAR, while reflectivity data are used through the cloud analysis procedure. Five-min intermittent assimilation cycles are performed within a 70-min long assimilation window from 2030 to 2140 UTC. The temperature adjustment scheme based on the moist adiabatic temperature profile (MA scheme, Hu et al. 2006a) is used in the cloud analysis scheme. The mass divergence constraint is not imposed on the 3DVAR analysis of radial velocity except in the last 2 analysis cycles at 2135 and 2140 UTC in which a 2D divergence constraint is used with a weighting coefficient of 1000. Basically, the assimilation configurations of the 1-km control experiment are the same as those of 3-km experiment 5B30E30MA except for the use of the mass divergence constraint in the last 2 cycles and the 10-min longer assimilation window. To eliminate negative impacts of the storm south of the OKC tornadic thunderstorm (storm A, c.f. Fig. 4.2) on the assimilation, the reflectivity and radial velocity data associated with that storm are not included in the assimilation. Also, only reflectivity data exceeding 40 dBZ are used in the cloud analysis so as to avoid introducing weak cells that tend to grow spuriously in the model. Starting from the assimilation results, a 140-min forecast is made.

Three additional experiments are conducted, namely, Div2D1km, NoDiv1km, and CNTLZ1km. Experiment Div2D1km employs a 2D mass divergence constraint in all analysis cycles, while experiment NoDiv1km does not include the mass divergence constraint at all. They are designed to study the impact of the mass divergence constraint on the storm structures in the forecast at a higher spatial resolution. Data denial experiment CNTLZ1km excludes the radial velocity data, and is intended to isolate the effects of such data. Otherwise, the settings of these experiments are the same as control experiment CNTL1km.

4.3.1.2 Experiment results

4.3.1.2.1 Results of data assimilation

The analyzed radial velocity and reflectivity fields from CNTL1km, valid at 2135 UTC and mapped to the 1.45º elevation of the KTLX radar are plotted in Fig. 4.14, together with the corresponding 2136 UTC observations of the same radar.

At 2136 UTC, the southwestern end of the observed OKC storm showed a hook-shaped echo that was colocated with a strong cyclonic vortex center, as indicated by a strong radial velocity gradient at about (-54 km, -18 km) (Fig. 4.14a, b). Also, a strong left-moving split cell existed due north of the main OKC storm.

The 2135 UTC analysis of CNTL1km correctly captures the main OKC storm, but the hook-shaped echo and the smaller left-moving cell are nearly absent (Fig. 4.14d). The use of only reflectivity data exceeding 40 dBZ is part of the reason for missing weaker features and smaller-scale structure; the smoothing to the hydrometeor fields in the cloud analysis is another contributor. On the other hand, the analyzed radial velocity field closely replicates the pattern and intensity of the observed cyclonic vortex center

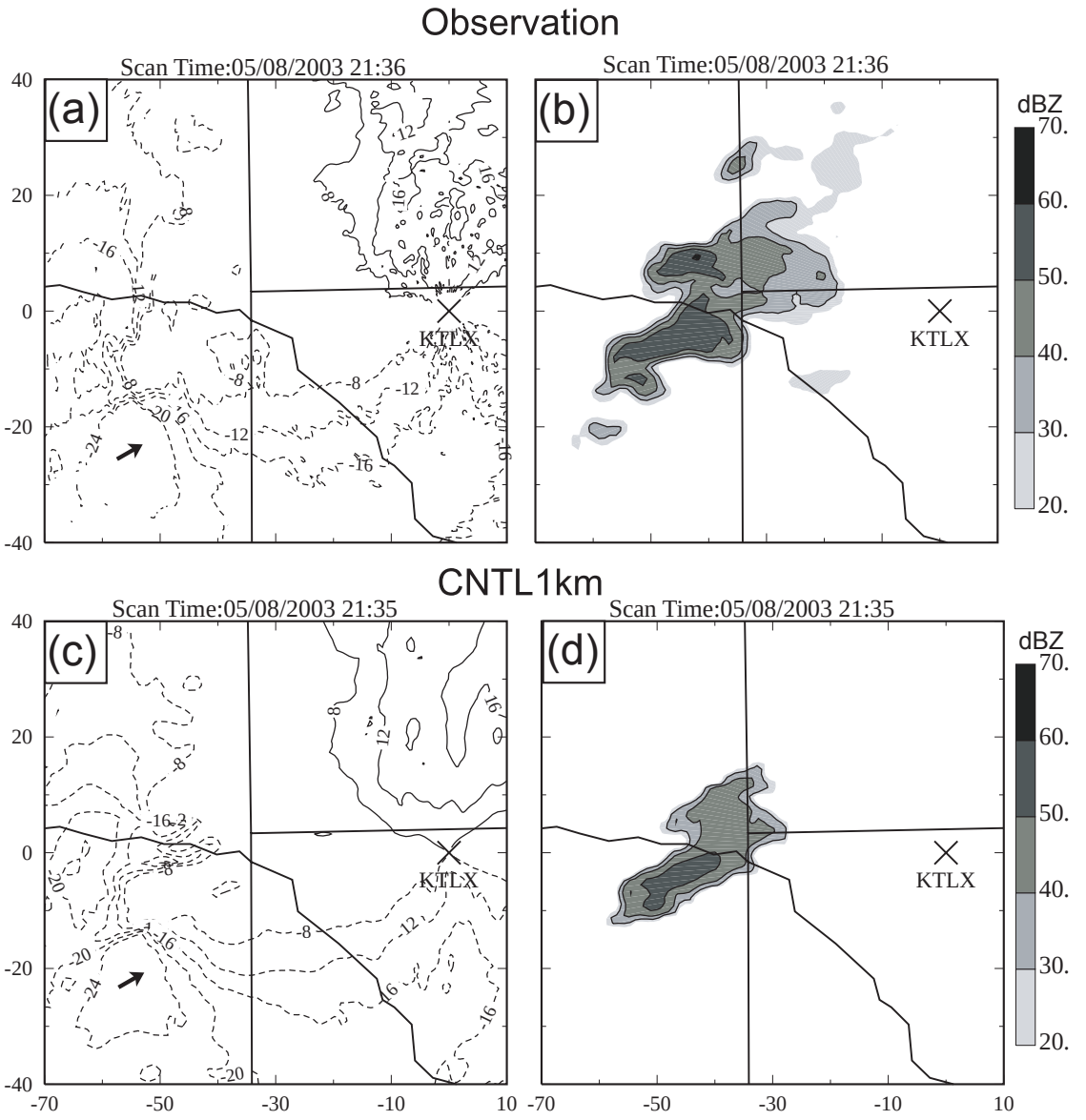

Fig. 4.14 The observed radial velocity and reflectivity fields at 2136 UTC from the KTLX radar at the 1.45º elevation (upper panels) and the corresponding fields from the 2135 UTC CNTL1km analysis mapped to the same elevation (lower panels). The x and y distances are in kilometer and are relative to the KTLX radar marked by '×'. Positive radial velocity values are contoured as solid lines from 8 to 24 m s^{-1} with 4 m s^{-1} intervals and negative as dashed lines from -24 to -8 m s^{-1} with the same intervals. The reflectivity values are plotted as shaded contours at 30, 40, 50, and 60 dBZ. The domain shown is 80 km on each side, representing to the portion of the1-km grid between 70 and 150 km in the east-west direction and from 50 to 130 km in the north-south direction. The short arrows in radial velocity panels show the direction of radial velocities near their peak value.

and the environmental winds (Fig. 4.14c).

The analyzed radial velocity fields at 2135 UTC from experiments CNTLZ1km, Div2D1km, and NoDiv1km are plotted in Fig. 4.15. The analyzed reflectivity fields of these experiments are the same as that in Fig. 4.14d because the same data and cloud analysis procedure are used.

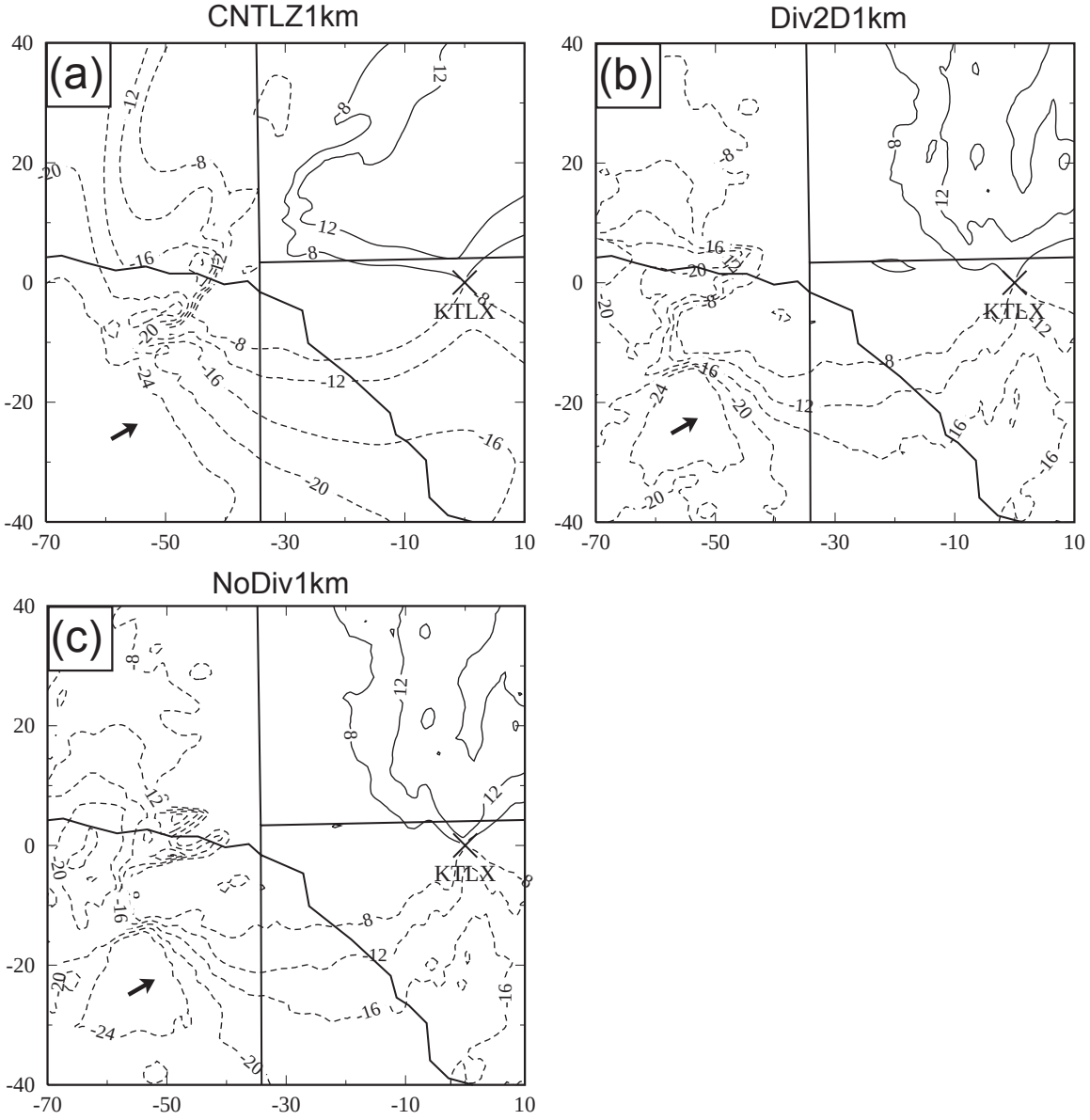

Fig. 4.15 Similar to radial velocity part of Fig. 4.14, except that they are analyzed radial velocity at 2135 UTC from experiments CNTLZ1km, Div2D1km, and NoDiv1km.

The analyzed radial velocity fields Div2D1km and NoDiv1km also show similar patterns of the cyclonic rotation center and of the environmental winds as the observed ones despite the difference in the use of the mass divergence constraint (Fig. 4.15b, c). When the radial velocity data are not used, as in CNTLZ1km, the analyzed radial velocity field is much smoother and loses the cyclonic vortex center at the southwestern end of the OKC storm entirely (Fig. 4.15a). The environmental flow pattern also deviates from the observations more, at this and other levels (latter not shown).

Clearly, the analysis of radial velocity via the 3DVAR is able to provide detailed flow structures on the 1-km grid.

4.3.1.2.2 Forecasting results

4.3.1.2.2.1 Maximum surface vertical vorticity

To examine the intensity of low-level rotation, the time series of the predicted maximum vertical vorticity at the surface in the OKC storm are plotted (Fig. 4.16) for the first hour of forecast for experiments CNTL1km, CNTLZ1km, Div2D1km, and NoDiv1km.

For all three experiments that assimilate radial velocity data, the maximum surface vorticity before 2205 UTC exhibits some oscillations, with increases that reach up to 0.014 s^{-1} but all reach a minimum value blow 0.006 s^{-1} at around 2205 UTC. During the second period from 2205 to 2240 UTC, which covers the OKC tornado outbreak, the maximum surface vorticity in CNTL1km rapidly increases to a high value of about 0.013 s^{-1} within about 5 minutes and remains above 0.009 s^{-1} for about 20 minutes, while those of Div2D1km and NoDiv1km remain mostly below 0.007 s^{-1}. An examination of the surface vorticity fields of CNTL1km shows that the maximum values between 2148 and

2155 UTC correspond to one vorticity center while those between 2110 and 2130 UTC correspond to another.

For experiment CNTLZ1km, in which radial velocity data are not analyzed, the maximum surface vorticity is always much lower than those of the other three experiments, indicating the important impact of the radial velocity analysis on the formation of strong low-level vorticity centers.

Guided by the above analysis of the maximum surface vorticity, we discuss the forecast fields in the first and second periods, respectively.

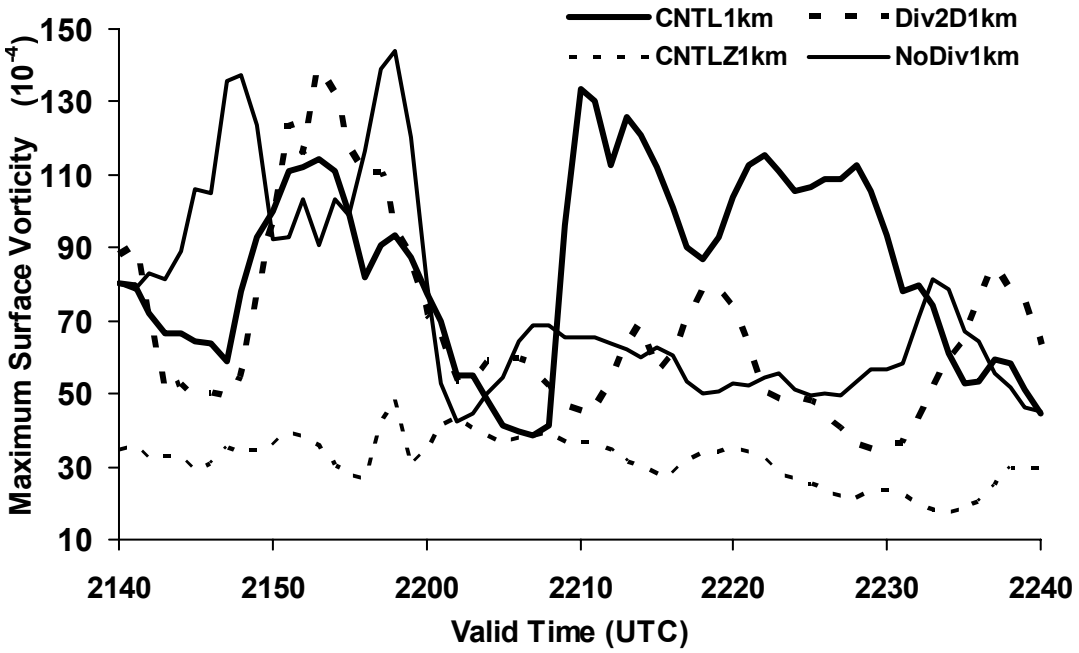

Fig. 4.16 Maximum surface vertical vorticity in the predicted OKC tornadic thunderstorm during the first hour of forecast for experiments CNTL1km, CNTLZ1km, Div2D1km, and NoDiv1km.

4.3.1.2.2.2 Forecast in the first period

The predicted radial velocity and reflectivity fields 10 minutes into the forecast from CNTL1km, CNTLZ1km, Div2D1km, and NoDiv1km are shown in Fig. 4.17. As before, the fields are mapped to the 1.45º elevation of the KTLX radar, and the corresponding observed fields at 2151 UTC are also plotted.

Comparing the observations at 2136 (Fig. 4.14a, b) and 2151 UTC (Fig. 4.17a, b), it can be seen that the observed OKC storm propagated east-northeastward by about 10 km in this 15 minutes period. The main storm had a weak hook-shaped echo at its southwestern end and a strong left-moving split cell to its north (Fig. 4.17b). The low-level cyclonic rotation at its southwestern end became weaker than 15 minutes ago but was identifiable, with its center located at (-42 km, -10 km) (Fig. 4.17b).

At 2150 UTC, the 10-minute forecast of CNTL1km captures well the main part of the OKC storm in terms of the reflectivity pattern (Fig. 4.17d). The low-level cyclonic rotation is also evident (Fig. 4.17c), with a sharp hook-shaped echo found at the southwestern end of the storm and a clear cyclonic radial velocity couplet found near (-40 km, -5 km). The rotation actually appears stronger in the forecast than in the observation. The weaker, left-moving cell is also present in the prediction, but is attached to instead of being separate from the main cell.

Experiment CNTLZ1km overpredicts the propagation of the main storm during the same period, and misses the cyclonic rotation at the southwestern end (Fig. 4.17e, f). Instead, a small anticyclonic feature centered at around (-35 km, 0 km) is identifiable in both reflectivity and radial velocity fields. The left-moving cell is completely missing.

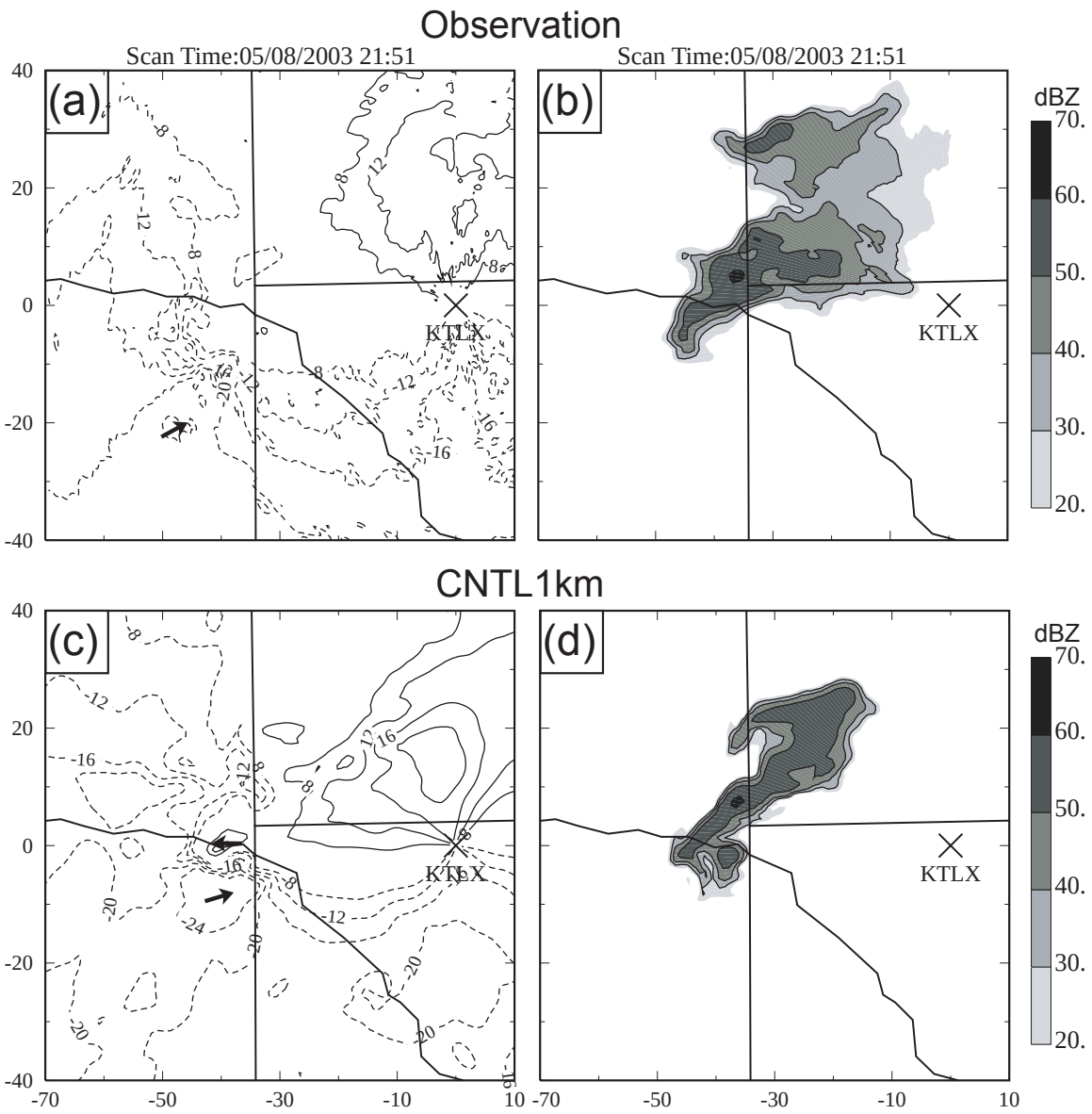

Fig. 4.17 Similar to Fig. 4.14, except that they are observations at 2151 UTC and 10-minute forecast from experiments CNTL1km, CNTLZ1km, Div2D1km, and NoDiv1km.

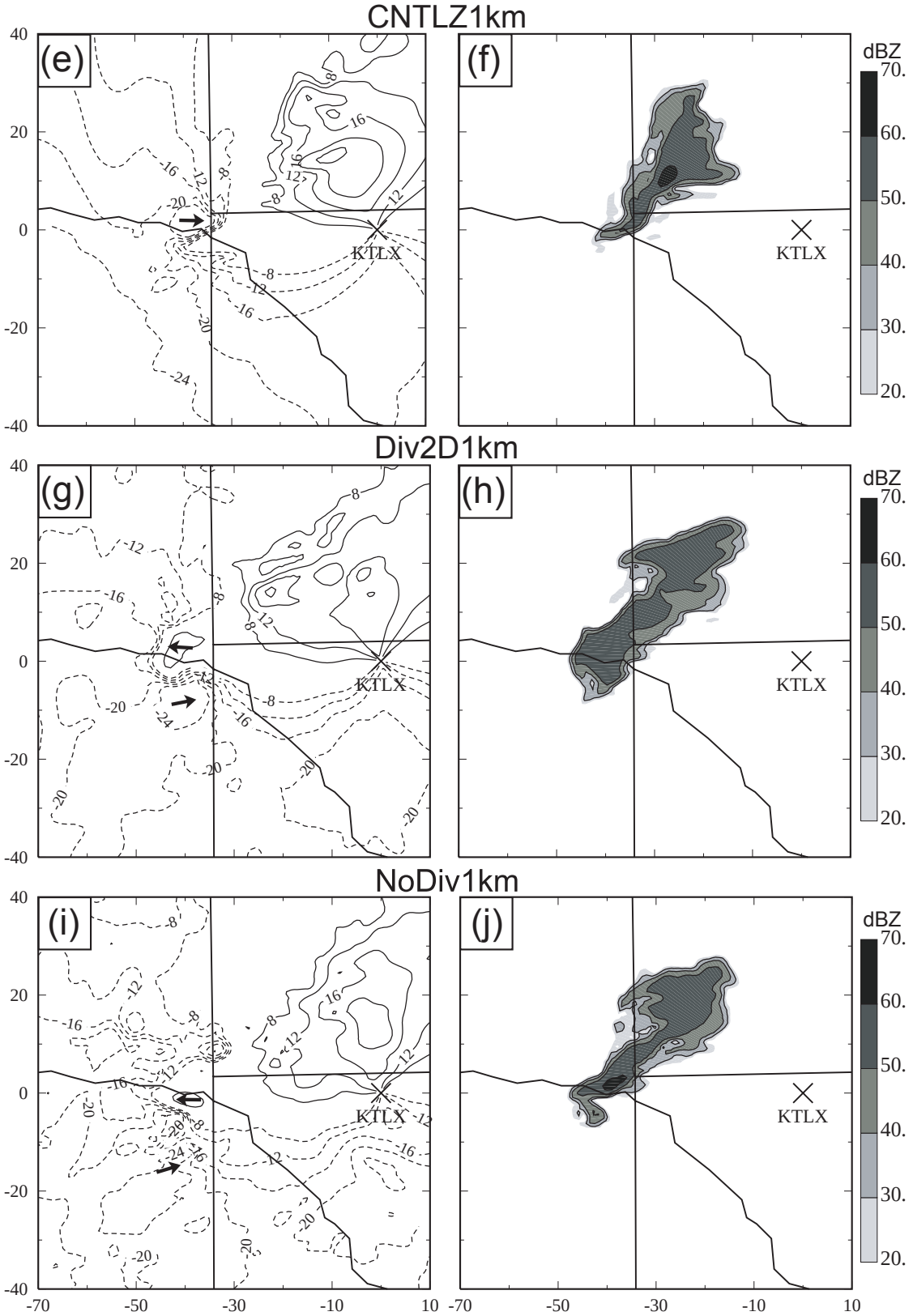

Fig. 4.17 Continue

Div2D1km and NoDiv1km differ from CNTL1km only in the use of the mass divergence constraints. Their forecasts are similar to that of CNTL1km but with some small differences (Fig. 4.17g-j). The hook-shaped echo of the main storm is not captured by Div2D1km (Fig. 4.17h). A cyclonic radial velocity couplet is captured in the forecasts of both Div2D1km and NoDiv1km, as is in CNTL1km, but the radial velocity field of the former is much smoother because of the use of a 2D mass divergence constraint, while that of the latter is much noisier because of the absence of any mass divergence constraint (Fig. 4.17c, g, i).

The above analysis indicates that the initial low-level cyclonic rotation analyzed using the 3DVAR with radial velocity data is spun up during the first 20 minutes of forecast on the 1 km grid. The use of radial velocity data in the assimilation noticeably improves the quality of the short-term forecast for the main storm in terms of both wind and reflectivity fields.

4.3.1.2.2.3 Forecast in the second stage

The maximum surface vertical vorticity in CNTL1km shows large values from 2210 to 2230 UTC which partially coincide with the occurrence of the tornado from 2210 to 2238 UTC of that day. To evaluate the forecast in terms of the tornadic features such as mesocyclone and hook echo, the observed reflectivity fields at the 1.45º elevation of the KTLX radar (left column) and the corresponding predicted reflectivity fields from CNTL1km (right column) are plotted in Fig. 4.18, at 5-minute intervals from 2210 to 2230 UTC. The corresponding radial velocity fields are plotted in Fig. 4.19.

The observed reflectivity field of the OKC storm at 2211 UTC showed a hook-shaped echo at its southwestern end (Fig. 4.18a), indicating the presence of a tornadic

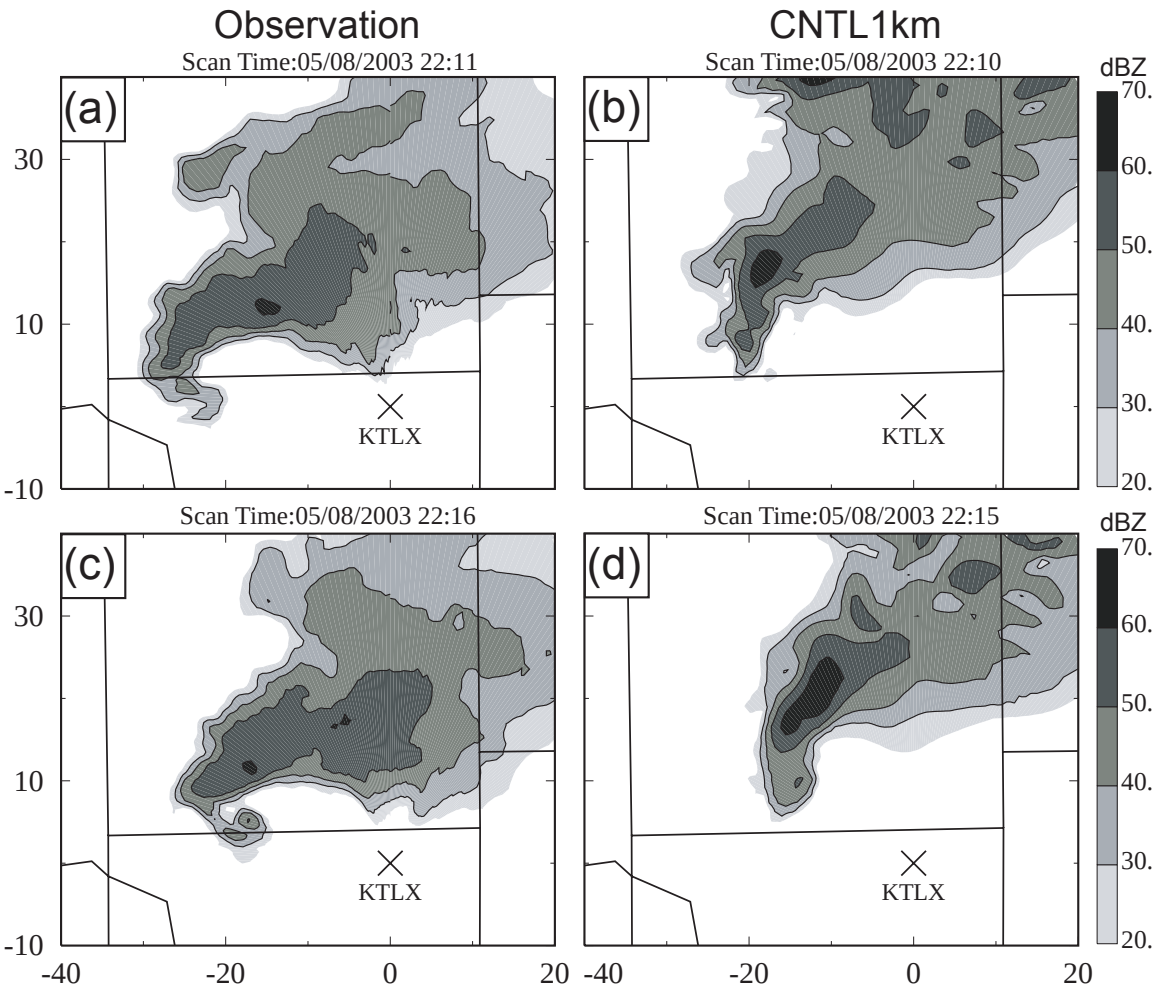

Fig. 4.18 The observed reflectivity fields at the 1.45º elevation of the KTLX radar (left column), and the predicted reflectivity fields at the same elevation from experiment CNTL1km (right column), at 5-minute intervals from 2210 to 2230 UTC 8 May 2003. The x and y distances are in kilometer and are relative to the KTLX radar marked by X. The reflectivity contours are at 30, 40, 50, and 60 dBZ. The domain shown is 60 km by 50 km, representing the portion of the 1-km grid between 102 and 162 km in the east-west direction and from 80 to 130 km in the north-south direction.

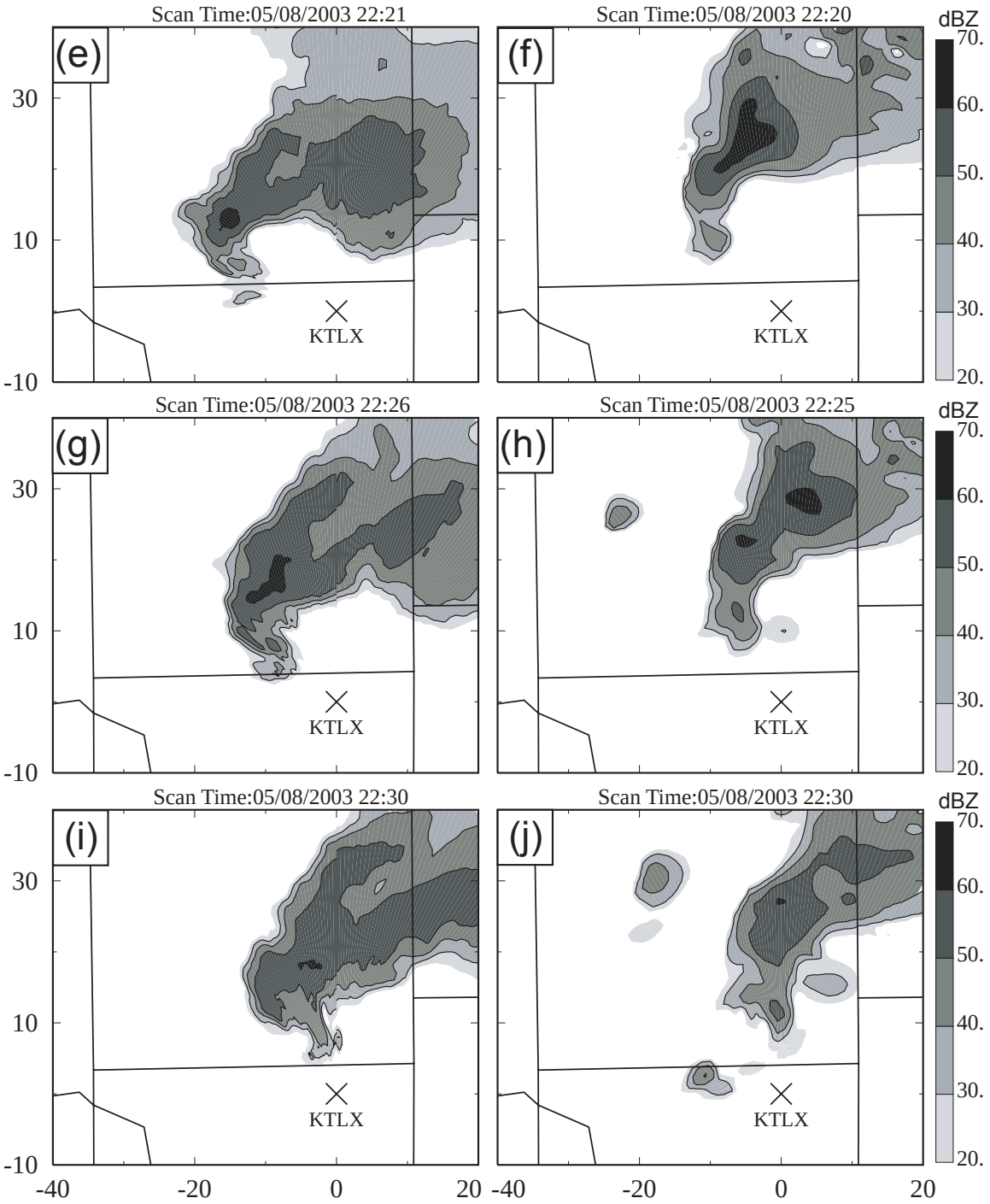

Fig. 4.18 Continue

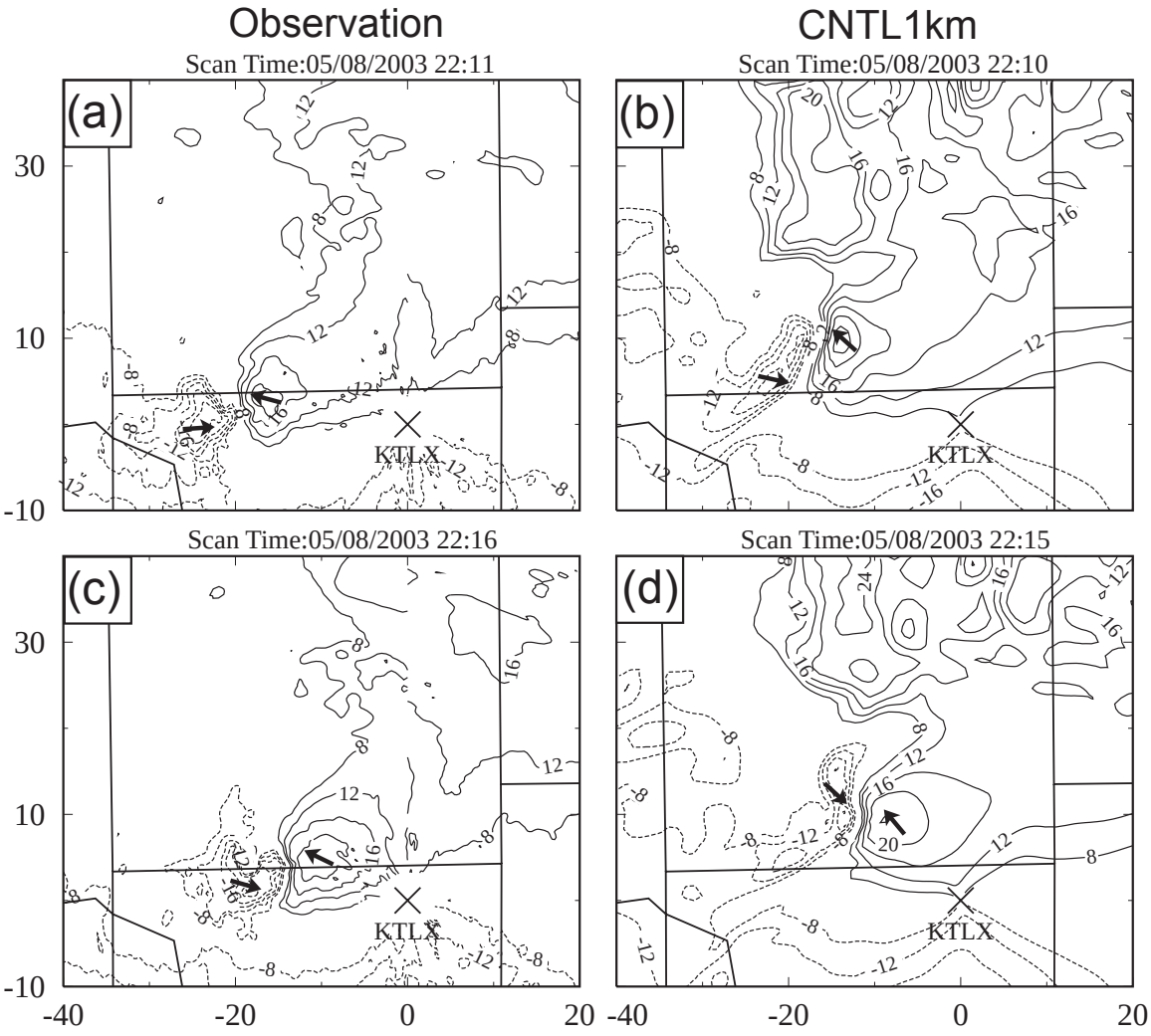

Fig. 4.19 The observed radial velocity fields at the 1.45º elevation of the KTLX radar (left column), and the predicted radial velocity fields at the same elevation from experiment CNTL1km, at 5-minute intervals from 2210 to 2230 UTC 8 May 2003. The domain and x and y coordinates are same as Fig. 4.18. The positive radial velocity is contoured as solid lines from 8 m s^{-1} to 24 m s^{-1} with 4 m s^{-1} intervals and negative as dashed lines from -8 m s^{-1} -24 m s^{-1} with the same intervals. The short arrows show the direction of radial velocity in their maximum value area.

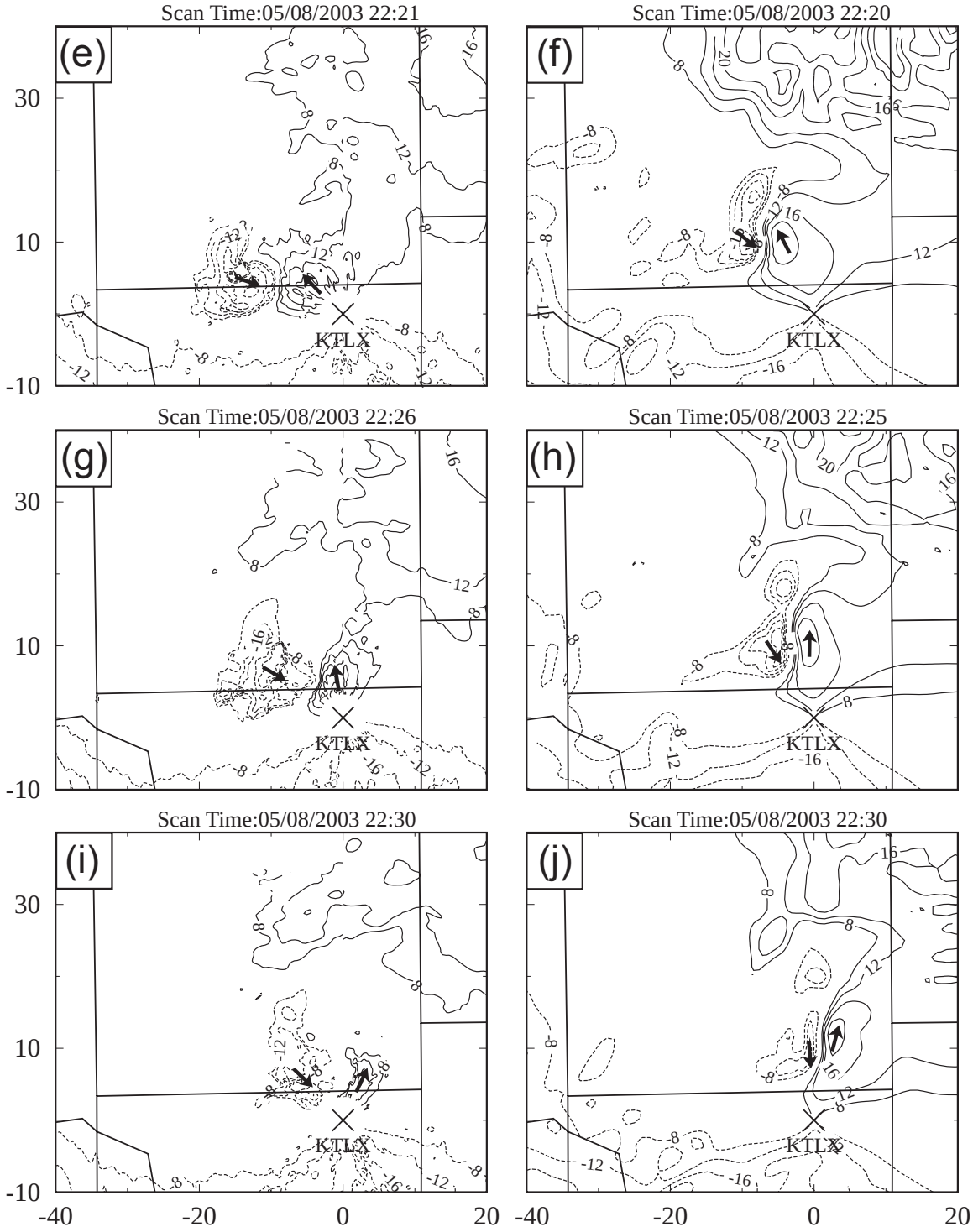

Fig. 4.19 Continue

circulation. In the next 20 minutes, the main OKC storm propagated east-northeastward, maintaining the, although weaker, hook echo (Fig. 4.18c, e, g, i). The forecast of the main OKC storm propagates in the similar direction and speed as the observed one did but with about 10-km northeastward displacement error throughout the period. The most interesting feature of the predicted storm is that it also develops and maintains a hook echo at its southwestern end (Fig. 4.18b, d, f, h, j), although the hook is not as sharply defined as in observations.

In the observation of 2211 UTC, a strong mesocyclone-scale radial velocity couplet was found colocated with the hook echo (Fig. 4.19a, Fig. 4.18a). From 2211 to 2230 UTC, this velocity couplet moved mainly eastward, approaching the KTLX radar with a slight northward component, and became weaker and less organized (Fig. 4.19a, c, e, g, i). However, the damage survey of the OKC tornado indicates that the tornado became stronger during these 20 minutes. One possible reason for this discrepancy is that when the mesocyclone approached the KTLX radar from the 25 to 5 km in radial range, the height of the observed mesocyclone at the 1.45° elevation decreased from 630 m to 127 m. The mesocyclone became weaker and less organized in near surface level because of fraction and turbulence.

At 2210 UTC, CNTL1km predicts a strong cyclonic radial velocity couplet located about 10 km northeast of the observed one and also colocated with the predicted hook echo (Fig. 4.19a, b, Fig. 4.18b). The predicted couplet then propagates mostly eastward at a similar speed as the observed one (Fig. 4.19b, d, f, h, j); it remains strong and well-defined up to 2225 UTC and becomes weaker afterwards. In the predicted radial velocity fields, large unobserved perturbations exist in the northeastern part of the

domain. These perturbations are associated with the split left-moving cells in the model that split later and evolve slower than the observation; the observed left mover was out of the domain at these times.

The above analysis shows that the mesocyclone associated with the OKC tornado is captured by CNTL1km at the right time and about the right place. To further study the vertical structure of this mesocyclone, vertical vorticity and wind fields at the surface, 1 km, 2 km, and 3 km MSL from the 35-minute forecast are plotted in Fig. 4.20. At the surface, a strong isolated vorticity center with a maximum value of 0.011 s^{-1} is located at the center of the radial velocity couplet discussed earlier (Fig. 4.20a and Fig. 4.19d). Immediately northeast of the vorticity center is a strong surface convergence center, indicating the presence of a strong updraft adjacent to the vorticity center. At 1 km and 2 km MSL, strong vorticity centers with maximum values of over 0.02 s^{-1} are located right above the surface one. At 3 km MSL, the vorticity center is still strong with a maximum value of 0.025 s^{-1} but is located slightly north of the low-level ones. Clearly, the predicted mesocyclone extends through the lower levels of atmosphere and suggests a high possibility of tornadogenesis but the 1-km grid spacing is too coarse to resolve the tornado itself.

To analyze the results of the other three experiments, the predicted radial velocity and reflectivity fields at the 1.45º elevation from the 30 and 40-minute forecasts (valid at 2210 and 2220 UTC) of Div2D1km, NoDiv1km, and CNTLZ1km are plotted in Fig. 4.21, Fig. 4.22, and Fig. 4.23, respectively.

In CNTL1km, the 2D mass divergence constraint is imposed on the last two 3DVAR radial velocity analyses only to help organize the analyzed circulations. In

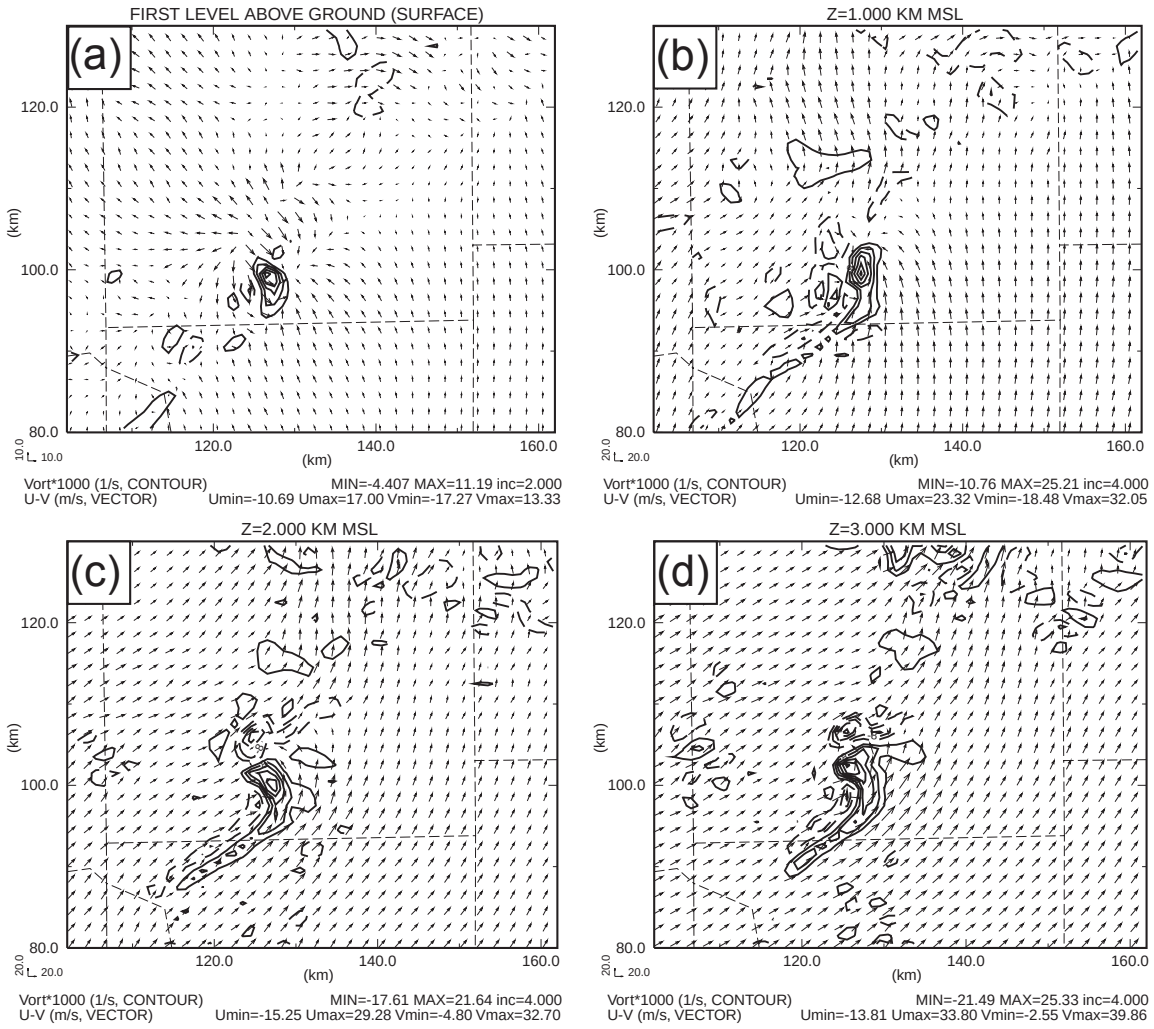

Fig. 4.20 Predicted vertical vorticity and wind fields at the surface, 1 km, 2 km, and 3 km MSL from the 35-minute forecast (valid at 2215 UTC) of experiment CNTL1km. The domain is the same as Fig. 4.18.

Div2D1km, the same constraint is imposed on all analysis cycles. Interestingly, the half-hour predicted reflectivity has only a very weak hook echo at the southwestern end of the main storm and the corresponding radial velocity field only shows a weak couplet (Fig. 4.21a, b, Fig. 4.18b, and Fig. 4.19b). Ten minutes later, the radial velocity couplet and hook echo are enhanced but are still much weaker and not as well-defined as those in

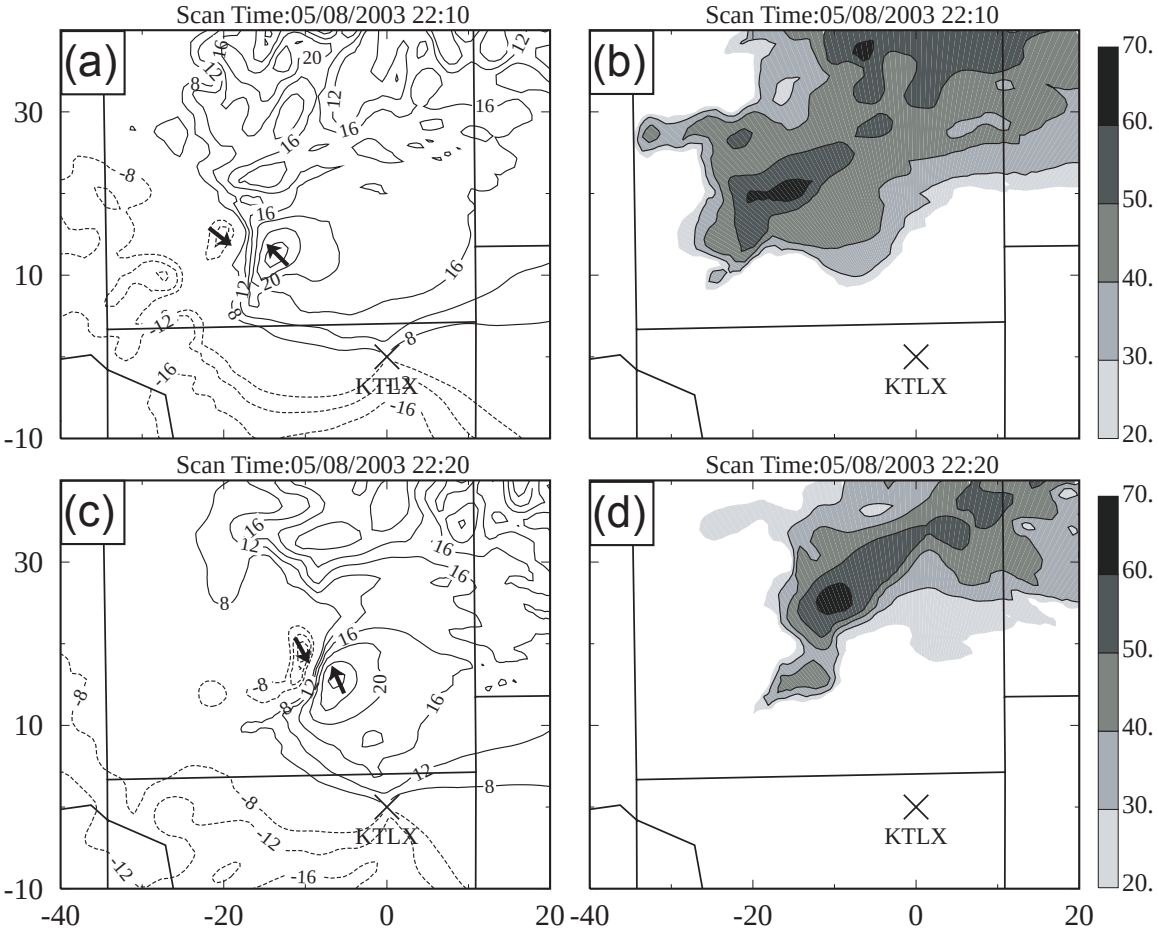

Fig. 4.21 Left column is similar to Fig. 4.19 and right column is similar to Fig. 4.18, except that they are for the forecasts of experiment Div2D1km at 2210 and 2220 UTC 8 May 2003.

CNTL1km (Fig. 4.21c, d, Fig. 4.18f, and Fig. 4.19f). Apparently, the effect of the 2D constraint used is too strong and serves to weaken the low-level convergence and rotation. On the other hand, when no mass divergence constraint is used in the analysis cycles, as in NoDiv1km, the predicted mesocyclone circulation and hook echo are not as strong and well-defined either compared to CNTL1km (Fig. 4.22, Fig. 4.18b, f, Fig. 4.19b, f). Therefore, the mass divergence constraint needs to be used carefully because it apparently has a significant impact on the detailed structures of the predicted storms.

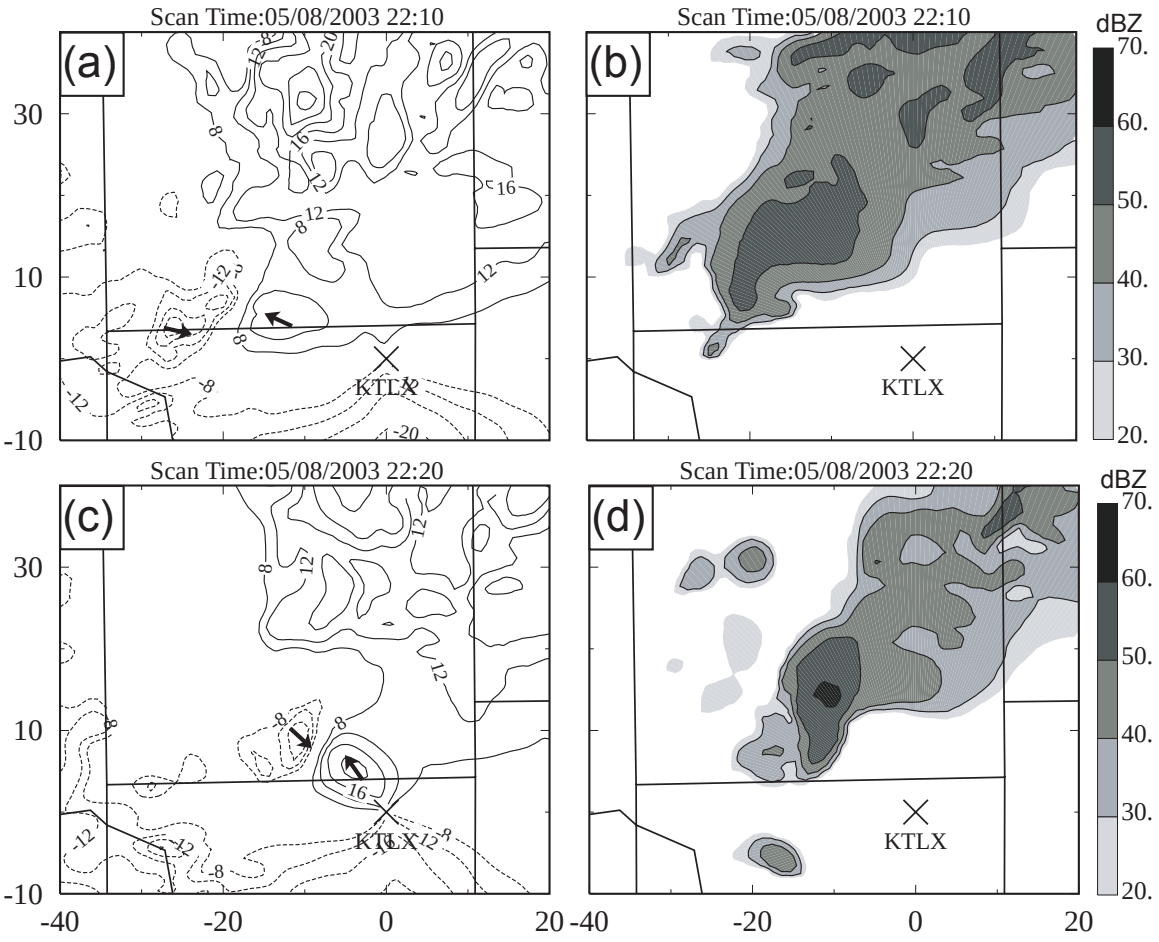

Fig. 4.22 Left column is similar to Fig. 4.19 and right column is similar to Fig. 4.18, but for experiment NoDiv1km at 2210 UTC and 2220 UTC 8 May 2003.

Although the above experiments with different mass divergence constraint for radial velocity analysis result in different detailed storm structures, they all predict, more or less, the mesocyclone. When radial velocity data are not used in experiment CNTLZ1km, no hook echo or cyclonic circulation is found in the prediction at either 2210 or 2220 UTC (Fig. 4.23). There is a radial velocity couplet at 2210 UTC (Fig. 4.23a), but it appears more like a divergence center than a circulation center. The large

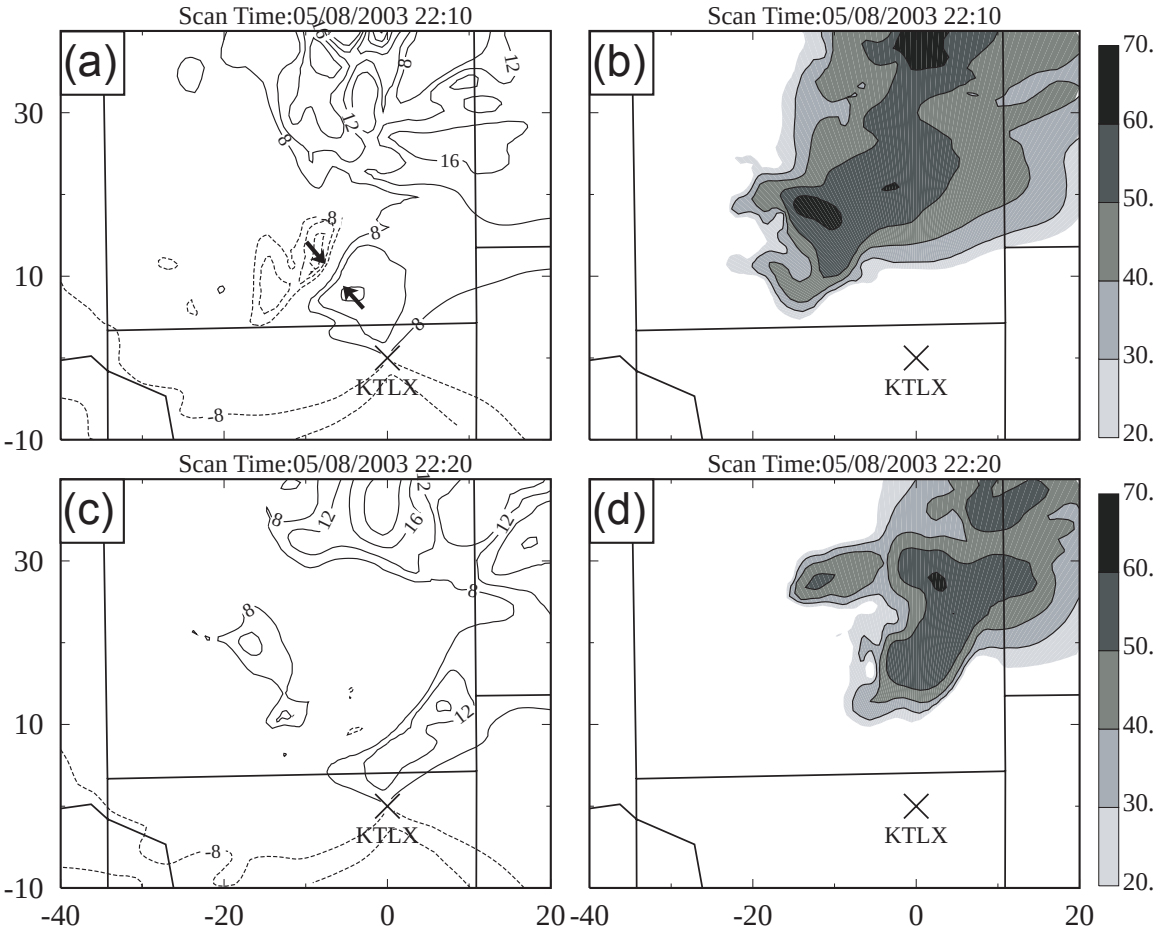

Fig. 4.23 Left column is similar to Fig. 4.19 and right column is similar to Fig. 4.18, but for experiment CNTL1km at 2210 UTC and 2220 UTC 8 May 2003.

differences found between the forecasts with and without radial velocity data indicate that the radial velocity analyses are important in building up the cyclonic rotation in the initial conditions, which affect significantly the subsequent forecast

4.3.1.2.3 Remaining problems with 1-km forecasts

It is found from the above 1-km experiments that the high-resolution ARPS

system is capable of reproducing many of the detailed tornadic structures of the OKC storm up to 50 minutes when the radial velocity data are properly assimilated. However, several problems are also found in even longer forecasts (over 1 hour) and need to be solved to further improve the overall forecast.

In the 1-km forecasts, we often find many small, spurious, cells popping up in the solution. In CNTL1km, these cells begin to appear at 40 minutes of forecast and severely contaminate the forecast after 1 hour. As an example, the predicted composite reflectivity field from the 1-hour forecast of CNTL1km, valid at 2240 UTC, is plotted in Fig. 4.24. At this time, the entire forecast domain has two clusters of storms: the southern one that is related to the main OKC storm, and the northern one that can be related to another observed storm cluster that produced the Red Rock tornado at 2310 UTC though it has a large position error. Both predicted clusters include many small, spurious, cells around the larger cells. We did not find such problems in the similar 3-km experiments reported earlier. A detailed diagnosis will be required to fully understand the cause. One possible reason is that there may be too much surface heating that makes the boundary layer too unstable. The increased resolution allows for better resolution and easier development of smaller cells.

The other problems found from the 1-km experiments include: the predicted OKC storm generally propagates faster than its counterpart in the 3-km experiments and most of the times faster than the observed one too; the path of the predicted OKC usually deviates from the observation more than that of the 3-km experiments. Further investigations on these issues will be performed in the future.

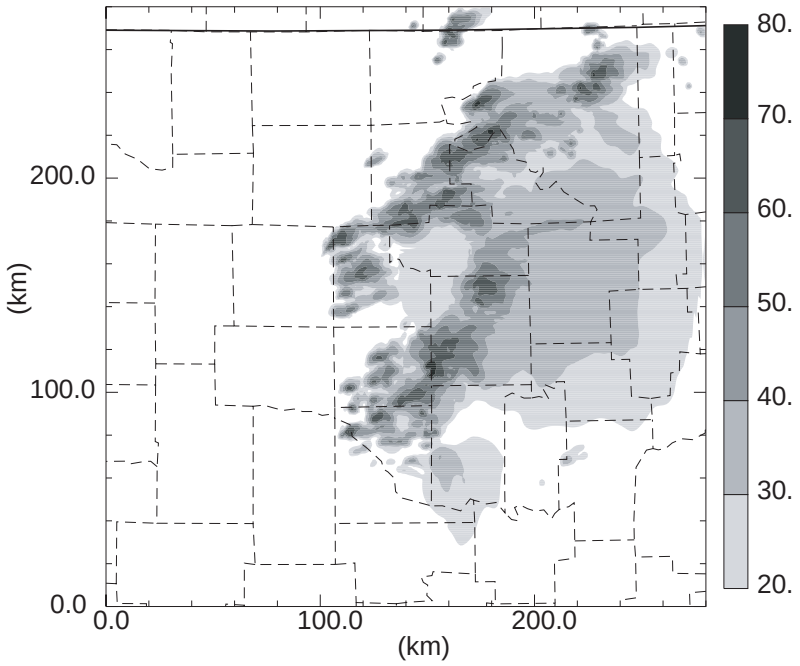

Fig. 4.24 Composite reflectivity at 2240 UTC from experiment CNTL1km.

4.3.1.3 Summary

In this section, four experiments with a 1-km horizontal grid spacing are conducted to study the impact of assimilating radar data at a higher resolution and the ability of the ARPS system in better capturing the detailed structures of the 8 May 2003 OKC tornadic thunderstorm as compared to the earlier 3-km studies. Rapid intermittent assimilations at 5-minute intervals, with a 70-minute assimilation window are used to generate the initial conditions for 140-minute forecasts. The radial velocity data are analyzed by the ARPS 3DVAR and the reflectivity data through the ARPS cloud analysis procedure.

By assimilating radial velocity and reflectivity data while imposing a 2D mass divergence constraint on the last two analyses, the control experiment successfully builds

up a low-level cyclonic rotation center in its final analysis. The control experiment predicts the spinning up of the rotation center and the development of a hook-shaped echo at the southwestern end of the main OKC storm in the first 10 to 15 minutes of forecast. The forecast between 2210 and 2230 UTC (30 to 50 minutes of forecast) reproduces the development and propagation of the tornadic mesocyclone and associated hook-shaped echo with a displacement error of about 10 km only. Therefore, the 1-km control experiment captures great details of the OKC storm in its first 50 minutes of forecast.

The two experiments that use radial velocity data while impose the 2D mass divergence constraint on all analysis cycles or on none of the cycles, respectively, are also able to build up the low-level cyclonic rotation center in the assimilated fields and predict the spin-up of the rotation center in the first 10 to 20 minutes of forecast. However, the predicted mesocyclone and hook echo of the main storm during the period of the real tornado are much weaker and less well-defined than those in the control experiment.

Another experiment in which no radial velocity data are used fails to analyze and predict almost all the features associated with the low-level cyclonic rotation. Such large differences confirm the importance of assimilating radial velocity data for the definition of the low-level tornadic circulations that subsequently intensify in the model prediction.

The 1-km experiments also have some remaining problems. The most severe one is the formation of many small, spurious, cells in the forecast. The others include that the predicted cells propagate too fast and their path deviates from the observed one. These problems will be carefully investigated in the near future.

Despite some remaining problems with the forecast, the forecast of the main OKC storm is rather realistic, and it provides us with an opportunity to further refine the simulation and to attempt to predict the tornado itself, by using a much higher spatial resolution. This is the topic of the next section.

4.3.2 Preliminary experiment with 100-m horizontal grid spacing

4.3.2.1 Experimental design

Our preliminary 100-m experiment is one-way nested within a 1-km experiment, which assimilates both reflectivity and radial velocity data using 5-minute intermittent assimilation cycles. The assimilation window is 1-hour long and covers 2030 to 2130 UTC. A 3D mass divergence constraint is imposed on all radial velocity analyses. Although the settings of this 1-km experiment differ from those of NoDiv1km described in the previous section, it gives similar predictions as NoDiv1km for the OKC storm.

The 100-m grid is 72 km × 72 km in size and its center is located at the location of the OKC tornado. The same vertically stretched grid is used as in the 1-km experiment. The 100-m forecast is initialized by interpolating the 1-km analysis at 2130 UTC. The physics options used in the 100-m experiment are the same as those of the 1-km run except that a full 3-D turbulence formulation is used instead of the vertical-only formulation. So far, only a 9.5-minute prediction has been completed and some of the results are presented here.

4.3.2.2 Experiment results

The goal of the 100-m experiment is to try to capture the tornado itself, instead of just the parental circulation when a coarse resolution is used. To determine the success of

this tornado forecast, several tornadic indicators are examined in the following analysis.

Firstly, the time series of the maximum surface vertical vorticity, the maximum surface wind speed and the minimum surface pressure are plotted in Fig. 4.25 to determine the possible period of tornadogenesis and the tornado intensity. From 4 minutes of forecast on, the maximum surface vertical vorticity and wind speed quickly increase to much higher values and remain at high values in the rest of the forecast; at about the same time, the minimum surface pressure quickly drops to a minimum value of about 930 hPa at 7 minutes of forecast (Fig. 4.25). An examination of the surface fields shows that these extrama are associated with a small region of strong low-level rotation (not shown). In fact, the maximum surface wind reaches the intensity of an F1 tornado (32-50 m s^{-1}) by 4.5 minutes and F2 intensity (50-70 m s^{-1}) between 5.5 and 9.0 minutes. The maximum surface vorticity increases from 0.2 s^{-1} at 4.5 minutes to over 0.5 s^{-1} within a period of 2 minutes, and the minimum surface pressure drops by about 20 hPa from 4 to 7 minutes. Clearly, the intensity of this simulated vortex, in terms of the above measures, qualifies it as an actual tornado.

Secondly, the predicted reflectivity and wind fields at the surface and 2 km MSL from 5 to 9 minutes of forecast are plotted in Fig. 4.26 at 2-minute intervals to study the tornadic features of the storm. The 5-minute forecast valid at 2135 UTC produces a small hook echo at around (9 km, 7 km) (Fig. 4.26a), which is colocated with a convergence center at the surface. At 2 km MSL, the tornadic features of the storm are evident (Fig. 4.26b). At 2135 UTC, the eastern flank of the southwestern part of the predicted reflectivity exhibits a well-defined hook echo with a small-scale hook echo appendage at around (9.5 km, 8 km). The winds also show a cyclonic circulation around the hook echo.

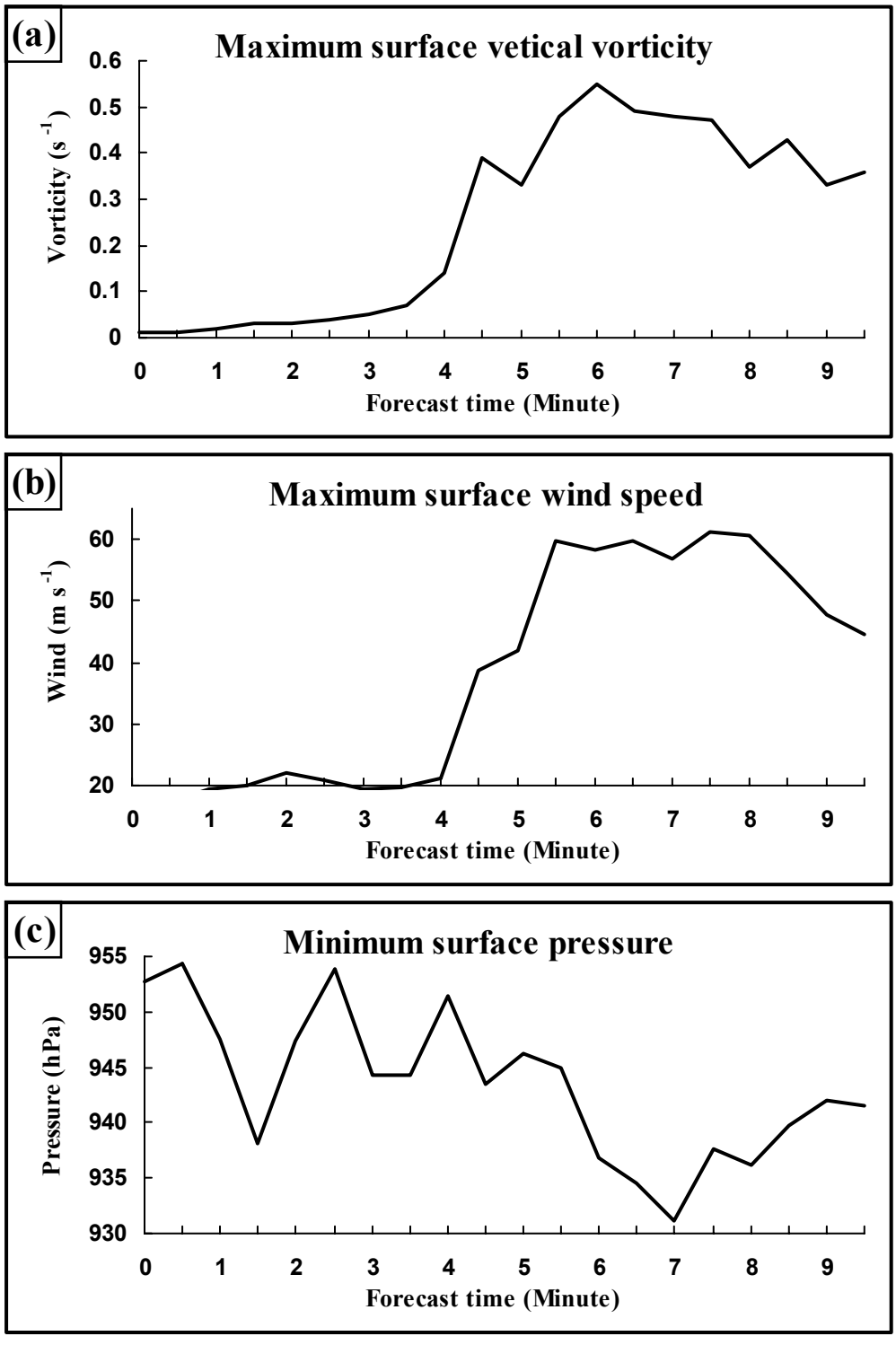

Fig. 4.25 The time series of maximum surface vertical vorticity, maximum surface wind speed, and minimum surface pressure in the 100-m forecast.

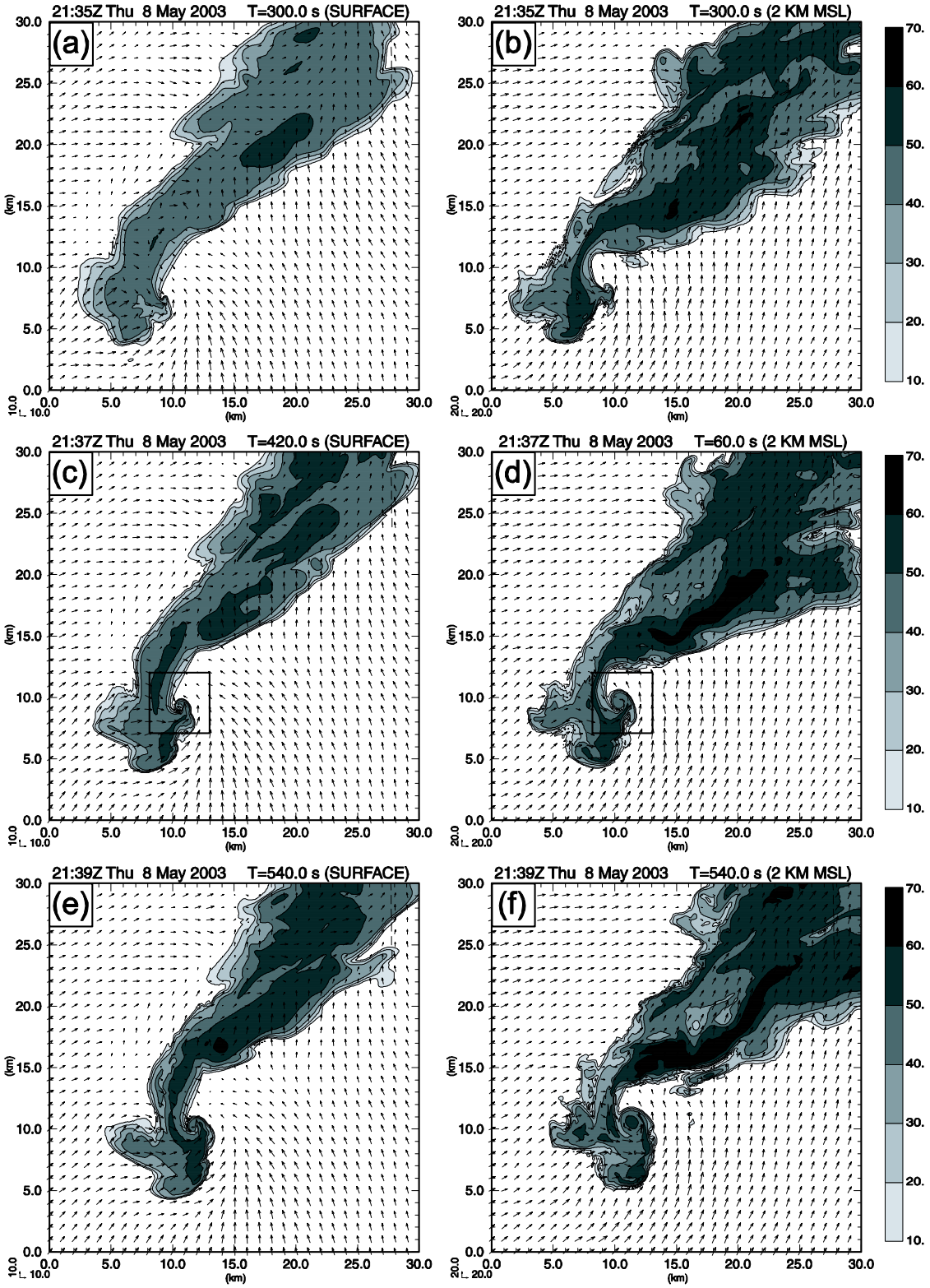

Fig. 4.26 Predicted reflectivity and wind fields at the surface (left column) and 2 km MSL (right column) from the 5 to 9 minutes of forecast at 2-minute intervals. Domain is 30 km by 30 km large. The squares in (c) and (d) indicate the area that is zoomed in by the next figure. Wind vectors are plotted every 10 grid points

Two minutes later, at 2137 UTC, the surface small-scale cyclonic circulation becomes more evident. The strong winds are circulating around a clear hook echo at the center of the square in Fig. 4.26c. At 2 km MSL, the small-scale hook echo appendage has formed a spiral pattern into the circulation center (Fig. 4.26d) by this time. These well-defined hook echoes and cyclonic circulations remain similar in the next 2 minutes, with the hook echo appendage becoming more wrapped up at 2139 UTC (Fig. 4.26e, f). Recalling that the observed OKC storm during its tornadic phase had a well-defined hook echo at its southern flank and a small-scale hook echo appendage at its southwestern end (Fig. 4.18), the 100-m forecast captures the main tornadic features of the storm well, although the time and location of the features do not exactly match the observations.

Finally, we zoom into a 5 km × 5 km area, as indicated by the square in Fig. 4.26c, to examine the detailed structures of the hook echo and circulation associated with the tornado. The reflectivity, wind, and vertical vorticity fields at the surface and 2 km MSL in this domain are plotted in Fig. 4.27 for the 7th minute of forecast valid at 2137 UTC. The Y-Z cross section of the reflectivity and vertical vorticity fields along the line indicated in Fig. 4.27a are plotted in Fig. 4.28. At this time, the hook echo appendage wraps around the cyclonic circulation center at both the surface and 2 km MSL (Fig. 4.27). The surface circulation in the domain is almost axisymmetric around the center of strong vorticity, with the wind speeds increasing dramatically toward the center and reaching a maximum value over 45 m s^{-1} (Fig. 4.27c). There is also clearly a radial component of winds into the circulation enter, and the surface friction must have played a role in enhancing the low-level convergence. The circular-shaped surface vorticity center has a width of about 500 m and a maximum vorticity value of 0.478 s^{-1}. At 2 km MSL,

the winds are not axisymmetric, with the winds on the northwest side of the vorticity center being the weakest (Fig. 4.27d). The circulation is weaker but larger in size than at the surface and has a maximum vorticity value of 0.268 s^{-1}. The intensity of the wind and circulation suggests that there is an F1 to F2 tornado in the model at this time, and the tornado lasts for about 5 minutes.

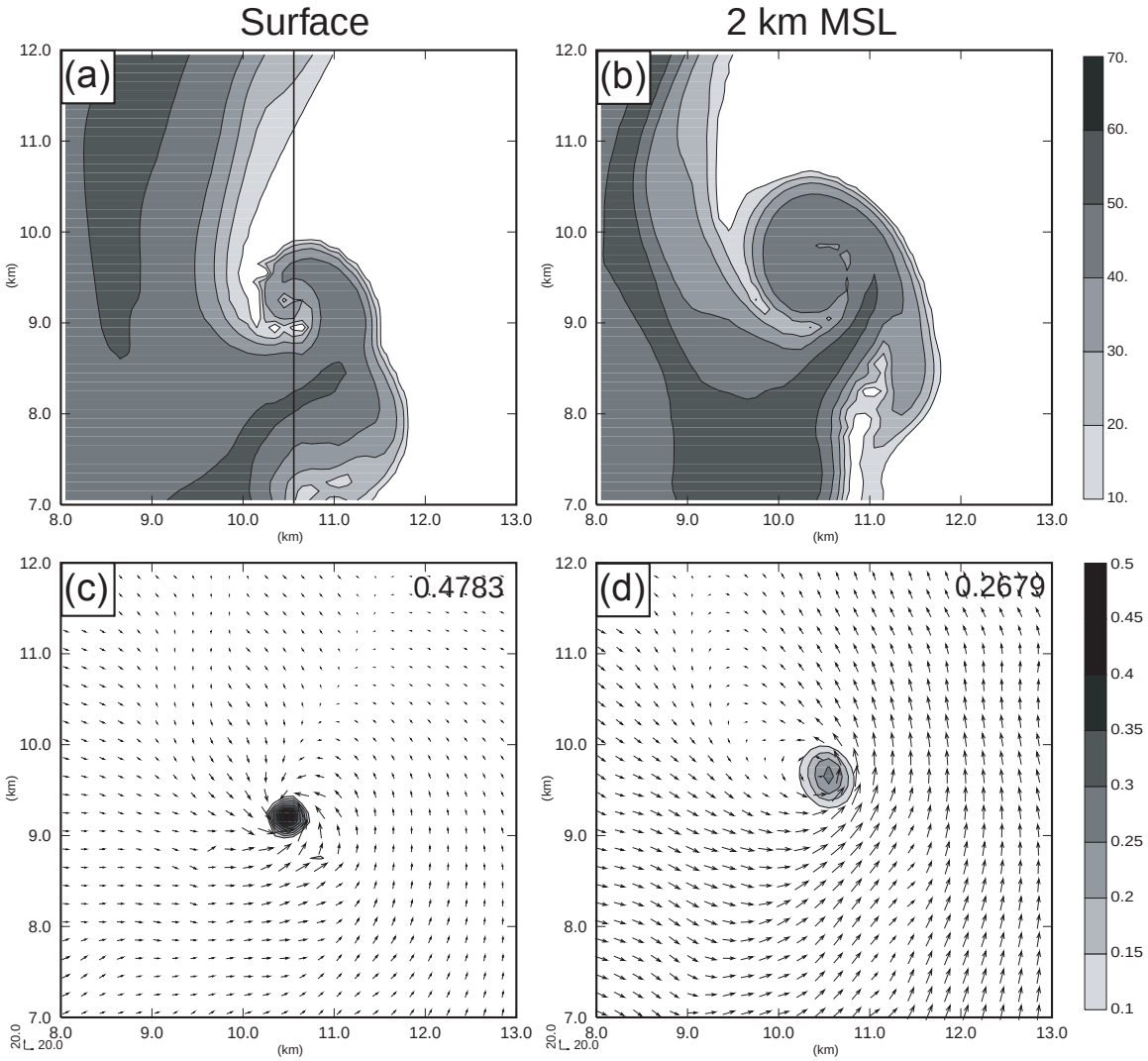

Fig. 4.27 Predicted reflectivity, wind, and vertical vorticity fields at the surface (left column) and 2 km MSL (right column) from the 7 minutes of forecast valid at 2137 UTC. The domain is 5 km by 5 km and covers area indicated by the squares in Fig. 4.26c and d. The numbers at the upper-right corner of panel (c) and (d) are the maximum vertical vorticity value in s^{-1}.

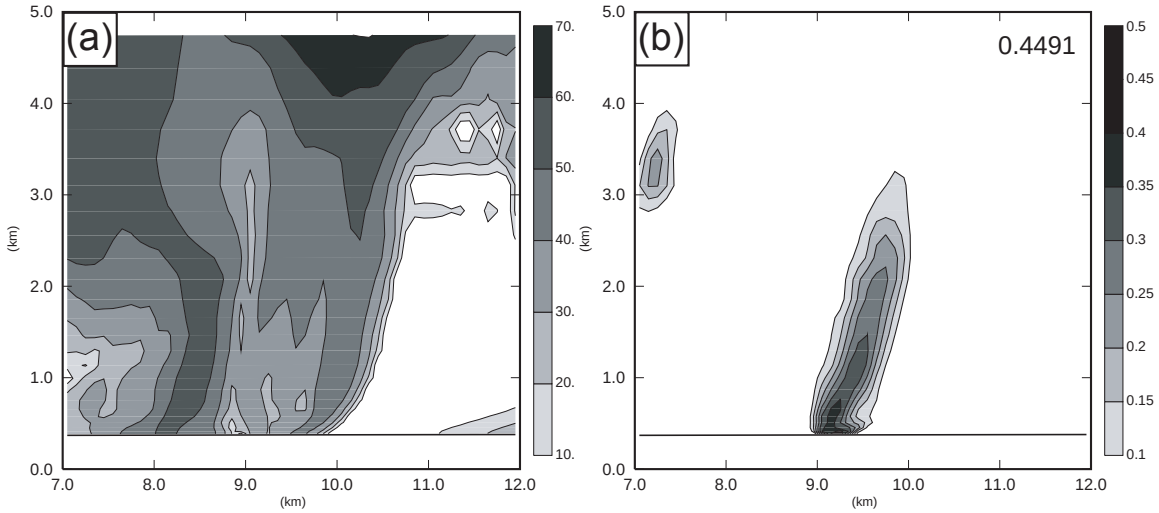

Fig. 4.28 Y-Z cross-section of predicted reflectivity (left) and vertical vorticity (right) fields along the line indicated in Fig. 4.27a from the 7 minutes of forecast valid at 2137 UTC. The number at the upper-right corner of (b) is the maximum vertical vorticity value in s^{-1}.

The Y-Z cross section of the vertical vorticity fields through the tornado (Fig. 4.28b) shows an isolated column of strong vorticity with a depth of nearly 3 km and a slightly northward tilt of the axis. The largest vorticity in the column is near the surface and is centered at a region of relatively weak reflectivity (near y = 9 km in Fig. 4.28a). Two high-reflectivity bands, one at about y = 8 km and the other at about y = 10 km, wrap around the strong vorticity center, indicating a rain-wrapped tornado at this time.

4.3.2.3 Summary and discussion

In this section, a 100-m forecast that is one-way nested within a 1-km forecast is conducted to simulate the 8 May 2003 OKC tornado. One 9.5-minute forecast is completed so far and a 5-minute long, F1 to F2 intensity tornado is obtained in the model at the southwestern portion of the predicted storm, while, in the real world, the OKC tornado occurred at the same portion of the storm near Moore about half an hour later.

A small low-level cyclonic circulation that had been observed by the KTLX radar starting from 2120 UTC in the OKC storm is assimilated into the 1-km initial condition through the ARPS 3DVAR. Apparently, starting from this initial condition, a 100-m grid is able to spin up this circulation and produce a realistic tornado.

Although the predicted tornado is not at the correct time and location of the real OKC tornado, it is still very encouraging because it is the first successful simulation of such a type, which uses a full physics model and an initial condition analyzed from the real data. With these such realistic simulations, the mechanism of tornadogenesis and tornado dynamics can be studied in details. We plan to pursue this in the future, after obtaining hopefully more accurate predictions.

Chapter 5

29 May 2004 Central Oklahoma Tornadic Thunderstorm Case

5.1 The case

In the late afternoon through evening of 29 May 2004, a long-lasting tornadic thunderstorm swept through central Oklahoma and produced 16 tornadoes in its long journey from Custer County, west-central Oklahoma, to Mayes County, northeastern Oklahoma (Fig. 5.1). The first tornado from the tornadic thunderstorm touched down 7 km southwest of Thomas at 1729 CST (Central Standard Time, or 2329 UTC) 29 May. More than 7 hours later, the last tornado from the same tornadic thunderstorm occurred 4 km southeast of Murphy at 0051 CST (0651 UTC) 30 May. Table 5.1 lists the main features of these 16 tornadoes. In CST, most of these tornadoes occurred in the afternoon and at night of 29 May and they struck mostly the central Oklahoma area. This case is therefore named as the 29 May 2004 central Oklahoma (COK) tornadic thunderstorm case. For the convenience of comparison between model simulations and radar observations, which are usually marked in Universal Time (UTC), we use UTC hereafter and most of the tornadoes actually happened on 30 May 2004 in UTC.

According to Table 5.1, 5 of the tornadoes are rated F0 and 8 more are rated F1. They happened in rural areas and caused little damages. Only 2 tornadoes are rated F2 and 1 is rated F3 among the sixteen. Most of the damages came from the seventh tornado rated F2 that struck the northwestern metro area of Oklahoma City and caused 5 million dollar worth of damages. No injury or fatality was reported for the entire tornado outbreaks. Among these tornadoes, the second has some special features: it lasted for

about one hour (from 0017 to 0115 UTC), its path was 32 km long and 1.6 km wide, and caused 2.5 million dollar worth of damages. Also among them all, at least two (the third and fourth tornado in Table 5.1) were anticyclonic.

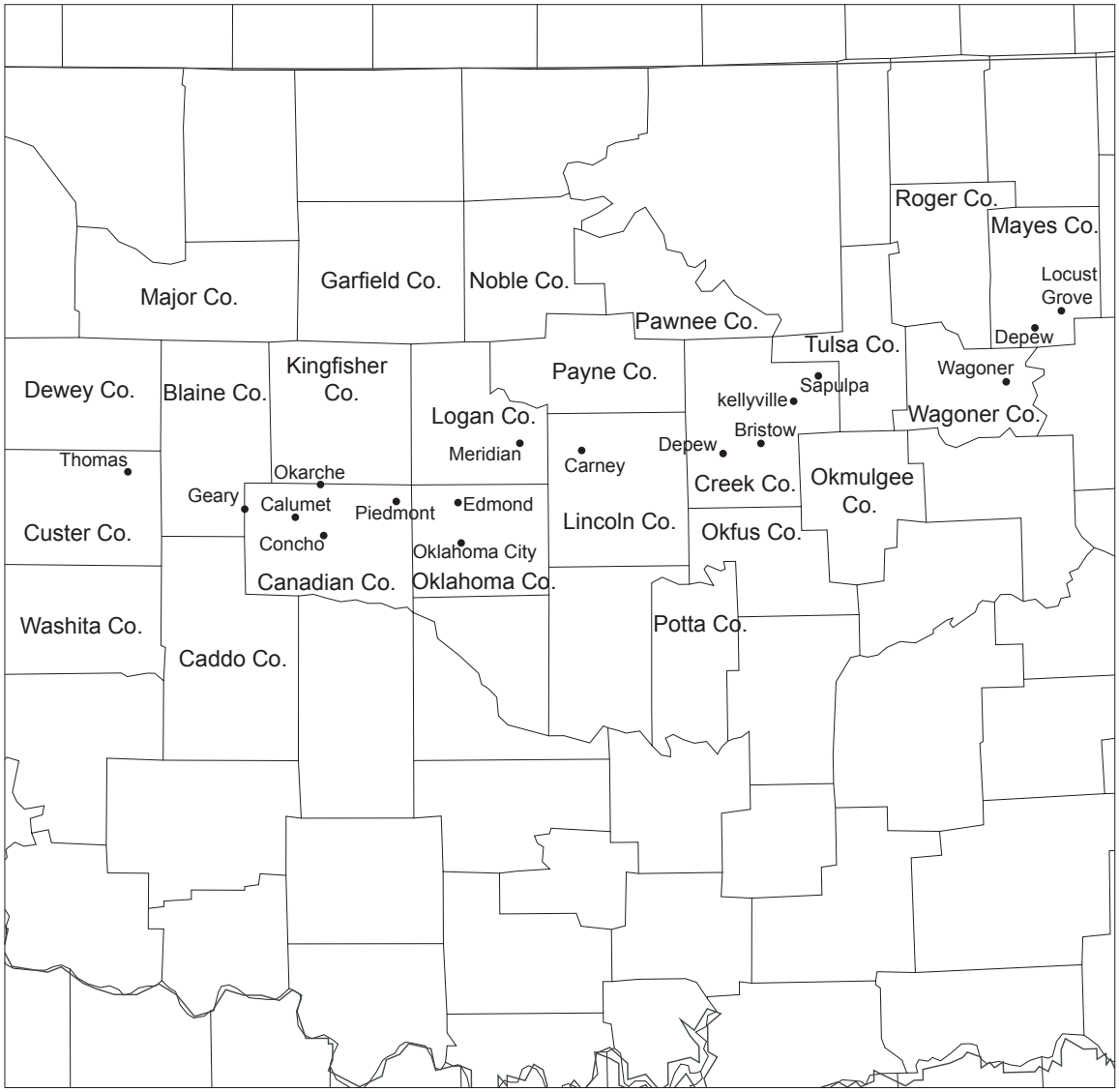

Fig. 5.1 Map of Oklahoma Counties and Cities (dot) related to the 29 May 2004 central Oklahoma tornadic thunderstorm case. Sixteen tornadoes were spawned from the same tornadic thunderstorm that swept through central Oklahoma area from Custer County to Mayes County.

Table 5.1* The features of the 29 May 2004 central Oklahoma tornadoes

Tornado Number	Time** (UTC)	Length of path (miles)	Width Of path (yards)	F-scale	Property Damage ($)	County	Location***
1	2329-2340	6	200	F0	1K	Custer	4.5 SW - 6.5 SSE Thomas
2	0017-0115	20	1760	F2	2.5M	Blaine/ Canadian/ Kingfisher	9 WNW Geary – 2.5 N Geary – 9.2 NNW Calumet (11 W Okarche)
3	0104-0114	4.5	50	F1	25K	Canadian	2 N Calumet – 4.5 ENE Calumet
4	0114-0120	2	20	F1	10K	Canadian	4 NNE Calumet – 3.5 WNW Concho
5	0122	0.1	20	F0		Canadian	2 NW Concho
6	0145-0147	1	50	F1	150K	Canadian	6.5 W - 5.5 W Piedmont
7	0204-0210	4.6	100	F2	5M	Oklahoma	10.3 WNW Edmond - 7.1 NW Edmond
8	0301-0303	0.3	50	F1	50K	Logan	5 SSE Meridian
9	0317-0325	4	100	F0		Logan	5 SE Meridian - 6 E Meridian
10	0327-0332	2.5	300	F1	250K	Lincoln	3.5 WSW - 1 SW Carney
11	0418-0433	7.5	700	F3	350K	Creek	6.2 WNW - 4.9 NNE Depew
12	0433-0444	4.6	425	F1	150K	Creek	4.7 NNE Depew - 4.1 NNW Bristow
13	0512-0526	5.4	200	F1	25K	Creek	3.6 W - 2.8 NE Kellyville
14	0533-0534	0.1	75	F0	5K	Creek	3.2 SW - 3.1 SW Sapulpa
15	0642-0650	3.5	300	F0	15K	Wagoner	7.4 NNW - 8 N Wagoner
16	0651-0705	7.2	600	F1	25K	Mayes	2.5 SE Murphy - 5.9 SW Locust Grove

* This table is from the website of National Weather Service (NWS) Norman Forecast Office.

** The times of tornado outbreaks have been converted to UTC from CST times in the original table.

*** Unit for location is in terms of mile. For example, for the first tornado, the path is from 4.5 miles SW of Thomas to 6.5 miles SSE of Thomas.

The tornadic thunderstorm that spawned these tornadoes was recorded by the WSR-88D Doppler radar near Oklahoma City (KTLX). As examples, the low-level reflectivity and radial velocity fields from the KTLX radar at 0058 and 0417 UTC are plotted in Fig. 5.2. At 0058 UTC, during the second tornado outbreak (F2), a hook echo was located west of Okarche (Fig. 5.2a) and further west was the center of a mesocyclone (Fig. 5.2b). According to the tornado report (for the second one in Table 5.1), we determine that the tornado was at 17 km west of Okarche at this time. At 0417 UTC, the beginning of the eleventh tornado outbreak (F3, about 8 km north of Depew, Table 5.1), the locations of the hook echo and the strong mesocyclone also match the reported location of the tornado well (Fig. 5.2c, d).

Northern Oklahoma and southern Kansas had a favorable environment for tornado outbreaks on 29 May. At the surface, Oklahoma was controlled by the southeastern part of a deep low on 29 May and the southerly flow had dominated in Oklahoma and Texas since 0600 UTC 29 May. By 1200 UTC, a weak dryline formed in western Texas and in the Oklahoma panhandle. This dryline intensified and moved eastward during the next 12 hours as the surface low system moved northeastward. By 0000 UTC 30 May, a strong north-south oriented dryline had moved to the western border of Oklahoma. At the 500 hPa level, Oklahoma was located behind a ridge and ahead of a trough during the daytime (1200 UTC 29 May to 0000 UTC 30 May) and was mainly under midlevel southwesterly flows. The speed and the westerly component of 500 hPa winds over Oklahoma were increased dramatically before tornadoes happened.

The Norman, Oklahoma, (OUN) sounding at 0000 UTC 30 May had not been affected by the tornadic thunderstorm that was producing a tornado at the northwestern

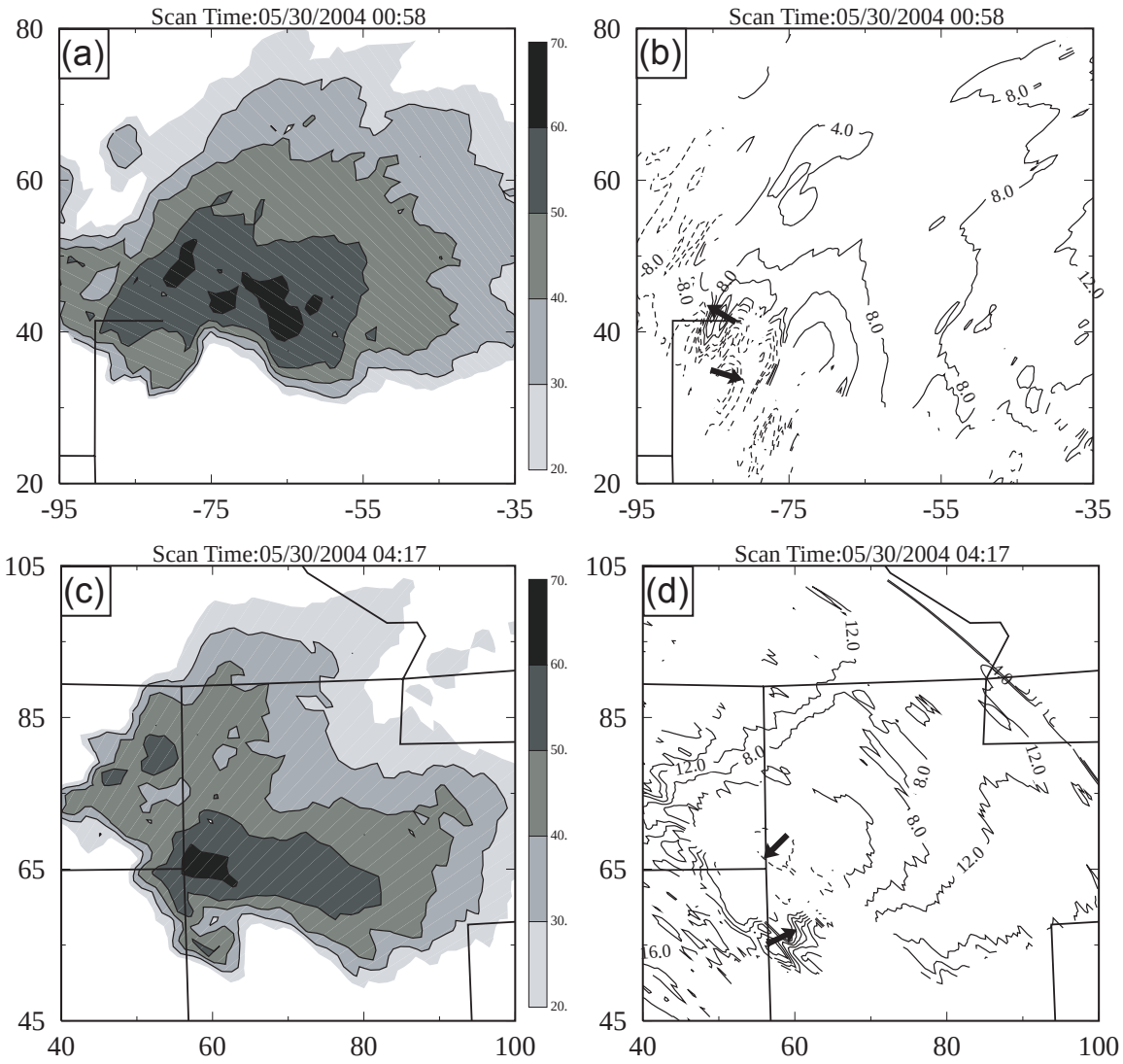

Fig. 5.2 Observed reflectivity (left) and radial velocity fields (right) at low level scan from the KTLX radar observations. (a) and (b) were observations at 0058 UTC 30 May 2004, while (c) and (d) were observations at 0417 UTC. The short arrows in radial velocity fields indicate the direction of radial velocities near their peak value.

corner of Canadian County. The sounding showed a moderate instability with a CAPE of 2261 J kg^{-1} and a CIN of 62 J kg^{-1}. The vertical wind veered with height from 19 m s^{-1} near the surface to 50 m s^{-1} at round the tropopause and the vertical shear over the lowest 6 km is near 24 m s^{-1}. Both the instability and shear suggest the potential of supercell and tornadoes.

By 1930 UTC 29 May, several small convective cells were triggered along the dryline and had been detected by the Fredrick (KFDR) radar located at the southwestern corner of Oklahoma. The low-level scans of the KFDR radar from the initial stage of the COK tornadic thunderstorm to the mature stage when it produced the first tornado are plotted in Fig. 5.3. At 2001 UTC, several small convective cells initiated from the dryline were lined up near the western border of Oklahoma (Fig. 5.3a) and moved north-northeastward. By 2100 UTC, the cell at the central portion of the line grew fastest and became a strong storm, but it was the smaller cells located at the southern portion of the line (pointed to by arrows) that evolved into the COK tornadic thunderstorm later (Fig. 5.3b). During the next hour, the line of storms moved northeastward further with the northern cells decaying and the southern cells (two small cells pointed by arrow) intensifying (Fig. 5.3c, d). By 2259 UTC, the southern cells had merged together and became a single strong supercell that was approaching the northern cell (Fig. 5.3e). The southern supercell grew very fast from 2300 to 2330 UTC and spawned the first tornado at 2329 UTC 29 May (Fig. 5.3f). During the period, the northern cell dissipated presumably because its low-level southerly inflow was disrupted by the fast growing southern storm (Fig. 5.3e, f). So, it took at least 2.5 hours for the COK tornadic thunderstorm to grow into a tornado spawning one.

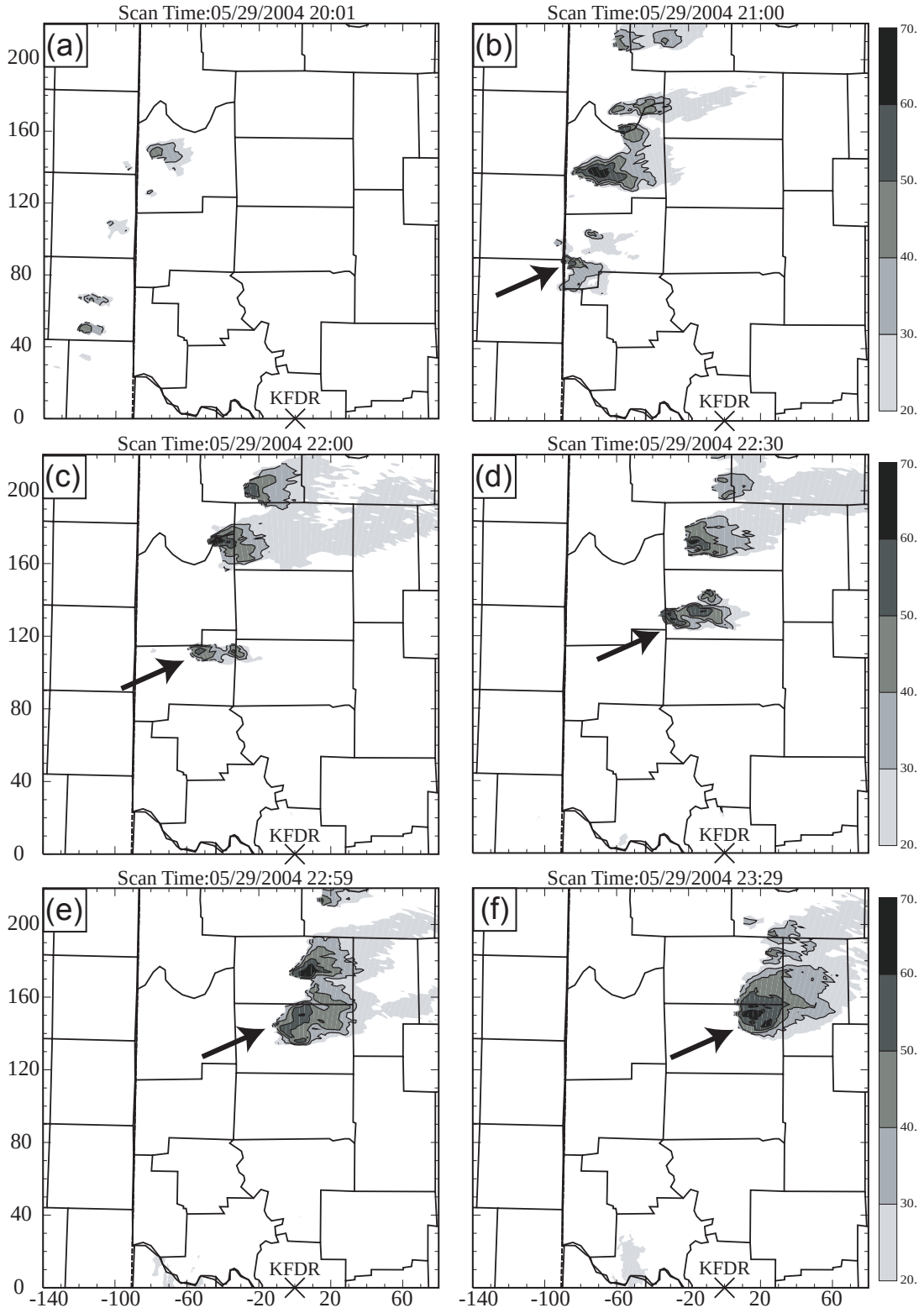

Fig. 5.3 Observed reflectivity fields at the 1.67° elevation from the KDFR radar at 1-hour intervals from 2001 to 2200 UTC and at half hour intervals from 2200 to 2329 UTC 29 May. Arrows point to the central Oklahoma tornadic thunderstorm.

5.2 Design of experiments

From the experiments for the cases of the Fort Worth and OKC tornadic thunderstorm, it is found that the predicted tornadic thunderstorms usually have a life span of about 3 hours. In this case, the observed central Oklahoma tornadic thunderstorm was a single supercell that lasted for over 9 hours and spawned 16 tornadoes. Among them, 15 were produced after 0000 UTC 30 May. We therefore start our assimilation at 0000 UTC 30 May for the forecast to cover the most significant period of tornado outbreaks. Also, the observational data are most complete at 0000 UTC. At this time, the thunderstorm was at its mature stage and had already produced its first tornado at the northeastern corner of Custer County about half an hour ago.

In these experiments, Eta model analysis at 0000 UTC and 3 hourly forecasts starting from the same time are used to provide the analysis background and boundary conditions for 3-km grid. The area of the 3-km grid is 580 km × 580 km and covers entire Oklahoma and southern Kansas. Vertical stretched grid is used again with the vertical grid spacing increasing from 20 m at the surface to 770 m at the model top that is located about 21 km height. Again, the general ARPS settings given in Chapter 2 are employed in the model forecast.

Two sets of experiments are performed for this case: one set examines the efficacy of applying a simple phase-correction scheme in removing the large position errors of the storm in the analysis background therefore also the initial condition, and the other investigates the effectiveness of dual-Doppler analysis of radial velocity data on the storm forecast.

Two experiments, PCLD and PCLDPC, are conducted to study phase correction

for the assimilated storms. Starting from the analysis at the end of a 1-hour long assimilation from 0000 to 0100 UTC 30 May with 10-minute intervals, the forecast is run for 3 hours in both experiments. To make the experiments simple, the radial velocity analysis in the 3DVAR is turned off and only reflectivity data from the KTLX radar are used by the cloud analysis procedure. It is found that large system position errors develop in the forecast of the thunderstorms in PCLD. Analysis shows that these position errors start during the assimilation period, while the model cells are still weak and propagate too fast due to advection. The cloud analysis is able to correct some of that, by removing hydrometeors associated with the misplaced cells but it is incapable of removing completely the disturbances in other fields. In an effort to correct this problem, a simple phase-correction scheme is designed and implemented during the assimilation period for experiment PCLDPC.

Because the COK thunderstorm was observed by both the Oklahoma City (KTLX) and Vance Air Force Base (KVNX) radars from about the same distances and at nearly a 90º angle between 0000 and 0100 UTC, dual-Doppler instead of single-Doppler wind analyses can be performed using the ARPS 3DVAR during the assimilation cycles. Four experiments are performed to study the impact of the dual-Doppler wind analyses (Table 5.2), they are: SnglVrZ, in which reflectivity (Z) and radial velocity (V_r) data from KTLX are assimilated, DualVrZ, in which V_r data from both radars are used for wind analysis but only Z data from KTLX are used in the cloud analysis, DualVr, in which V_r data from both radars are used but the cloud analysis procedure is turned off, and SnglVr, in which V_r data from KTLX are used without the cloud analysis. Otherwise, these four experiments are same and all employ a 1-hour assimilation window from 0000 to 0100

UTC 30 May with 5-minute analysis cycles, and the forecast is run for 3 hours from the assimilation results.

Table 5.2 List of the 3-km experiments testing the dual-Doppler analysis

Name	Radial velocity		Reflectivity	
	KTLX	KVNX	KTLX	KVNX
SnglVrZ	Yes	No	Yes	No
DualVrZ	Yes	Yes	Yes	No
SnglVr	Yes	No	No	No
DualVr	Yes	Yes	No	No

5.3 Results of phase correction experiments

In this section, results from the experiments of phase correction for the central Oklahoma tornadic thunderstorms are discussed. Firstly, the forecast of PCLD is compared with radar observations to evaluate the quality of the forecast for this case. Then, the problem of phase error in the forecast of PCLD is presented and discussed. Finally, a proposed solution to this phase error problem is introduced and the testing experiment, PCLDPC, is discussed.

5.3.1 Forecast from experiment PCLD

For the verification purpose, the observed low-level reflectivity fields from the KTLX radar during the forecast period are plotted first in Fig. 5.4. From 0132 to 0400 UTC 30 May, the COK tornadic thunderstorm propagated slowly east-northeastward from southeastern Kingfisher County to northeastern Lincoln County (Fig. 5.4). The thunderstorm remained as a supercell with a large area of high reflectivity and a well-

defined hook echo at its south side. According to Table 5.1, five tornadoes (from the 6th to the 10th) were reported during this 2.5 hour period, but the 3-km resolution used by the analysis and forecast is too coarse to identify any tornado or tornado vortex explicitly. Our discussions focus on the forecast of the intensity and location of the storm.

A reasonable 3-hour forecast is obtained in experiment PCLD. The predicted reflectivity fields corresponding to the observed fields in Fig. 5.4 are plotted in Fig. 5.5, at half hour intervals from 0130 to 0400 UTC 30 May. At half hour of forecast valid at 0130 UTC, the predicted COK storm splits into two strong cells located in the central Garfield County and in the conjoint areas of Kingfisher, Logan, and Garfield Counties (Fig. 5.5a), respectively, while the radar observations at 0132 UTC show that the real storm was in southeastern Kingfisher County, nearly one county south-southwest of the predicted southern cell (Fig. 5.4a). From 0130 to 0200 UTC, the northern predicted cell dissipates, but its southern one maintains its strong reflectivity center and moves slowly eastward (Fig. 5.5b), just as the observed one did during this period, but it also maintains a 40 km displacement error (Fig. 5.4b). The observed COK storm moved eastward between 0202 and 0301 UTC (Fig. 5.4c, d) then east-northeastward between 0301 and 0400 UTC (Fig. 5.4e, f). Apart from the displacement error, the predicted thunderstorm captures the main characteristics of the propagation of the observed one. During the entire 3 hours of forecast, the predicted storm maintains its intensity and exhibits a hock-shaped echo on its southern flank for most of its life time.

The wind and vertical vorticity fields at the surface and 3 km MSL from PCLD are plotted in Fig. 5.6 for 0200, 0300, and 0400 UTC 30 May. At all of these times, an isolated, well-organized column of strong vorticity is evident near the southern edge of

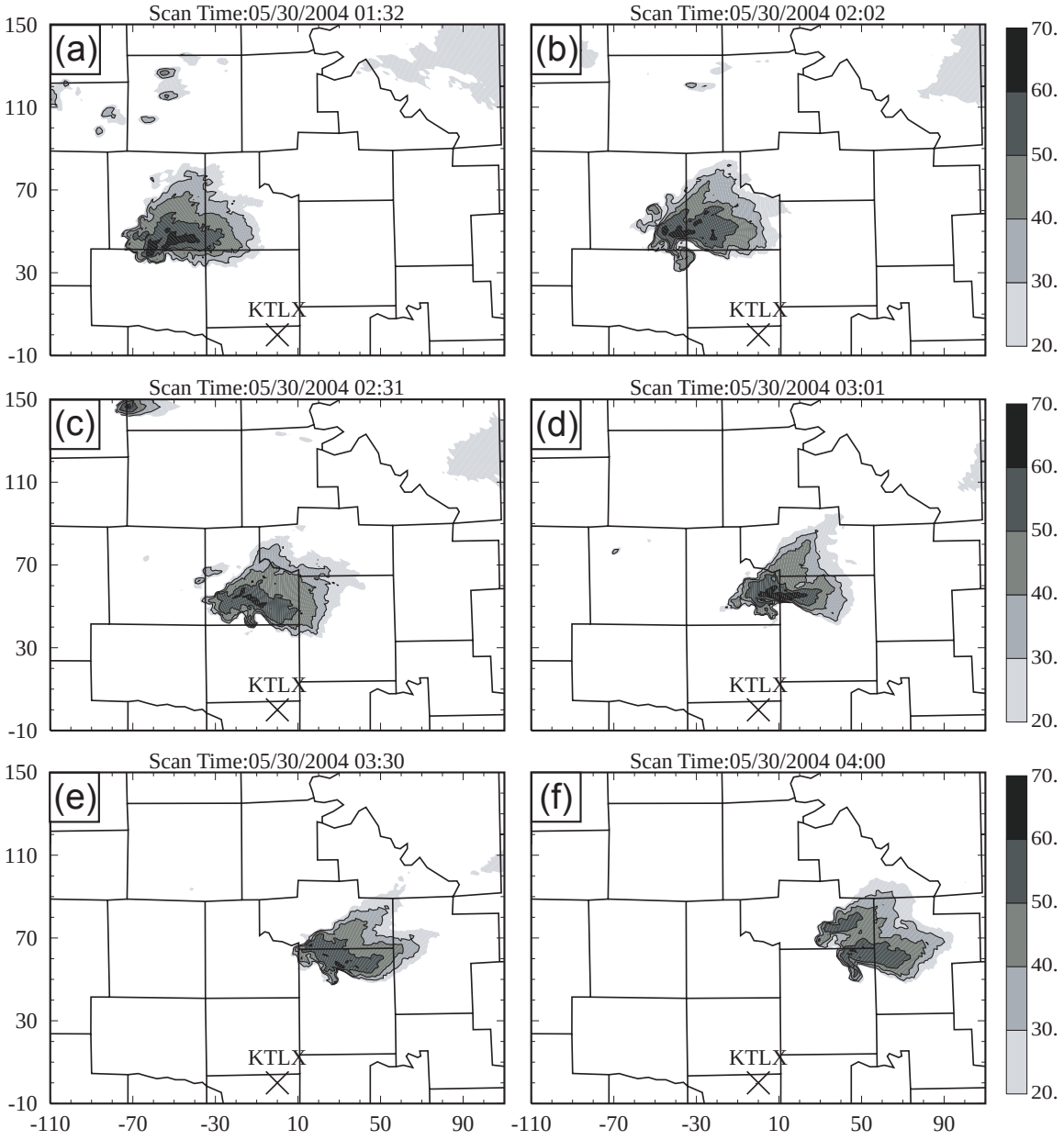

Fig. 5.4 The observed low-level reflectivity fields from the KTLX radar from 0132 to 0400 UTC May 30 with about half hour intervals. The analysis domain shown is about 250 km on each side, representing the portion of the 3-km grid between 195 and 445 km in the east-west direction and from 170 to 420 km in the north-south direction.

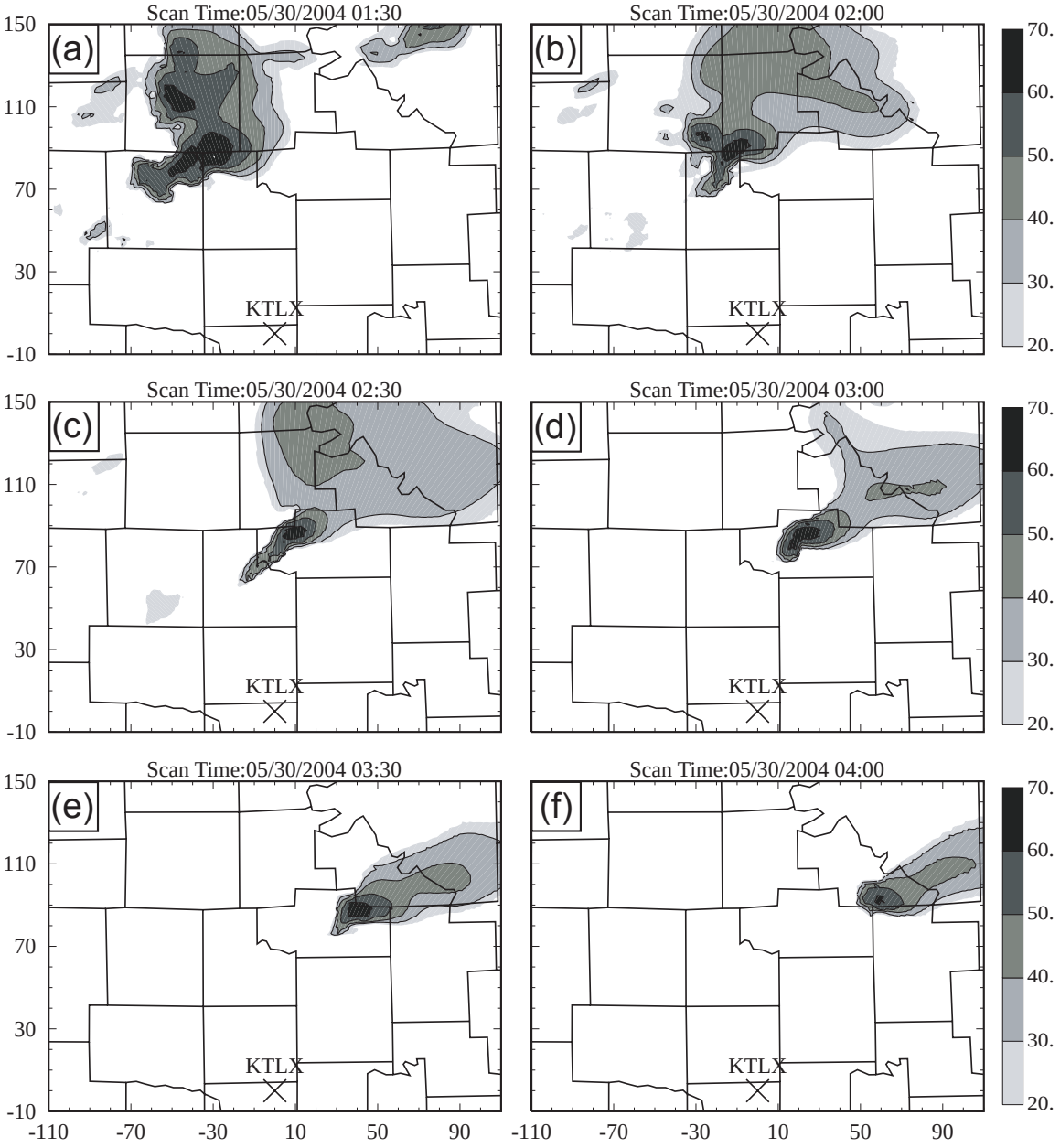

Fig. 5.5 Predicted reflectivity at the same elevation as those shown in Fig. 5.4, but from experiment PCLD. Shown are times at half hour intervals from 0130 to 0400 UTC 30 May 2004.

the strong echo region or of low-level cold pool (Fig. 5.6). Colocated with the surface vorticity center is a strong convergence center at 0200 and 0300 UTC (Fig. 5.6a, c). The predicted hook-shaped echo and the strong vorticity column indicate high potential for tornadogenesis in the forecast storm during the entire forecast period, which is consistent with the observations of tornadoes.

The essentially constant amount of displacement error of the predicted storm during the entire forecast period tells us that the position error is already present in the initial condition. To see this more clearly, the observed reflectivity field, reflectivity field from the analysis background at 0100 UTC, the analysis at 0100 UTC, and the 10-minute forecast of PCLD are plotted in Fig. 5.7. The fields have been mapped to the 1.14° elevation of the KTLX radar.

In the background, the COK storm has three cells lining up from northwestern Garfield County to northeastern Kingfisher County (Fig. 5.7b), while the observed thunderstorm is located at the southwestern corner of Kingfisher County or about 50 km south-southwest of the background ones (Fig. 5.7a, b). Using radar data, the cloud analysis at 0100 UTC restores the model precipitation fields to the right position (Fig. 5.7c), but it cannot correct or remove disturbances in the wind, temperature, and pressure fields related to the misplaced storms in the background. In the forecast, the storms redevelop and actually dominate over the storm newly introduced by the cloud analysis at the right location; as a result, the location error of the forecast storm persists. More specifically, in the forecast, the new storm disturbances added by the cloud analysis dissipate in about 10 minutes, while at the same time, the old cells redevelop (Fig. 5.7b, and d). Therefore, the 50 km north-northeastward displacement error is restored in the

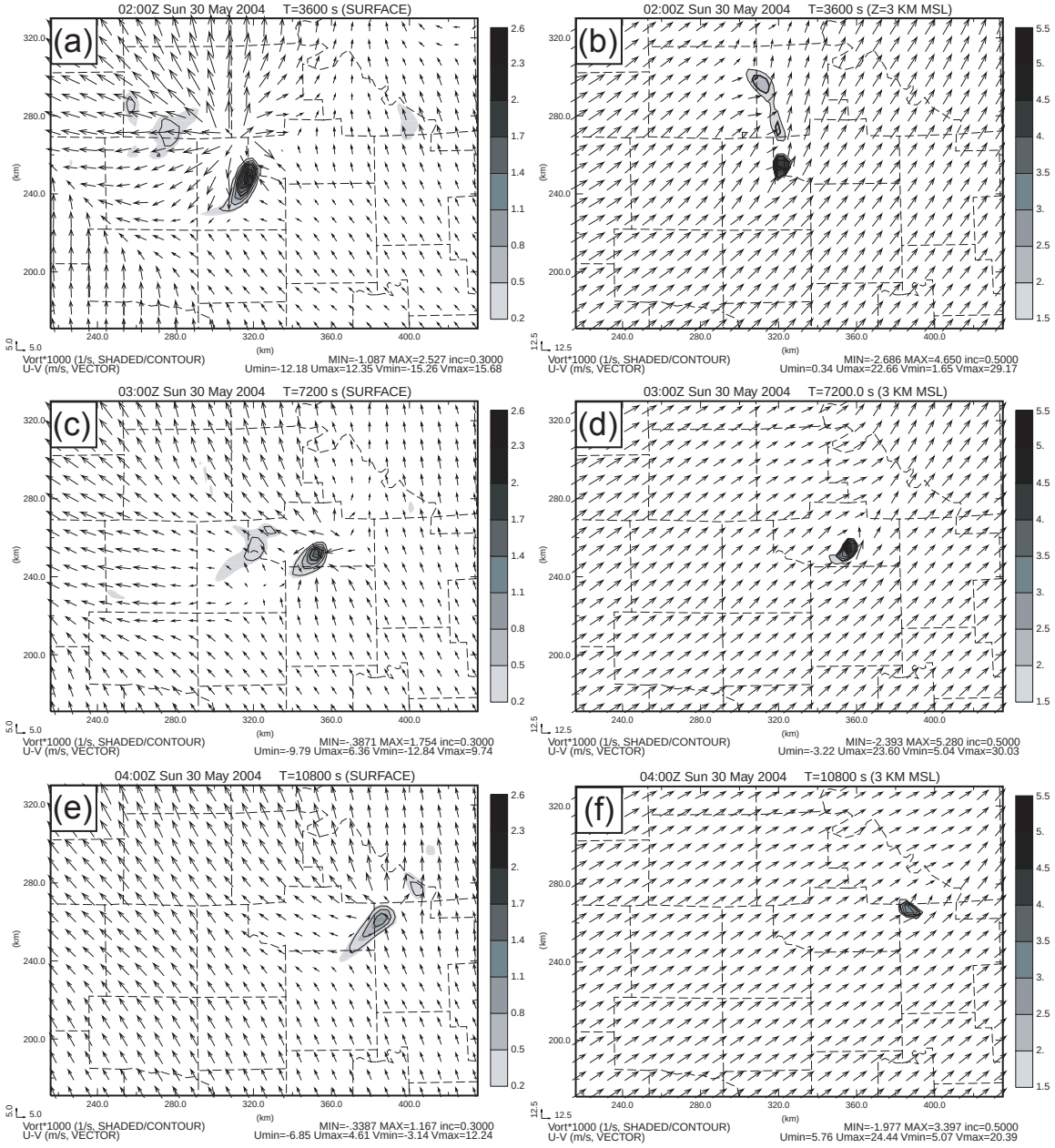

Fig. 5.6 The predicted wind and vertical vorticity fields at the surface (left column) and 3 km MSL (right column) from PCLD at 0200, 0300, and 0400 UTC 30 May.

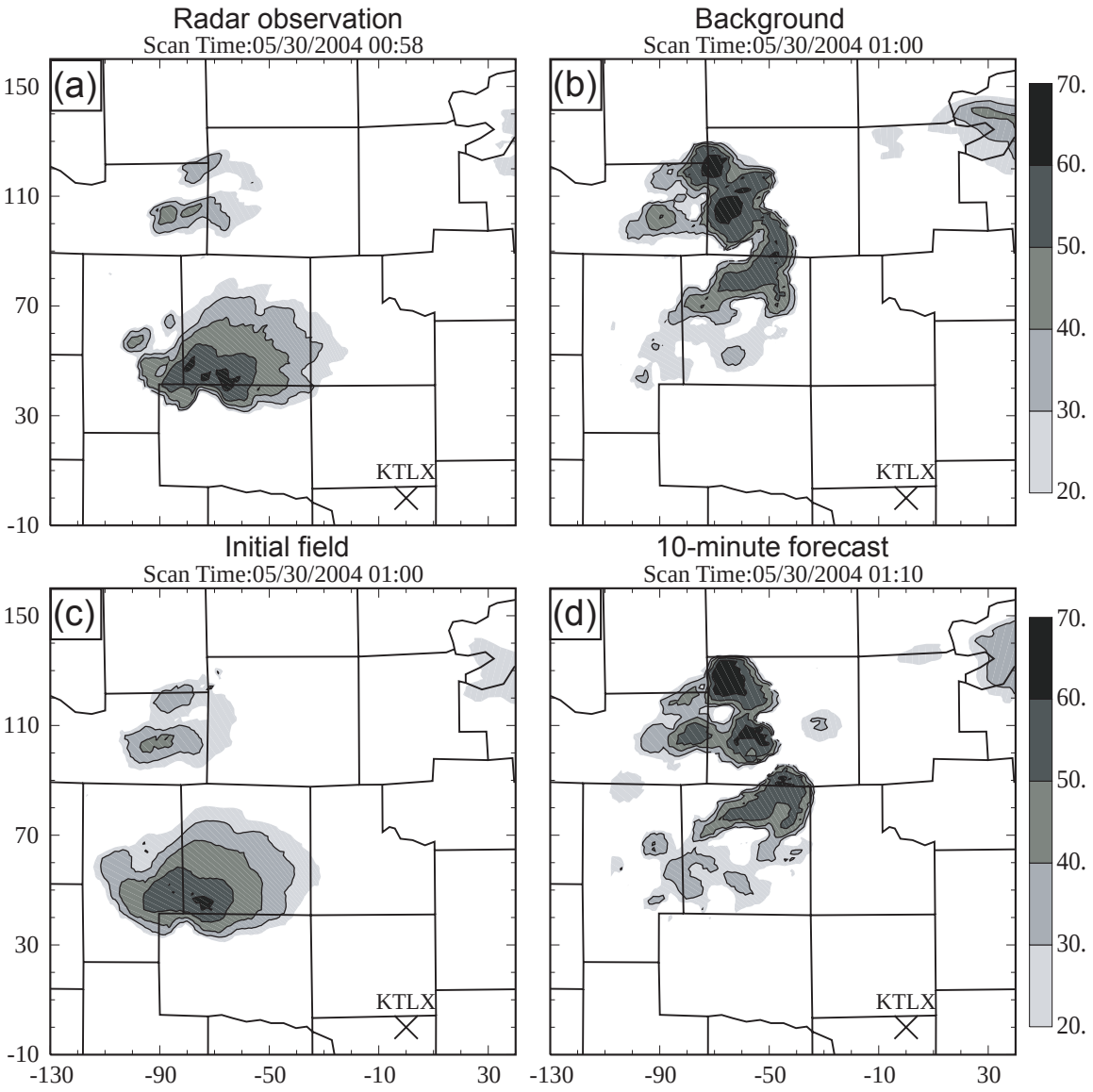

Fig. 5.7 Reflectivity fields of radar observations, the analysis background at 0100 UTC (for the last analysis of the assimilation cycles), the initial condition, and the 10-minute forecast from experiment PCLD. Reflectivity fields have been mapped to the 1.14° elevation of the KTLX radar

first 10 minutes of forecast and remains throughout the entire 3 hours of forecast.

The above analysis indicates that the new storm disturbances added by the cloud analysis procedure are not sufficient in building up a properly balanced storm in the initial condition. On the other hand, the original well developed storm systems in the

background are not effectively removed. One approach to solving this problem is to shift the background storms to the right location while preserving their structure. This idea has been exploited in Brewster (2003a, b) with some success. In the next section, a simple phase correction method is applied to this case and its effectiveness is examined.

5.3.2 Results of phase-corrected assimilation and forecast

In last section, it is found that the large phase errors of storm systems in the analysis background can cause the large phase errors in the forecast. Actually, such phase errors are common sources of problems in the storm-scale predictions. Brewster (2003a; 2003b) developed an automated system of identifying and correcting forecast displacement errors using high-resolution data such as those from radar. Here, for simplicity, we test a simple method that extracts storm disturbances from their incorrect locations in the background and then move them to the proper location. The amount of spatial displacement is currently determined subjectively.

In our simple scheme, a 1-hour 3-km forecast is made starting from a 0000 UTC analysis that includes only conventional data without the cloud analysis. No convective storms develop during the forecast. The storm disturbances in the background of the final analysis (at 0100 UTC) in original PCLD are extracted by subtracting the aforementioned 1-hour forecast valid at the same time. The extracted storm disturbances are then moved south-southeastward by 50 km based on the radar observation of the real storm, and they are then added to the aforementioned 1-hour forecast fields to form a new background to be used by the 0100 UTC analysis. Forecast then starts from this analysis. This experiment is named PCLDPC and the results of its 3-hour forecast are shown in Fig. 5.8 for the same times shown in Fig. 5.5.

Comparisons among the radar observations and the forecasts of PCLD and PCLDPC show that this simple phase correction procedure works effectively in reducing the location error of the predicted storms (Fig. 5.4, Fig. 5.5, and Fig. 5.8). The displacement error of the predicted storm is reduced to less than 10 km during most of 3-hour forecast, much smaller than the previous 50 km. Similar to PCLD, a hook-shaped echo is also present at the southern flank of the predicted storm in PCLDPC. However, two extra deficiencies are also noticed with the forecast of PCLDPC. One is a spurious, strong, left-moving cell that is located in west-central Garfield County at 0130 UTC (Fig. 5.8a) and lasts for over 1 hour (Fig. 5.8b). The same spurious cell also appears in PCLD but decays faster than in PCLDPC (Fig. 5.5a, b, and Fig. 5.8a, b). Another deficiency is that the predicted COK storm starts to dissipate 2.5 hours into the forecast in PCLDPC (Fig. 5.8e, f), but the storm persists in PCLD as a strong cell with maximum reflectivity exceeding 60 dBZ (Fig. 5.5f) throughout the forecast, which is closer to the observations. These deficiencies indicate that our simple phase correction scheme is not perfect, and it might cause certain undesirable disruption to the coherent storm structure present in the analysis background.

The wind and vertical vorticity fields at the surface and 3 km MSL from PCLDPC are shown in Fig. 5.9 for 0200, 0300, and 0400 UTC 30 May. Similar to PCLD, an isolated, well-organized column of strong vorticity is found due north of Piedmont at 0200 UTC (Fig. 5.9a, b) and due south of Meridian at 0300 UTC (Fig. 5.9c, d). This strong vorticity column gives a good indication of tornadogenesis potentials that in reality produced several tornadoes (see Table 5.1). Similar to the reflectivity field, the strong vorticity column also disappears a little too fast.

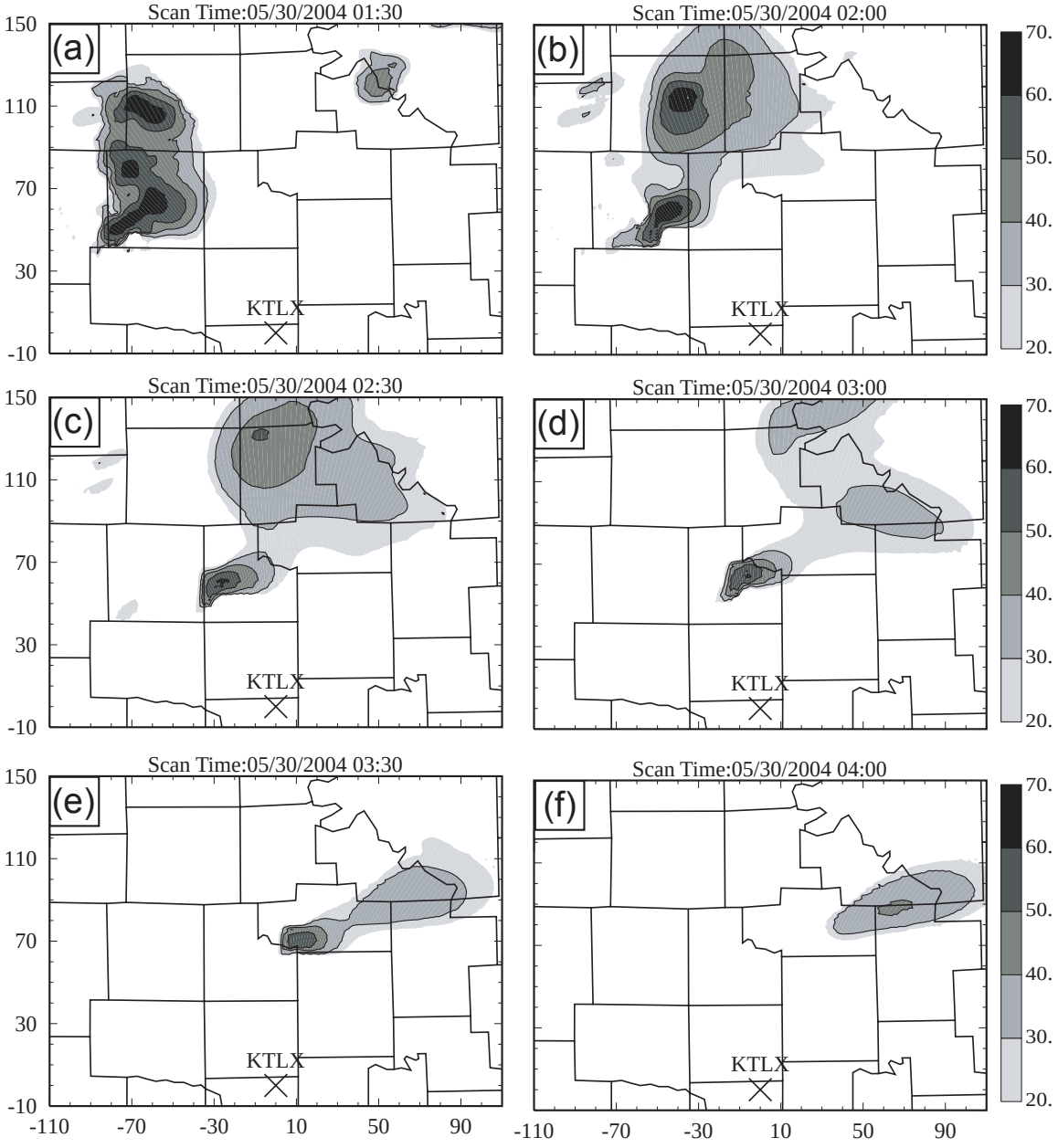

Fig. 5.8 Similar to Fig. 5.5, except that they are from experiment PCLDPC.

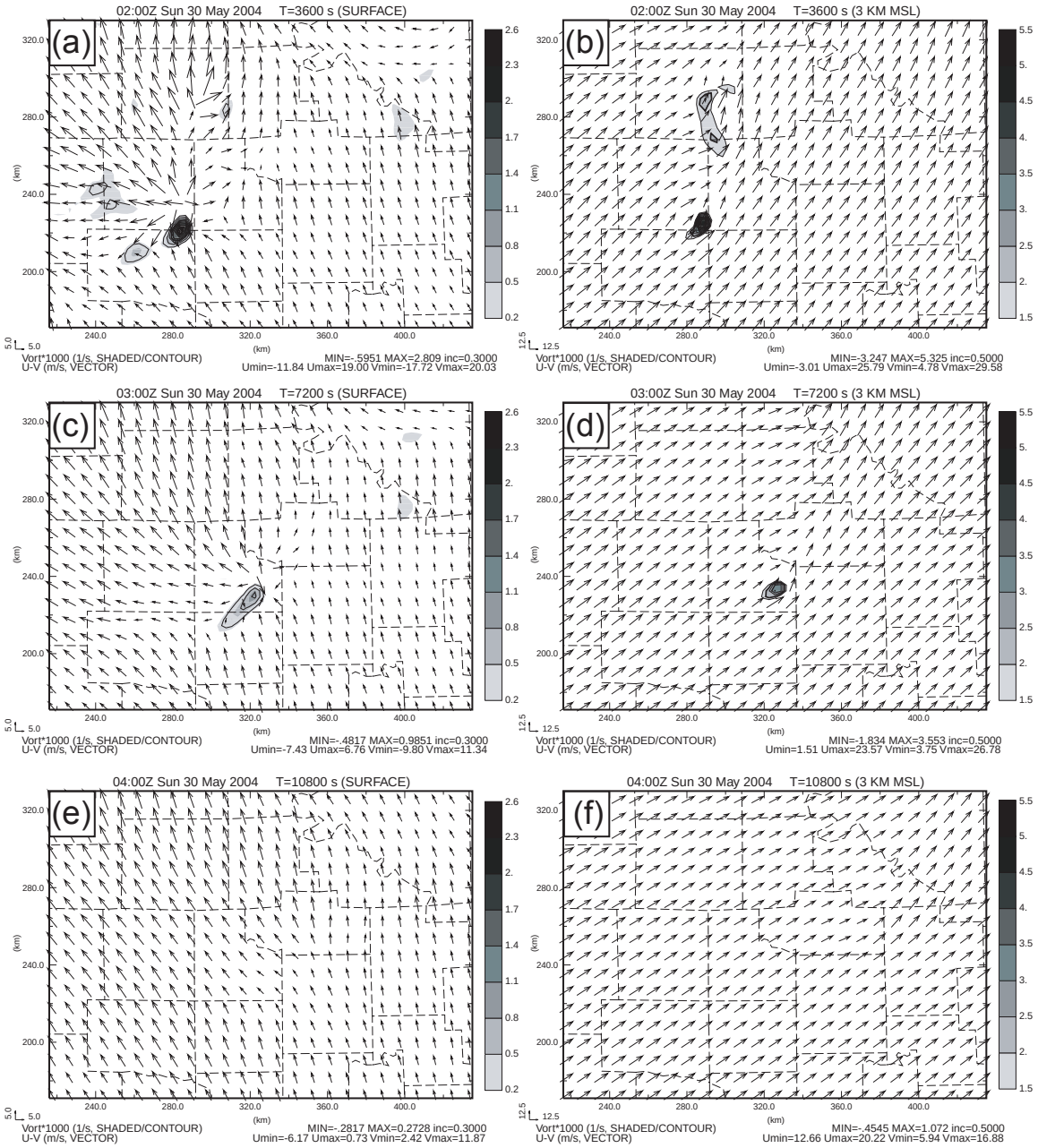

Fig. 5.9 Similar to Fig. 5.6, except that they come from PCLDPC

5.4 Results of experiments on dual-Doppler analysis of radial velocity data

In this section, the results from four experiments, SnglVrZ, DualVrZ, SnglVr, and DualVr (c.f. Table 5.2), are analyzed to study the use of dual-Doppler analysis of radial velocity data.

5.4.1 Results of 3DVAR radial velocity analysis

To study the impact of the dual-Doppler analysis of radial velocity data using the ARPS 3DVAR, the analysis increment fields of horizontal winds at the 11th level of the analysis grid for 0100 UTC, using both KTLX and KVNX radars or one of the two, are plotted in Fig. 5.10b, c, and d, respectively, while the observed low-elevation level reflectivity field from the KTLX radar at 0058 UTC is plotted in Fig. 5.10a. At this time, the central Oklahoma storm (the COK storm) was observed by the two radars from about the same distance and at nearly a right angle (Fig. 5.10a). The storm showed a well-defined hook echo at its southern flank (Fig. 5.10), indicating strong circulations here. When single-radar radial velocity data are used without the mass divergence constraint, the wind analysis increments are all along the beam direction and no cross-beam components are created by the analysis (Fig. 5.10c, d). However, the wind increments analyzed from different radar are almost perpendicular to each other in the storm area (c.f., Fig. 5.10) and the analysis using data from both radars successfully creates a cyclonic circulation around the western part of the storm and a convergence center at the center of the hook echo (Fig. 5.10a, b).

As an indicator of the vigor of the storms, the vertical velocity, *w*, at 4 km MSL from the assimilation results of all four experiments are plotted in Fig. 5.11, together with

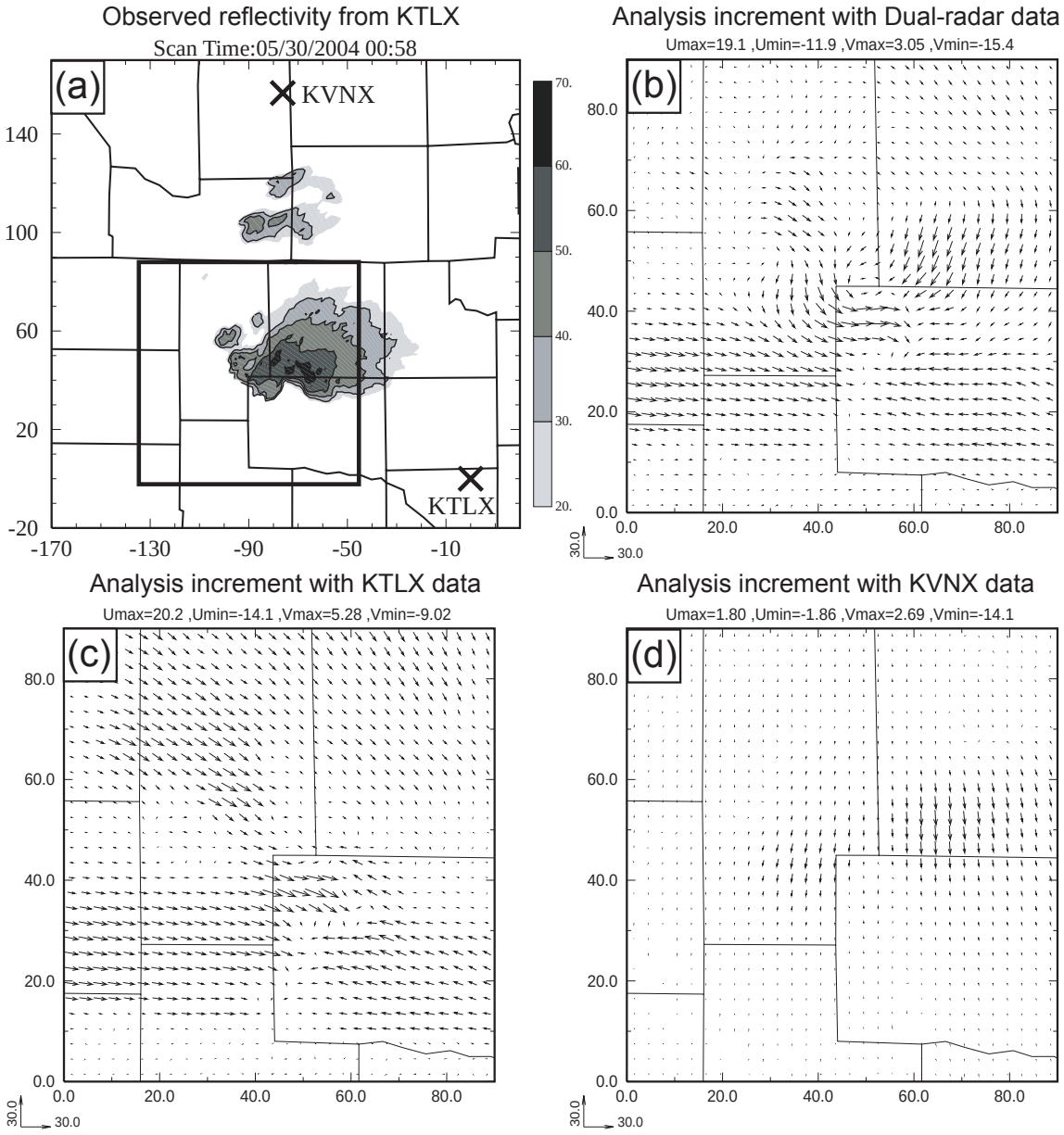

Fig. 5.10 (a), observed low-elevation level reflectivity from the KTLX radar at 0058 UTC and the locations of the KTLX radar and KVNX radar (marked as ×). The square shows the domain of panels (b)-(d). (b), horizontal wind analysis increments at the 11th level of the analysis grid from 0100 UTC radial velocity analysis using both the KTLX and KVNX radar observations. (c), the same as (b) except that only the KTLX radar observations are used. (d) the same as (b) except that only the KVNX radar observations are used.

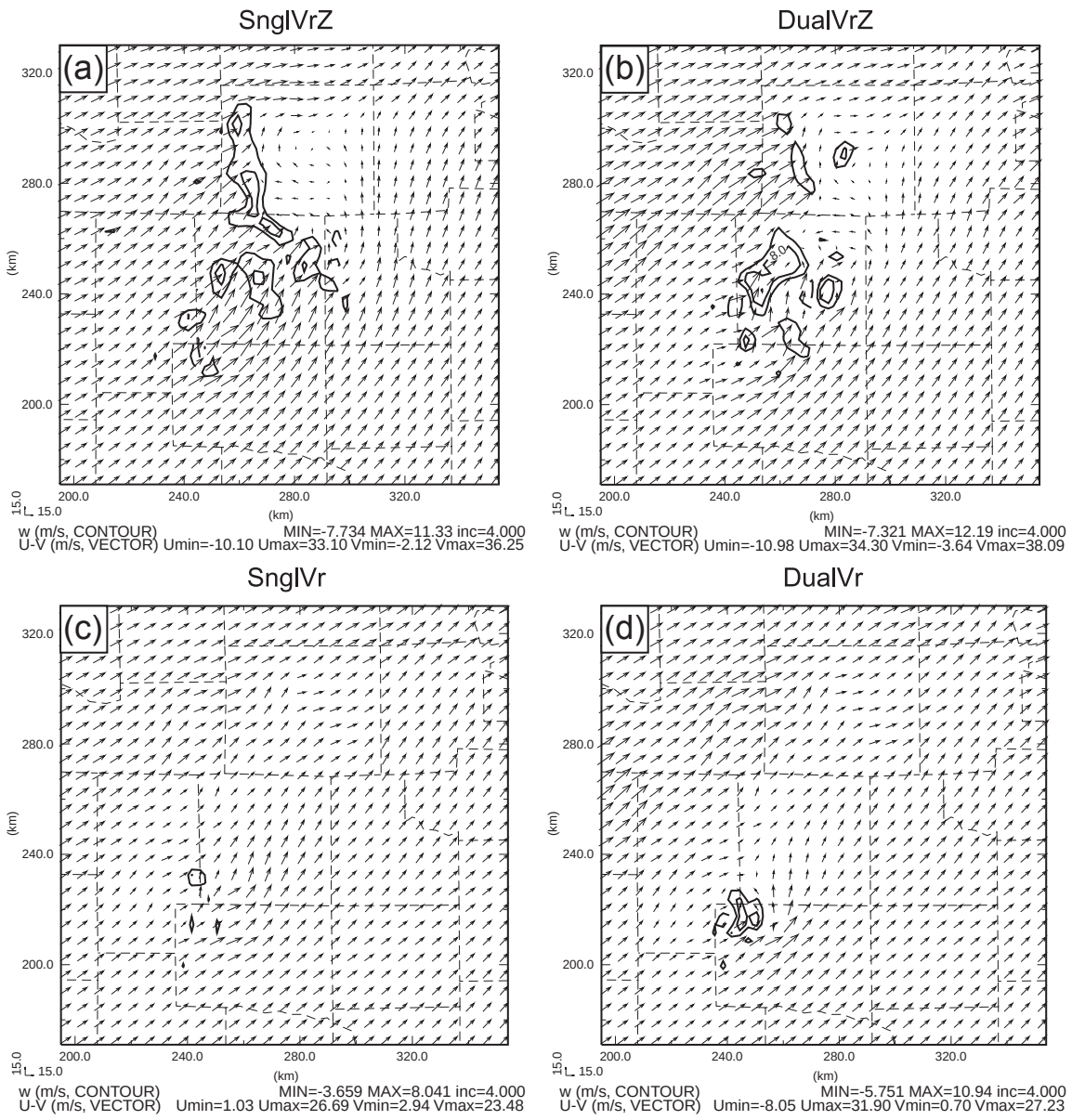

Fig. 5.11 Vertical velocity (contour) and wind fields (vector) at 4 km MSL from the assimilation results of experiments SnglVrZ, DualVrZ, SnglVr, and DualVr. The domain shown is 60 km × 60 km in size, covering the portion of the 3-km grid between 195 to 355 km in the east-west direction and 170 to 330 km in the south-north direction.

the horizontal wind vectors. When reflectivity is used through the cloud analysis procedure in SnglVrZ and DualVrZ (Fig. 5.11a, b), the main centers of *w* related to the COK storm are large and strong but lead the observed storm toward the northeast in

position by about 30 km (Fig. 5.10a). When the reflectivity is not used in SnglVr or DualVr (Fig. 5.11c, d), the main *w* centers are small but at the right position near the hook echo of the storm (Fig. 5.10a). So, the temperature, moisture, and hydrometer adjustments in the cloud analysis procedure based-on the reflectivity dominate the building up of the storm in the assimilation. With the use of data from both radars, the *w* centers related to the COK storm in DualVrZ are better organized than in SnglVrZ (Fig. 5.11a, b) and those in DualVr are stronger and larger than in SnglVr (Fig. 5.11c, d).

5.4.2 Results of the first-hour forecasts

In the study on the 28 March 2000 Fort Worth case in Chapter 3, we find that the use of radial velocity data can incrementally improve the storm forecast, especially for the wind fields, but the storms built up from the assimilation using radial velocity data alone last for only half an hour (c.f. results of experiment VR of Chapter 3). In this section, the goal is to study the impacts of the single and dual-Doppler wind analyses on the storm forecast; and the first-hour forecasts, between 0100 and 0200 UTC, from the four experiments are analyzed in detail in this section.

The observed low-elevation level reflectivity fields from the KTLX radar are plotted in Fig. 5.12 at 0058, 0119, 0142, and 0202 UTC 30 May 2004. During the period of the first-hour forecast, the observed COK storm propagated eastward from southwestern to southeastern Kingfisher County (Fig. 5.12), with a well-defined hook echo located at its southern flank, which indicates the supercell and tornadic characteristics of the storm.

For SnglVrZ, which uses both V_r and Z data from the KTLX radar only, the predicted reflectivity fields mapped to the 1.23° elevation of the KTLX radar from the

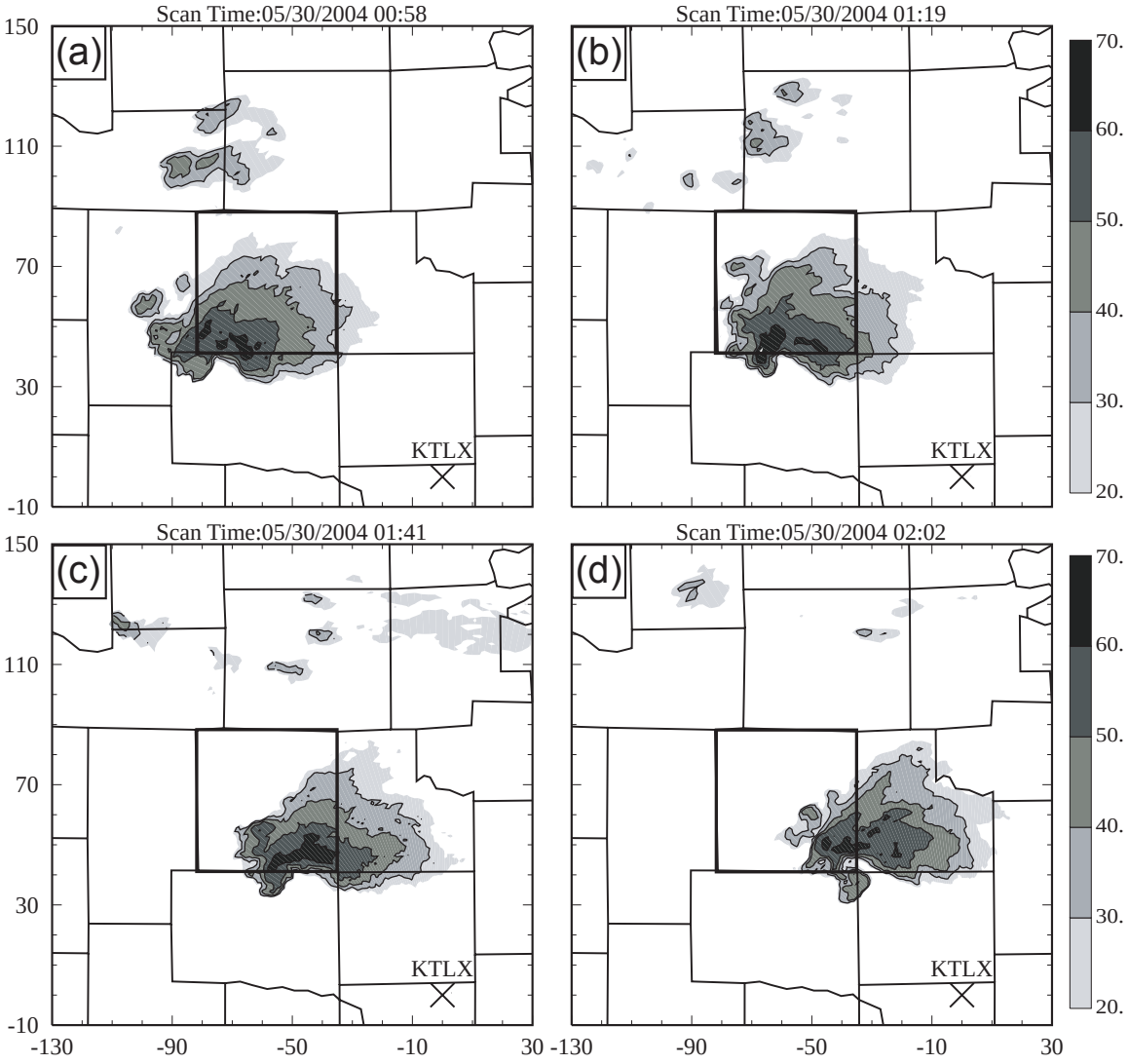

Fig. 5.12 Observed low-elevation level reflectivity fields from the KTLX radar at 0058, 0119, 0142, and 0202 UTC 30 May 2004. The domain is the same as Fig. 5.11. The x and y distances are in kilometer and are relative to the KTLX radar marked by ×. Kingfisher County is highlighted.

first hour of forecast are plotted in Fig. 5.13 at 20-minute intervals. The reflectivity field in the initial condition (Fig. 5.13a) should more or less match the observations shown in Fig. 5.12a because the direct use of the observations in the cloud analysis; it does not contain as many of the details though because of the relatively coarse 3-km resolution of

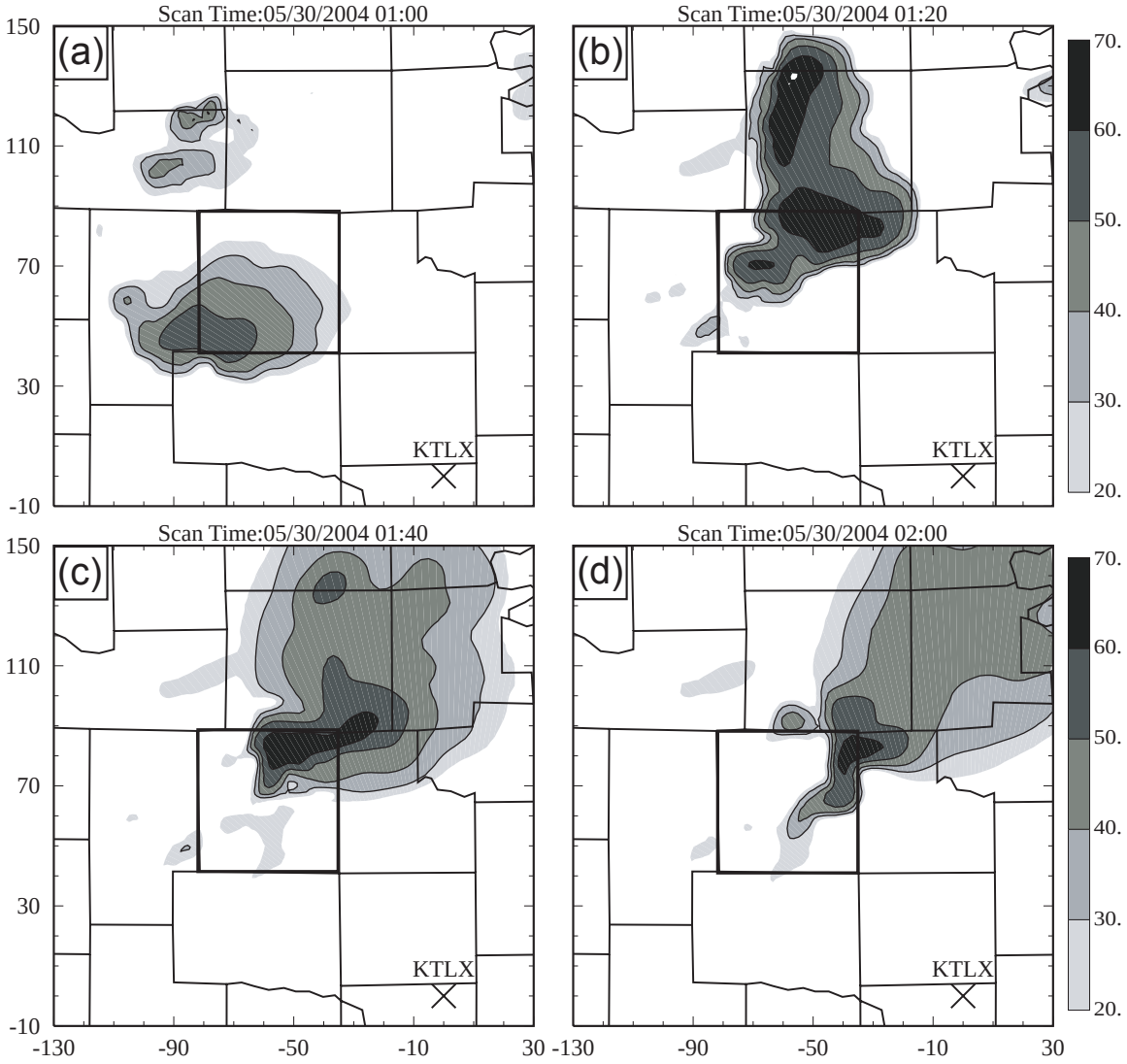

Fig. 5.13 Predicted reflectivity fields mapped at the 1.23° elevation of the KTLX radar from the first-hour forecast of experiment SnglVrZ at 20 minute intervals. The domain and coordinates are the same as Fig. 5.12. The reflectivity contours are 30, 40, 50, and 60 dBZ. Kingfisher County is highlighted

the analysis grid. Only 20 minutes into the forecast, the predicted storm at 0120 UTC has quickly propagated to the northeastern corner of Kingfisher County and leads the observed storm north-northeastward in position by about 40 km (Fig. 5.13b, Fig. 5.12b). The reason for this large position error is discussed in section 5.3 and the error can be

effectively removed through a simple phase correction procedure. Here, although the radar data are used at a higher frequency (every 5 minutes) than in section 5.3 (10 minutes there), the large phase error still develops in the initial period of forecast. Similar to experiment PCLD in section 5.3, the ensuing 40-minute forecast predicts a slow eastward propagation of the COK storm, which ends up on the northern portion of the east border of Kingfisher County (Fig. 5.13c, d); this eastward propagation is similar to that of the observed storm, except for the northward displacement error of about 40 km throughout this 40-minute period (Fig. 5.12c, d). The predicted storm at 0200 UTC also contains a well-defined hook echo (Fig. 5.13d), indicating the supercell feature of the predicted storm. There is more of a north-south orientation in the predicted storm while the observed one has a more east-west orientation at this time.

The corresponding predicted reflectivity fields from DualVrZ are plotted in Fig. 5.14. When the additional radial velocity observations from the KVNX radar are included in the 3DVAR wind analysis in this experiment, the northward displacement of the COK storm during the first 20 minutes still occurs (Fig. 5.14b), which is again followed by a slow eastward propagation (Fig. 5.14c, d). The similar quality of forecast in DualVrZ and SnglVrZ appears to be because the reflectivity data through the cloud analysis play the dominant role in building up the storm during the assimilation period, a result that is consistent with the finding of Chapter 3, on the Fort Worth case.

To isolate the effects of the radial velocity analysis, especially the dual-Doppler analysis, experiments SnglVr and DualVr, in which the cloud analysis procedure is turned off, are conducted. As for the previous two experiments, the same predicted reflectivity fields are plotted for these two experiments in Fig. 5.15 and Fig. 5.16,

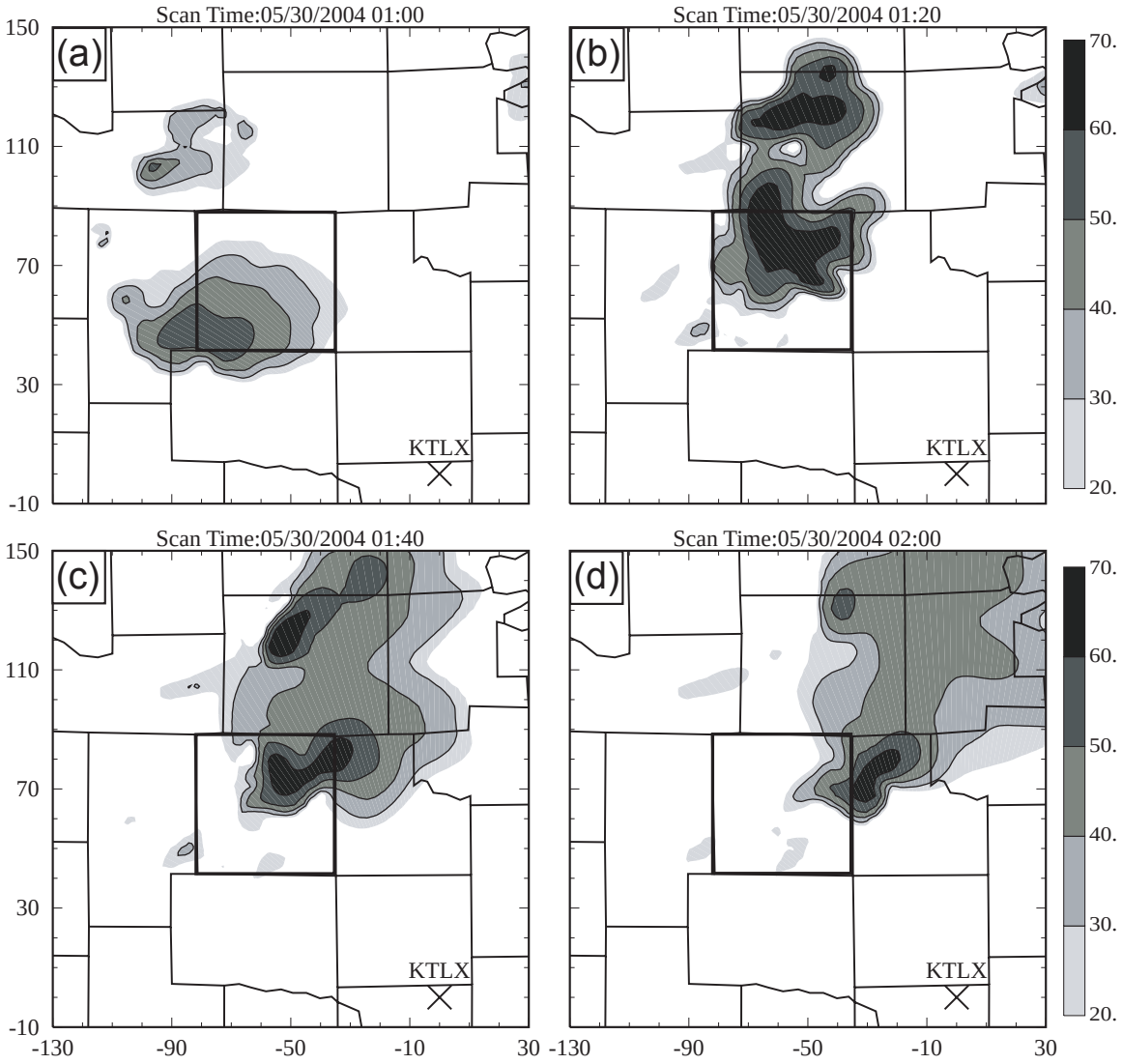

Fig. 5.14 Similar to Fig. 5.13, except that they are from experiment DualVrZ.

respectively. In these two experiments, the data assimilation still manages to build a storm by the end of assimilation (Fig. 5.15a, Fig. 5.16a), but the storm is much smaller and weaker than in the earlier experiments (c.f., Fig. 5.13a, Fig. 5.14a) and than the observations. In fact, only the western portion of the observed storm is established in the either experiment (Fig. 5.15a, Fig. 5.16a), consistent with the facts that the storm circulation is mainly located in the western portions of the storm system (Fig. 5.10b) and

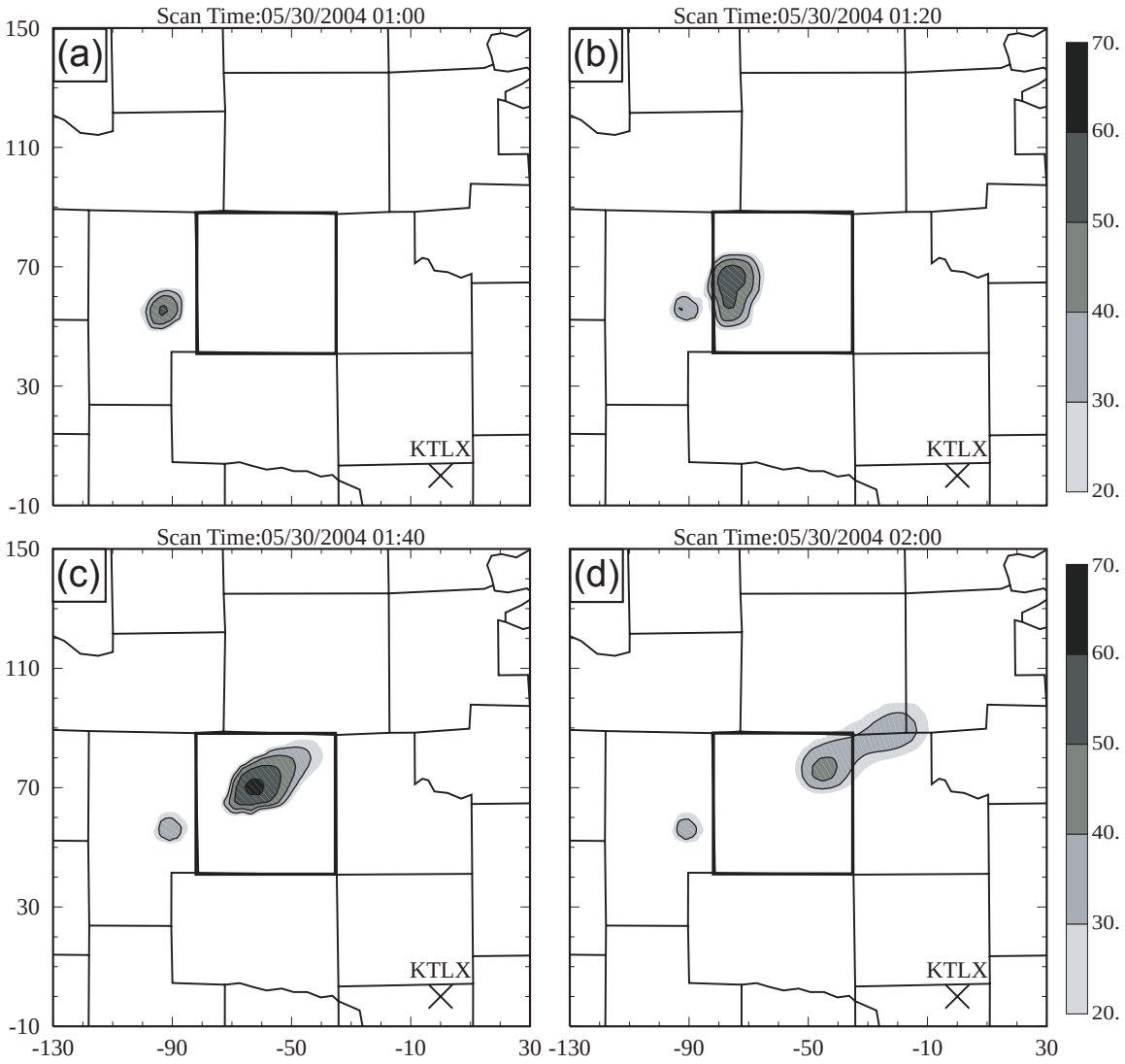

Fig. 5.15 Similar to Fig. 5.13, except that they are from experiment SnglVr.

only radial velocity data are assimilated. Helped by the additional data from KVNX, the analyzed storm in DualVr is stronger than that in SnglVr.

The SnglVr and DualVr forecasts in the first hour show large differences in the propagation of the COK storm. In SnglVr, the predicted storm propagates northeastward and ends up at the northeastern corner of Kingfisher County (Fig. 5.15b-d) by 0200 UTC. Note that the large position errors of the predicted storm in SnglVr dose not result from

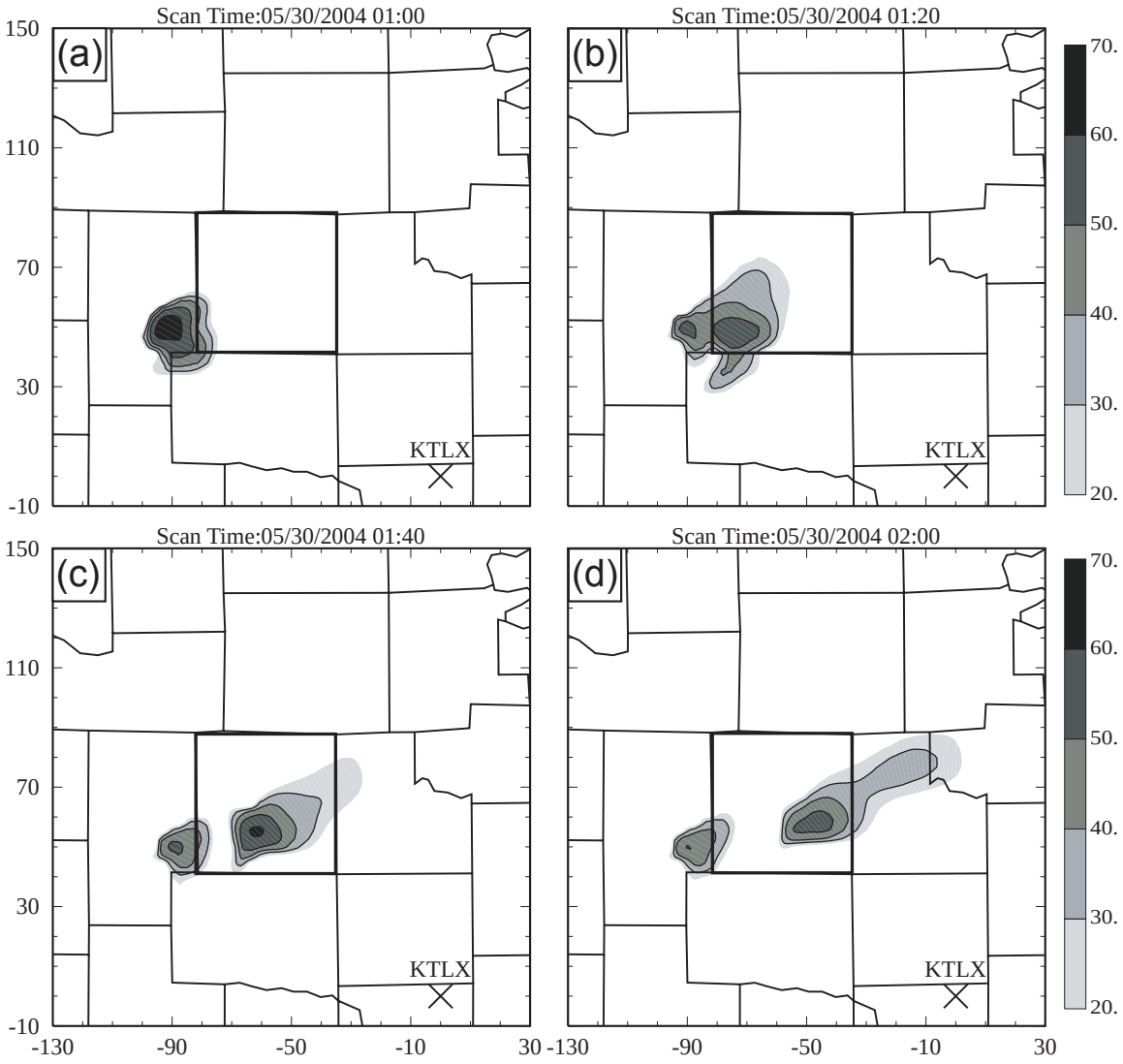

Fig. 5.16 Similar to Fig. 5.13, except that they are from experiment DualVr.

the assimilation but from the forecast. Different from all the other three experiments, DualVr predicts the storm moving eastward from the beginning of the forecast and ending up near the southeastern corner of Kingfisher County (Fig. 5.16b-d), which is close to the observed position at this time (Fig. 5.16, Fig. 5.12); the predicted storm, however, is too weak throughout the period and a spurious cell is left behind, near the southwestern corner of Kingfisher County.

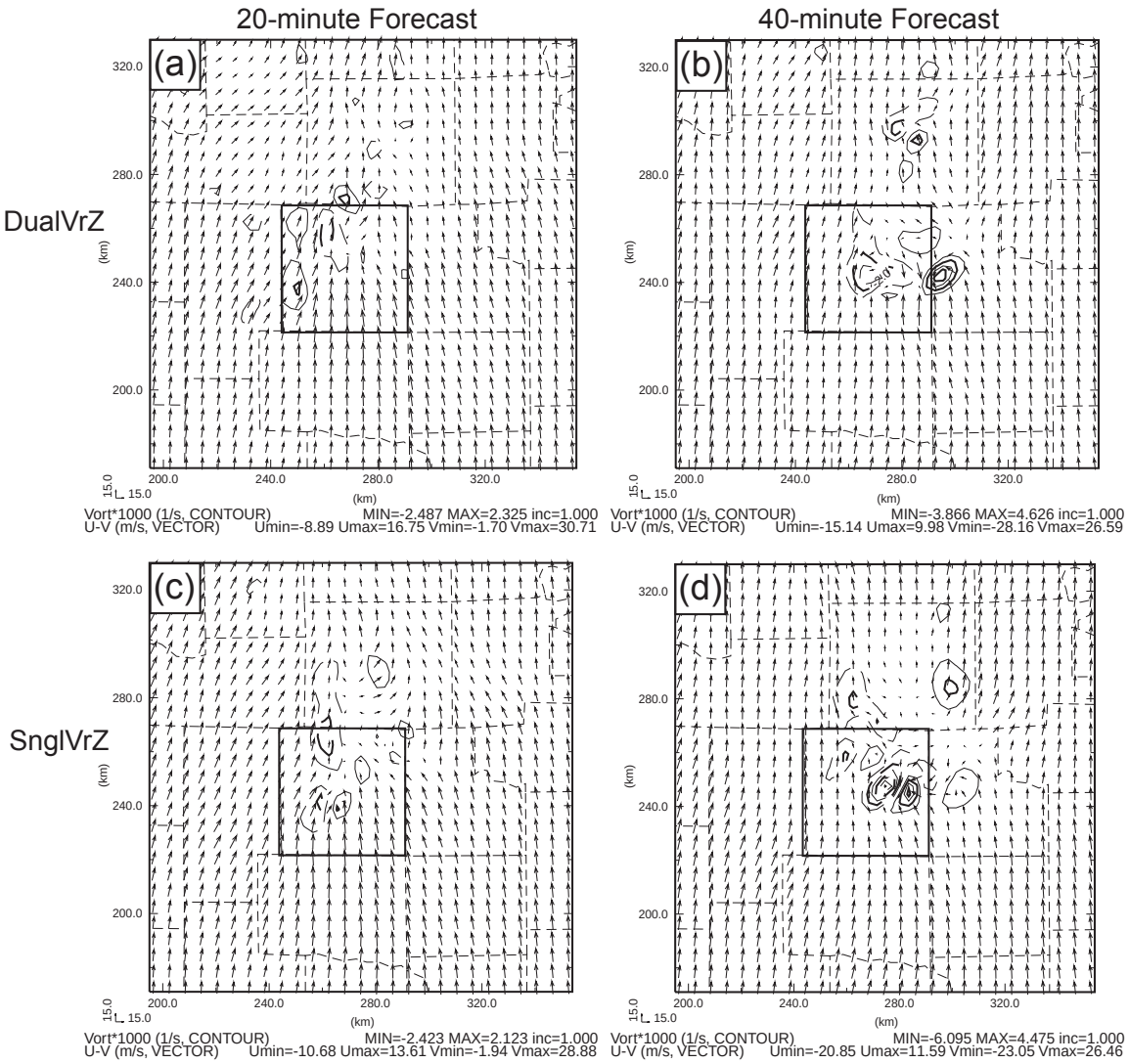

Fig. 5.17 Predicted wind (vectors) and vertical vorticity (contours) fields at 1 km MSL for 20 and 40 minute forecast of experiments DualVrZ, SnglVrZ, DualVr, and SnglVr. The domain is the same as Fig. 5.11. Kingfisher County is highlighted

To further investigate the effect of the dual-Doppler radar radial velocity data, the predicted wind and vertical vorticity fields at 1 km MSL from the 20 and 40-minute forecasts of DualVrZ, SnglVrZ, DualVr, and SnglVr are plotted in Fig. 5.17. Like the reflectivity fields, the predicted wind fields of DualVrZ and SnglVrZ show a large area of the disturbances related to the storm (Fig. 5.17a-d), while the wind fields of DualVr and

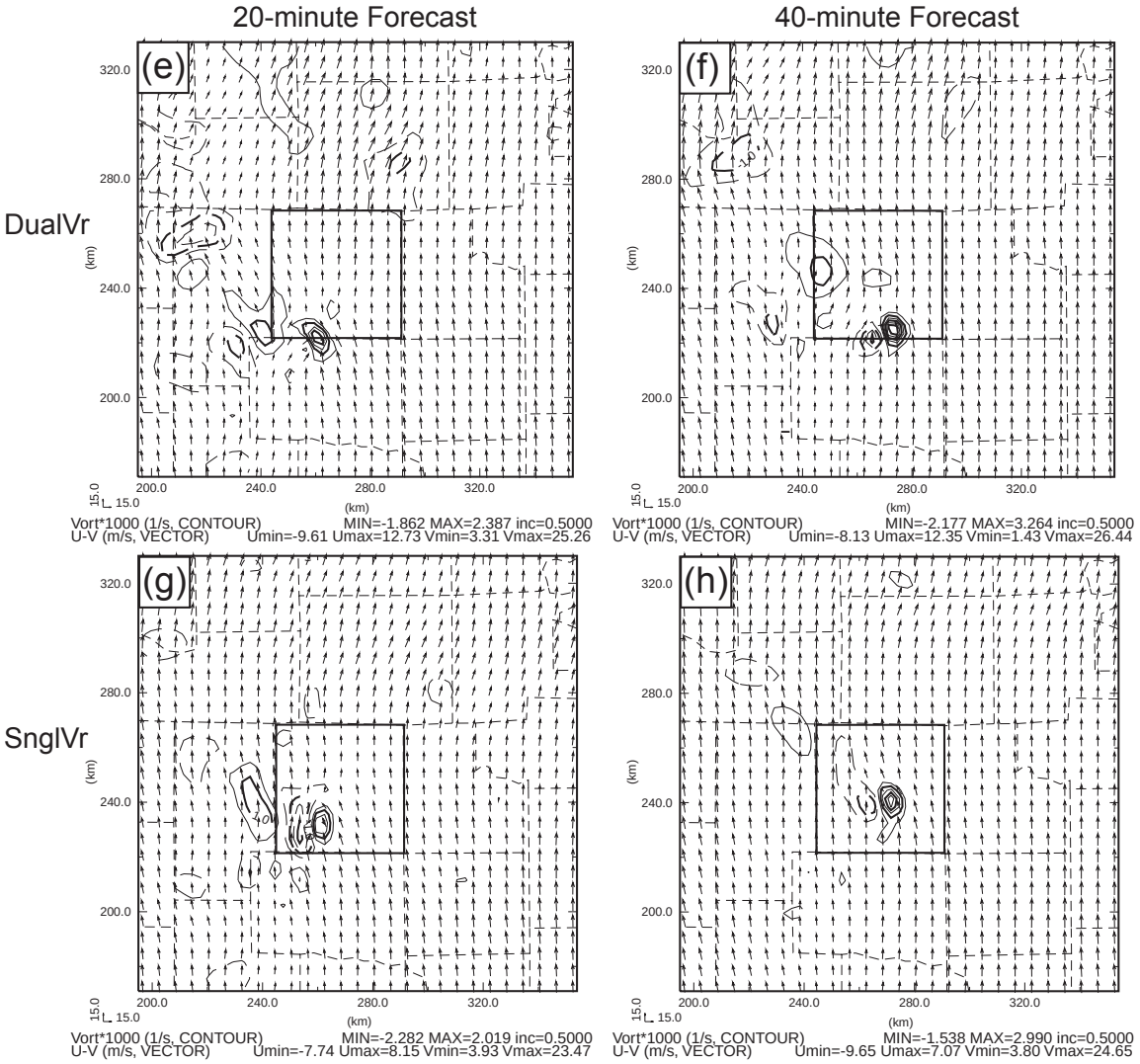

Fig. 5.17. Continued.

SnglVr contain only small areas of disturbances near the predicted storm (Fig. 5.17e-h). For all four experiments, the vorticity centers associated with the storm are all located at the southern flank of the echoes and their propagation follows the reflectivity fields. When radial velocity data are used alone in DualVr and SnglVr, the vorticity centers are better organized but weaker than in DualVrZ and SnglVrZ.

5.4.3 Long-term forecasting

Beyond the first hour, we show only the forecasts at 2 hours, or at 0300 UTC. The predicted reflectivity fields mapped at the 1.14° elevation of the KTLX radar are plotted in Fig. 5.18(a)-(d) for the four experiments, together with the corresponding observation. At this time, the COK storm in DualVr and SnglVr has totally disappeared (Fig. 5.18a, b). On the other hand, the storm in both DualVrZ and SnglVrZ remains as a supercell with a hook echo in its southern flank (Fig. 5.18c, d), but the location of the predicted storm deviates northward from the observed one by about 20 km for SnglVrZ and 30 km for DualVrZ (Fig. 5.18a, b, e). Again, these results are consistent with the previous results from the experiments on the phase correction (section 3 of this Chapter) and the use of the radial velocity analysis (section 3.4.3 in Chapter 3).

5.5 Summary and discussion

In this chapter, the 29 May 2004 central Oklahoma tornadic thunderstorm case is described and six preliminary 3-km experiments are conducted to initialize and predict the evolution of the tornadic thunderstorm from 0000 to 0400 UTC May 30. Two of the six experiments are used to identify the problem of large position error of the predicted storm and to test a simple procedure that corrects the location of the background storms. The other four experiments test the impact of assimilating data from an additional radar, and the relative effects of radial velocity and reflectivity data.

In the first two experiments either with or without the phase correction, the general characteristics of the central Oklahoma thunderstorm are captured. The rotation characteristics are clearly revealed in the forecasts by the presence of a hock echo and a strong column of large vertical vorticity. The predicted storm in the non-phase-corrected

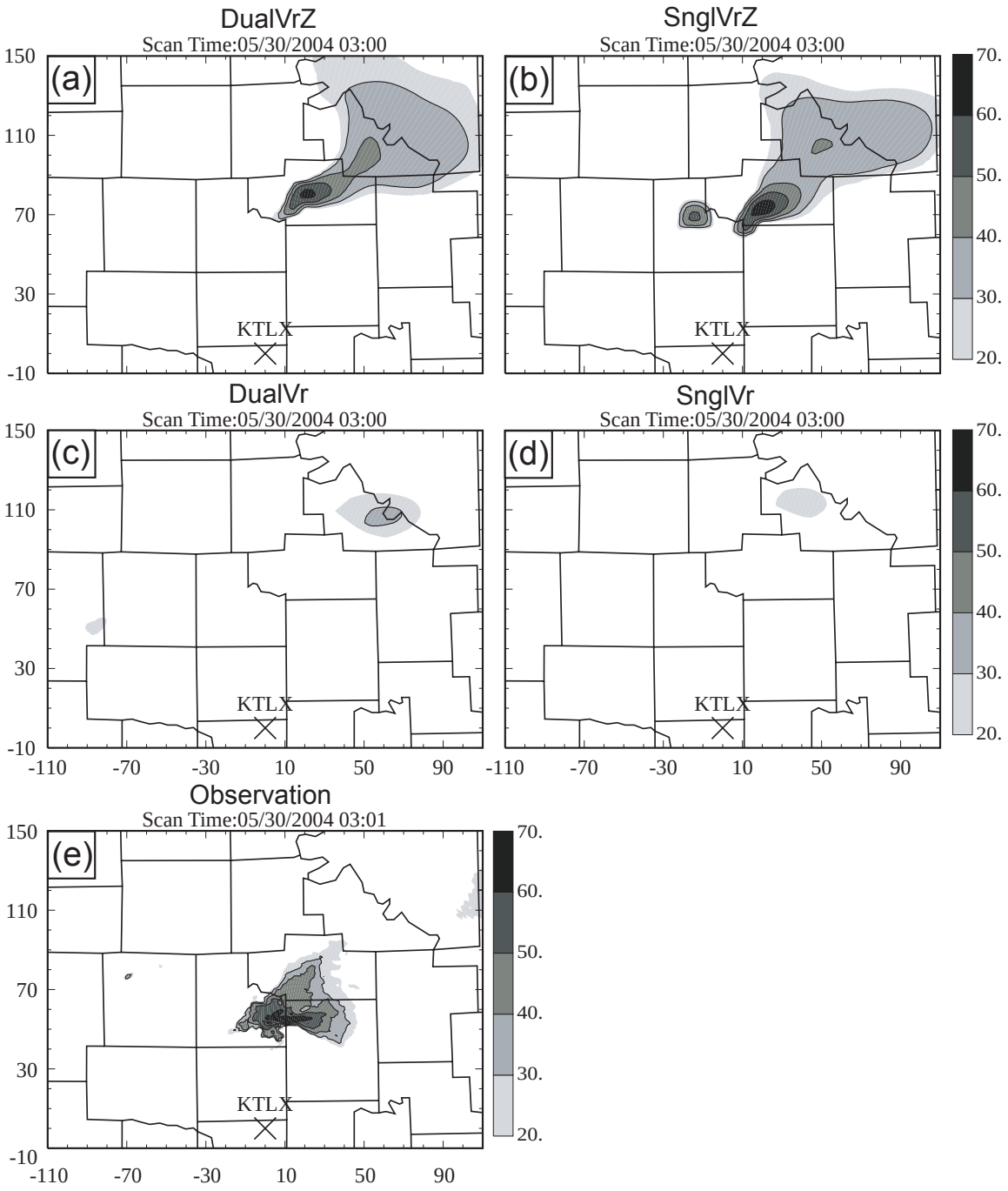

Fig. 5.18 (a)-(d): Predicted reflectivity fields mapped at the 1.14° elevation of the KTLX radar from the 2-hour forecasts of experiments DualVrZ, SnglVrZ, DualVr, and SnglVr. (e): Observed low-elevation level reflectivity field from the KTLX radar at 0301 UTC. The domain shown is 220 km by 160 km, representing the portion of the 3-km grid between 215 to 435 km in the east-west direction and 170 to 330 km in the north-south direction. The reflectivity contours are 30, 40, 50, and 60 dBZ. The x and y distances are in kilometer and are relative to the KTLX radar marked by ×.

case maintains its intensity and rotational characteristics for the entire 3 hours of forecast, as did the real storm. The phase-corrected storm propagates along the same path as the observed storm but starts to dissipate 2.5 hours into the forecast. The cause of this need further study. Imbalances among model fields introduced by the phase-correction procedure might be the cause.

To study the use of dual-Doppler radar radial velocity data, four 3-km experiments are conducted with 4 different radar data combinations: the use of single-radar radial velocity and reflectivity, the use of dual-radar radial velocity along with the single-radar reflectivity, the use of single-radar radial velocity alone, and the use of dual-radar radial velocity alone. Otherwise, the experiments use the same assimilation and forecast configurations, specifically, a one-hour long assimilation window from 0000 to 0100 UTC with 5-minute intervals and a 3-hour forecast starting from assimilated initial condition.

It is found that, with the current ARPS 3DVAR and cloud analysis procedure, the cloud analysis with reflectivity data plays a key role in establishing the model storms during the assimilation period; the subsequent forecast produces a long-lasting strong supercell but with a significant displacement error that persists throughout the forecast. In contrast, assimilating radial velocity data alone is far from sufficient to establish a well-balanced storm; the predicted storm is weak and only lasts for about one hour. Although these conclusions are consistent with those drawn from the previous experiments, an interesting behavior is found with the experiment in which only dual-Doppler radar radial velocity data are assimilated; in this case, the predicted storm propagates at the similar speed and direction as the observed storm during the first hour of forecast.

The large differences in the storm motion are from the cloud analysis and 3DVAR analysis of radial velocity data. We found in section 3 of this Chapter that the current cloud analysis procedure can not effectively remove disturbances associated with spurious storm cells in the analysis background. When dual-Doppler radar analysis of radial velocity data is performed without reflectivity data, spurious disturbances either do not develop or are more effectively suppressed.

From the high resolution experiments of Chapter 4, it is found that the storm in the 1-km experiments can be triggered much faster and is stronger than that in the 3-km experiments. Also, a 1-km grid can more effectively retain circulation details contained in the radial velocity data from two Doppler radars, and the dual-Doppler wind analysis will be more accurate. We plan to repeat the experiments on the dual-Doppler wind analysis of this chapter using a 1-km grid.

Chapter 6

General Summary and Future Work

In this study, the WSR-88D Doppler radar observations on three tornadic thunderstorms, namely, the 28 March 2000 Fort Worth tornadic thunderstorms (the Fort Worth case), the 8 May 2003 Oklahoma City tornadic thunderstorm (the OKC case), and the 29 May 2004 central Oklahoma tornadic thunderstorm (the central OK case), are used in the ARPS assimilation and forecast system to study the impact of radar data on thunderstorm forecast.

Although all three cases use a similar procedure of intermittent assimilation cycles with the radial velocity and conventional data analyzed by the ARPS 3DVAR and the reflectivity data analyzed by the ARPS cloud analysis procedure, they have their own unique features and each focuses on different aspects of the use of radar data. The Fort Worth case included a cluster of thunderstorms; the impacts of reflectivity and radial velocity data together or individually, recent modifications to the cloud analysis procedure, and different formulations of the mass divergence constraints are studied in detail. The OKC case involved a single fast-growing supercell; the impact of the various configurations of radar data assimilation on the storm forecast and the use of radar data at a higher grid resolution are studied. For the central OK case that included a single long-lasting supercell, a simple phase-correction scheme and the dual-Doppler wind analyses are tested. From these three cases, several general conclusions can be drawn.

When applied to the above three cases, the ARPS 3DVAR shows a good ability in analyzing observations from different sources, including those from radiosonde, wind

profilers, surface stations, and Doppler radars. Combined with intermittent data assimilation cycles and a cloud analysis procedure, the positive impacts of radar data are effectively demonstrated for thunderstorm initialization and forecasting.

Starting from the assimilated initial conditions that include radar data, the best prediction for tornadic thunderstorms in the Fort Worth case is able to match up individual storm cells on the 3-km grid for up to two hours into the prediction with timing errors of less than 15 minutes and location errors of less than 10 km. For the OKC case, the forecast from the initial condition in which radar data are properly assimilated can accurately capture the propagation of the storm for 2.5 hours. The best 3-km forecast for the central OK case is from the initial condition that employs the phase-correction procedure during the assimilation.

To obtain the best predictions, many factors in the assimilation configurations and the analysis schemes need to be considered. In this study, the modifications to the new cloud analysis procedure, especially the in-cloud temperature adjustment scheme, the coefficients and formulations of the mass divergence constraints in the 3DVAR analysis, the analysis frequency of cycles, the length and coverage of the assimilation window, the phase correction procedure, and the use of dual-Doppler radar data, are carefully designed and tested to maximize the positive impacts of assimilating the radar data.

Further, from the 3-km experiments of the Fort Worth and the central OK cases, it is found that reflectivity has a greater positive impact on the storm forecast than radial velocity when using the current 3DVAR and cloud analysis procedure, while the use of radial velocity along with the reflectivity via the cloud analysis does incrementally improve the storm forecast, especially in terms of the strong low-level vorticity centers

associated with tornadogenesis. When single-Doppler radar radial velocity data (in addition to conventional data) are used without reflectivity data, the predicted storms dissipate too quickly in the forecast, but when dual-Doppler radar radial velocity data alone are assimilated for central OK case, the predicted storm is better established and the storm propagation is significantly improved in the first hour of forecast.

The 1-km horizontal resolution experiments for the OKC case capture in great details the parental features of the tornado such as the mesocyclone and the associated hook echo in both the assimilation and the first 50 minutes of forecast. The experiments also indicate that the use of radial velocity data is crucial on the 1-km grid, in order to induce these tornadic circulations; a suitable imposition of the mass divergence constraint can also improve the prediction of detailed flow structure.

Starting from the fields interpolated from a 1-km assimilation result, a 100-m horizontal resolution forecast produces an F1 to F2 tornado that lasts for 5 minutes in a 9-minute forecast. This results, though still preliminary, presents that the first successful simulation of such a type, which uses a full physics model and an analyzed initial condition from real data.

In this study, the ARPS assimilation and forecast system shows a considerable ability in radar data assimilation and storm forecasting, but there remains much room for improvement. In the near future, additional studies are planned to further investigate the assimilation of radar data and the forecast of storms.

So far, the dual-Doppler analysis has only been tested on a 3-km grid for the 29 May 2004 central Oklahoma case, but experiments with a 1-km grid should improve the analysis and forecast. The dual-Doppler wind analyses will be performed on a 1-km grid.

Also, this storm was observed by two Shared Mobile Atmospheric Research and Teaching (SMART) radars at short distances during the times of some of the tornadoes. Data from these additional radars can potentially be analyzed and they may further improve the wind analysis, especially at the low levels where the WSR-88D radars can not observe at a distance.

The 1-km experiments capture many of the details of the tornadic features in the first 50 minutes of forecast but give rise to a large number of small, spurious, cells in the forecast after one hour. Also, the predicted main storm propagates too quickly. The cause of these problems will be carefully investigated

In this study, the preliminary 9-minute forecast at a 100-m horizontal resolution demonstrates the ability of the ARPS model in producing a realistic tornado. Longer 100-m forecasts with the initial condition and boundary conditions from a better 1-km forecast are planned in an effort to produce more realistic tornado forecasts. Nested within the 100-m grid, experiments at even higher resolutions of, e.g., 50-m and 25-m are planned to hopefully capture the internal structures of the tornadoes. With model data at high spatial and temporal resolutions, the mechanisms of tornadogenesis and evolution can be analyzed to help us better understand the real-world tornado events.

The simple phase-correction scheme applied to remove large position errors in the assimilation results of the 29 May 2004 central OK thunderstorm case can be replaced by a more sophisticated scheme such as the one described by Brewster (2003a; 2003b). The application of a more complex, variational scheme is expected to reduce the inconsistencies among variables induced by the phase-correction procedure and hopefully produce longer-lasting storms than currently achieved in the forecast

The experiments with the 3-km horizontal resolution for all three cases capture well the propagation and evolution of the storms for up to 2 hours during the forecast. However, the longer forecasts show large increases in both position and intensity errors for the predicted storms. Predictability analyses on convective storm forecast at a 3-km resolution will be valuable, before we spend more time trying to improve various aspects of our data assimilation and prediction.

References

Albers, S. C., J. A. McGinley, D. A. Birkenheuer, and J. R. Smart, 1996: The local analysis and prediction system (LAPS): Analysis of clouds, precipitation and temperature. *Wea. Forecasting*, 11, 273-287.

Baldwin, M. E., S. Lakshmivarahan, and J. S. Kain, 2002: Development of an "events-oriented" approach to forecast verification. *15th Conf. Num. Wea. Pred.*, San Antonio, TX, Amer. Meteor. Soc.

Bratseth, A. M., 1986: Statistical interpolation by means of successive corrections. *Tellus*, 38A, 439-447.

Brewster, K., 1996: Application of a Bratseth analysis scheme including Doppler radar data. *Preprints, 15th Conf. Wea. Anal. Forecasting*, Norfolk, VA, Amer. Meteor. Soc., 92-95.

—, 2002: Recent advances in the diabatic initialization of a non-hydrostatic numerical model. P*reprints, 15th Conf on Numerical Weather Prediction and 21st Conf on Severe Local Storms,* San Antonio, TX, Amer. Meteor. Soc., J6.3.

Brewster, K. A., 2003a: Phase-correcting data assimilation and application to storm-scale numerical weather prediction. Part I: Method description and simulation testing. M*on. Wea. Rev.,* 131, 480-492.

—, 2003b: Phase-correcting data assimilation and application to storm scale numerical weather prediction. Part II: Application to a Severe Storm Outreak. Mo*n. Wea. Rev.,* 131, 493-507.

Bryan, G. H., J. C. Wyngaard, and J. M. Fritsch, 2003: Resolution Requirements for the Simulation of Deep Moist Convection. Mo*nthly Weather Review,* 131, 2394-2416.

Crum, T. D. and R. L. Alberty, 1993: The WSR-88D and the WSR-88D operational support facility. Bu*ll. Amer. Meteor. Soc.,* 74, 1669-1687.

Davies-Jones, R., R. J. Trapp, and H. B. Bluestein, 2001: Tornadoes and tornadic storms. Severe Convective Storms, I. Ch*arles A. Doswell, Ed., Amer. Meteor. Soc.,* 167-221.

Dowell, D. C. and L. J. Wicker, 2004: High-resolution analyses of the 8 May 2003 Oklahoma City storm. Part II: EnKF data assimilation and forecast experiments. Pr*eprints, 22nd Conf. on Severe Local Storms,* Hyannis, MA,, Amer. Meteor. Soc., CDROM, 12.5.

Droegemeier, K. K., 1990: Toward a science of storm-scale prediction. Pr*eprint, 16th conf. on Severe Local Storms,* Kananaskis Park, Alberta, Canada, Amer. Meteor. Soc., 256-262.

—, 1997: The numerical prediction of thunderstorms: Challenges, potential benefits, and results from real time operational tests. WMO *Bulletin, 4*6, 324-336.

Gal-Chen, T., 1978: A method for the initialization of the anelastic equations: Implications for matching models with observations. Mon*. Wea. Rev., 1*06, 587-

606.

Gao, J., M. Xue, A. Shapiro, and K. K. Droegemeier, 1999: A variational method for the analysis of three-dimensional wind fields from two Doppler radars. Mon. *Wea. Rev., 1*27, 2128-2142.

Gao, J., M. Xue, K. Brewster, and K. K. Droegemeier, 2004: A three-dimensional variational data analysis method with recursive filter for Doppler radars. J. *Atmos. Ocean. Tech., 2*1, 457-469.

Gao, J., M. Xue, A. Shapiro, Q. Xu, and K. K. Droegemeier, 2001: Three-dimensional simple adjoint velocity retrievals from single Doppler radar. J. *Atmos. Ocean Tech., 1*8, 26-38.

Gao, J., M. Xue, K. Brewster, F. Carr, and K. K. Droegemeier, 2002: New Development of a 3DVAR system for a nonhydrostatic NWP modeol. Pre*print, 15th Conf. Num. Wea. Pred. and 19th Conf. Wea. Anal. Forecasting, S*an Antonio, TX, Amer. Meteor. Soc., 339-341.

Harris, B. A. and G. Kelly, 2001: A satellite radiance-bias correction scheme for data assimilation. Qua*rterly Journal- Royal Meteorological Society, 1*27, 1453-1468.

Hayden, C. M. and J. Purser, 1995: Recursive filter objective analysis of meteorological fields: Applications to NESDIS operational processing. J. *Appl. Meteor., 3*4, 3-15.

Hu, M. and M. Xue, 2006: Impact of configurations of rapid intermittent assimilation of WSR-88D radar data for the 8 May 2003 Oklahoma City tornadic thunderstorm case. Mon. *Wea. Rev., C*onditionally accepted.

Hu, M., M. Xue, and K. Brewster, 2006a: 3DVAR and Cloud analysis with WSR-88D Level-II Data for the Prediction of Fort Worth Tornadic Thunderstorms. Part II: Impact of radial velocity analysis via 3DVAR. Mon. *Wea. Rev., I*n press.

Hu, M., M. Xue, J. Gao, and K. Brewster, 2006b: 3DVAR and Cloud analysis with WSR-88D Level-II Data for the Prediction of Fort Worth Tornadic Thunderstorms. Part I: Cloud analysis and its impact. Mon. *Wea. Rev., I*n press.

Kessler, E., 1969: On *the Distribution and Continuity of Water Substance in Atmospheric Circulations. V*ol. 32, Met*eor. Monogr., 8*4 pp.

Lilly, D. K., 1990: Numerical prediction of thunderstorms - Has its time come? Qua*rt. J. Roy. Meteor. Soc., 1*16, 779-798.

Lin, Y.-L., R. D. Farley, and H. D. Orville, 1983: Bulk parameterization of the snow field in a cloud model. J. *Climate Appl. Meteor., 2*2, 1065-1092.

Lorenc, A. C., 1992: Iterative analysis using covariance functions and filters. Qua*rt. J. Roy. Met. Soc., 1*18, 569-591.

Qiu, C. and Q. Xu, 1992: A simple adjoint method of wind analysis for single-Doppler data. J. *Atmos. Oceanic Technol., 9*, 588-598.

—, 1994: A spectral simple adjoint method for retrieving low-altitude winds from single-Doppler data. J. A*tmos. Oceanic Technology, 11*, 927-936.

Rogers, R. R. and M. K. Yau, 1989: A Sh*ort Course in Cloud Physics. 3r*d ed. Pergamon Press, 293 pp.

Schaefer, J. T., 1990: The critical success index as an indicator of warning skill. Wea. *Forecasting, 5,* 570-575.

Shapiro, A., S. Ellis, and J. Shaw, 1995: Single-Doppler radar retrievals with Phoenix II data: Clear air and microburst wind retrievals in the planetary boundary layer. J. *Atmos. Sci., 52*, 1265-1287.

Smith, P. L., Jr., C. G. Myers, and H. D. Orville, 1975: Radar reflectivity factor calculations in numerical cloud models using bulk parameterization of precipitation processes. J. A*ppl. Meteor., 14*, 1156-1165.

Snyder, C. and F. Zhang, 2003: Assimilation of simulated Doppler radar observations with an ensemble Kalman filter. Mon. *Wea. Rev., 13*1, 1663-1677.

Sun, J. and N. A. Crook, 1997: Dynamical and microphysical retrieval from Doppler radar observations using a cloud model and its adjoint. Part I: Model development and simulated data experiments. J. A*tmos. Sci., 54*, 1642-1661.

—, 1998: Dynamical and Microphysical Retrieval from Doppler Radar Observations Using a Cloud Model and Its Adjoint. Part II: Retrieval Experiments of an Observed Florida Convective Storm. J. At*mos. Sci., 55,* 835-852.

Sun, J., D. W. Flicker, and D. K. Lilly, 1991: Recovery of three-dimensional wind and temperature fields from simulated single-Doppler radar data. J. At*mos. Sci., 48,* 876-890.

Tong, M. and M. Xue, 2005a: Ensemble Kalman filter assimilation of Doppler radar data with a compressible nonhydrostatic model: OSSE Experiments. Mon. *Wea. Rev., sub*mitted.

—, 2005b: Ensemble Kalman filter assimilation of Doppler radar data with a compressible nonhydrostatic model: OSS Experiments. Mon. W*ea. Rev., 133, 1789-1807*.

Warner, J., 1970: On steady-state one-dimensional models of cumulus convection. J. Atm*os. Sci., 27,* 1035-1040.

Weygandt, S. S., A. Shapiro, and K. K. Droegemeier, 2002a: Retrieval of Model Initial Fields from Single-Doppler Observations of a Supercell Thunderstorm. Part I: Single-Doppler Velocity Retrieval. Mon. W*ea. Rev., 130,* 433-453.

—, 2002b: Retrieval of Model Initial Fields from Single-Doppler Observations of a Supercell Thunderstorm. Part II: Thermodynamic Retrieval and Numerical Prediction. Mon. We*a. Rev., 130,* 454-476.

Wicker, L. J. and D. C. Dowell, 2004: High-resolution analyses of the 8 May 2003 Oklahoma City storm. Part III: An ultra-high resolution forecast experiment. Preprin*ts, 22nd Conf. Severe Local Storms,, Hyann*is, MA, Amer. Meteor. Soc., CDROM, 12.6.

Xu, Q., C. Qiu, and J. Yu, 1994: Adjoint-method retrievals of low-altitude wind fields

from single-Doppler reflectivity measured during Phoenix II. J. Atmos. *Oceanic Technology, 11, 2*75-288.

Xue, M., K. K. Droegemeier, and V. Wong, 2000: The Advanced Regional Prediction System (ARPS) - A multiscale nonhydrostatic atmospheric simulation and prediction tool. Part I: Model dynamics and verification. Meteor. *Atmos. Physics, 75, 1*61-193.

Xue, M., M. Tong, and K. K. Droegemeier, 2005: An OSSE framework based on the ensemble square-root Kalman filter for evaluating impact of data from radar networks on thunderstorm analysis and forecast. J. Atmos. *Ocean Tech., Under* review.

Xue, M., K. K. Droegemeier, V. Wong, A. Shapiro, and K. Brewster, 1995: ARPS Ver*sion 4.0 User's Guide. [Avai*lable at http://www.caps.ou.edu/ARPS], 380 pp.

Xue, M., D.-H. Wang, J.-D. Gao, K. Brewster, and K. K. Droegemeier, 2003: The Advanced Regional Prediction System (ARPS), storm-scale numerical weather prediction and data assimilation. Meteor. *Atmos. Physics, 82, 1*39-170.

Xue, M., K. K. Droegemeier, V. Wong, A. Shapiro, K. Brewster, F. Carr, D. Weber, Y. Liu, and D.-H. Wang, 2001a: The Advanced Regional Prediction System (ARPS) - A multiscale nonhydrostatic atmospheric simulation and prediction tool. Part II: Model physics and applications. Meteor. *Atmos. Phy., 76, 1*43-165.

Xue, M., K. K. Droegemeier, V. Wong, A. Shapiro, K. Brewster, F. Carr, D. Weber, Y. Liu, and D. Wang, 2001b: The Advanced Regional Prediction System (ARPS) - A multi-scale nonhydrostatic atmospheric simulation and prediction tool. Part II: Model physics and applications. Meteor. *Atmos. Phys., 76, 1*43-166.

Zhang, F., C. , Snyder, and J. Sun, 2004: Impacts of initial estimate and observations on the convective-scale data assimilation with an ensemble Kalman filter. Mon. We*a. Rev., 132,* 1238-1253.

Zhang, J., 1999: Moisture and Diabatic Initialization Based on Radar and Satellite Observation, School of Meteorology, University of Oklahoma, 194.

Zhang, J., F. Carr, and K. Brewster, 1998: ADAS cloud analysis. Preprin*ts, 12th Conf. on Num. Wea. Pred., Phoen*ix, AZ., Amer. Met. Soc., 185-188.

Appendix. Boundary Conditions of Multipass Recursive Filters

To mitigate the errors caused by lateral boundary conditions in recursive filter when it is used in a limited domain, Hayden and Purser (1995) derived general equations of boundary conditions for right-moving filter, which can simulate the effect of filter applied to infinite lines of values. The assumption of derivation is that all the filter coefficients along the line of values to be filtered are equal to the coefficient at the starting point at the edge of the domain. Then according to property that filters with uniform coefficients applied to infinite lines of values commute. The follow formula can be obtain,

$$\sum_{\mathrm{r}=0}^{p}(-\alpha)^{\mathrm{r}}C_r^p B_{r-1}^p = 0\,, \tag{A1}$$

which can be combined together with the following p equations obtained from the standard recursive filter definitions:

$$B_q^p = (1-\alpha)A_q^p + \alpha B_{q-1}^p, \text{ for } q = 0,\cdots,p-1, \tag{A2}$$

to give sufficient equations for the p+1 unknowns, $B_q^p, q = 0,\cdots,p-1,$. Where α is filter coefficient, A is input values and B is output values of a right-moving filter. Superscript p indicates the number of times the opposing filter has already been used in the production of this distribution A^p. Subscript q is the index of grid point, which 0 represents edge.

For the first right-moving filter, there is no left-moving yet and p = 0. Eq. A1 gives

$$B_{-1}^0 = 0$$

and Eq. A2 gives

$$B_0^0 = (1-\alpha)A_0^0 + \alpha B_{-1}^0.$$

Hence, the left boundary condition for first right-moving filter is

$$B_0^0 = (1-\alpha)A_0^0$$

The left boundary condition for second right-moving filter and right boundary condition for first left-moving filter each has one opposing filter, p=1, and they has same form. For example, the left boundary condition is decided by

$$B_{-1}^1 + (-\alpha)^1 B_0^1 = 0$$

$$B_0^1 = (1-\alpha)A_0^1 + \alpha B_{-1}^1.$$

Getting rid of unknown value B_{-1}^1, the left boundary condition for second right-moving filter is:

$$B_0^1 = \frac{(1-\alpha)A_0^1}{1-\alpha^2}$$

For the right boundary condition of first left-moving, replace index 0 to N+1, and get:

$$C_{N+1}^1 = \frac{(1-\alpha)B_{N+1}^1}{1-\alpha^2}$$

Follow the same procedure, the equations that can decide boundary condition of third right-moving filter are:

$$B_{-1}^2 - 2\alpha B_0^2 + \alpha^2 B_1^2 = 0$$

$$B_0^2 = (1-\alpha)A_0^2 + \alpha B_{-1}^2$$

$$B_1^2 = (1-\alpha)A_1^2 + \alpha B_0^2$$

Getting rid of unknown B_{-1}^2 and B_1^2, the boundary condition has form:

$$B_0^2 = \frac{(1-\alpha)}{(1-\alpha^2)^2}(A_0^2 - \alpha^3 A_1^2)$$

The second left-moving filter has the form of boundary condition but different index as follow:

$$C_{N+1}^2 = \frac{(1-\alpha)}{(1-\alpha^2)^2}(B_{N+1}^2 - \alpha^3 B_N^2)$$

For the forth right-moving, we have four equations from A1 and A2

$$B_{-1}^3 - 3\alpha B_0^3 + 3\alpha^2 B_1^3 - \alpha^3 B_2^3 = 0$$

$$B_0^3 = (1-\alpha)A_0^3 + \alpha B_{-1}^3$$

$$B_1^3 = (1-\alpha)A_1^3 + \alpha B_0^3$$

$$B_2^3 = (1-\alpha)A_2^3 + \alpha B_1^3$$

Getting rid of unknown variables B_{-1}^3, B_1^3 and B_2^3. The boundary condition is:

$$B_0^3 = \frac{1-\alpha}{1-3\alpha^2+3\alpha^4-\alpha^6}(A_0^3 - 3\alpha^3 A_1^3 + \alpha^4 A_2^3 + \alpha^5 A_1^3)$$

The boundary condition of third left-moving filter is:

$$C_{N+1}^3 = \frac{1-\alpha}{1-3\alpha^2+3\alpha^4-\alpha^6}(B_{N+1}^3 - 3\alpha^3 B_N^3 + \alpha^4 B_{N-1}^3 + \alpha^5 B_N^3)$$